



UNIVERSITÀ  
DEGLI STUDI  
DI PADOVA

#### English

This thesis is devoted for studying the tectonic features and the relationship between faults and pit-chains within Noctis Labyrinthus in order to reconstruct a deformational model of its formation which still poorly understood. In particular, we interpreted high-resolution remote sensing images, the kinematics, the intersection geometries and the cross-cutting relationship of the identified faults system. We finally produced a structural map of the concerned area and we proposed a succession of events responsible about the formation of the rift and troughs network in Noctis Labyrinthus.

While studying the extensional tectonic of Noctis Labyrinthus on Mars, we used NASA MDIS MESSENGER composed images to produce a geological map for 1/2 of the Eminescu (H-09) quadrangle. Precisely, we will deliver a morpho-stratigraphic map at 1:3M output scale as part of the global mapping project for Mercury's surface (Galluzzi et al., 2019), in the frame to support the ESA-JAXA BepiColombo mission to Mercury.

#### Italian

Questa tesi è dedicata allo studio delle caratteristiche tettoniche e del rapporto tra faglie e pit chains all'interno di Noctis Labyrinthus al fine di ricostruire un modello deformativo della sua formazione che è ancora piuttosto ignota. In particolare abbiamo interpretato immagini telerilevate ad alta risoluzione, la cinematica, le geometrie e le relazioni di intersezione tra i diversi sistemi di faglie riconosciuti. Abbiamo quindi realizzato una mappa strutturale per la zona concernata e abbiamo proposto una successione di eventi responsabili della formazione del sistema di rift e delle depressioni in Noctis Labyrinthus.

Mentre durante lo studio della tettonica estensionale di Noctis Labyrinthus su Marte, abbiamo utilizzato le immagini composte della sonda NASA MDIS MESSENGER per realizzare la carta geologica di 1/2 del quadrangolo Eminescu (H-09). Precisamente, forniremo una mappa morfo-stratigrafica con scala di output 1:3M come parte del progetto di mappatura globale della superficie di Mercurio (Galluzzi et al., 2019), al fine di supportare la missione ESA-JAXA BepiColombo su Mercurio.



Structural analysis of the fault networks in Noctis Labyrinthus (Mars)  
and preliminary geological mapping for 1/2 of the Eminescu (H-09) quadrangle in Mercury

Head Office: Università degli Studi di Padova

Centro di Ateneo di Studi e Attività Spaziali "Giuseppe Colombo" - CISAS

Ph.D. COURSE IN: SCIENZE TECNOLOGIE E MISURE SPAZIALI

CURRICULUM: Misure meccaniche per l'ingegneria e lo spazio

### Structural analysis of the fault networks in Noctis Labyrinthus (Mars) and preliminary geological mapping for 1/2 of the Eminescu (H-09) quadrangle in Mercury

Thesis written with the financial contribution of Fondazione CARIPARO

**Coordinator:** Prof. Francesco Picano

**Supervisor:** Prof. Matteo Massironi

**Co-Supervisor:** Ch.mo Prof. Stefano Debei

**Ph.D. student :** Mayssa El Yazidi

M. El Yazidi



Thesis cover:

Artistic view for Noctis Labyrinthus pit-chains and faults by Elena Rampazzo. Painting with "Acquerello" (28.01.2022, Padova)





UNIVERSITÀ  
DEGLI STUDI  
DI PADOVA

Head Office: Università degli Studi di Padova

Centro di Ateneo di Studi e Attività Spaziali "Giuseppe Colombo" - CISAS

Ph.D. COURSE IN: SCIENZE TECNOLOGIE E MISURE SPAZIALI

CURRICULUM: Misure meccaniche per l'ingegneria e lo spazio

**Structural analysis of the fault networks in Noctis Labyrinthus (Mars) and preliminary geological mapping for 1/2 of the Eminescu (H-09) quadrangle in Mercury**

Thesis written with the financial contribution of Fondazione CARIPARO

**Coordinator:** Prof. Francesco Picano

**Supervisor:** Prof. Matteo Massironi

**Co-Supervisor:** Ch.mo Prof. Stefano Debei

**Ph.D. student :** Mayssa El Yazidi

## *Declaration*

The author declares that the presented Ph.D. research project is an original work. This thesis contains no material published elsewhere or extracted in whole or in part from a thesis by which I have qualified for or been awarded another degree or diploma. No other person's work has been used without due acknowledgment in the main text of the thesis. This thesis summarises findings established on the basis of structural analysis and mapping, based on satellite data obtained from planetary probes: Mars Express, Mars Reconnaissance Orbiter, Mars Global Surveyor and Mercury Surface, Space Environment, Geochemistry, and Ranging. This work has been done in cooperation with the Department of Geosciences at the University of Padova, CISAS, INAF, PLANMAP, and GMAP authorities, namely my supervisor Prof. Matteo Massironi, Dr. Valentina Galluzzi, Dr. Riccardo Pozzobon, Dr. Luca Penasa, Prof. Angelo Pio Rossi and Prof. Francesco Mazzarini, are acknowledged.

Padova 16<sup>th</sup> November, 2022

Mayssa El Yazidi



## Abstract

The objective of my thesis is to carry out a model that describes the formational story of Noctis Labyrinthus rift system and troughs. This area has been a topic of many discussions due to its complexity and the poor understanding of the possible processes and mechanisms involved in its formation. Noctis Labyrinthus is formed by an extended branched network of scalloped Pit chains, faults and grabens of different dimensions and trends. Many models explained the formation of Noctis Labyrinthus karst landscape with associated caves and water-related processes (Weitz et al., 2011, Baioni et al., 2017, Rodriguez et al., 2016, Jackson et al., 2011, Bibring et al., 2006), a network of lava tubes (Leone, 2014), the product of a volcano-tectonic activity (Mège et al., 2003, Schultz, 1998) related to the Noctis Labyrinthus formation. However, up to date, none of these models has found a general consensus as a possible mechanism for Noctis Labyrinthus.

In this thesis we produced a structural map for all faults and graben in Noctis Labyrinthus, in order to analyse their geometrical attributes, kinematics, distribution, and orientations, but also to understand the tectonic context and the deformational history of this district. To achieve these objectives, the mapping has been realised using two HRSC orthoimages, bearing a resolution of 19.5 m/pixel, whereas the faults displacement and length have been extracted from MOLA DEM bearing a resolution of 463 m/px. We also mapped the pit chains and their floor which is often presenting Hummocky materials. After completing the mapping, the final results show a large distribution of faults, densely distributed on the southern sector, whereas the northern sector is characterised by NS faults, extended for tens of kilometres. We categorised the faults into two classes according to their size: i) Major faults (length > 4km) and, ii) Minor faults (length ≤ 4km). The analysis of the Displacement-Length scaling relationship in our work didn't support any proportional relationship for the fault's geometrical attributes. However, the cumulative frequency plot helped to identify that the minor faults are bounded to a shallow brittle mechanical layer while the major faults cut across the whole brittle crust. The analysis of the faults in Noctis Labyrinthus led to identify three main systems of faults oriented as the following: 1) NS and NNE faults, 2) EW and ENE-WSW faults and 3) NNW-SSE, NW-SE and WNW-ESE faults. The multiple cross-cutting relationship between these three fault systems didn't aid in identifying the deformational phases since some faults seem to be reactivated, however, the faults shaped intersections approach of Collanega et al., 2020 helped to have insight about the possible deformational phases. In particular, we identified two phases of perpendicular extension (bi-directional synchronous), and this has been supported by the dominant distribution of X-shaped and T-shaped intersections between the faults. The NS and NE-SW faults are most likely generated during the first phase, and they are expressed mainly on the north sector. This phase was subsequently followed by a second phase displayed by the formation of the ENE-WSW to EW fault system, expressed mainly on the south sector. These two faulting phases are followed by a final isotropic radial deformation developed in the south sector which reactivated few of the former faults but also generated a new fault system oriented NW-SE. During the formation of the second phase, pit chains developed in strict association with faults. In this thesis, we propose that pit chains are formed through a volcano-tectonic processes most likely associated to radial dike and concentric sheet

intrusions both departing from Syria Planum volcanic centre. Hence the grabens may be the expression of late structures concentric to Syria Planum and associated to hydrothermal fluid circulation.

As an additional work in this thesis, we carried out the geological mapping for ½ of the Eminescu quadrangle on Mercury. This mapping has been done in the frame of the 1:15M global mapping project (Galluzzi, 2019) for the surface of Mercury. The map will help target interesting surface features during ESA/JAXA Bepi-colombo space mission to Mercury, launched in October 2018, and scheduled to reach Mercury in 2025. To produce the map, we used data derived from MDIS, from NASA MESSENGER spacecraft. We followed the same symbology, mapping rules, unit and scale used by Galluzzi et al., 2019. Our preliminary analysis for the mapped area shows a large distribution of the craters with a dimension between 5 to 20 km more than craters with a diameter of < 5 km. Some craters present a smooth floor but with degraded or old rims, indicating that volcanoes have been responsible for the resurfacing of some districts. Several impact craters and basins are cross-cut by lobate scarp and swarm of wrinkle ridge within their floor, as the case of the Beagle rupes that deform the floor of Sveinsdóttir crater, creating a complex feature.

# Acronyms

**BDR:** Basemap reduced **Data Record**

**DTM:** Digital Terrain **Model**

**GY:** Giga **Year**

**HIE:** High-Incidence **East-illumination**

**HIW:** High-Incidence **West-illumination**

**HRIC:** High **Resolution Imaging Channel**

**HRM:** High **Reflectance Materials**

**HRSC:** High **Resolution Stereo Camera**

**LHB:** Late **Heavy Bombardment**

**LOI:** **LOW-Incidence Angle**

**MDIM:** Mars **Digital Image Model**

**MGS:** Mars **Global Surveyor**

**MLA:** Mercury **Laser Altimeter**

**MOC:** Mars **Orbiter Camera**

**MOLA:** Mars **Orbiter Laser Altimeter**

**MY:** Million **year**

**NAC:** Narrow **Angle Camera**

**STC:** **STereo imaging Channel**

**THEMIS:** **THermal EMission Imaging System**

**VIHI:** Visible and near-**Infrared Hyperspectral Imaging channel**

**WAC:** Wide **Angle Camera**



# Table of contents

<b>Declaration</b> .....	<b>IV</b>
<b>Abstract</b> .....	<b>V</b>
<b>Acronyms</b> .....	<b>VII</b>
<b>Table of contents</b> .....	<b>VIII</b>
<b>1. Introduction</b> .....	<b>9</b>
<b>2. Mars: Overview</b> .....	<b>10</b>
<b>2.1.Tharsis rise and Syria Planum provinces</b> ... ..	<b>15</b>
<b>2.2.Valles Marineris and the related rift system</b> .....	<b>22</b>
<b>3. Noctis Labyrinthus mapping and faults analysis</b> .....	<b>27</b>
<b>3.1.Datasets</b> .....	<b>29</b>
<b>3.2.Methodology</b> .....	<b>34</b>
<b>3.3.Results</b> .....	<b>37</b>
3.3.1. General framework.....	37
3.3.2. Cumulative throw and faults density.....	47
3.3.3. Faults system in North and South transect and kinematic indicators.....	50
3.3.4. Pit chains and faulting.....	61
<b>3.4. Discussion</b> .....	<b>68</b>
<b>4. Mercury: Overview</b> .....	<b>72</b>
<b>5. Eminescu (H-09): Mapping and structural study</b> .....	<b>94</b>
<b>5.1.Basemaps and topographic datasets</b> .....	<b>95</b>
<b>5.2.Mapping strategy</b> .....	<b>97</b>
<b>5.3.Preliminary mapping results</b> .....	<b>99</b>
<b>5.4.Bepicolombo-SIMBIOSYS priority target definition</b> .....	<b>104</b>
<b>5.5.Compressive deformation within the b12 basin on Eminescu</b> .....	<b>109</b>
<b>5.6.Discussion on Eminescu geological features mapping</b> .....	<b>111</b>
<b>6. Discussions and conclusions</b> .....	<b>113</b>
<b>Appendix A</b> .....	<b>116</b>
<b>A.1. Mercury MESSENGER MDIS Basemaps</b> .....	<b>116</b>
<b>References</b> .....	<b>124</b>

## Chapter I – Introduction

Tectonism and volcanism majorly contributed to the surface geomorphology and the geological history for Mars and Mercury. This has been recorded on their bedrocks and distinctly expressed on the surface of these planets. The surface of Mars displays huge and very large volcanoes, some of them possibly related to very recent activity. These volcanoes are covering a large area of the planet's surface (Horvath et al., 2021), and represented by the two major volcanic provinces of Tharsis and Elysium, as well as the volcanic unit of Hesperia Planum, Malea Planum and Syrtis Major, and some other regions possibly related to explosive volcanism like Tyrrhena and Hadriaca Paterae (Crown & Greeley, 1993).

On Mars, a marked topographic difference is observed between the young plains in the northern hemisphere and the old terrain in the south. This division is described by the North-South dichotomy, separates the highland from the lowland terrain and is expressed by dramatic difference in the morphology, the structural characteristics, the crustal thickness and the crater density and distribution. Several hypotheses based on endogenic and exogenic factors have been proposed to explain this difference between the Martian hemispheres like: two tectonics plates, mantle overturn, or a large meteorite impact (Robinson, 1995, Lenardic et al., 2004, Watters et al., 2007, Citron et al., 2018). Tectonic features are expressed on different districts, and in close vicinity or associated to certain volcanic provinces (e.g., Tharsis and Elysium Planitia). In particular mentioning, the extensional tectonic in the western hemisphere within Valles Marineris, Olympus mons, Alba patera, Noctis Labyrinthus, and many other districts (Schultz, 1991, Wilson & Head, 1994, Werner, 2009, Yin, 2012a, 2012b).

Further, Mercury is characterised by its old and densely-cratered surface, with a frequency distribution for the large craters of 100-500 km in diameter (Rothery, 2015). According to previous studies, the tectonism in Mercury seems to have been initiated probably before 3.5 GY. Most of the surface of this planet displays compressional features such as lobate scarp and wrinkle ridges (Rothery & Massironi, 2010, Giacomini et al., 2020). Global contraction of the planet has been supported by the frequent distribution of the lobate scarps, indicating the predominance of the contractional features compared to the extensional ones (Rothery & Massironi, 2010, Byrne, 2014). The effusive volcanism in Mercury developed mainly before 3.5 GY ago, due to the planet cooling and contraction (Rothery, 2015).

## Chapter II – Mars: Overview

Mars was highly reached by space missions, around 42 space probes including 17 orbiters, 8 Landers, 6 rovers, and one helicopter was dedicated to studying this planet from different perspectives (Composition, geology, atmosphere, seismology, stratigraphy). A formalised stratigraphy presented within the 25M geologic map for Mars was realised by Scott & Carr, 1978 based on crater counting for craters with 4-10 km of diameter, together with the overlap relations and degradational degree. The map units were classified and placed into three stratigraphic periods (Fig 2.1):

- Noachian (4.1 - 3.7 GY): Characterised by rugged, heavily cratered material;
- Hesperian (3.7 - 2.9 GY): Characterised by ridged plains material;
- Amazonian (2.9 GY - to present): Characterised by relatively smooth, moderately cratered plains materials and polar deposits.

A period of pre-Noachian origin has been also identified, even without physical evidence for its existence. The names for these stratigraphic sequences were selected from regions having representative and widespread exposures of the terrains used as reference (Scott & Carr, 1978, Tanaka, 1986, Werner et al., 2011).

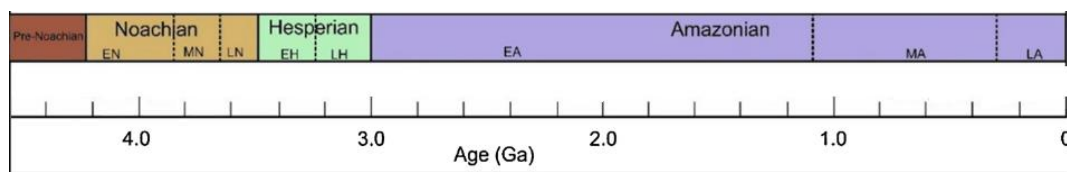


Figure 2.1. Mars geologic aeons (After Grady., 2020-Modified)

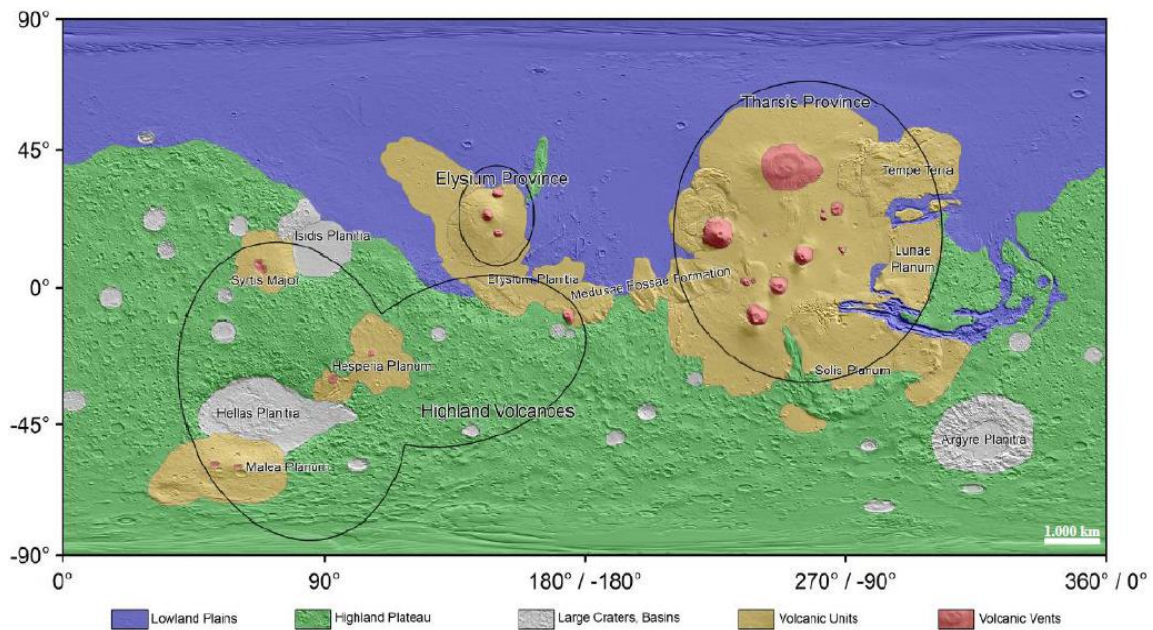
The volcanic activity on Mars seems to have started at a very early age (Hartmann et al., 1999, Neukum et al., 2004). This long period of volcanism generates the formation of different styles of volcanoes that played a major role in the planet's resurfacing (Wilson & Head, 1994). It has been estimated that the surface of Mars is covered by almost 46% of volcanic flows (Greeley & Schneid, 1991). The total volume of extrusive and intrusive magma generated on Mars for over the last approximately 3.8 GY was estimated to be  $654 \times 10^6 \text{ km}^3$  for magma flow rates of about  $0.17 \text{ km}^3/\text{yr}$  (Greeley & Schneid, 1991, Wilson & Head, 1994). The extensive volcanism on Mars is uniformly expressed on the surface (Werner, 2009), represented by diverse volcanic landforms, plains and domes. The lack of plate tectonics accounts for the enormous volcanoes of Elysium and Olympus Mons since the magmatic activity remained focused in one place for a long period (Wilson & Head, 1983), with volcanic eruptions separated by long temporal intervals (Wilson & Head, 1983).

When the gravity of the planet is low, this means lower buoyancy hence larger volumes needed for the magma to reach the surface and this indicates larger dikes (Wilson & Head, 1994). Dikes in this case would be several times larger compared to the dikes in the Earth, and therefore the amount of lava erupted could be 5 times greater. Moreover, the magma chambers on Mars are expected to be deeper than on Earth, and the lava flows are longer due to the gravity. Indeed, the gravity on Mars is low, the lava flows can be thicker, and don't cool as effectively. As a response to the low gravity and wide dikes on Mars, the lava flows can be six times longer than those on Earth (Wilson & Head, 1994).



Carr & Head, 2010 proposed that volcanism was started in the Noachian period ( $< 3.7$  Ga) on Mars, however, some districts are dating to the late Amazonian (200 to 100 Ma) within the Tharsis region, expressed by patches of smoothly young terrains (Werner, 2009). Two major volcanic provinces have been documented on the surface of Mars: Tharsis and Elysium provinces (Fig 2.2). In addition to these major volcanic provinces, some other regions reveal indications of explosive volcanic activity, like for example the Tyrrhena Patera and Hadriaca Patera.

Olympus Mons is a large shield volcano on Mars, located between  $18^{\circ} 39'N$  and  $226^{\circ} 12'E$ , bordered by Alba Patera on the Northeast, Amazonis Planitia on the Northwest and Tharsis rise on the southeast. This volcanic construct is composed of basaltic lava accumulations (Carr, 1973, Greeley & Spudis, 1981), and it's characterised by 624 km of basal diameter, 25 km high, and surrounded by a nearly circular escarpment of 6 km. The caldera on the summit is about 80 km wide (Fig 2.3. a), some lobes of voluminous aureole deposits (Helgason, 1999) distributed beyond the escarpment in an asymmetric ring of landslide deposits (De Blasio, 2011, Crosta et al., 2018). The volcanic construction of Olympus Mons might be dated in between 3.67-3.53 GY (Isherwood et al., 2013), others suggested a much younger age, that could be the late Amazonian era  $< 300$  MY (Scott & Tanaka, 1986, Hartmann & Neukum, 2001).



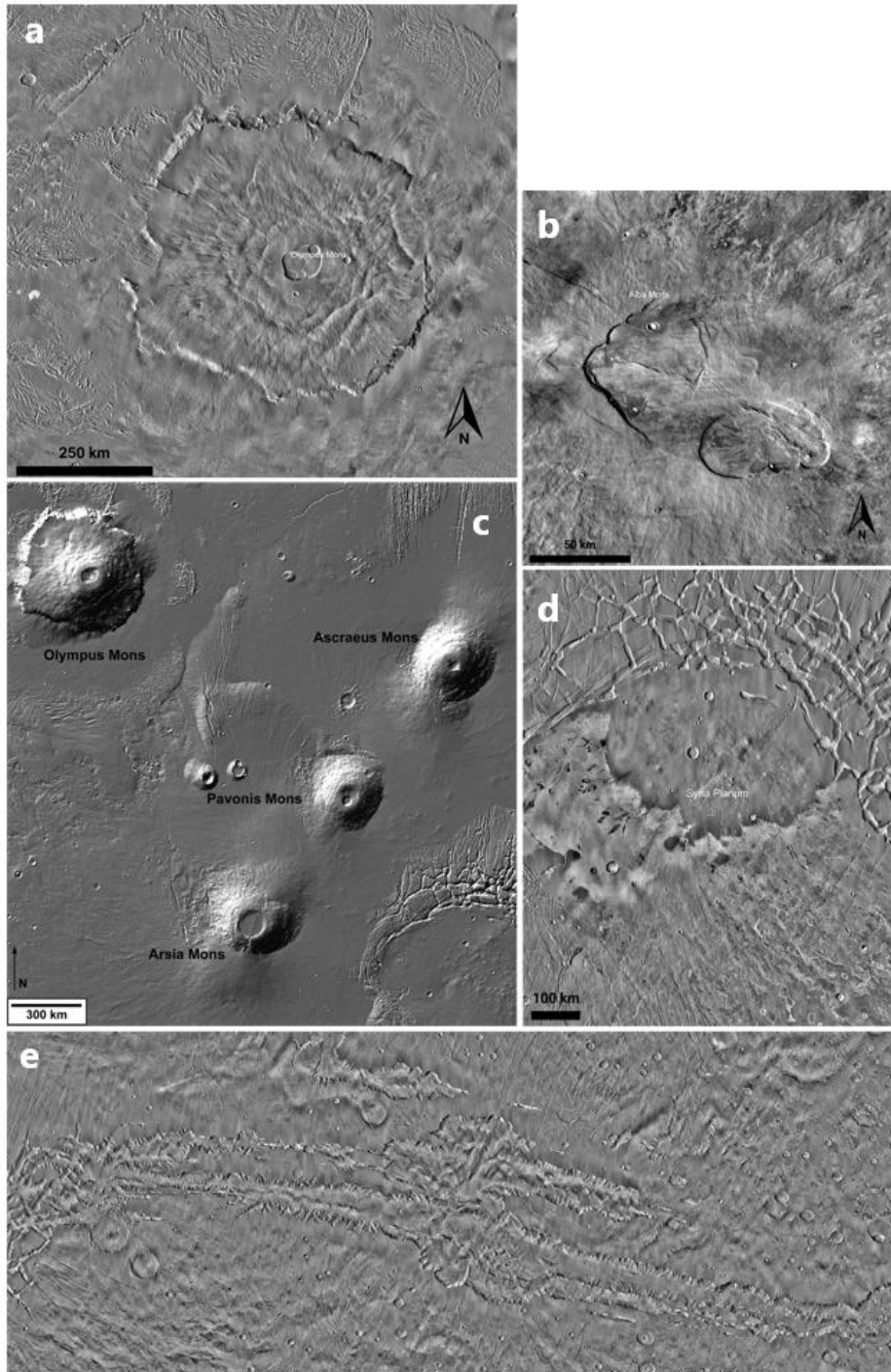
**Figure 2.2.** Tharsis and Elysium volcanic provinces are marked with black circles. The Highland volcanoes in the south are identified by volcanic units. The low shield volcanoes of the Syria Planum are not marked here. The NS dichotomy is well-observed between the lowland plains and highland plateau. The background topography is given as a MOLA shaded-relief map (After Werner, 2005).

Alba Mons, known also as Alba Patera, belongs to the Tharsis region, located on the northeast margin of the Olympus Mons and with the summit, centred at  $245-255^{\circ}E$ ,  $32.5-47.5^{\circ}N$ . Alba Patera is one of the most prominent features of magmatic-driven activity identified in the Tharsis district, and it's characterised by a set of grabens that extend from the south of the Alba Mons up to the northern plains. This low-relief volcano is the biggest volcano on Mars in terms of surface area, and it is characterised by volcanic flow fields

that extend for a minimum of 1,350 km, (Fig 2.3.b). Alba Mons is a relatively young shield volcano, about 6.8 km high. This volcano, characterised by a complex and unusual shape of caldera, appears as a unique feature on the Tharsis region, identified by ~170 km by 100 km across at the centre of the summit dome with a small caldera in the southern side of ~ 65 km by 45 km. Around the periphery, two grabens extend in the north-south direction, and curve around this volcano: the Alba Fossae on the west, and Tantalus Fossae on the east. The identification of the pyroclastic deposits in the Alba Patera region, suggests that this district could be transitional form a older pyroclastic-dominated highland paterae to a younger effusive central-vent like the shield volcanoes of the Tharsis area (Chuang et al., 2019), and there with the volcanic deposits of Alba Patera straddle the transition from the Hesperian to the Amazonian systems (Scott & Tanaka, 1986, Ivanov & Head, 2006).

On the southeast of Olympus Mons, and in the top northwest of Valles Marineris is located the outstanding three enormous shield volcanoes of the Tharsis volcanic plateau named from south to north: Arsia Mons, Pavonis Mons, and Ascraeus Mons, (Fig 2.3.c). They are spaced at an average of 500 km from each other and the whole volcanic province covers nearly a quarter of the planet's surface (Hodges & Moore, 1994, Richardson et al., 2013). Some data suggest a gradual formation of this volcanic trio, starting by the formation of the Arsia Mons up to Ascraeus Mons (Beuthe et al., 2012), perhaps by the movement of one mantle plume under the surface. The terrains in this region seem to be of basaltic composition.

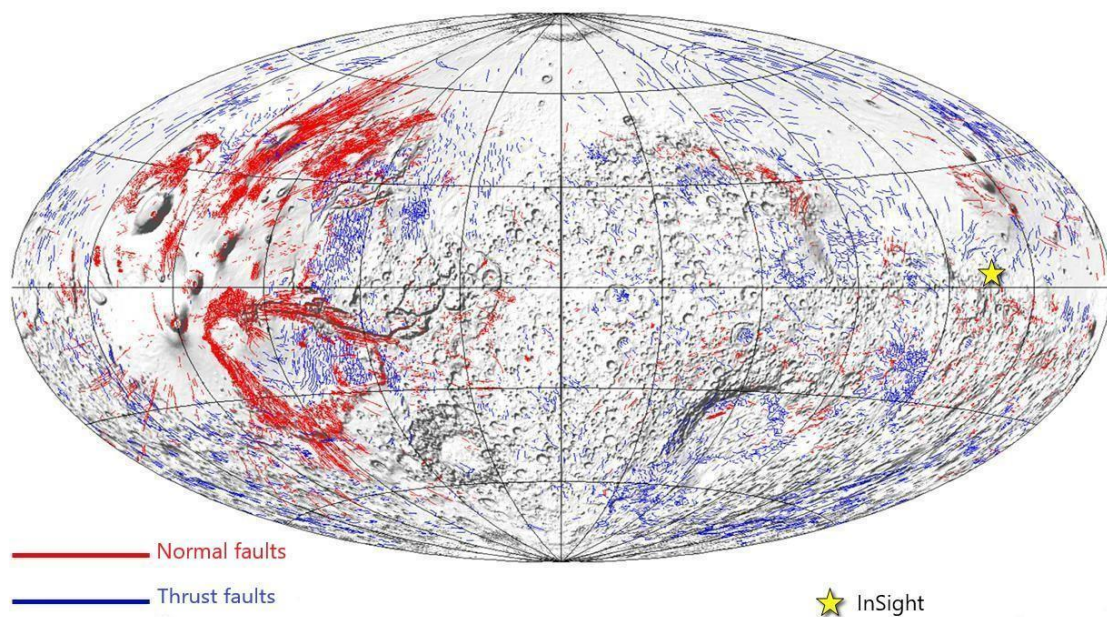
To the SE of the Tharsis alignment is the broad shield of Syria Planum, identified by the coordinates 8-23°S and 110-93°W, bordered by Claritas Fossae to the west, Solis Planum to the southeast, and Noctis Labyrinthus to the north (Fig 2.3.d). This region appears as a very smooth and young terrain, created by small volcanic edifices with 10s of km in diameter, and extensive volcanic plains, forming a regional plateau with a maximum elevation of 8000 m according to the MOLA data (Richardson et al., 2013). This district displays a combination of volcano-tectonic activity during its evolutionary stage (Baptista et al., 2008). A study released by Richardson et al., 2013, shows that Syria Planum presents a minimum of 263 vents, in between 205 catalogued as volcanic vents and 58 catalogued to be possibly volcanic. Syria Planum have been several times recalled as the most prominent features for a magmatic-driven activity identified in the Tharsis bulging (Anderson et al., 2004, Yin, 2012), and displays a series of graben occurring over great distances. The age of Syria Planum is suggested to be Noachian-Early Hesperian (Mège & Masson, 1996, Brustel et al., 2017), but not a precise age has been identified yet.



**Figure 2.3.** Tharsis province and the most important regional topographic features. (a) Olympus Mons volcano (b) A view of Alba Mons complex caldera, showing the large NW and small SE caldera (c) A shaded relief view of the Tharsis trio with the Olympus Mons on the top west and Noctis Labyrinthus on the southwest, distinguished by the related rift system and troughs. The image is obtained from MOLA datasets onboard MGS. Photo credit: ESA (d) Syria Planum plain with its related volcanic edifices, limited by the rift systems of Noctis Labyrinthus from the top north (e) THEMIS Day IR Global Mosaic for the Valles Marineris (100m/px). The widest segment on the central part of the Valles Marineris is called Melas Chasma, in the top north of the image, we found Candor Chasma, one of the largest troughs in the Valles Marineris, divided into two equities: The East and West sector. The width of the image is about 2670 km (d). The figures (a), (b), (c) and (d) are displayed over THEMIS Day IR 100m/px global mosaic from Mars Odyssey Orbiter.

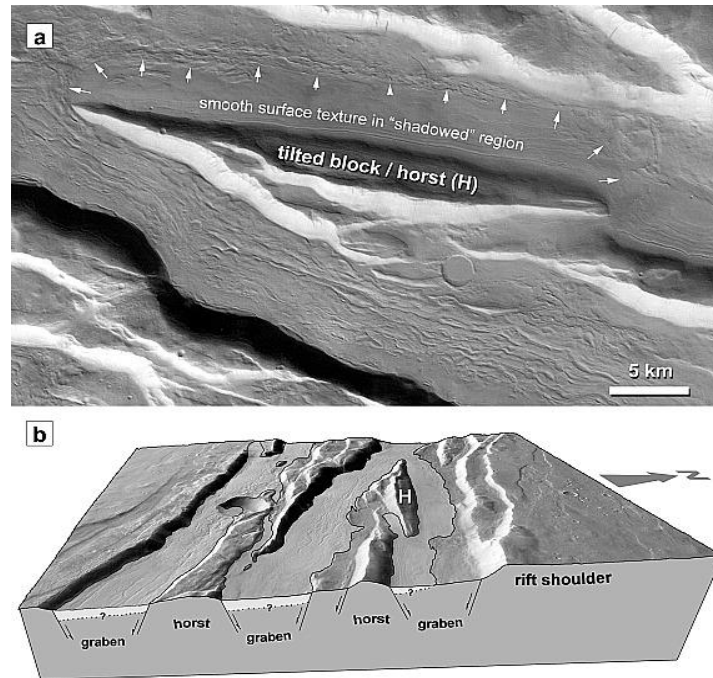


Up to date, there is no evidence of plate tectonics on Mars, and this is suggesting that the structural features in this planet are probably formed in one single and stable plate (Sleep, 1994, Platz et al., 2015). The crustal deformation on Mars is reported to be initiated immediately after its origin, at about 4.6 GY (Baker et al., 2007), and it is expressed by extensional (grabens, normal faults) and compressional (wrinkle ridges and lobate scarps) features (Fig 2.4), globally abundant on the surface, accompanied by intensive volcanism. The most common type of extensional tectonic feature on Mars is simple graben; these grabens define the enormous radial fracture system around Tharsis (Wise et al., 1979). The surfaces evidence shows recent deformation from the Amazonian epoch, and this has been supported by an additional observation related to some tectonic processes that are younger than the volcanic units since some fault-bounded tectonic grabens are not filled with lava and are associated to relatively smooth young terrains (Brož, 2010). All these evidences suggest that faulting was active less than a few tens of millions of years ago.



**Figure 2.4.** Structural map for Mars's surface, indicating the distribution of normal and thrust faults. Map in Hammer's projection, centred to 0°N 0°E (Image credit: DLR -Modified).

Other than Valles Marineris, Acheron Fossae is a particularly well-developed system of grabens (Fig 2.5). The eastern Acheron Fossae rift is interpreted to be related to a volcanic centre, caused by local magmatic uprisings with a related involvement of the lithosphere. The extension across the Acheron Fossae reaches values between 1.2 km and 8.7 km, and the crater counting indicates an absolute age between ~3.9 GY and 3.7 GY for the rifting. Various large graben systems in the Claritas region, in Tempe Terra, and in the Thaumasia province have been also considered as possible rift structures. All these complex extensional systems are tens to hundreds of kilometres wide and sometimes more than a thousand kilometres long; some of them are associated with volcanic centres (Tanaka et al., 1991, Anderson et al., 2001, Hauber & Kronberg, 2005, Kronberg et al., 2007).



**Figure 2.5.** Acheron Fossae grabens topographic depressions from HRSC orbit 37 (a) Example of a graben filled with young smooth deposits (b) 3D view of the same region noted by the letter “H” in (a). The figure displays a series of successive graben, expressed by the configuration of “Horst/graben” (After Kronberg, 2007).

## 2.1. Tharsis rise and Syria Planum provinces

The Tharsis volcanic and tectonic activity are probably started in the early Noachian, between 4.1-3.95 GY, accompanied by a crustal thickening developed during the mid-late Noachian, from 3.95 to 3.7 GY, (Johnson & Phillips, 2005, Brustel et al., 2017). The striking Tharsis region that extends for almost 25% of Mars's surface hosts essentially most of the volcanic activity on Mars. This volcanic province is elevated to 11 km, encountering the NS dichotomy on the top, extending in the NW by the sharp topographic edges of the Olympus Mons, Acheron Fossae and Alba Patera from the NW (Carr, 1974, Andrews-Hanna et al., 2008a, Werner, 2009, Yin, 2012). In the NE of this region are located the Ascraeus, Pavonis, Araia Montes, and Valles Marineris. The Tharsis volcanotectonic activity is estimated to be started in early epoch, perhaps during the Noachian (4.1-3.95 GY), but some features suggest a recent activity dating to the late Amazonian (Anderson et al., 2001, Richardson et al., 2013). This province includes five major shield volcanoes, seven partly buried volcanoes, vast lava plains, and a vast range of smaller eruptive vents (Greeley & Spudis, 1981, Mouginis-Mark et al., 1992, Hodges & Moore, 1994, Richardson et al., 2013).

The Tharsis rise formational history has been attributed to magmatic underplating and consequent mantle uplift in several previous studies (Wise et al., 1979, Mège & Masson, 1996a, 1996b, Baker et al., 2007, Dohm et al., 2007, Yin, 2012). Some models suggested that the Tharsis highland might be also generated by a voluminous volcanic deposit induced by lithospheric deformation or an impact (Sleep, 1994, Yin, 2012). The

volcanism within the Tharsis province could be represented by four grouped volcanic eruption centres initiated from the NE segment (Yin, 2012):

- The first centre (Late Noachian - Early Hesperian): Most of the volcanoes lie in the SE margin (Thaumasia Plateau and Coprates rise) and expand afterward to the NW (Fig 2.6). Perhaps some volcanic edifices were also placed within the Valles Marineris during this period (Williams et al., 2003).

- The second centre (Early Hesperian): The activity moved northward (Fig 2.6) of Syria Planum and was expressed by a volcanic-plain unit (Dohm & Tanaka, 1999). Small shield volcanoes (5-20 km of diameters), were potentially formed across Syria Planum (Baptista et al., 2008). However, this zone might record local later-stage volcanism, possibly related to the Amazonian epoch (Dohm et al., 2001).

- The third centre (Late Hesperian-Late Amazonian): The volcanic plains during this epoch are related to the Tharsis trio plus Uranus Patera and the volcanoes in northern Tempe Terra (Yin, 2012). The Tharsis volcanic eruption is described by diffusely volcanic effusion along small volcanic veins (Bleacher et al., 2007, 2009, Yin, 2012). The shield volcano of the Syria Planum and its surrounding plains were affected by NE-oriented graben systems from the Late Amazonian (Platz et al., 2015, Yin, 2012).

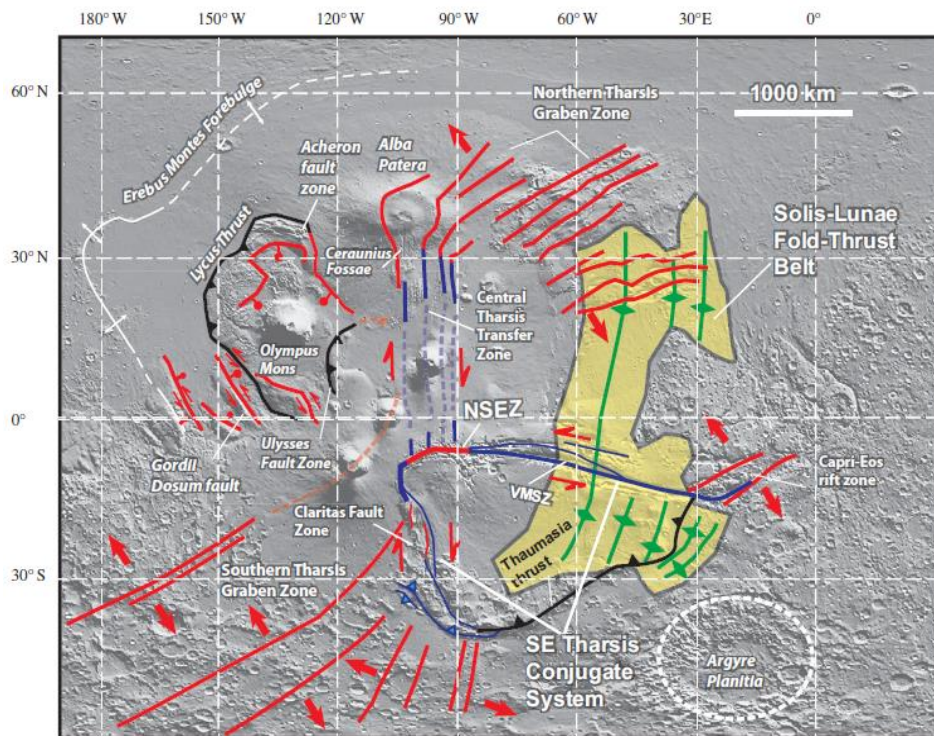
- The fourth centre (Started from Latest Hesperian/Early Amazonian -?): Includes the Olympus Mons and Alba Patera. The Hesperian Eruptions at Alba Patera shows that volcanism in the SE appears younger compared to the NE and it's dominated by lava fields without obviously identified sources. This region has been classified as a regional centre of magmatic and tectonic activity within the Tharsis rise (Anderson et al., 2001, Yin, 2012), and seems to be active recently (Scott & Tanaka, 1986, Hartmann & Neukum, 2001, Werner, 2009, Yin, 2012).

Different faults systems with diverse kinematics are documented within the Tharsis district (Wise et al., 1979, Plescia & Saunders, 1982, Scott & Tanaka, 1986, Schultz & Tanaka, 1994, Dohm & Tanaka, 1999, Schultz, 2000, Anderson et al., 2001, 2004, Anderson et al., 2001, 2004, 2008, Andrews-Hanna et al., 2008b, Yin, 2012a, 2012b), and these faults might be grouped into eight different faults systems (Fig 2.6 and Fig 2.7):

- System 1: Is the Tharsis graben zone, formed by large S-shaped grabens which pass across the Tharsis rise diagonally. The central segment of this graben system extends from Claritas Fossae to the south of Alba Patera, overlapped by young volcanic flows from Syria Planum and Ascraeus Mons. This graben is in turn superimposed by the NE-oriented grabens related to Noctis Labyrinthus which is linked with the Valles Marineris faulting district (Tanaka & Davis, 1988, Carr & Head, 2010, Yin, 2012).

- System 2: Formed by the Solis-Lunae fold and thrust belt that was probably created in the Early Hesperian (Watters, 1993) however, recent studies suggest that this fold and thrust belt could be dated even to the Noachian (Dohm et al., 2001), and perhaps prior to the embryonic stage of Tharsis.

- System 3: Consist of the Thaumasia thrust, and it was formed probably during the Early Noachian (Schultz & Tanaka, 1994, Dohm et al., 2001, Baker et al., 2007, Dohm et al., 2007, Yin, 2012).
- System 4: This is constituted by the Valles Marineris trough system (Masson, 1977,1985, Frey, 1979, Plescia & Saunders, 1982, Lucchitta et al., 1992, Peulvast & Masson, 1993, Schultz & Lin, 2001).
- System 5: This sequence contains the Lycus thrust (Harris,1977), expressed in NE trend and continues to the NW edge of Acheron Fossae by a left-slip transpressional fault system (Yin, 2012).
- System 6: It is the Gordii Dorsum fault zone (Forsythe & Zimbelman, 1988) which display a system of normal faults (Scott & Tanaka, 1986) or a left-lateral strike-slip fault (Forsythe & Zimbelman, 1988). However, a recent study by Yin, 2012, suggests the presence of left-transensional kinematics. The Gordii Dorsum southside is buried by the Tharsis Montes magmatic flow.
- System 7: Formed by the Acheron fault zone (Kronberg et al., 2007). This region is characterised by EW normal faults.
- System 8: It's the Ulysses fault zone (Scott & Dohm, 1990), an arc-shaped topographic feature in the NW of the Tharsis rise and SE of Olympus Mons, possibly dating to the Amazonian. The origin of the Ulysses thrusts could be related to a west-directed thrust fault. These thrust faults are limited to the west by the old aureole deposits of Olympus Mons. The formation of the Ulysses Fossae, seems to be coeval with the early volcanic phase of the Tharsis region, and probably postdates the principal phase of Olympus Mons development.

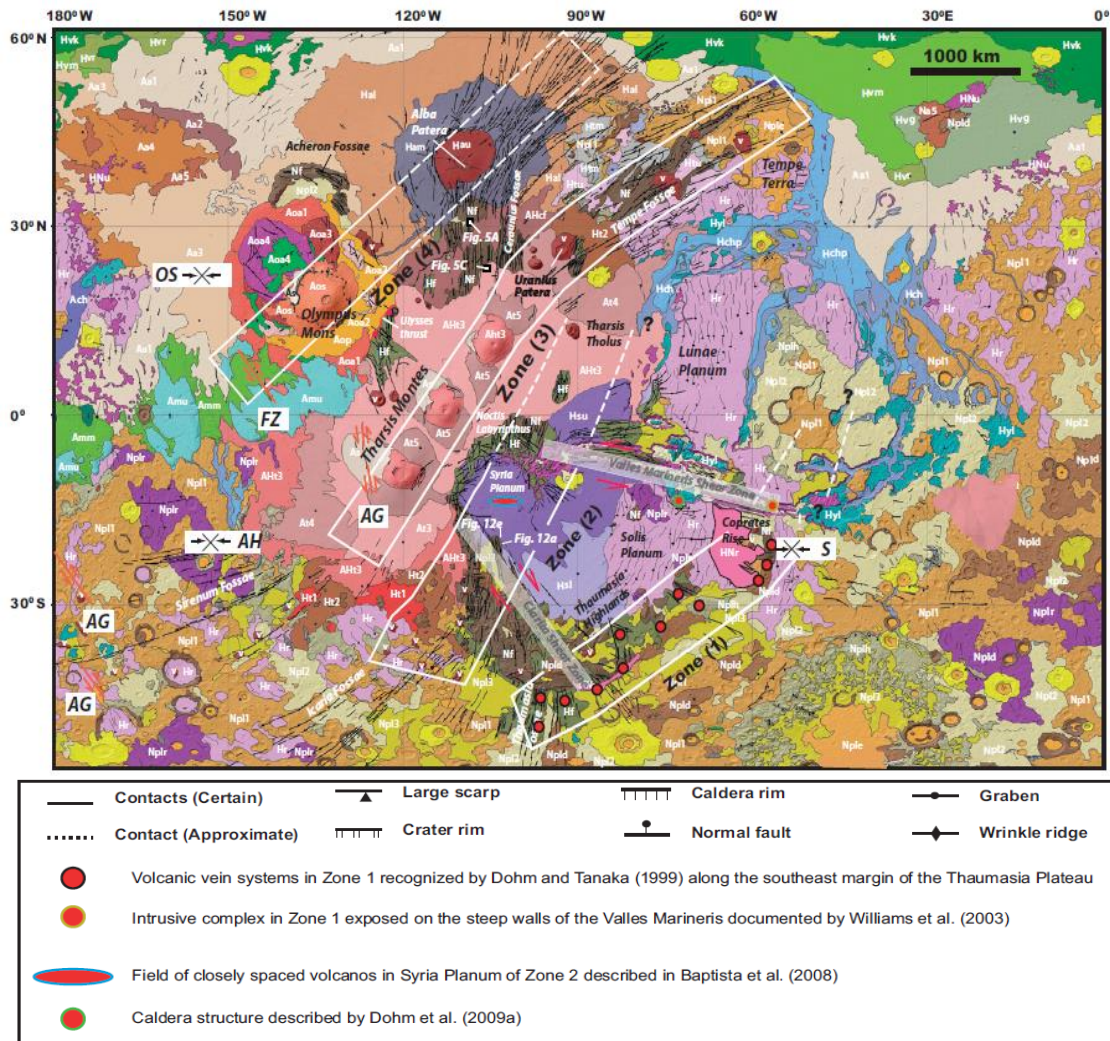


**Figure 2.6.** Tharsis rise and the main tectonic features as described during the eight fault systems. The Red lines represent the trends of the major extensional structures, the black lines represent the thrust faults, the blue lines represent transtensional strike-slip fault zones, the green lines define the traces of major folds expressed as wrinkle ridges and the white lines represent the concluded trace of the flexural bulge. NSEZ is the Noctis Labyrinthus-Syria Planum Extensional Zone and VMSZ is the Valles Marineris Shear Zone (After Yin, 2012).

The large and extensive activity of the Tharsis bulge yielded to an intensive period of several distinct magmatic and tectonic centres observed even with stratigraphic relations at the surface. Grabens are radially prominent around the Tharsis rise and this was interpreted to be caused by the dike injection (Mège & Masson, 1996, Wilson & Head, 2002). These arcuate dikes are directed towards Syria Planum are probably associated with the early stage of Tharsis volcanism and the graben systems formations.

Within the NE segment of Tharsis, are identified old and intensively fractured terrains, locally superposed by very young volcanic units including the low shield volcanoes of Syria Planum (Brož, 2010). These shield volcanoes are typically distributed in groups or “clusters” (Hauber et al., 2010) and seem to be related to the faults and grabens of the area (Wilson & Head, 1983). Recent studies in southern highlands of Mars, demonstrate two distinct dominant phases of tectonic activities: The first phase is an extensional event, ended at around 3.8 GY, while the second phase is compressional, and ended approximately 3.5-3.6 GY. The prior prevails in the western hemisphere (Golombek & Phillips, 2010, Ruj et al., 2019), and have been explained as an incipient development of Tharsis and surrounding districts (Anderson et al., 2001).





**Figure 2.7.** Tharsis rise geologic map after Scott & Tanaka., 1986. The white boxes are the four grouped volcanic eruption centres as described in the above text. The AG, FZ, AH, OS, and S are all locations where strike-slip faults have been identified around the Tharsis rise margin. Lithology units based on age according to Scott and Tanaka., 1986; Skinner et al., 2006: *N*—Noachian; *H*—Hesperian; *A*—Amazonian; *Nf*—highly fractured Noachian terrane; *Npld*—highly eroded crater unit consisting of a mixture of lava flows, pyroclastic material, and impact breccias; *Nplh*—relics of highland volcanic rocks and impact breccia; *Hr*—extensive flows of low viscosity erupted in the Early Hesperian; *Ht1*, *Ht2*, *AHt3*, *At4*, *At5*, *At6*—volcanic units in the Tharsis Montes region; *Aoa1*, *Aoa2*, *Aoa3*, *Aoa4*—units in the Olympus aureole zone; *Aos*, *Aop*—lava flow units from Olympus Mons; *Hal*, *Aam*, *Aau*—volcanic units of the Alba Patera; *Htl*, *Htm*, *Htu*—Tempe Terra Formation consisting of many small (<10 km in diameter) central volcanoes and collapsed structures (After Yin, 2012)

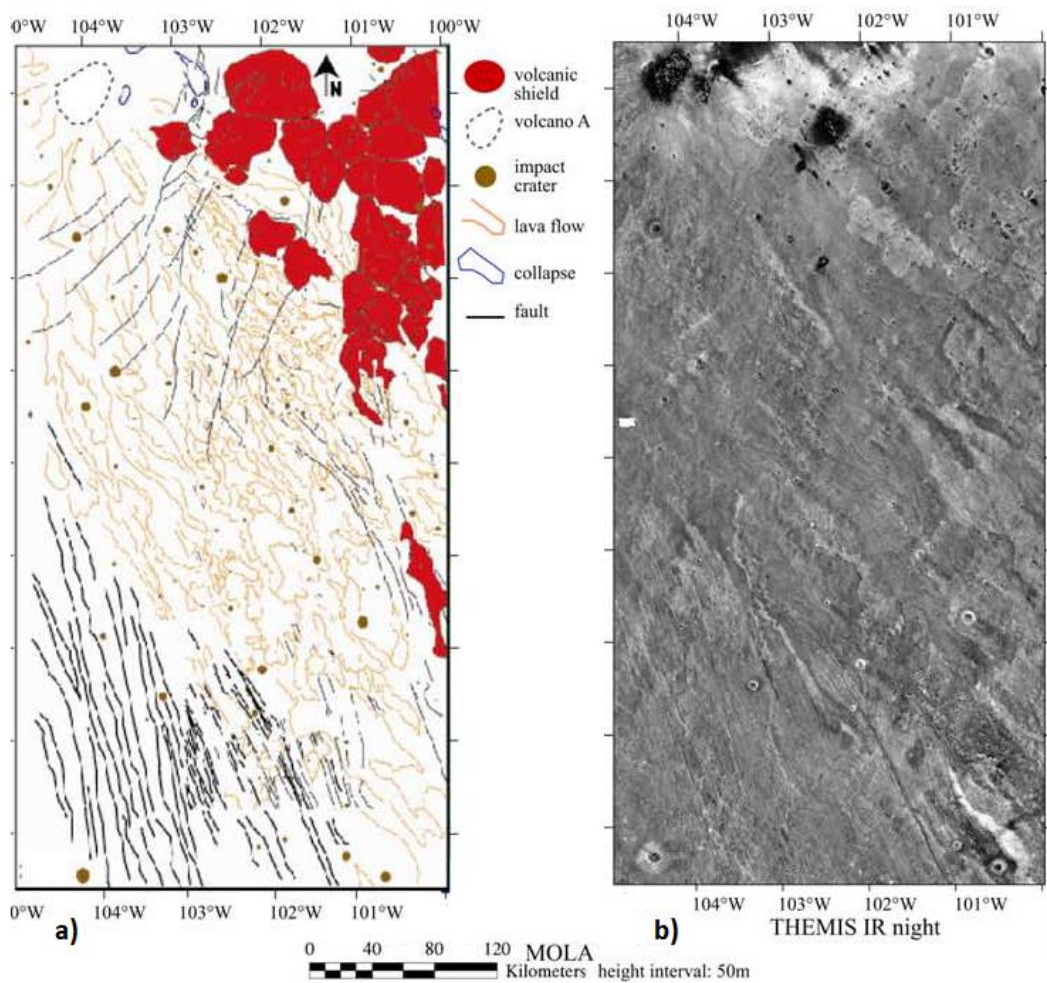
Syria Planum is well known as a possible driving process for an extended magmatic plumbing and the related surface collapse within the surrounding areas. This region is characterised by a major constructional edifice that exceeds 2000 km in diameter (Fig 2.8). Intrusive and extrusive magmatic activity has been documented in this area, and additional observation confirms that this zone was the centre of the Tharsis activity during the early Noachian.



The formation of Syria Planum is represented by four deformational phases: 1) The first phase is characterised by faults generation, displayed by fissure-related lava flows, probably associated to distinct sequences of tectonic activity, simple grabens are distributed in almost uniform densities, dating probably to the Late Noachian (Frey, 1979, Plescia & Saunders, 1982, Anderson et al., 2001, Baptista et al., 2008), several of these grabens occur over greater distances, and are characterised by width of 2.5 km on average, and ranging between 1 to 6 km. Tanaka & Davis, 1988, suggested an extensional tectonic affecting Syria Planum from the early to the late Noachian, generating EW faults through flexural uplift, and accompanied by the formation of some large volcanoes. 2) The second phase started during the late Noachian to the Early Hesperian (Williams et al., 2008, Baptista et al., 2008), with a radial faulting possibly related to a major stress field associated with magma plume (Williams et al., 2008, Baptista et al., 2008, Richardson et al., 2013). 3) The third phase started in the late Hesperian, where a series of faults and grabens display in Syria Planum, and they are probably related to local tectonic activity of the Tharsis region (Baptista et al., 2008). Afterward, a series of faults in the SW of Syria Planum together with radial pattern in the south of the planum occurred during the late Hesperian, generated either by a collapse associated with the magmatic eruption (Tanaka & Davis, 1988, Baptista et al., 2008), or by flexure of the lithosphere due to volcanic infilling. During this phase the radial fault system in Syria Planum could have been reactivated (Baptista et al., 2008). 4) The last phase of the Syria Planum evolution dates back to the late Hesperian to early Amazonian, and is characterised by the formation of Noctis Labyrinthus grabens and the troughs network, probably caused by a local uplift (Tanaka & Davis, 1988, Yin, 2012). This stage is followed by one last phase of Syria Planum tectonic evolution, represented by NW normal faults in Noctis Fossae and Claritas rise, which seems to be related to a regional subsidence (Baptista et al., 2008).

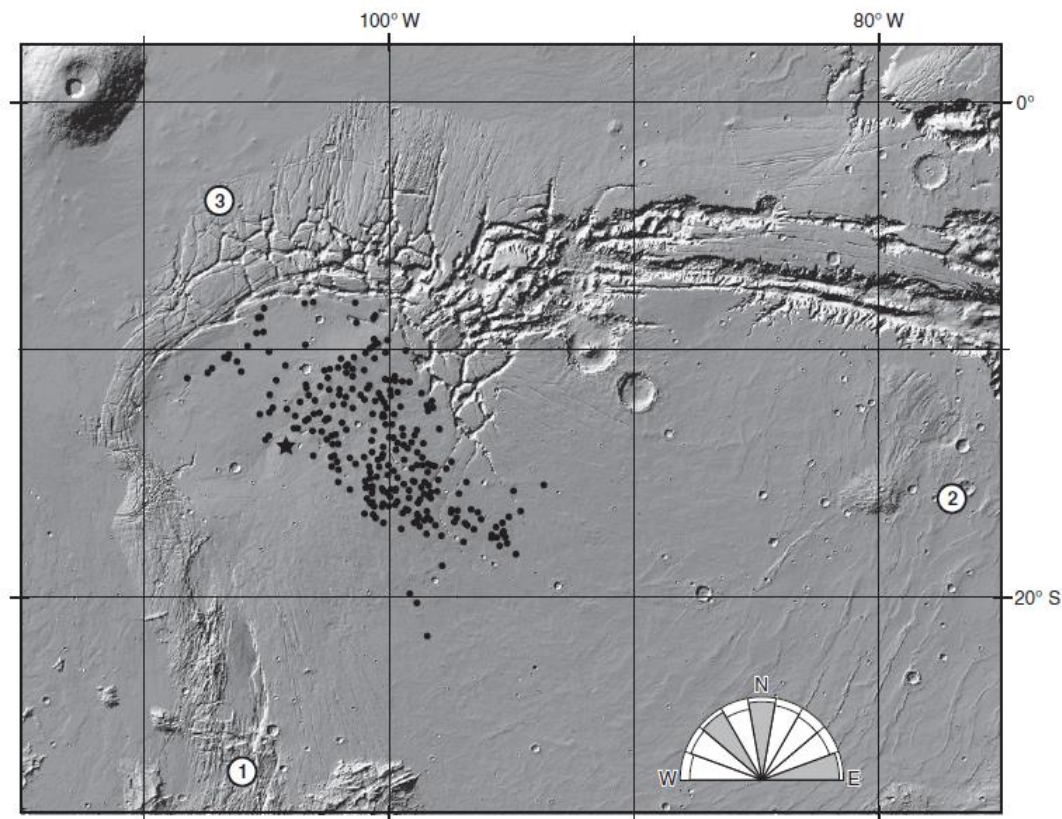
The Syria Planum fault system merged with the large and distinctive tectonic structures of Noctis Labyrinthus. This region is distinguished by intensely fractured north and west margins. The centred activity peaked for Syria Planum is the Noachian according to Dohm & Tanaka, 1999. The extensive lava flows within the Syria Planum suggest the presence of numerous small volcanic landforms of various types (Plescia, 1981, Mougini-Mark et al., 1992, Hodges & Moore, 1994) to generate such a feature. The volcanic edifices of Syria planum are accompanied to the west by a medium size volcano, probably responsible of lava flows that extend over >200 km (Baptista et al., 2008) and fissure-fed eruptions with a basaltic to andesitic composition resulting from high effusion rates (Baptista et al., 2008). Previous studies from Anderson et al., 2004, proposed that the magmatic activity of Syria Planum was associated with an episode of intensive tectonic during the late Noachian to the early Hesperian, that declined afterward to a volcanic activity (Williams et al., 2008, Baptista et al., 2008, Richardson et al., 2013).

Seemingly, Syria Planum was the centre of tectonic activity before the emplacement of the volcanic plains, the different faulting phases mentioned above (Tanaka & Davis, 1988) may be explained by various volcano-tectonic activities (Masson, 1980, Williams et al., 2008, Baptista et al., 2008). Some graben systems have been interpreted within a dike-related graben context, however, the collapse features in the north region of Syria Planum could be related to a period of major subsidence in Noctis Labyrinthus (Baptista et al., 2008).



**Figure 2.8.** Syria Planum broad plateau (a) Geomorphologic map of Syria Planum shows a group of 10 to 60 km diameter of small volcanic edifices. Legend is labelled on the figure. The impact craters and the lava flows are traced by two families of faults that become wider in the south. (b) THEMIS IR night images show relatively circular features corresponding to the topographic protuberances. This swarm of protuberances displays a distinct pattern of coalesced landforms, and some of these protuberances located to the northern edge of the swarm have a higher albedo, interpreted as a dust cover, as confirmed by the low brightness in the image (After Baptista et al., 2008-Modified)

The tectonic history of the Syria Planum (Dohm & Tanaka, 1999, Anderson et al., 2001, 2004, Richardson et al., 2013) is explained by the tectonic phases mentioned above and could be represented by three volcano and tectonic centres (Fig 2.9): The first centre is Syria and Claritas Fossae (Noachian), the second centre is along the south-central part of Valles Marineris (Late Noachian and Early Hesperian), and the last centre is the NW of Syria Planum (Early Hesperian).

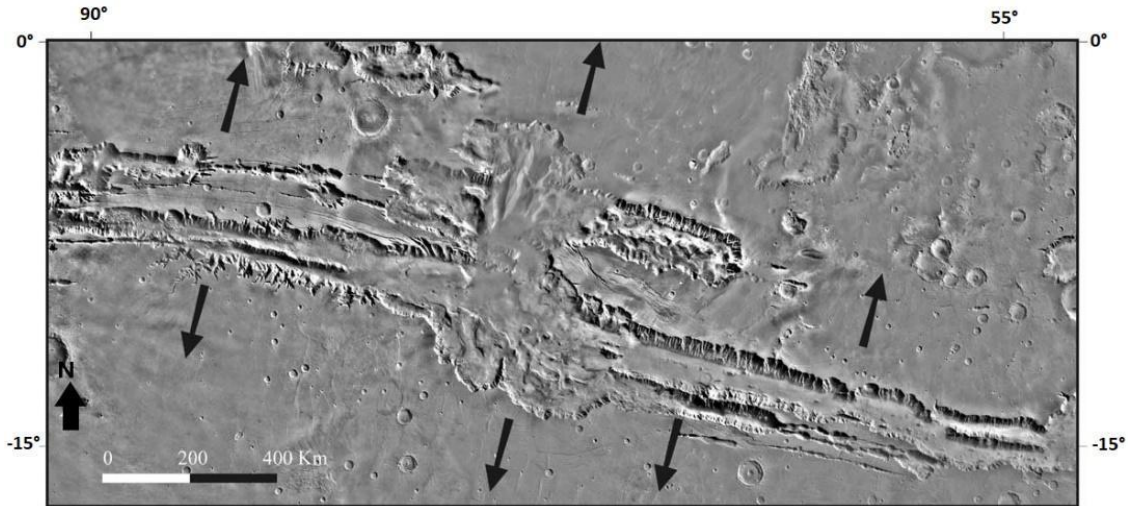


**Figure 2.9.** View for the three major described tectonic centres as mentioned by Anderson et al., 2001. These centres are noted by a number of circles: (1) Noachian centre (2) Late Noachian and Early Hesperian centre and (3) Early Hesperian centre. The black circles indicate the vents studied in Richardson et al., 2013. The polar plot in the bottom right indicates the direction distribution of inter-vent alignments (After Richardson et al., 2013).

## 2.2. Valles Marineris and the related rift system

The second biggest feature after the Olympus Mons on Mars is the vast canyon system of the Valles Marineris, classified to be the widest canyon system in the solar system. Valles Marineris located between 13.9°S 59.2°W, bordered to the west by Noctis Labyrinthus, the Lunae Planum region to the north, and Aurorae Chaos to the east, where Coprates Chasma is. This canyon system seems to be generated by a major extension and an up-arching in the Mar's lithosphere (Lucchitta et al., 1992, Jackson et al., 2011), creating a large rifting system in the crust. The Valles Marineris large rift dominates the tectonic landscape of the Tharsis province, and it's indicative of an important planetary extension. The formation of these rift and troughs system (Fig 2.10) is widely held to involve some combination of horizontal extension and vertical subsidence or collapse (Adams et al., 2009, Mège & Bourgeois, 2011, Jackson et al., 2011, Hanna, 2012a, 2012b). However, a water-related activity is also considered to be involved in its formation, especially after some studies that indicated the presence of hydrated mineral stratigraphy in Ius Chasma (Roach et al., 2010). Several faults system have been identified and studied within the Valles Marineris canyon, these systems have been considered to be only extensional and related to the evolution of several tectonic centres developing from the Noachian to the Amazonian (Anderson et al., 2001, Bistacchi et al., 2004).





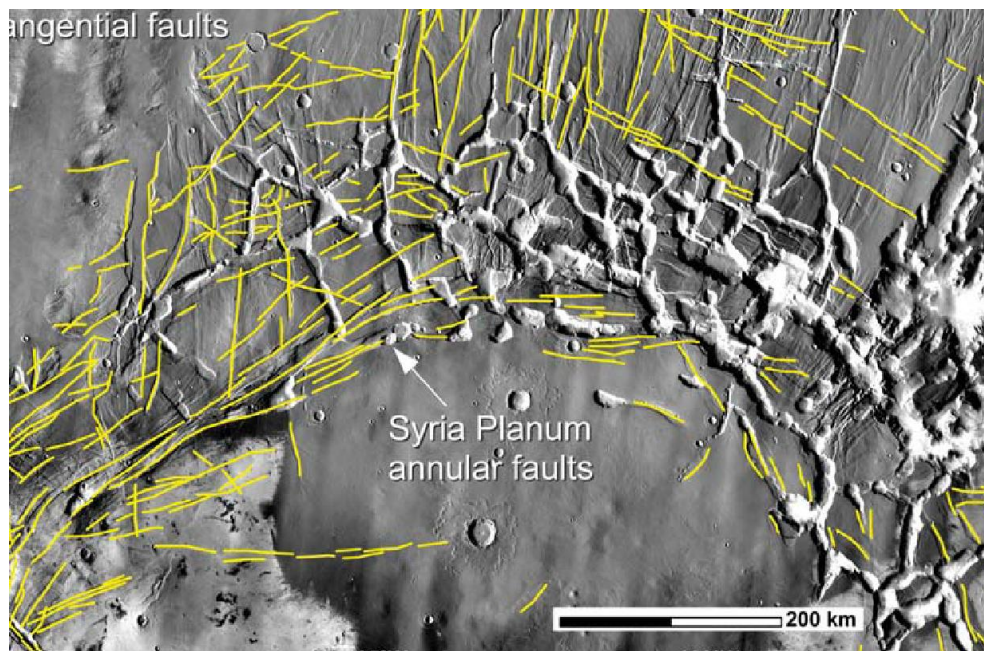
**Figure 2.10.** Valles Marineris and the neighbouring canyons over a MOC global mosaic. The black arrow indicates the sense of the extension (Modified after Bistacchi et al., 2004).

Although Valles Marineris is one of the most imaged features on Mars's surface, the tectonic and volcanic context for the Valles Marineris is poorly understood. Terrains in this canyon date from the Noachian to the Amazonian eras. Valles Marineris may be formed by normal faulting, collapse, or in response to the magmatic intrusions. It still many discussions about its origin which could be related to: i) massive dike emplacement causing ground-ice melting and thus catastrophic formation of outflow channels, ii) interaction among Tharsis-driven activity and an ancient Europe-sized basin, iii) large-scale right-slip or left slip faulting related to plate tectonics, iiiii) lateral extrusion or alternatively continental-scale mega landslide emplacement as reported by Yin, 2012. Among these models that have been proposed, two scenarios seem to be much more reasonable: i) An elongated magma chambers with a dike's emplacement and regional tectonic as a driving process for a large opening of the valles Marineies and the related trough (Andrews-Hanna, 2012a, 2012b, 2012c), ii) alternatively, the Tharsis volcanic and tectonic centres have induced crustal extension to form the Tharsis radial grabens and Valles Marineris through normal faulting (Schultz & Lin, 2001). Further, the effect of a pre-existing crust weakness or the combination of one or several of the above-mentioned processes, should also be taken into consideration (Lucchitta et al., 1994, Schultz, 1998, Dohm et al., 2009).

The deformation in Valles Marineris, Ius and Coprates Chasmata rift zone is expressed by three different kinematic indicators: i) transtentional faults and NE-trending extensional features as joints, bounding the troughs ii) NE-oriented extensional structures (joints), iii) NW-oriented contractional structures (thrusts and folds), plus local minor NW-oriented faults within the trough zones, or alternatively across the plateau margins (Yin, 2012). A set of N70 and N65 striking faults was documented in Candor Chasma (Birnie et al., 2012, Brustel et al., 2017), and Hebes Chasma (Brustel et al., 2017) respectively. These fault sets are both formed during the Hesperian (Flahaut et al., 2010). An observation of NW-striking right-slip faults generated by the east-trending left-slip faults have been documented by Yin., 2012. These faults appear to be formed simultaneously, based on their crosscutting relationship (Yin, 2012). The Right-slip and left-slip strike-slip faults are parallel to Valles Marineris, associated with wrinkle ridges,

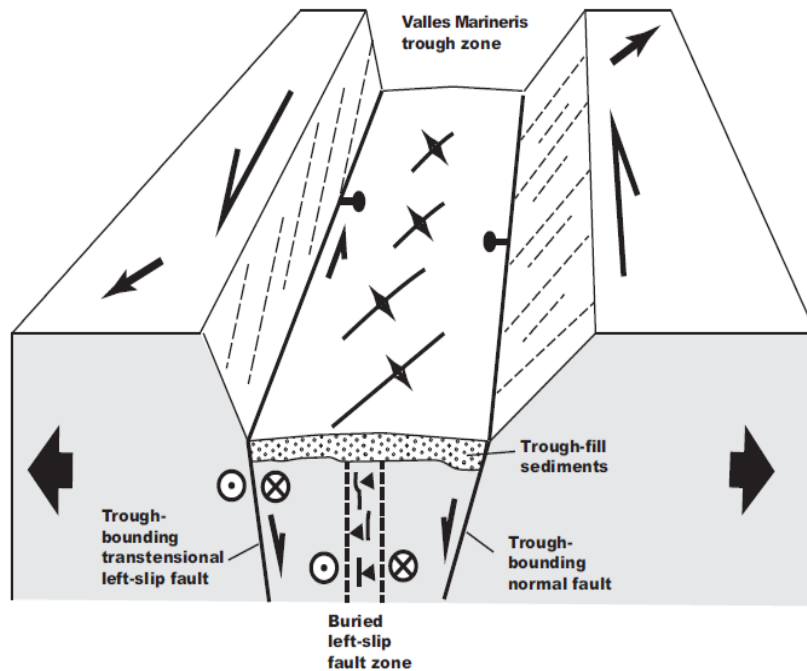
and may be developed during the formation of the contractional wrinkle ridges as transfer faults rather than the left-slip faulting of the Late Amazonian.

Five principle tectonic centres were identified within Valles Marineris, based on linear structures interpretation (Anderson et al.,2001), but it is still difficult to connect them to a source centre. The Thaumasia plateau and its morphology display a mega-slide, where the extensional deformation of Syria Planum and Noctis Labyrinthus connects via lateral zones of transtension and strike-slip Valles Marineris and Claritas Fossae, to an extended zone of compressional uplift and shortening, represented by thrust faults and truncated craters along the Thaumasia highlands and Coprates rise. Documented polygonal patterns of extensional grabens in Noctis Labyrinthus, have been studied by Montgomery et al., 2009 (Fig 2.11). These extensional features display two generations and orientations of faults: an old NNE striking grabens and a concentric fracture set ringing Syria Planum and curving into Valles Marineris, younger than the previous faults set.



**Figure 2.11.** Noctis Labyrinthus and Syria Planum intersecting sets of NS-striking and normal faults labeled in yellow, forming regional polygonal chaos. The faults interpretation by Montgomery et al., 2009. View from Shaded-relief Thermal Emission Imaging System infrared base.

Within the east part of the Valles Marineris, Capri-Eos rift host NW-SE extension (Masson, 1977, 1985), while the left-lateral slip along the Valles Marineris and the Claritas right-lateral slip faults form a V-shaped conjugate strike-slip system opening to the SE direction (Fig 2.12). This V-shaped conjugate Riedel should have been coeval with the development of the primary Tharsis graben zone (Yin, 2012). The Ius-Melas-Coprates fault zone (Fig 2.12) probably accommodated by the NW-SE extensional faults systems across Noctis Labyrinthus and Syria Planum (Yin, 2012) in the west and the extensional regime across Capri and Eos Chasmata in the east (Yin, 2012). The displacement on individual left-slip faults within Valles Marineris varies from a few metres to an average of 13 km. The total estimated left-slip motion across the long Ius- Melas-Coprates fault zone is  $160 \pm 50$  km,  $150 \pm 30$  km, and  $150 \pm 30$  km according to Yin, 2012.



**Figure 2.12.** 3D model for the Ius-Melas-Coprates fault zone that displays several fault systems, and a trough segment which could be strike-slip on one side and normal faults on the other side. This difference in the fault kinematic is probably due to the strain distribution of the transtensional tectonics within this locale (After Yin, 2012).

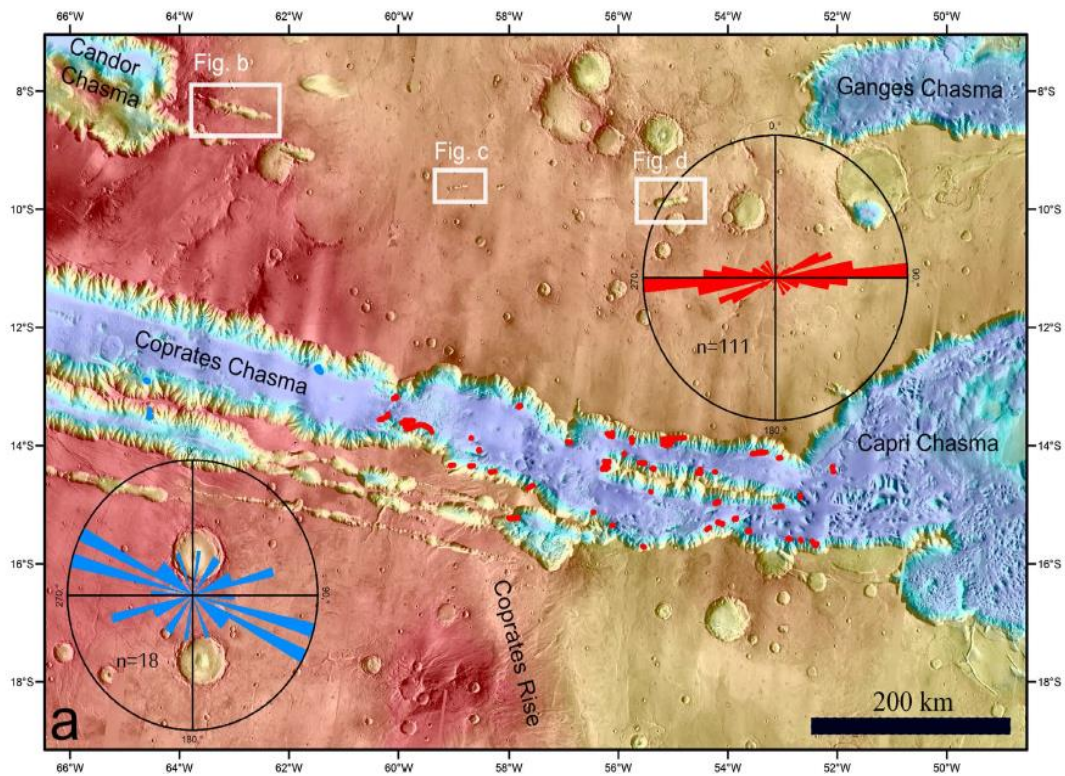
Some observation shows left-lateral structures might be dating to the Late Amazonian, although the regional complex tectonic pattern seems to be developed during the Noachian epoch. Moreover, some faults bounding the trough systems may even still be active, since they overlap young surface deposits and smooth plains that have nearly no impact craters (Yin, 2012).

Dikes are also present within the eastern segment of the Coprates Chasma (Fig 2.13), probably associated with the volcanic events from the Noachian and Hesperian (Brustel et al., 2017). These dikes often in relief are expressed generally as linear features but they could appear as slight arcuate lineaments, depending on the change of the topography highs, but often expressed in relief. The orientation of these dikes is approximately EW, roughly parallel to the troughs, suggesting that the model based in extensional tectonic and magmatic plumbing could be responsible of Valles Marineris, formation, thus, the magmatic intrusions could have directly led to the formation of Valles Marineris by tearing the crust and helping the block subsidence (Andrews-Hanna, 2012c). A second suite of dikes is produced by the volcanic centres in the Tharsis region and/or the Coprates Rise since two groups of dikes within the Coprates Chasma are not oriented as the Valles Marineris, these can be attributed to a third tectonic epoch, or generated from unrelated tectonic events (Brustel et al., 2017).

In Coprates Chasma, dikes are striking N90°, and they are oriented in a radial direction to Syria Planum, this suggests that they may be related to an early stage of the Tharsis grabens and volcanism formation. Some fault scarps appear to be younger to the Valles Marineris opening that started in the late Noachian and lasted to the Early Hesperian, or



even before (Yin, 2012). These scarps crosscut recent sediment and landslides in Valles Marineris and may still be active.

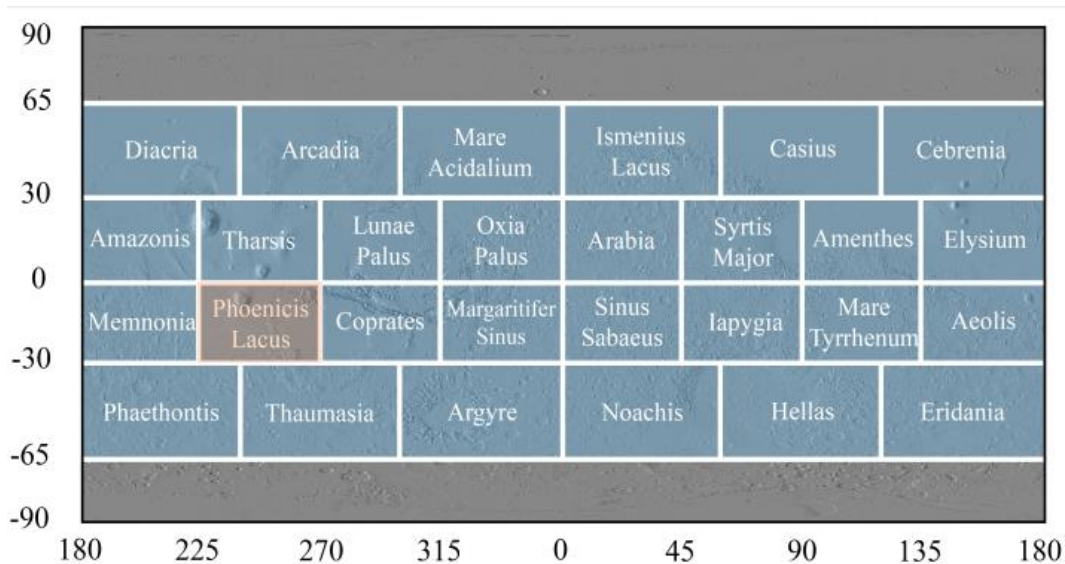


**Figure 2.13.** Dikes in the western and eastern sectors of the Coprates Chasma over a MOLA colored elevation plus THEMIS IR daytime basemaps. The dikes in the western part of Coprates Chasma (Blue polar plot) displays different direction (110° and 140°) compared to the dikes from the eastern side (Red polar plot) that are mostly oriented at 90° (After Brustel et al., 2017- Modified).

Interesting synthesis work of Mège and Masson, 1996, suggested that the Valles Marineris formation seems to be controlled by the radial extension in Syria Planum, and this was in accord with the studies of Brustel et al., 2017. The inflation events in the magma chamber produce extensional stress responsible for the radial extension, and the subsequent concentric extension. This deflation could explain the formation of the radial and concentric dikes and graben around Syria Planum. These features formed over the Tharsis province, displayed radially around the Tharsis dome, formed probably during the late Noachian to the early Hesperian. A swarm of dikes are approximately centred on the actual Tharsis Montes, and superimposing a group of old grabens. Dikes in this model play a fundamental role in the crustal extension, and the formation of grabens and troughs in the Valles Marineris as well as in the Noctis Labyrinthus.

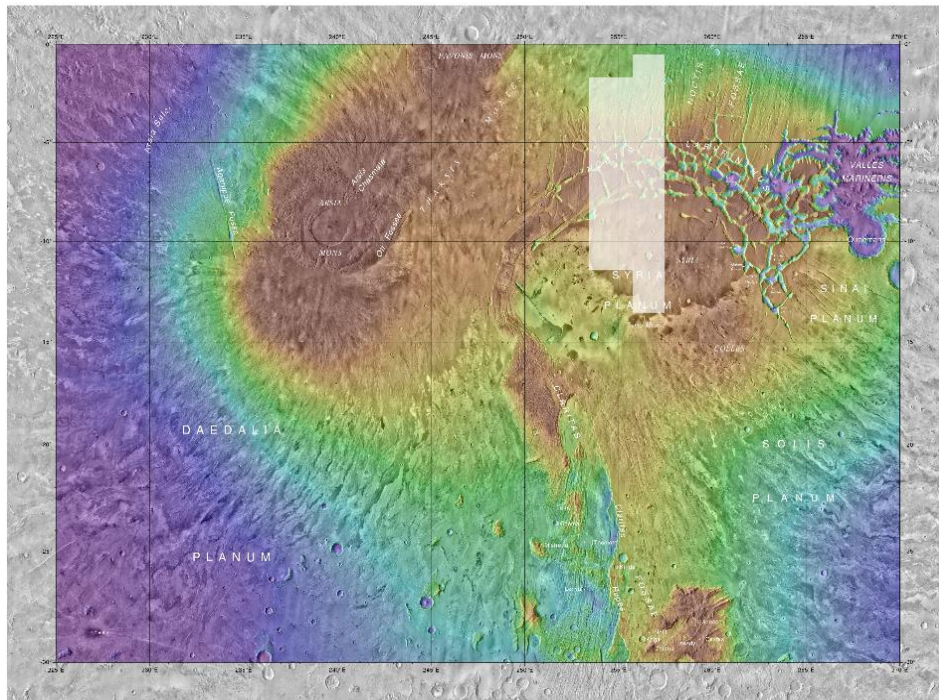
### Chapter III – Noctis Labyrinthus mapping and faults analysis

Noctis Labyrinthus is located between the western part of the Valles Marineris’ large tectonic rifting and the volcanic plateau of Tharsis Rise. Among the 30 Martian quadrangles, Noctis Labyrinthus belongs to Phoenicis Lacus (MC-17) quadrangle (Fig 3.1), and is identified on the surface by the coordinates:  $-6^{\circ}86' N$   $6^{\circ}54' S$   $267^{\circ}48' E$   $101^{\circ}12' W$ . The formational history of this region is still debated since several hypotheses have been proposed such as karst landscapes with associated caves and water-related processes (Ferrill et al., 2004, Bibring et al., 2006, Weitz et al., 2011, Weitz et al., 2013, Rodriguez et al., 2016, Baioni et al., 2017, Baioni, 2018), a network of lava tubes (Wyrick et al., 2004, Leone, 2014) or a volcano-tectonic activity (Lucchitta et al., 1992, Mège & Masson, 1996, Schultz, 1998, Mège et al., 2003, Dohm et al., 2009).



**Figure 3.1.** Mars Odyssey THEMIS-IR Global Mosaic, indicating the series of 30 quadrangles of Mars as defined by the USGS. Noctis Labyrinthus is located in Phoenicis Lacus (Highlighted quadrangle). The regions that are not shaded in blue are the North pole (top) and the South pole (bottom) (Photo credit: USGS-Modified).

Noctis Labyrinthus is characterised by a system of steep-walled canyons and valleys that give it the aspect of a naturally-formed maze or labyrinth. The surface in this district displays a complex interconnected network of pit chains and branched extensional systems of faults and grabens, following several directions, and continuing for hundreds of kilometres (Fig 3.2).



**Figure 3.2.** THEMIS IR Global Mosaic for Phoenixis Lacus, MC-17 covered by MOLA Elevation Model. The elevation is ranging between -1043m and 17,728m. The meshes indicate the extension of the mapped zone, for a margin of H3210\_0000 and H3221\_0000 from HRSC stereo images (Photo credit: ASU, USGS-Modified).

Three important deformational stages were proposed by Schultz, 1998 in order to explain the Valles Marineris troughs, where Noctis Labyrinthus is also involved: The first stage is represented by radial dike emplacement within Syria Planum from the Late Noachian to Early Hesperian age, the second stage is a crustal subsidence dated back to the post-Early Hesperian, generate the formation of ancestral basins such as the Hebes Chasma, this stage was followed by a last deformational stage of regional normal faulting, probably related with the loading stresses from the Tharsis region. These faults are generated during the Amazonian period onto the same area that was occupied previously by the subsidence depressions.

The age of Noctis Labyrinthus fault populations is still debated, however, some fault systems seem to be reactivated several times after their inception. Lucchitta et al., 1992, Schultz, 1991, suggests that Noctis Labyrinthus fault systems might be generated during the early Hesperian, based on fault mapping and their relationship with Valles Marineris chasmata. However, a subsequent work by Bistacchi et al., 2004, proposed two deformational phases in Noctis Labyrinthus, based on the cross-cutting relationships and the structures analysis carried out on Viking MDIM and MOC global mosaic. According to Bistacchi et al., 2004, the first tectonic event has been attributed to the Noachian, and is mainly expressed in the northern sector of Noctis Labyrinthus, by NNE transtensional faults associated with NS and WNW conjugate structures. The second tectonic event is represented by WNW oriented faults, and the reactivation of the previous NNE-trending faults system in response to a triaxial strain field. This deformational event seems to be related to the Valles Marineris opening and is dating to the Late Noachian-Early Hesperian. Finally, a third event was suggested by the authors, as a dextral strike-slip



shear along NW faults, cross-cutting the Valles Marineris rift System and probably of Late Hesperian-Amazonian age.

Only a few geological and structural maps of Noctis Labyrinthus have been realised. Some of them, with the classification of the structures and their approximate age determinations, cover a large area that extends to Valles Marineris or the volcanic plateau of Tharsis, (Mège et al., 2003, Bistacchi et al., 2004, Yin, 2012, Rodriguez et al., 2016, Kling et al., 2021), while other maps are display geological units' distinction (Yin, 2012). Thus, the limited studies and maps that have been realised for Noctis Labyrinthus motivated this work in order to carry out a detailed structural map including faults and pit chains. This will allow us to reconstruct the tectonic context of this district, and propose a deformational model that can explain the formation of Noctis Labyrinthus and the related driving processes.

In this chapter, we will present the data and the methodology we used for delivering a structural map and analyse the relationship among the different fault sets of Noctis Labyrinthus and between the fault network and the pit chains. We finally propose a model that can tentatively explain the observations and the formational history of Noctis Labyrinthus.

### 3.1. Datasets

To produce the structural map, we used available data from the High-Resolution Stereo Camera (HRSC) of Mars Express, which covers a large area of Noctis Labyrinthus with diverse resolution. In particular, the district we selected in Noctis Labyrinthus was completely covered by the two HRSC orthoimages h3210\_0000 and h3221\_0000 (Fig 3.3) of the Version 2 Reduced Data Record (RDRV2) bearing a resolution ranging between 18,4 and 19,5 m/pixel (Tab 3.1).

**Table 3.1.** List of the MEX HRSC Version 3 Reduced Data Record (RDRV3) with calibrated data

HRSC Image ID	Max resolution	Center Latitude	Center Longitude
H3210_0000_ND2	18.4 mpp	-7.7659	-0.796
H3221_0000_ND2	19.7 mpp	-6.6189	255.1419

The context Camera CTX dataset from Mars Reconnaissance Orbiter (MRO) display a way better resolution (Tab 3.2) compared to the HRSC data (average resolution of 5.91 m/pixel), but regrettably the image mosaic from the CTX was not encompassing the entire concerned zone (Fig 3.4), hence we used this mosaic only for analysis at local scale and for specific aims such as analysing the shapes of fault intersections, the Hummocky deposits and the pit chains floors.

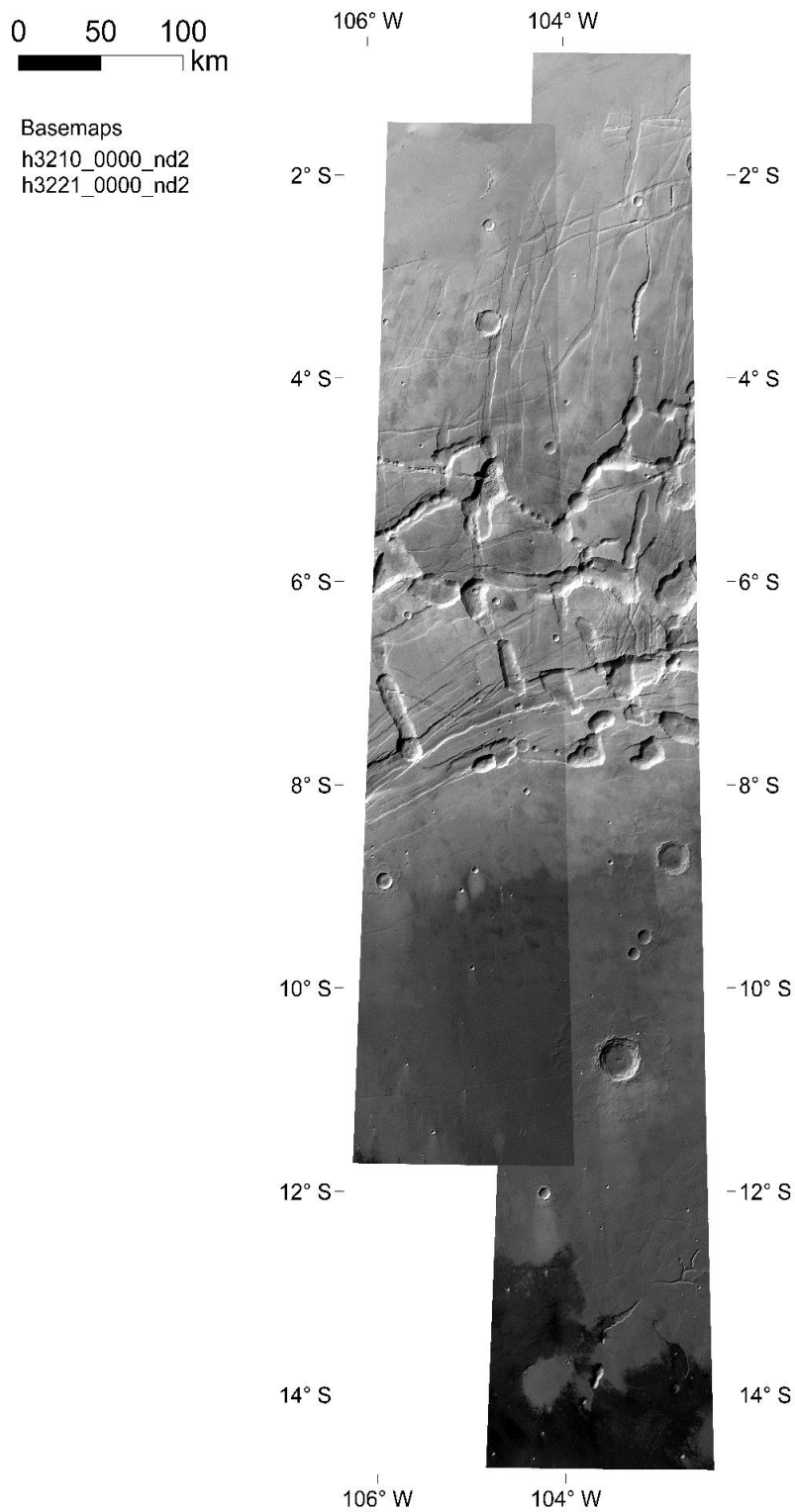
**Table 3.2.** The used images mosaic from MRO CTX Experiment Data Record (EDR)

<b>CTX Image ID</b>	<b>Map resolution</b>	<b>Incidence Angle</b>	<b>Emission Angle</b>
B01_010160_1757_XI_04S104W	5.56 mpp	58.75	12.62
B11_014063_1737_XN_06S103W	5.26 mpp	36.41	0.95
G02_019087_1727_XN_07S103W	5.53 mpp	57.53	18.04
J01_045170_1728_XI_07S103W	5.24 mpp	54.58	3.29
J02_045513_1744_XI_05S104W	6.11 mpp	54.47	22.35
J05_046937_1735_XN_06S104W	5.28 mpp	51.82	4.55
J11_049218_1737_XI_06S102W	5.6 mpp	34.96	14.67

Since the available MEX HRSC Digital Terrain Map Reduced Data Record (DTMRDR) was not covering the entire working field in Noctis Labyrinthus, so it has been decided to use the Digital Terrain Map (DTM) from the Mission Experiment Gridded Data Record (MEGDR) of Mars Orbiter Laser Altimeter (MOLA) onboard Mars Global Surveyor (MGS). The DTM from MOLA bears a resolution of 463m/px (Fig 3.5) and it covers a large number of the mapped faults. All data within this work has been projected according to the Equirectangular\_MARS coordinate system (Tab 3.3).

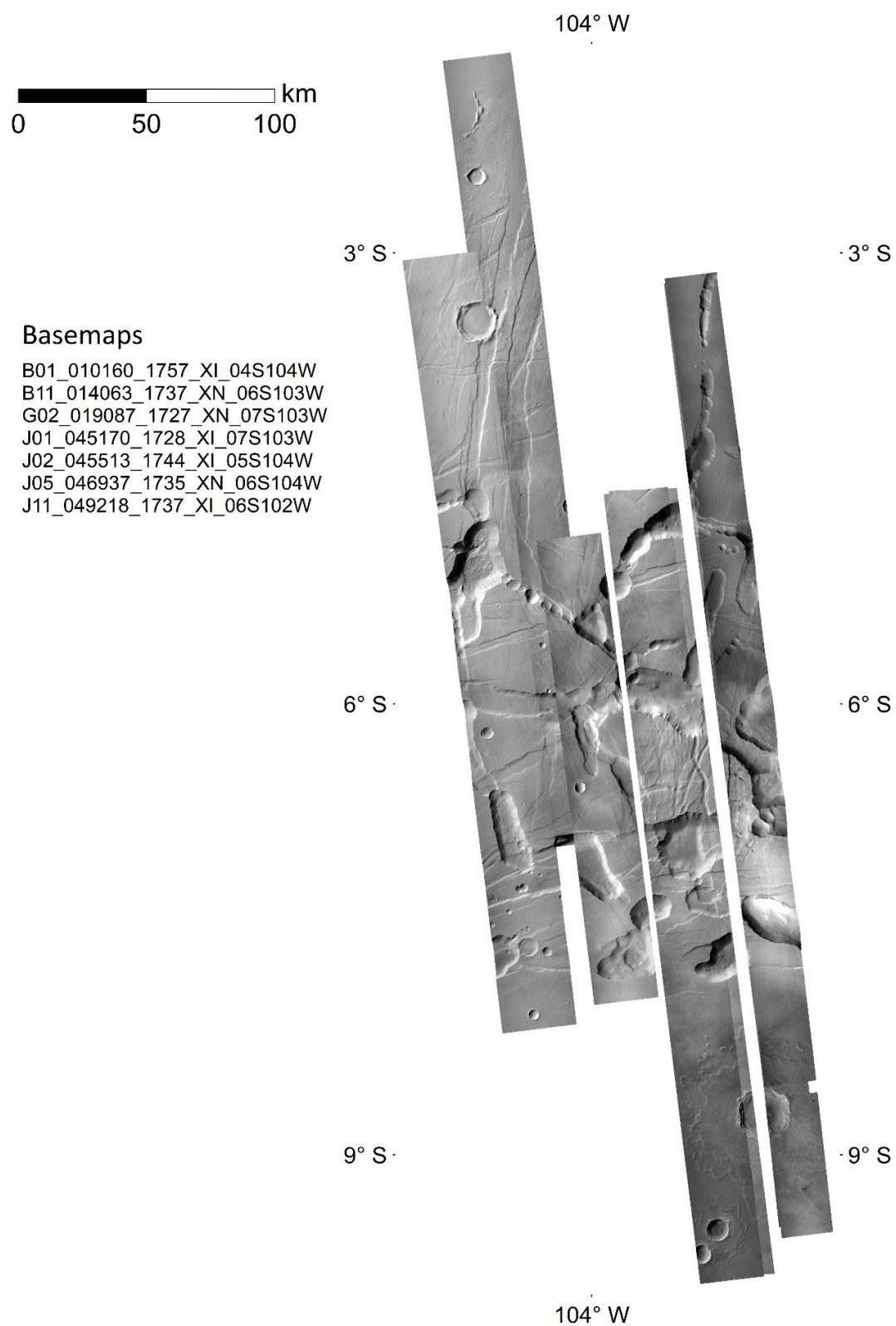
**Table 3.3.** Spatial reference and coordinate system projection.

<b>XY Coordinate System</b>	<b>Equirectangular_MARS</b>
<b>Linear unit</b>	Meter (1.000000)
<b>Angular unit</b>	Degree (0.0174532925199433)
<b>Central_meridian</b>	256.36326185222
<b>Standar_parallel_1</b>	-7.7692279045827
<b>Datum</b>	D_MARS

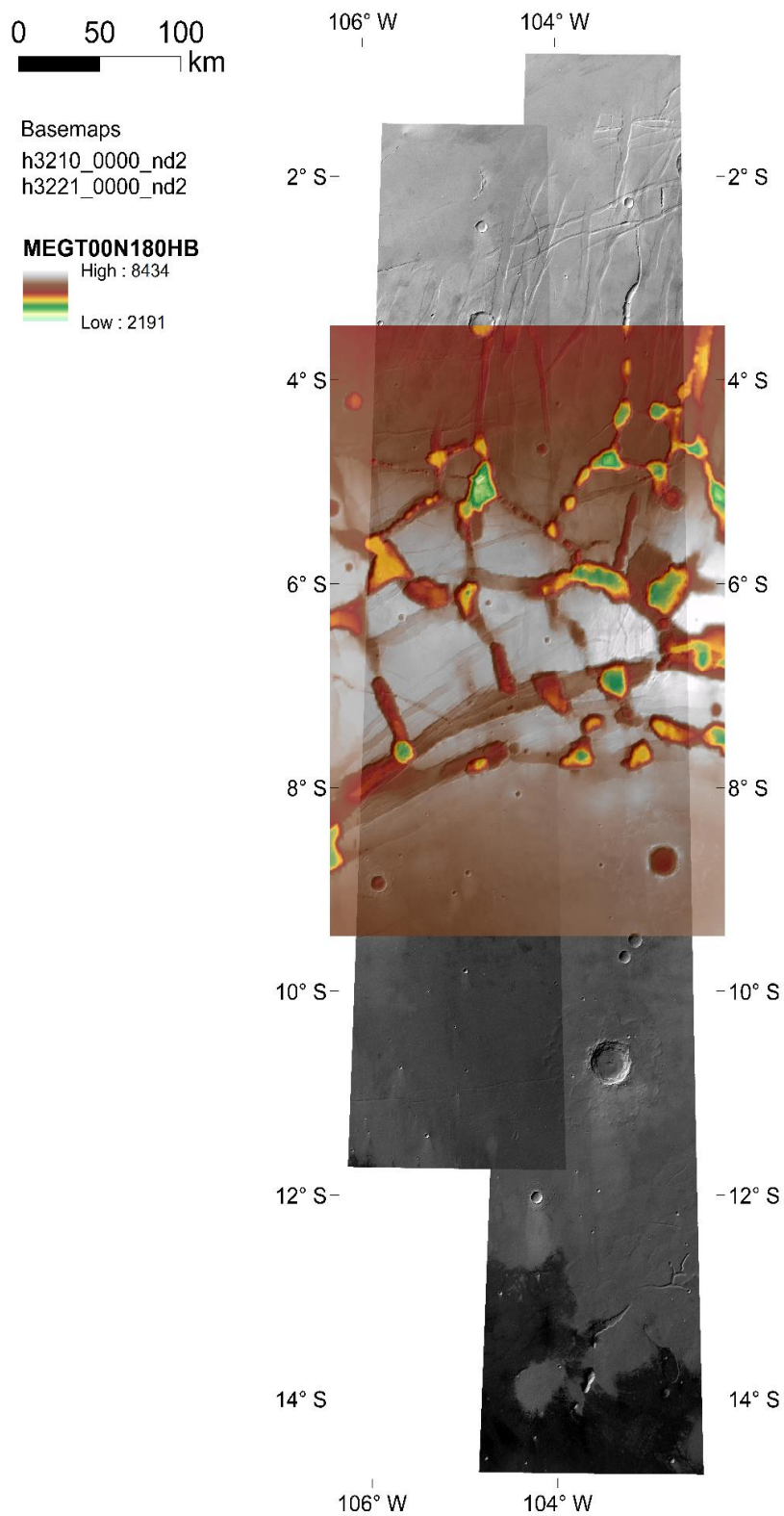


**Figure 3.3.** HRSC basemaps in Equirectangular\_MARS coordinate system. The figure displays both basemaps listed in Tab 3.1. H3210\_0000\_ND2 (right) bears a resolution of 18.4m/px, and H3221\_0000\_ND2 (left) has a resolution of 19.7m/px. Both images cover an area about 148374 sq.km





**Figure 3.4.** CTX basemaps in Equiarectangular\_MARS coordinate system, bearing a resolution between 5.24 to 6.11 m/pixel. Locally the resolution is better compared to the HRSC basemaps in the Fig.3.3, and thus this mosaic was used for regional scale analysis.



**Figure 3.5.** MOLA MEGT00N180HB topography layer at a nominal resolution of 463m/px, over the central part of HRSC basemaps.

### 3.2. Methodology

In this thesis, we have focused our attention on mapping all visible faults, grabens and pit chains. We checked the faults orientation, distribution and size. We also studied the relationship between faults and pit-chain interconnection and formation. Therefore, the photogeological mapping was a good tool to analyse the distribution of faults within the area and study the intersections between lineaments to understand the tectonic phases as well as the faults chronological order. From the resulting structural map, we also derived considerations on the stress field and faults kinematics.

In this section we will describe the methods that we used for the mapping, including the mapping scale, symbology, features classes and the measurements of the fault's geometrical attributes. We will also present the method that we used for delimiting the pit chains and determining their orientation.





#### *Mapping Scale*

To avoid any issues related to the pixelation or over-mapping for some features, we followed the recommendation of Tobler.,1987 concerning the mapping and output scales. Given the basemaps resolution, the digitization scale is  $2,000 \times$  the basemap raster resolution, thus, the mapping scale in our case was 1:39,000, and the map was delivered at 1:195,000 output scale. We mapped all features in Esri ArcMap 10.7.1 Geographic Information System (GIS) software, and the data has been projected within the Equirectangular\_MARS coordinate system.

#### *Symbology*

Faults were mapped with continuous simple bold lines but with different colours to distinguish their dimension (Tab 3.4). However, the pit chains and the Hummocky deposits were traced using a polygon shapefile. We classified faults into two categories according to their size: Minor faults are those who have length less or equal to 4 km, while the major faults are characterised by a length strictly greater to 4km.

**Table 3.4.** Faults size length labels and pit chains colours

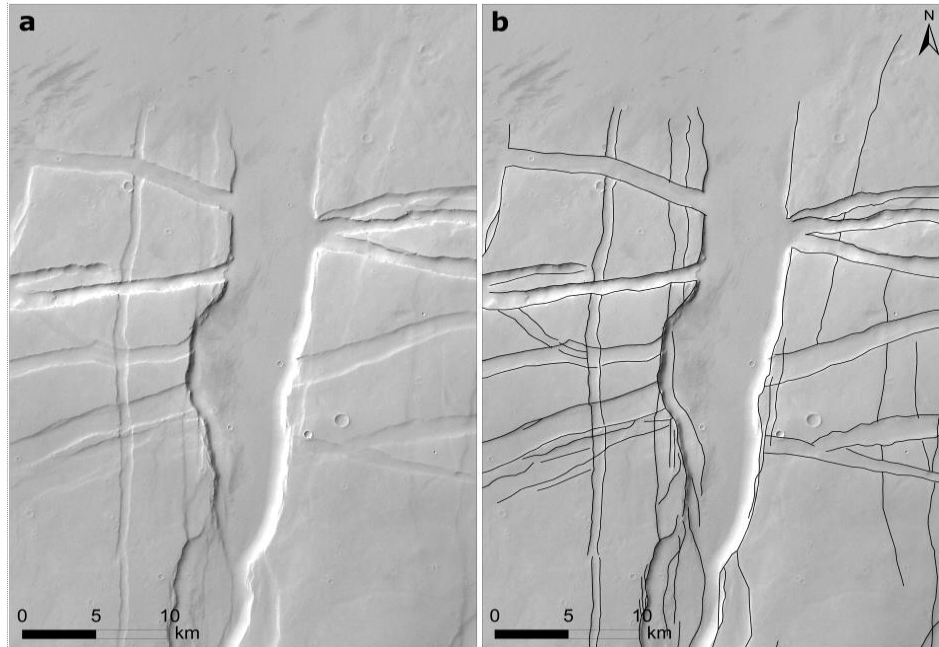
Feature	Attribute	Shapefile type
Major faults > 4km		Polyline
Minor faults $\leq$ 4km		Polyline
Pit chains		Polygon
Hummocky deposits		Polygon

#### *Faults and grabens mapping*

We mapped a large fraction of faults and grabens including branching, segmented, ramping and single isolated faults. These faults were mapped according to their cross-cutting relationships and continuity. Each fault was represented by a single polyline (Fig 3.6).

In the northern sector of the studied area, we identified a network of faults with a group of NS and NNE-SSW conjugate faults, transected by a second group of faults oriented from EW to ENE-WSW.

Some faults appear to be continuous at the intersection district, but others stop at the intersection and do not display any continuity (Fig 3.6).

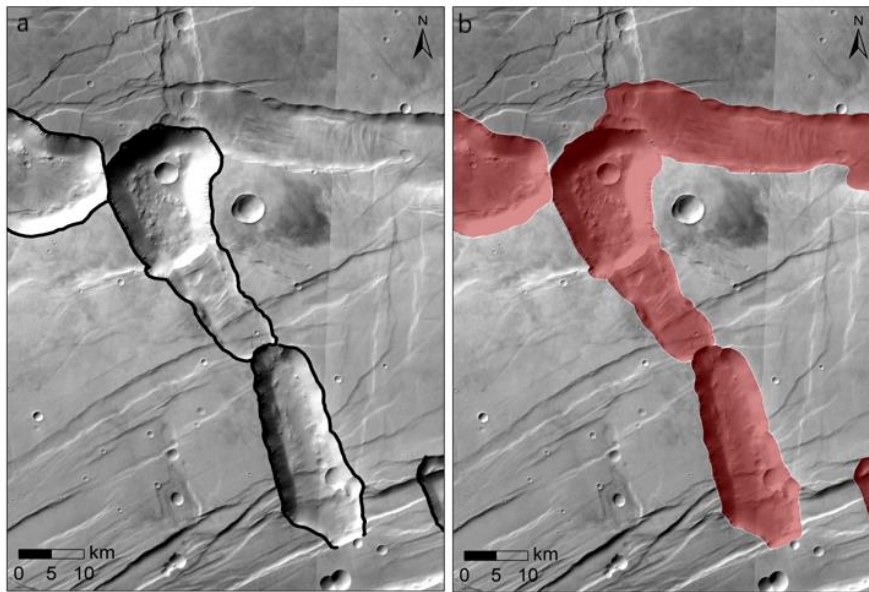


**Figure 3.6.** Faults length mapping. The figure shows some faults cut across other faults, and they do not continue after the intersection. The length of the polylines has been identified as the real length of the faults. Image centred at 256.729°E\_ -1.561°N over the HRSC layer.

The pit chains full shapes were mapped with a polygon shapefile, however to retrieve pit chains azimuth, we traced their edge by continuous polyline, and we used those polylines afterward to measure their azimuth (Fig 3.7). We mapped an extended network of pit chains, represented by 27 polygons. The real number of the pit chains is not consistent with the number of the polygons in Table 3.5 since some pits are robustly connected to each other, sharing the same borders, or even completely merged. In these cases, we mapped them with a single polygon.

**Table 3.5.** Pit chains polygons and the related polygons dimension

Shape	Perimeter (sq.km)	Shape_Area (sq.km)
Polygon 01	79.556971	367.758189
Polygon 02	66.976045	271.128298
Polygon 03	87.753728	425.374119
Polygon 04	49.906692	147.9107
Polygon 05	86.631343	335.511445
Polygon 06	131.173203	619.155629
Polygon 07	122.70492	753.770695
Polygon 08	103.82066	612.94808
Polygon 09	294.509529	1368.87047
Polygon 10	20.234916	25.893746
Polygon 11	35.091589	37.071407
Polygon 12	31.131994	43.756384
Polygon 13	74.066055	184.774809
Polygon 14	258.792755	1157.930297
Polygon 15	13.032668	12.26652
Polygon 16	6.73977	3.501992
Polygon 17	17.647196	13.268995
Polygon 18	5.924068	1.659529
Polygon 19	40.354517	25.390777
Polygon 20	8.354625	5.067245
Polygon 21	10.799557	2.981085
Polygon 22	31.545381	48.478729
Polygon 23	39.181609	115.709906
Polygon 24	454.125972	1705.681491
Polygon 25	721.323791	4771.516547
Polygon 26	116.5281	490.269409
Polygon 27	53.639307	175.394133

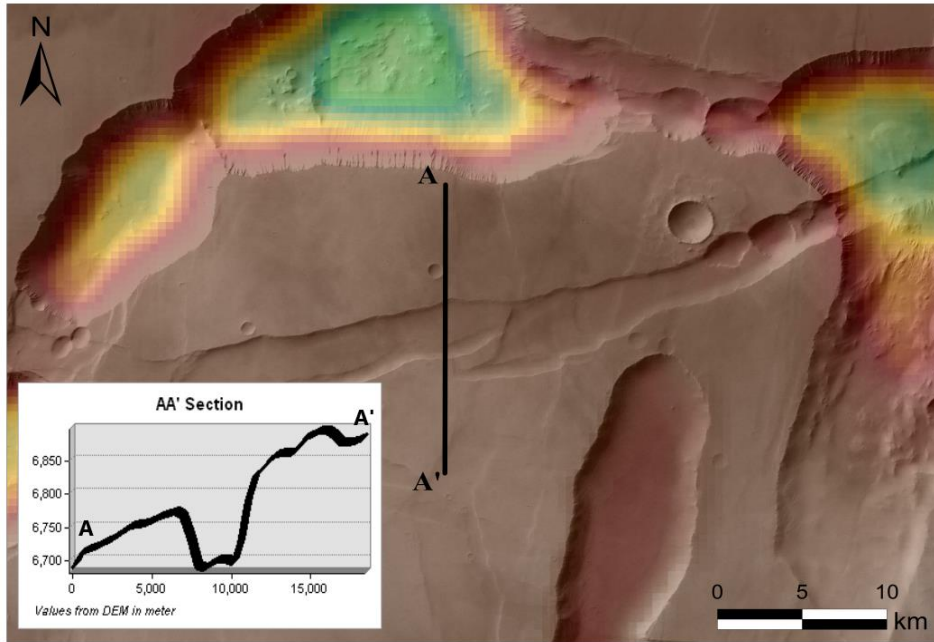


**Figure 3.7.** Pit chains shape and edge mapping (a) Pit chains edge mapping by a polyline shapefile that was traced according to the edge continuity and the connection to another pits rim (b) Pit chains full shape delineation using a polygon shapefile.

### ***Faults Maximum Displacement ( $D_{Max}$ )***

The continuity of the faults can be clearly observed on the north sector, unlike the south sector, where pit chains extend for tens of kilometres, overlapping the faults and making the identification of their continuity intricate. To measure the maximum displacement for the mapped faults, we did a topographic cross-section across all fault's polylines (Fig 3.8), each polyline was measured separately, including the segmented faults. The displacement has been inferred from the difference in elevation between the hanging wall

and the footwall. Not all of the faults are covered by a topographic dataset, since the MOLA basemaps do not cover the complete area. Only 3340 over 4414 mapped faults were considered for the vertical displacement ( $D_{Max}$ ) measurements.



**Figure 3.8.** Topographic cross-section across the pits, interpolating height from the selected surface. Profile displayed over HRSC monochrome basemap and overlapped by MOLA DEM.

### 3.3. Results

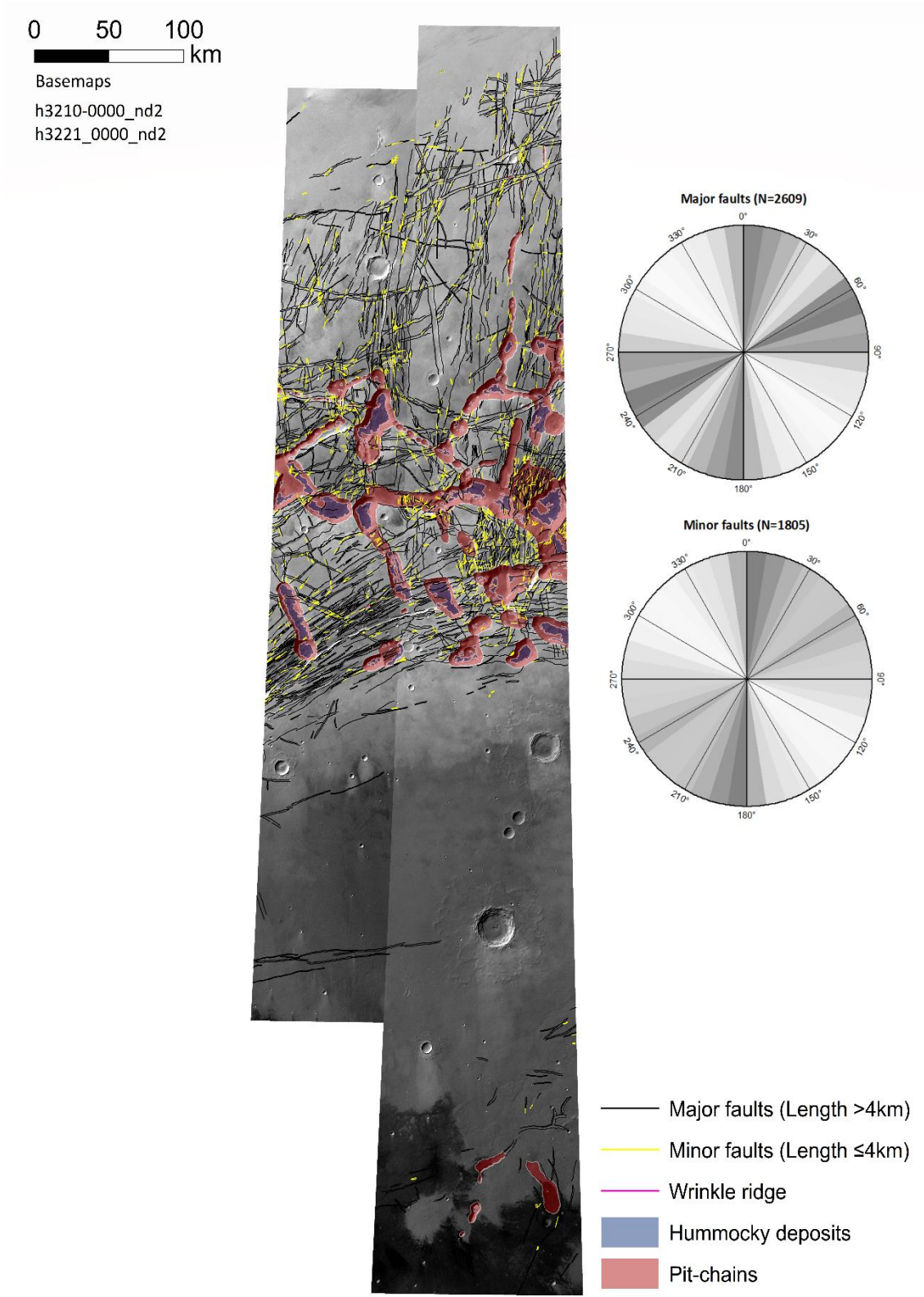
#### 3.3.1. General framework

The structural map shown in figure 3.9 displays a global view of all mapped faults. Indeed, the faults population is mainly dominated by faults with a length greater than 4 km (Table 3.6). A clear difference can be distinguished between the north and the south sectors, related to the pit chains and faults distribution. In the north, the terrains are smooth, lacking pit chains and characterised by the presence of major faults, oriented mainly NS, NNE-SSW, and ENE-WSW, while in the southern sector is outstanding the presence of rounded shaped pit chains of diverse dimensions, connected together to form a configuration of elongated troughs. These troughs are joint to several groups of ENE-WSW, NNW-SSE, NNE-SSW and EW faults. Most of the pit chains are parallel and spatially close to the faults, and/or grew into the graben of the southern sector.

**Table 3.6.** Faults size length attribute and number of polylines for each fault category

Faults class	Number of lineaments	Average length (km)
Major faults	2609	168,074 – 40,357
Minor faults	1805	3,998 – 0,255

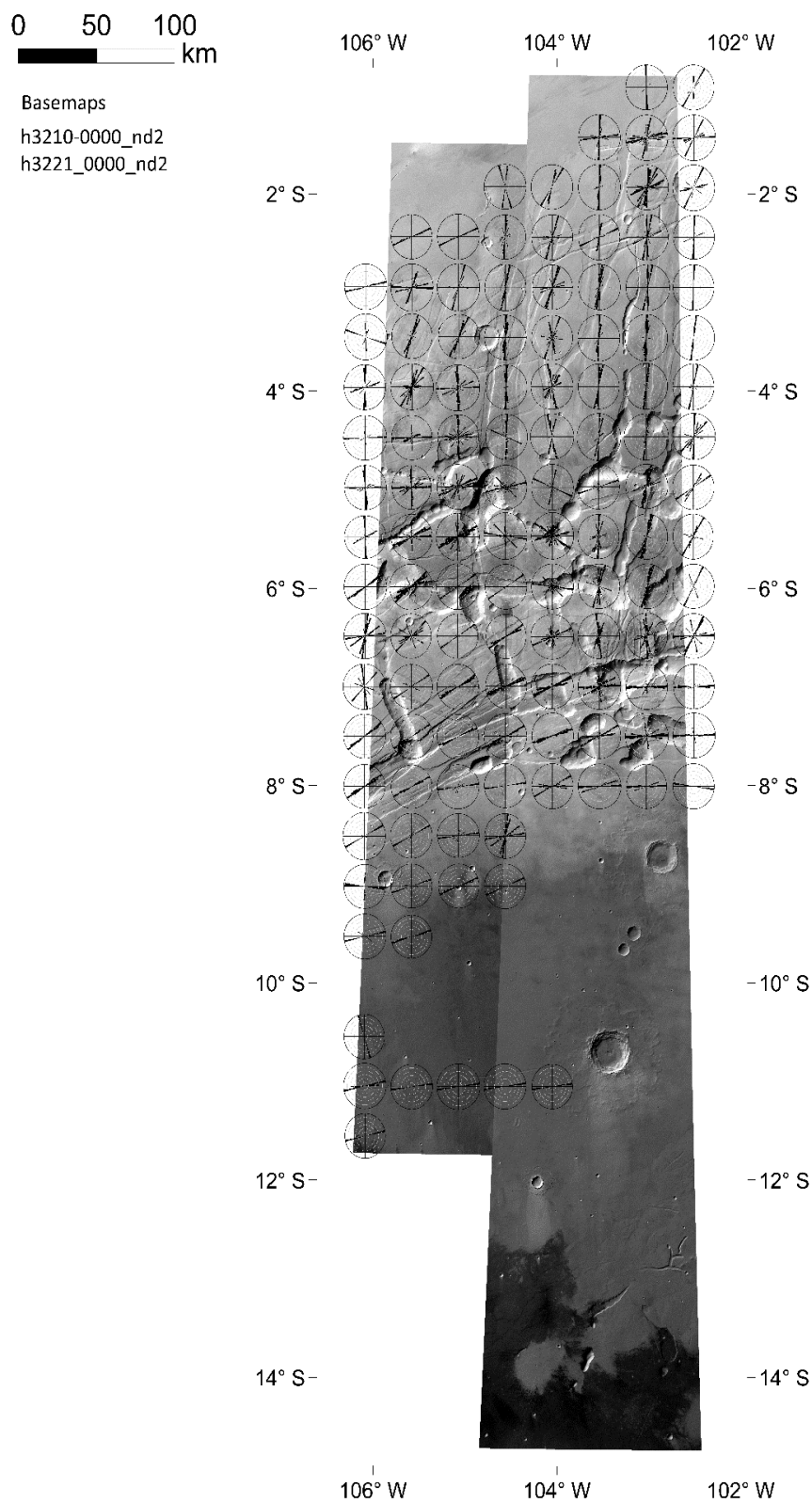




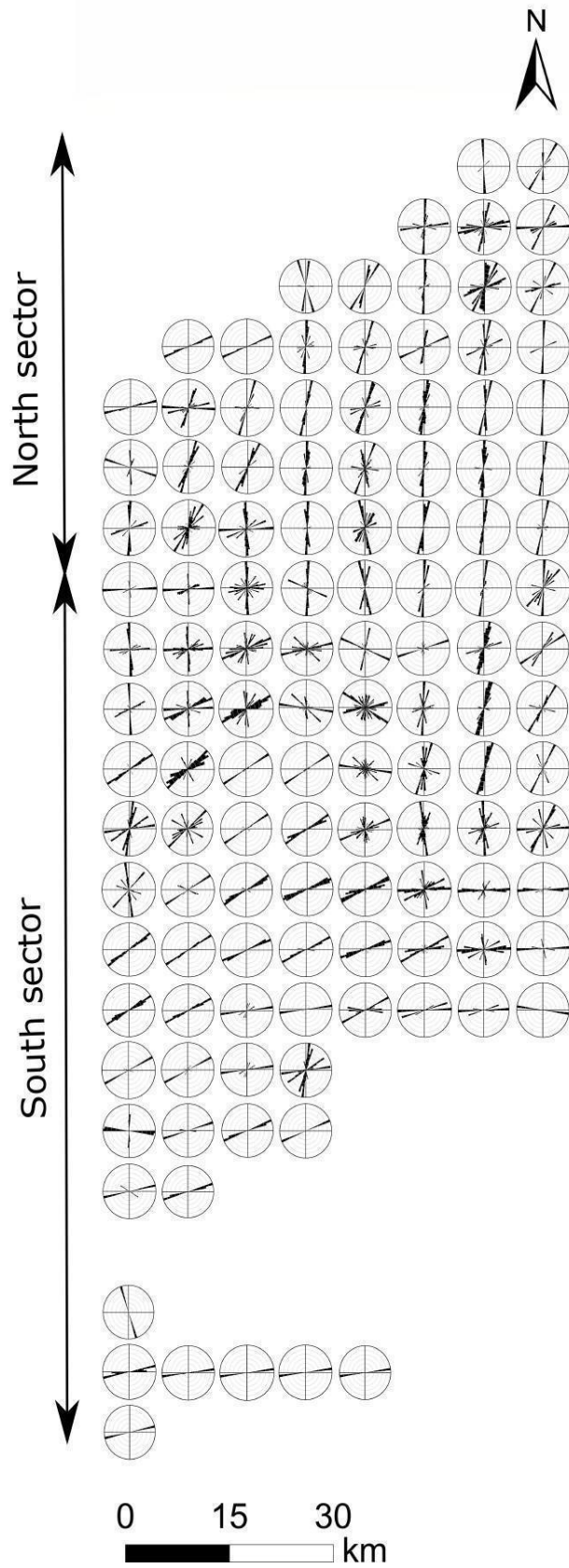
**Figure 3.9.** Structural Map of Noctis Labyrinthus at 1:39,000 mapping scale and 1:195,000 output scale. The polar plots indicate the trends for the major and minor mapped faults within Noctis Labyrinthus. These plots indicate four main directions: NS, NNE-SSW, ENE-WSW and EW, in addition to complementary slight trends on the NNW-SSE, NW-SE and WNW-ESE. The total number of fault measurements is 4414.

We also analysed the fault orientations through a mosaic of rose diagrams, made of a grid of 30X30 sq.km for each cell (Fig 3.10 and Fig 3.11). The results of these plots are represented in the figure. 4.2. This mosaic shows that faults in the northern sectors are usually more continuous and less ramified than faults in the southern sector which are oriented in diverse directions and interacting with the pit chains. Overall we identified three main systems of faults (Fig 3.12).

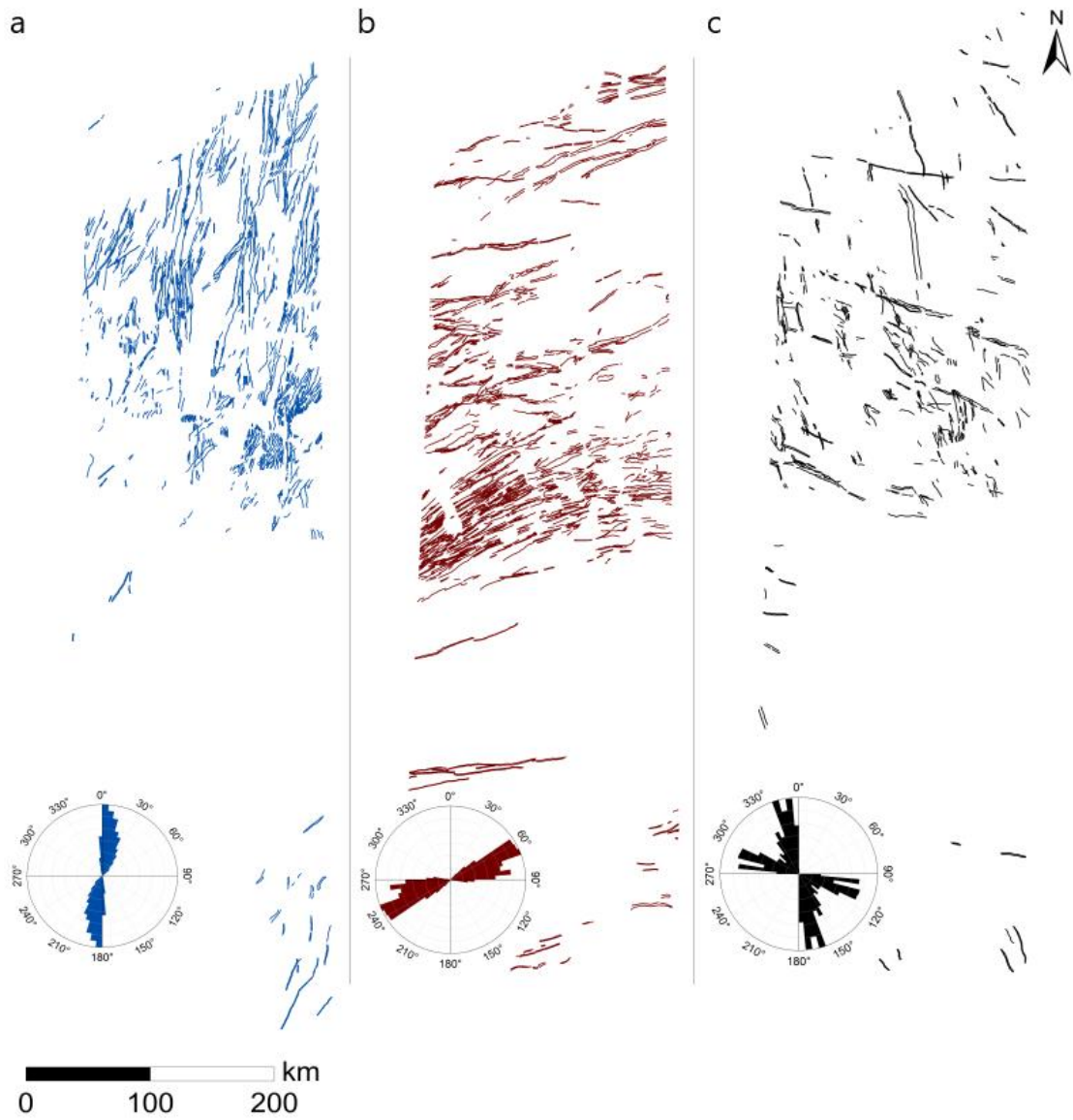
- NS to NNE-SSW Fault system (N=1792): This fault system is expressed mainly in the northern sector and slightly fades out by getting close to the pit chains area (Fig 3.13). The faults of this system are characterised by a length ranging between 70.532km and 0.427k



**Figure 3.10.** A mosaic of the rose diagrams for all the mapped faults, indicating the different trends where faults are mainly oriented. The grid is 30X30 sq.km per cell.

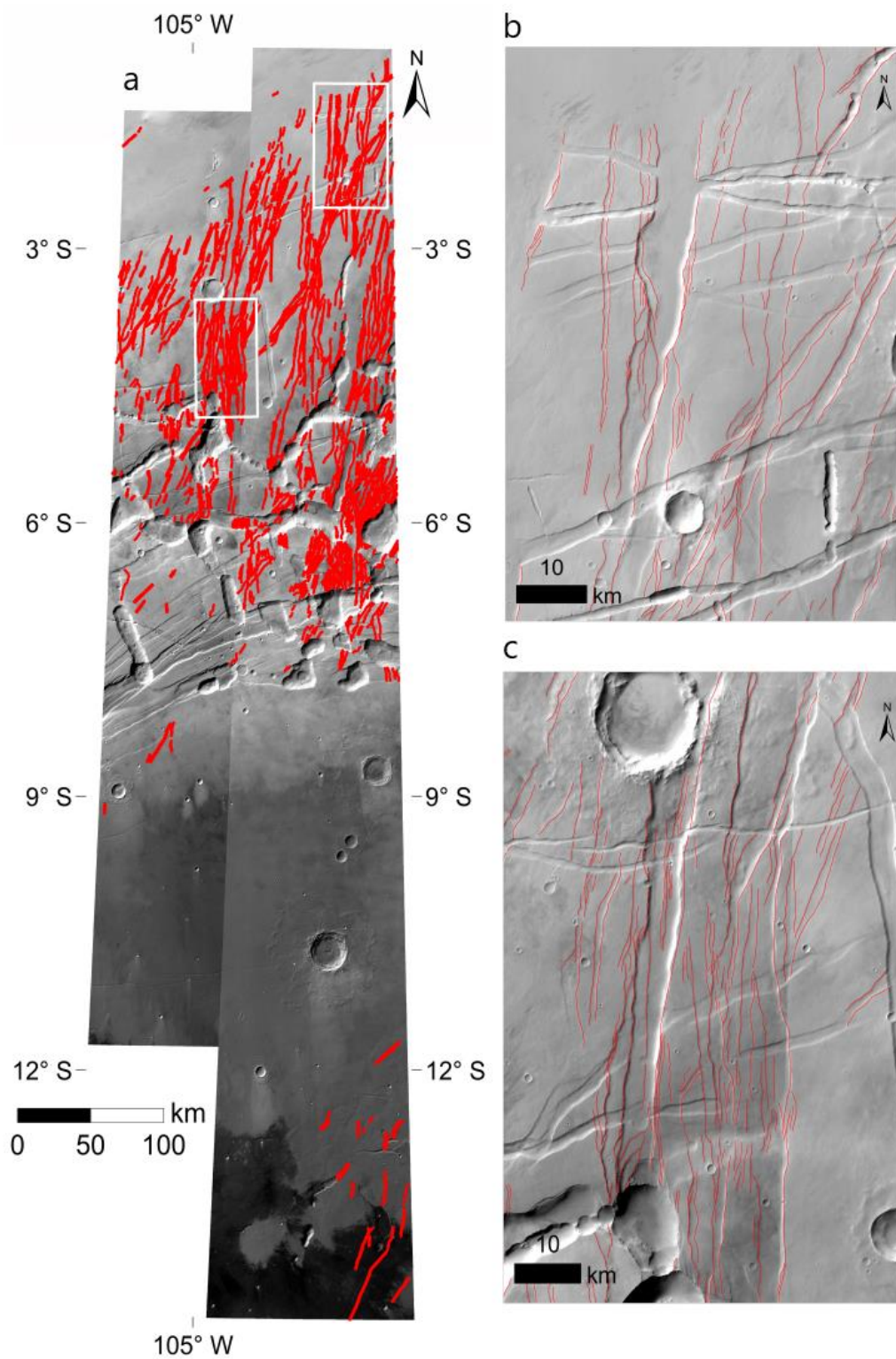


**Figure 3.11.** Polar plots mosaic for all the mapped faults in white background for the selected area displaying the orientation of the diverse polylines (mapped faults) between the north and the south sectors.



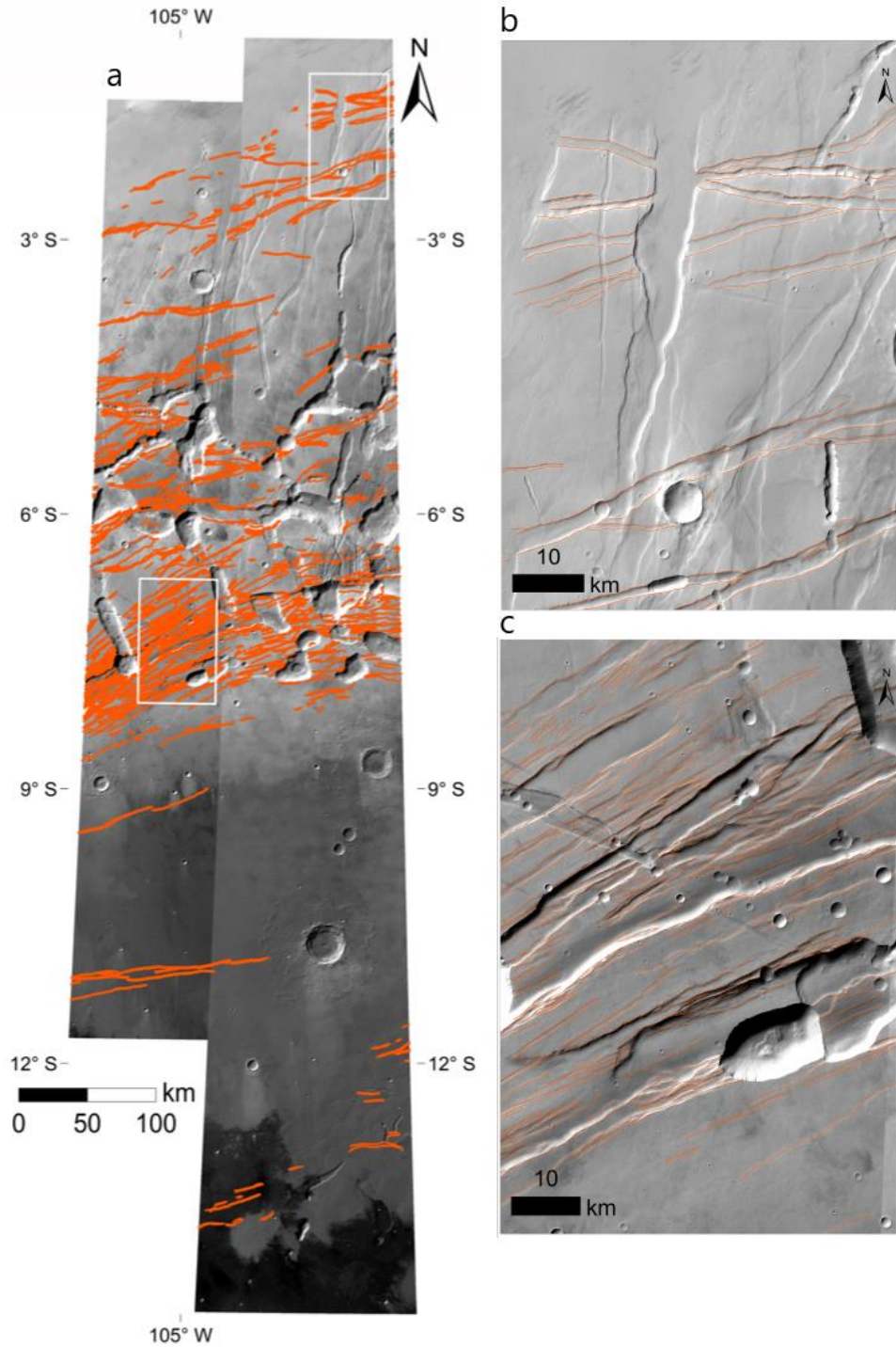
**Figure 3.12.** Fault distribution for the three faults systems (a) Fault system oriented NS to NNE-SSW (blue lines) (b) Fault system trending ENE-WSW and EW (dark umber lines) (c) Fault system oriented NNW-SSE, NW-SE, and WNW-ESE (black lines).





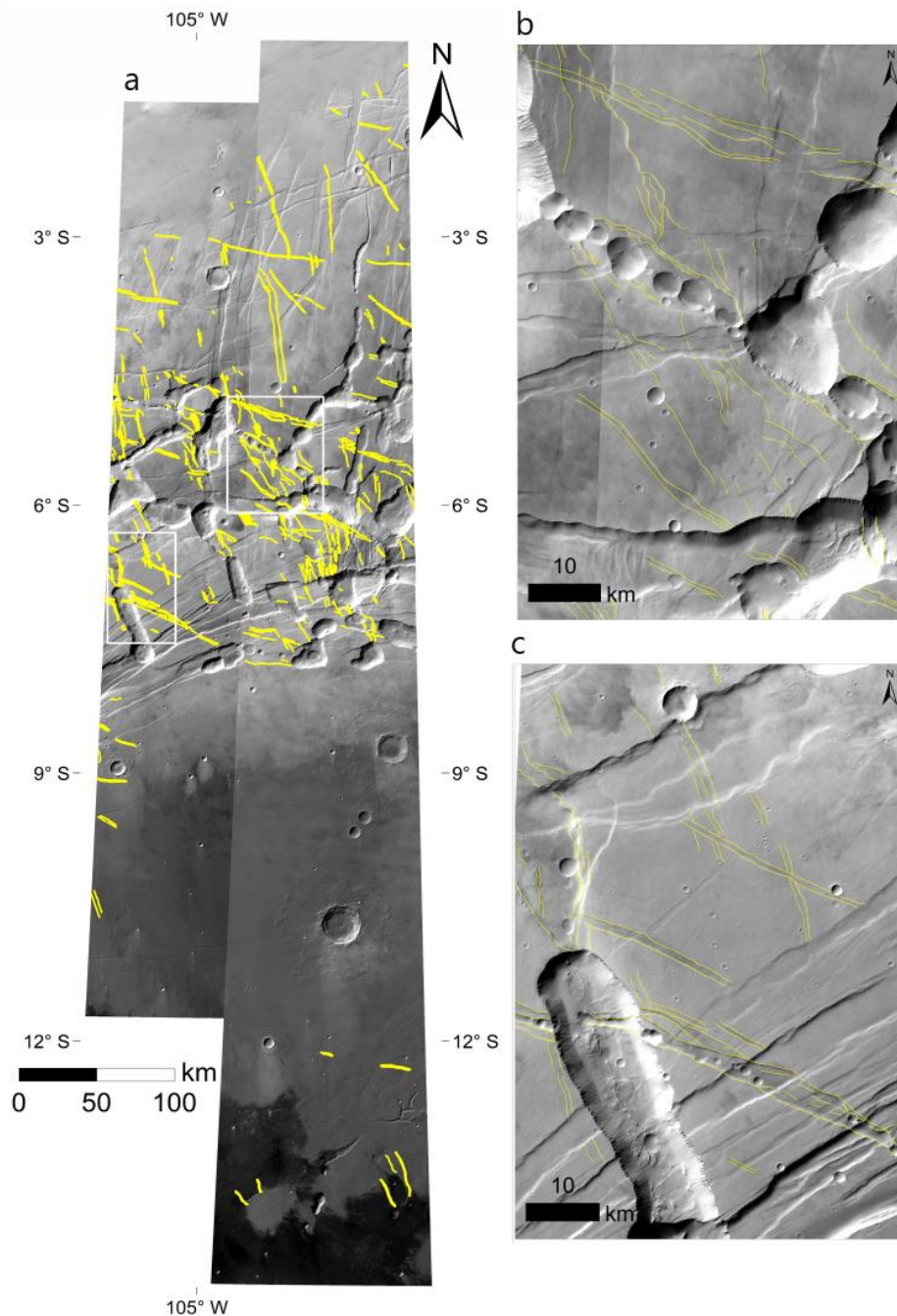
**Figure 3.13.** (a) Global view for the fault distribution that shows lineaments mainly oriented in NS and NNE-SSW (b) A closer view from the north sector, where faults are not connected to any pit chains (c) Section from an intermediate zone between the pit chains in the south sector and the faults of the north sector. Faults in this zone are mainly oriented NS.

- EW to ENE-WSW fault system (N=1759): Unlike the faults from the previous system, these faults are more frequent in the southern sector (Fig 3.14) and are strictly connected to the pit chains. Most of these faults are minor size faults, characterised by a length ranging between 0.372 km and 74.706km. Overall this system is concentric to Syria Planum.



**Figure 3.14.** (a) Global view for the fault distribution that shows lineaments mainly oriented in EW and ENE-WSW (b) A Closer view from the north faulted zone, showing EW and NS faults system (c) A closer view of the southern sector, where swarms of ENE-WSW size faults are densely present.

- NNW-SSE, NW-SE and WNW-ESE system (N=749): These faults are less numerous compared to the previous two systems (Fig 3.15), and they are always present in very close vicinity or connected to the pit chains. The faults from this system have lower dimensions, although some of them are tens kilometres long. The fault length of this system ranges between 0.598 km and 73 km.



**Figure 3.15.** (a) Global view for the fault distribution that shows lineaments mainly oriented in NNW-SSE, NW-SE, and WNW-ESE (b) Closer view from pit chains and faults joint features, showing some faults bordering the pit chains in NW-SE direction (c) Small and large faults bordering pit chains in the southern sector.

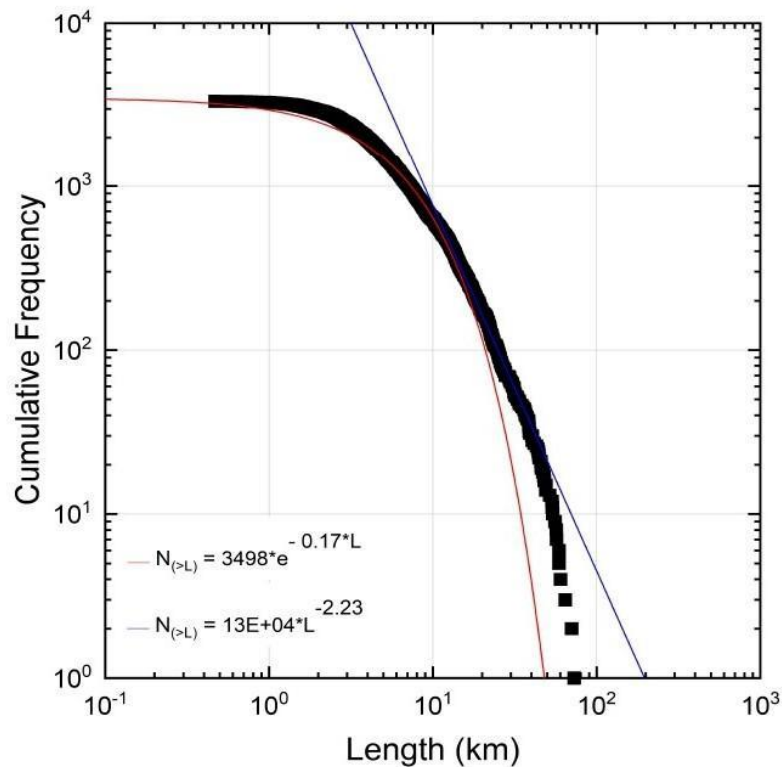


For analysing the fault network and the relationship between the faults and the pit chains, we subdivide the working area into two sectors:

- **North sector:** The faults on this sector are less frequent but more extended in length compared to the faults from the south. Three major trends of faults are expressed within this sector: NS, NNE-SSW and ENE-WSW. Additional observation shows that a group of NW-SE faults are slightly increasing their frequency and length by getting closer to the south sector and approaching the pit chains. A swarm of minor EW faults appearing in the north zone are clearly cut by some other faults from the ENE-WSW, interpreted to be the conjugate of the ENE-WSW faults.

- **South sector:** Dominated by ENE-WSW and EW faults shows an azimuth dispersion more evident and diffuse than in the north sector. A large group of the faults from this system begins from the southwest as an ENE-WSW set and progressively assumes EW strikes, towards the east side, creating an arc shaped structure concentric to Syria Planum. The NW-SE fault group is much more frequent and appears to be essentially connected or close to the pit chains. Even the ENE-WSW oriented faults become more dispersed in orientation when they are close to the pit chains area.

The fault length has been plotted on a cumulative frequency plot (Fig 16) for all the mapped fault data sets. The values are fitting exponential and power-law functions. For the power law, the limits of the lengths are around 9 to 52 km. All faults between these two length limits fit perfectly within a linear trend. However, for the exponential function, the length limits for the measurements that fit preferentially this function are varying between 400m and 18km. The equations for the exponential and power-law functions are labelled in Figure 3.16. Since the values that we are plotting can fit both exponential and linear functions, that might require the treatment of the long fault separately from the small ones. According to Soliva et al., 2008, in the case of the cumulative distribution of the faults' lengths that fit an exponential and power law function, as it's the case in figure 3.16, the small length faults are fitting an exponential function and bounded to a shallow brittle mechanical layer while the long faults are fitting with the power law distribution cut across the whole brittle crust.



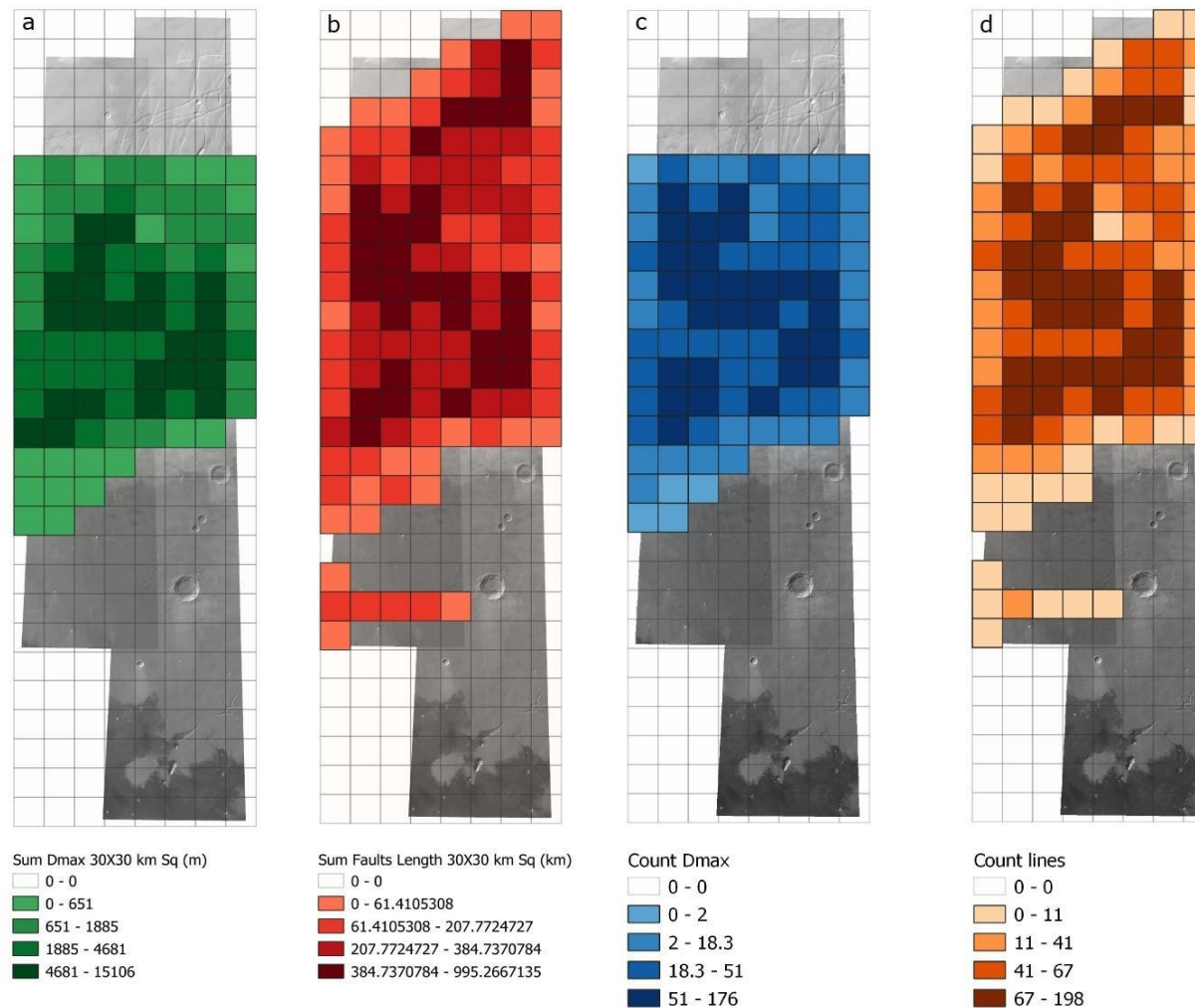
**Figure 3.16.** A log-log plot representation of the cumulative frequency plot for the fault's length distributions. The values scattering fits a power-law and exponential functions, according to the size of the faults.

### 3.3.2. Cumulative throw and faults density

To study the distribution of the accumulated maximum displacement and the sum of the fault's lengths (fault density) over the study area, we created a grid of 30X30 sq. km that cover all the area with available topographic datum (i.e., area covered by MOLA data). This grid led to an intensity map for the faults' length and displacement over each square of the grid (Fig 3.17). Some faults on the top north of the selected area were partially or completely not covered by MOLA topographic data, thus they were excluded from the vertical displacement measurements. Some of the faults are expressed over an individual cell of 30X30 sq. km grid and they do not extend for a long distance, whereas others are continuous for a long distance and transect more than one cell of the grid.

On the resulting maps it is evident that the displacement is highly intensified where pits and pit chains are associated with faults. The higher accumulated displacements range between 4681m and 15101m, and indeed are documented in pit chains areas. The sum of the fault lengths per square grid shows also a similar result, where the accumulated length is important in the pit chains district. This spatial correlation between the accumulated displacement, the sum of the fault length, and the presence of the pit chains, suggests a link between the fault's geometrical attributes and the coalescent pit chain-fault features.

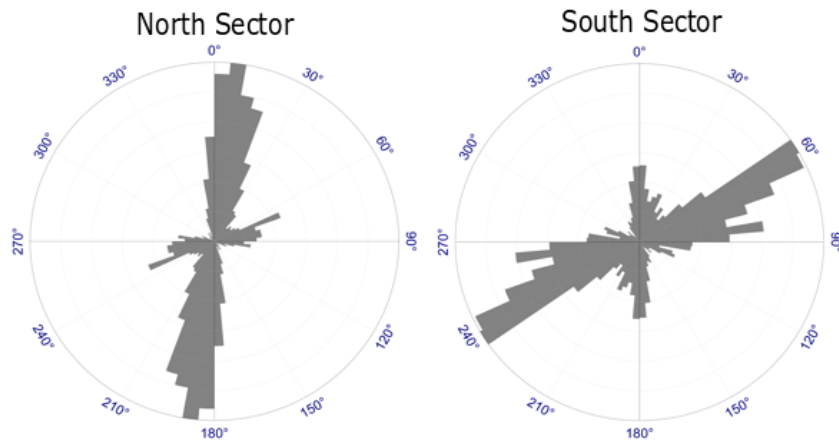




**Figure 3.17.** Maps of the fault cumulative length and throw distribution on a grid of 30X30 Sq.km (a) Map of the cumulative throw distribution (b) Map of the fault length distribution (c) Map of the number of throw measurements within each grid (d) Map of the number of length measurements in each grid.

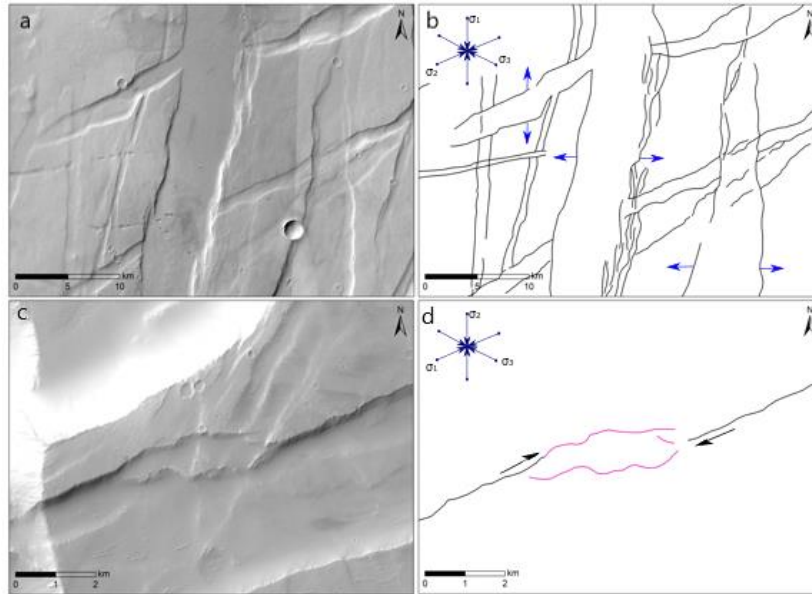
### 3.3.3. Faults system in North and South transect and kinematic indicators

This section of the thesis is dedicated to the study of the faults intersections, trends and kinematic in the north and the south sectors. The treatment of the north and south sectors separately will help to explain the difference between the faults, their difference in tectonic regime, and the role of the pit chains. As shown in figure 3.18, the orientations of the faults are different between the two sectors, and they appear more numerous and with more orientations in the southern sector.

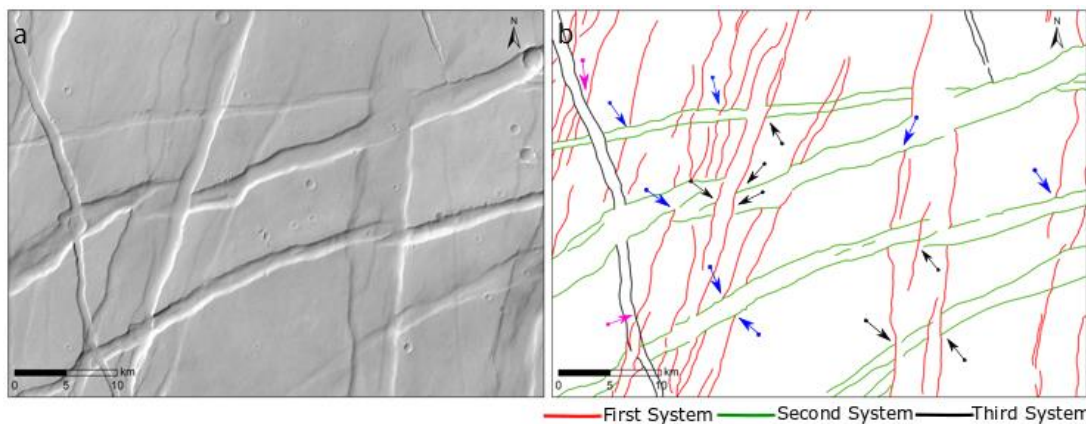


**Figure 3.18.** Polar plot for the North (Left diagram) and South (Right diagram) sectors, for all apparent faults.

The analysis of the faults pattern led to the identification of the presence of the two major types of faults: normal and transtensional (Fig 3.19 and Fig 3.20). The extensional tectonic strain generates a wide range of grabens, even bordering the pit chains. The strike-slip component on normal faults is scarcely present and detectable as splay or bending structures releasing bands (Fig 3.19) at small length scale (~2km), en-echelon arrangements and eventual riedel shear geometries.



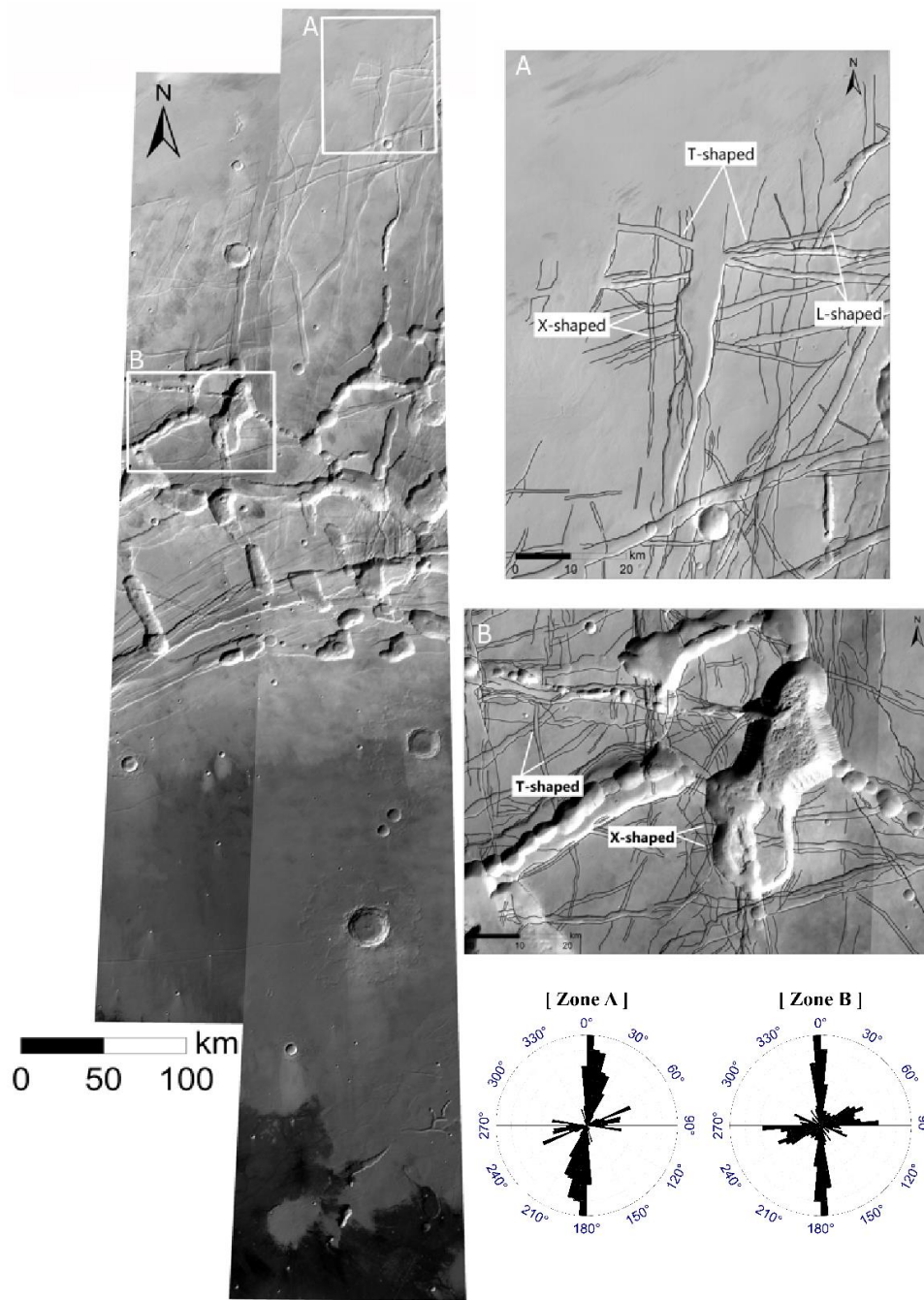
**Figure 3.19.** Fault distribution along the north and the south sector (a) Faults display within the north sector, showing the development of faults under extensional regime, generate the formation of parallel and cross-cutting series of grabens from the NS and ENE-WSW faults. HRSC basemap (b) Faults interpretation of image (a), showing the direction of the extension (blue arrow), (c) View of a releasing-bend, type spindle-shaped, generated in a dextral strike-slip system along ENE faults. J02\_045513\_1744\_XI\_05S104W CTX basemap (d) Lineaments interpretation of image (c), displaying the releasing bend. The shear components  $\sigma_1$ ,  $\sigma_2$  and  $\sigma_3$  are labelled within the image.



**Figure 3.20.** A close-up view for some cross-cutting faults from the three fault systems (a) HRSC basemaps without interpretation of the faults lineaments (b) Faults interpretation background show the three fault systems cross-cutting without a clear chronological order; The NS and NNE-SSW faults (red lines) interact with the EW and ENE-WSW faults (green lines). The intersections indicated by the blue arrows show the ENE-WSW fault system cross-cutting and superimposing the NS and NNE-SSW fault system, while the black arrows indicate the opposite where the EW and ENE-WSW are cross-cut and overlapped by the NS and ENE-WSW fault system. The ginger pink arrow shows some faults from the NW-SE fault system cross-cutting and overlapping some lineaments from the NNE-SSW system.

The relative chronology between the fault systems was not possible to be determined through the principle of superimposition because faults seem to repeatedly crosscut without any specific order (Fig 3.21). Hence, to analyse the intersections between the NS to NNE-SSW and the EW to ENE-WSW, we applied the concept of Collanega et al., 2020 according to which from the shape of the faults intersections (Fig 3.22) it is possible to determine if the systems were active together or following one each other and the strain

field under which they developed (radial extension, synchronous bidirectional extension, asynchronous bidirectional extension).



**Figure 3.21.** Faults intersection and sample district from the north and the south of the selected area (a) The location of the *zone A* on the north is labelled by (A), and the (B) is the *zone B* of the southern sector (b) *Zone A* presents clear cross-cutting relationship that generates the formation of rectangular blocks known as Chocolate-Tablet boudins, mainly T-shaped and X-shaped intersections between faults, with few L-shaped (c) *Zone B* presents a panoramic view of pit chains bounded by two parallel faults and a swarm of small-size faults (d) Rose diagram indicates the orientation of the faults in the *zone A* (Left polar plot), faults in this district are mainly oriented in NS, NNE-SSW with few faults trending in the ENE-WSW, and EW directions. The *zone B* is characterised by faults mainly oriented in NS, NW-SE, EW and ENE-WSW. The polar plots for both districts are derived from polylines by the polyline length of faults.

According to Collanega et al., 2020 (Fig 3.22) the intersection shapes between faults is mainly controlled by the maturity of the intersected lineaments, and is directly influenced by the relative faults system timing. In particular, faults intersections have been categorised into four groups (Fig 3.22):

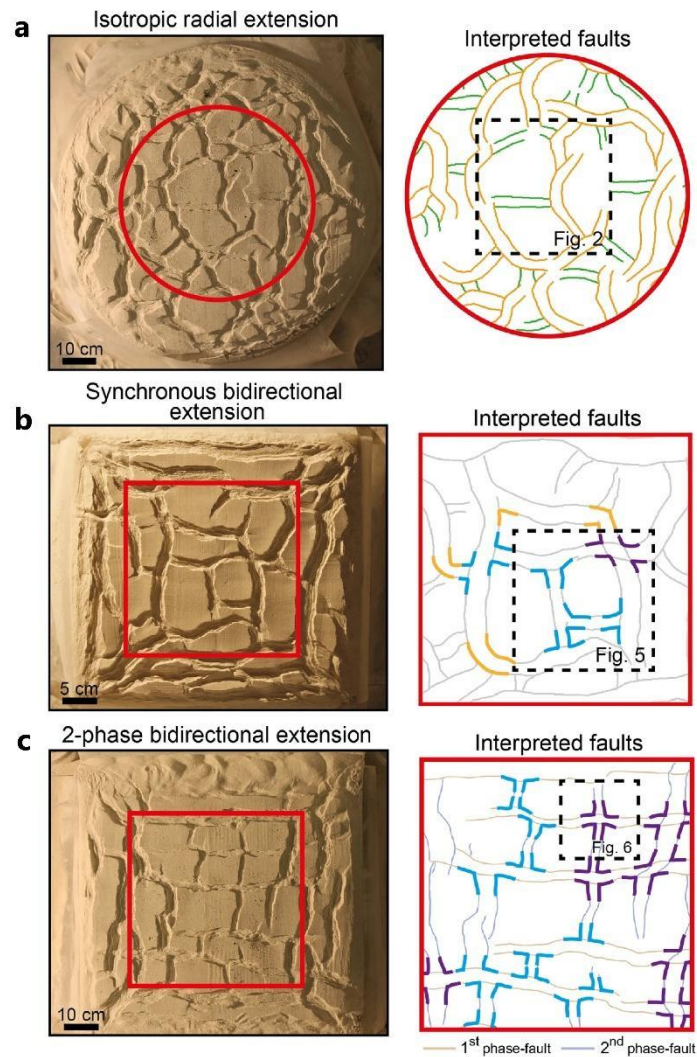
- The T-shaped intersection: are intersections generated by approximately orthogonal faults, bisecting at an angle of  $90^\circ$ , producing a perfect T-intersection. The faults in this case have different maturity and the T-shaped intersection is made up by a mature fault not transected by a perpendicular later fault.
- The L-shaped intersection: The faults in this category of intersection have the same maturity level. It is typical of synchronous bidirectional extensions.
- The X-shaped intersection: intersection produced by faults cross-cutting each other in an almost perfect orthogonal geometry. This intersection shape is most likely due to simultaneously active faults. The X-shaped intersection creates quadrilateral blocks with angles of around  $90^\circ$ .
- The Y-shaped intersection: These types of intersection are generally produced by an isotropic radial extension that results in a pattern of polygonal faults with a rather uniform strike distribution. Faults in this case intersect at high angles, between  $90^\circ$ - $120^\circ$ , forming major curvilinear grabens. The Y-shaped intersection is produced by a linear fault terminating against the high-sinuosity faults in their point of maximum curvature.

The different frequency of such intersections within a fault network are indicative of:

- Simultaneous bidirectional extension (synchronous bidirectional). The faults in this single phase terminate against each other in equal measure, and consequently faults from both directions are equally extending in terms of total length. The geometries of intersection between the different faults are in this case dominated mainly by T-shaped and L-shaped intersections.
- Two different phases of uniaxial extension (asynchronous bidirectional). In case of equal strain amount for the two phases the faults from the second phase preferentially terminate against the fault of the first phase which affect the total length of the two fault systems, and consequently faults from the second system are less extended compared to the faults from the first system. This cross-cutting between the two fault systems generates a large distribution of T-shaped intersections as a major geometry and some X-shaped intersections. The geometries of the faults intersection are in this case controlled by the timing of the two fault systems.
- Isotropic radial extension. In this case, normal faults intersect at high angles ( $90^\circ$ - $120^\circ$ ). Straight faults terminate on high-sinuosity faults in the point of maximum curvature, generating Y-shaped intersections, expressed in triple junctions of grabens.

We analysed the faults intersection in both sectors by taking a north and south sample zone. In accordance with what was previously mentioned, the faults geometrical attributes, pit chains distribution and the shaped intersection between lineaments are clearly unbalanced between the two sectors, consequently we will study each sector apart.

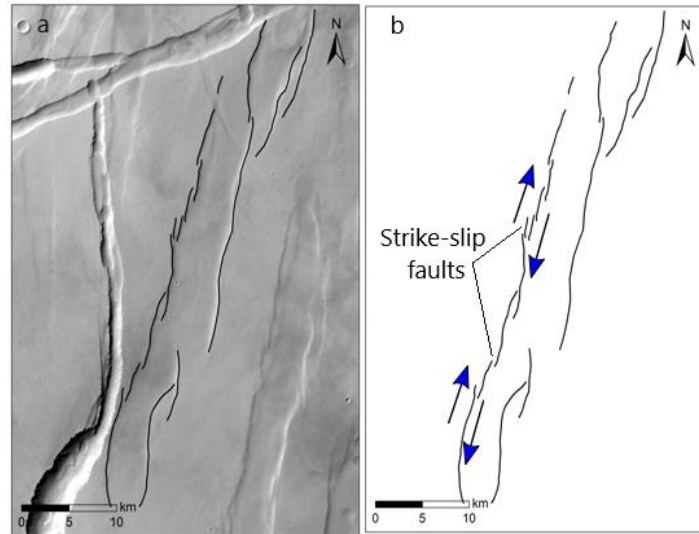




**Figure 3.22.** Faults shaped intersections. (a) Isotropic radial extension and final geometries of the faults intersection. The orange lines represent the major curvilinear faults who intersect the minor faults represented by green lines, in their points of maximum curvature (b) Synchronous bidirectional extension along two perpendicular directions and the final faults geometries. The faults in this case intersect each other at  $\sim 90^\circ$ , producing preferentially T-shaped and L-shaped intersections (c) 2-phase bidirectional extension and the related final fault geometries. In this case, the first deformational phase happens by applying N-S extension, then by applying EW extension, while the second phase of deformation faults systematically terminate against and occasionally crosscut first-phase faults, generating the formation of T-shaped and X-shaped intersections (Collanega et al., 2020 – Modified).

### Structural analysis of a north sample site

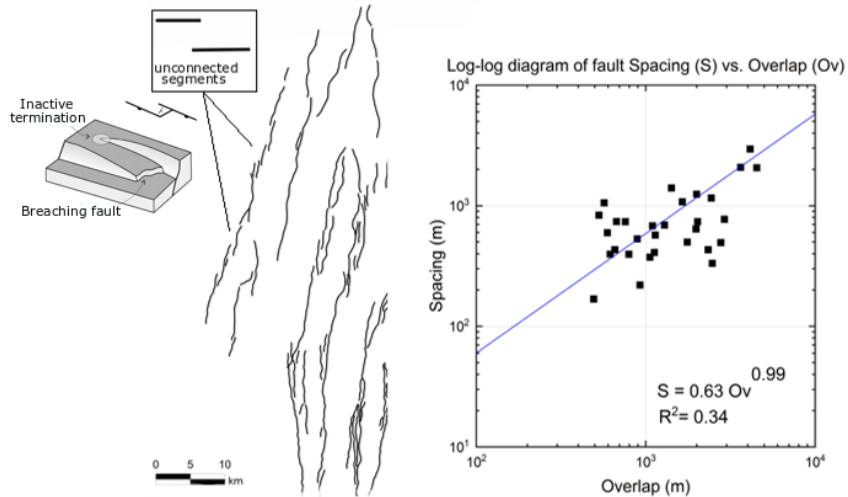
We selected a field sample from the northern sector to study closely the faults, geometries and intersections. The location of the selected area is indicated in figure 3.21, and displayed within figure 3.21.A. All the faults of the north sample site are characterised by an extensional kinematics but some of the NS to NNE oriented show also right steeping echelon segments (Fig 3.23), separated by releasing zones often without any linkage between the segments although in some cases (Fig 3.24).



**Figure 3.23.** Echelon of strike-slip faults in the north district (a) HRSC basemap, displaying a series of transtensional faults (b) transtensional faults as interpreted from the image (a), show a series of segments developed by relay ramping.

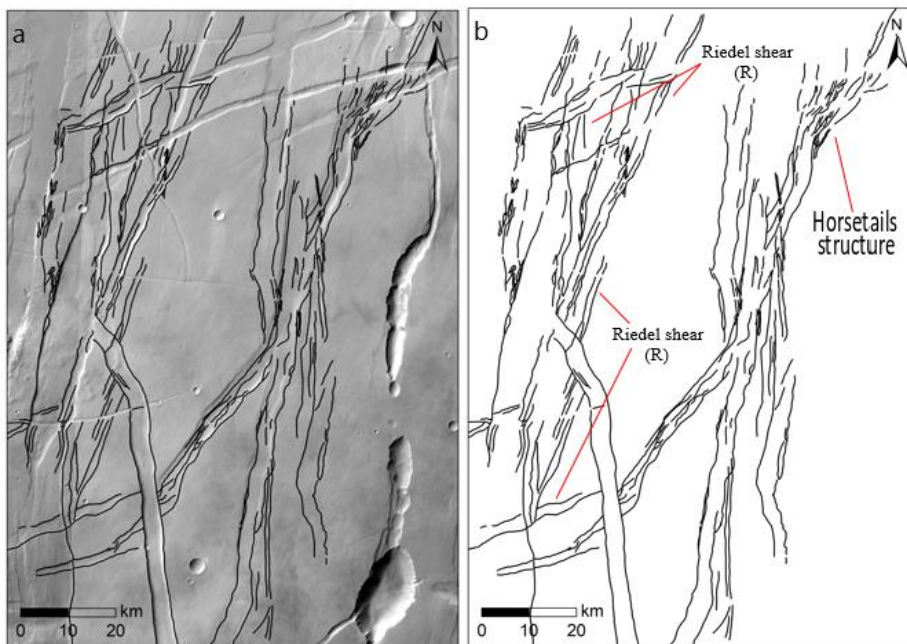
All the strike-slip kinematics that have been documented within the working area formed in an extensional context hence defining transtensional activity. The figure 3.22 presents an echelon of strike-slip faults in the north sector, which leads to a series of releasing-bends types within a dextral strike slip kinematics.

We measured the Spacing (S) and the Overlap (O) of thirty faults segments from the same orientation (more details on such measurements are in Walsh et al., 1999, 2003, Soliva et al., 2006, Torabi et al., 2019). Figure 3.24, shows a large scattering of the obtained values (i.e., over 168 m of spacing). Therefore, Spacing and Overlap of these fault segments cannot be fitted in a perfect proportional relationship and it seems that the faults geometries are controlled by other factors rather than the faults initial shear intensity stress (i.e. hosting rock thickness, stiffness, stress field, fault reactivation). The hosting rock can play the role of blocking barrier for the length extension (Soliva et al., 2006, Torabi et al., 2019), and consequently it prevents and/or limits the extension of faults for long distance. In this case faults will be presented in short or limited length, while in some cases, the hosting rocks aid on the extension of the faults' length through their brittle behaviour. The reactivation of faults contributes also to their length, since they can be further extended.



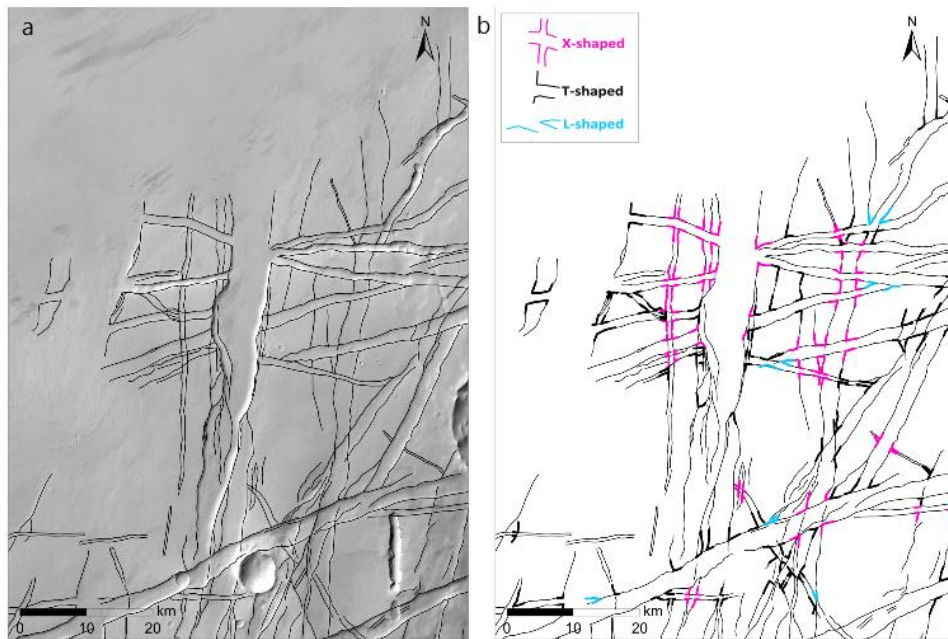
**Figure 3.24.** Echelon configuration of the fault segments sets in the Northeast flank of Noctis Labyrinthus. We measured the spacing and the overlap for 30 segments and we plotted the data in Spacing vs. Overlap diagram. The spacing is defined as the horizontal distance between two parallel to subparallel echelon discontinuities, while the overlap is the common length between two relay ramping segments (Rock block image in the left after Uzel, 2016-Modified)

A synthetic Riedel conjugate set propagates out from the main NS fault system demonstrating that the NNE fault set and the NS one could be conjugate and responding to a dextral transtensional kinematics. The figure 3.25, shows also horsetail splays faults departing from a major NNE graben. These horsetail structures tend to develop where slip dies out more gradually towards the fault tip; these features tend to be sub-parallel to the inferred  $\sigma_1$  direction. In our case they are indicating a right lateral component along the NS and NNE directions. Hence all the kinematic evidence of strike-slip activity (en echelon arrays, Riedel structures and horsetails) concurs in indicating a dextral transtensional along the NS to NNE fault system.



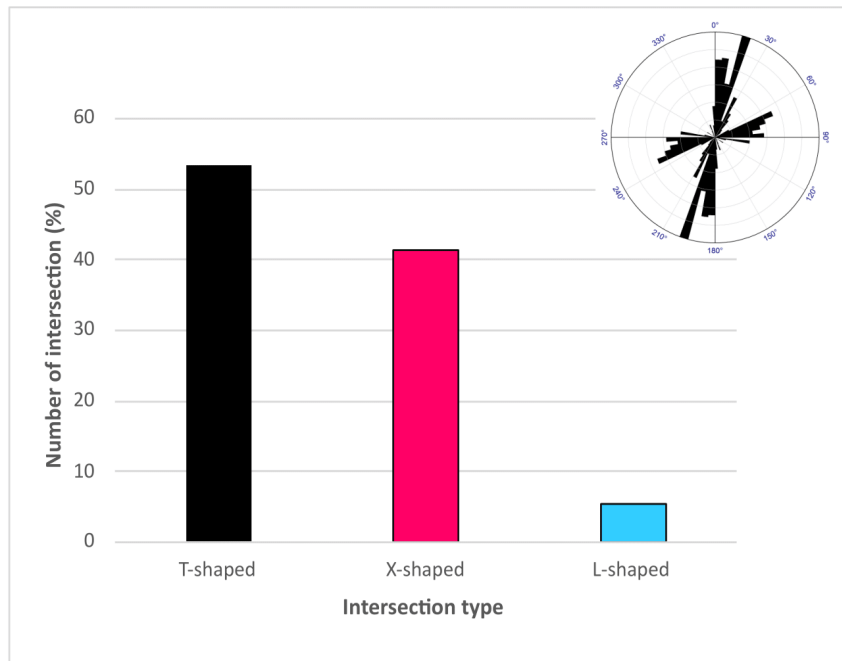
**Figure 3.25.** Riedel shear structures (R) in the northern sector (a) Interpretation over HRSC basemap (b) View of the interpreted lineaments, showing normal faults, with synthetic Riedel shears and horsetail branch faults.

The analysis of the cross-cutting relationships and intersections within the area (A) show that the T-shaped and X-shaped intersections appear to be the dominant, with a seldom appearance of the L-shaped intersection (Fig 3.26). The T-shaped intersections are slightly prevalent compared to the X-shaped intersections, and they often show one system terminating on another; there could be the possibility that one of the two systems began before. The X-shaped intersections suggest that the intersecting systems might be simultaneously active. In our case and taking the example of Zone A, the X-shaped and T-shaped intersections are generated by the cross-cutting relationship of faults oriented on: NS, EW, ENE-WSW and NNE-SSW. The L-shaped intersections are rare, and they are usually generated when two faults terminate one against the other.



**Figure 3.26.** Faults intersection shapes (a) and interpretations (b), dominated mainly by T-shaped and X-shaped intersections, indicating a bi-directional extension in the north sector. The type of the intersections is indicated by the following letter: **T**= T-shaped, **X** = X-shaped, **L** = L-shaped.

After identifying the different intersection shapes within the north zone (A), we determined their distribution through the histogram presented in figure 3.27. The sample field (A), covers a surface of 5857 sq.km, over which we documented 111 intersections of T-shaped, 86 intersections with X-shaped intersections, and 11 L-shaped intersections. The dominant intersection of T- and X-types, with the slight presence of L-shaped intersection, are interpreted to be the results of synchronous bidirectional extension along two perpendicular directions. This observation could be also confirmed by the rose diagram at the top of figure 3.27, where the values within the polar plot were derived from the length of the polylines (faults length). We also identified that faults from the first system are oriented NNE-SSW and NS, displaying a larger length compared to the faults from the second system, oriented EW and ENE-WSW. Thus, we are considering synchronous bidirectional extension along two perpendicular directions: NS to NNE-SSW and EW to ENE-WSW.

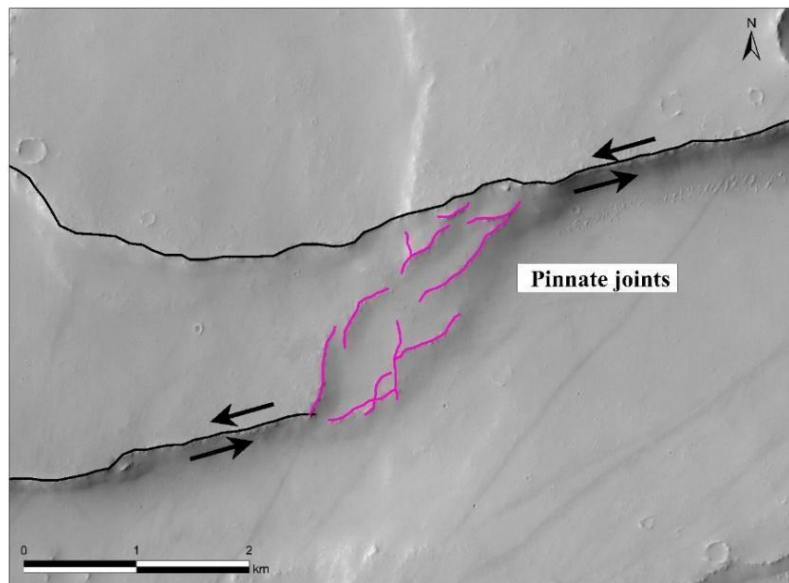


**Figure 3.27.** T-shaped, X-shaped and L-shaped intersection in the sample field (A) from the north sector. The histogram represents the number of the different intersections found on the zone (A). The rose diagram in the top right displays the orientation peaks by length of all faults present in zone (A).

### Structural analysis of a south sample site

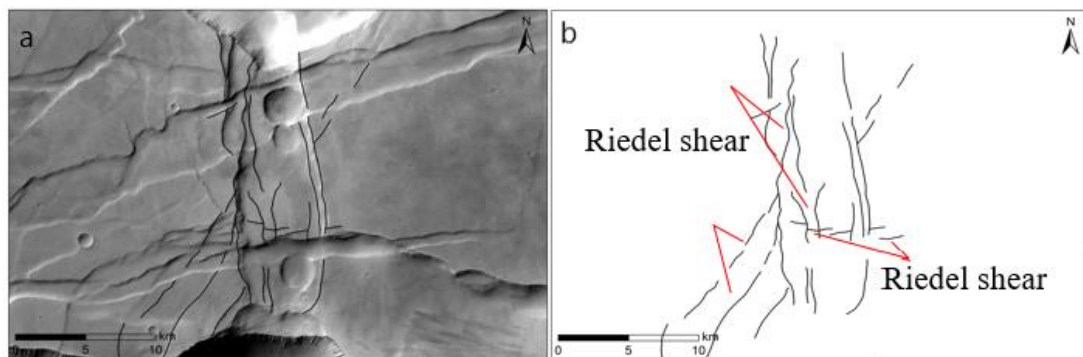
In the south sector, the faults from the second system (EW to ENE trending) are densely displayed, interacting with some faults from the first system (NS to NNE trending) and faults differently oriented potentially pertaining to a third system. This sector is characterised by a series of concentric grabens, mainly expressed in the south, and pit chains widely distributed over a large part of the sector. The faults in this sector are very long and ( $0.372 \text{ km} < L < 74.706 \text{ km}$ ) most of them border the pit chains or are connected to them. The faults within this sector are mainly normal, however, a few kinematic indicators of strike-slip components are locally present. Figure 3.28, shows a left-stepping sinistral transtentional generating a rhombohedral releasing bend along EW shear direction.





**Figure 3.28.** Rhomb-shaped pull-apart basin generated by sinistral transtensional kinematic of a Strike-slip fault (fault segments labelled in black lines), showing a stepover generating sidewall normal faults (pink lines) with a left-lateral shear zone, forming an angle of  $45^\circ$  to the horizontal plane. Image centred at  $256.35^\circ\text{E}$ ,  $-5.11^\circ\text{N}$  over CTX basemap.

As in the northern sector some Riedel has been found along a NS fault (Fig 3.29). The R Riedel faults in figure 3.29 are at acute angle  $\sim 30^\circ$  to  $35^\circ$  with respect to the main fault bounding, and they assume NE strike.

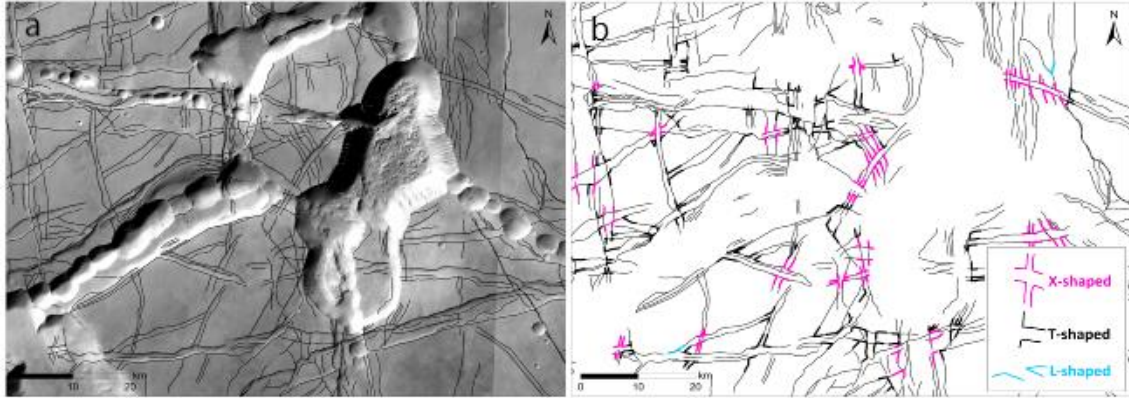


**Figure 3.29.** Riedel shear structures are associated to the main NS graben (a) View of the HRSC basemap, presenting a graben associated with Riedel structures and connected to a pit chain to the north and south (b) interpretation of the faults and Riedel shear lineaments in (a).

The presence of the pit chains within the south sector, might lead to assume that these features have a control on the faults geometrical attributes and orientation. In the next section we will discuss in detail the pit chains and faults relationship.

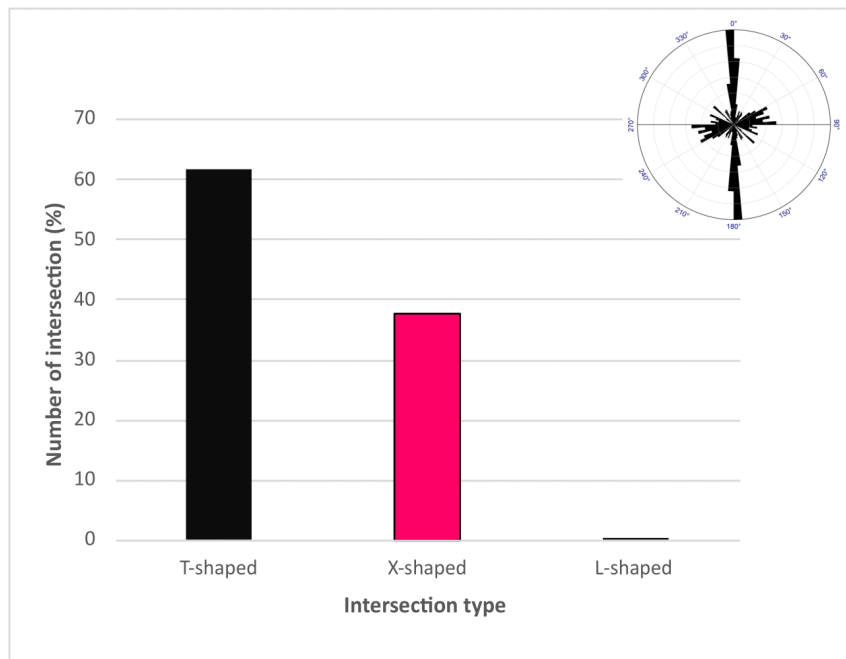
The faults in the south sector do not display rectangular blocks as in the north, since faults do not cross at higher angle, however, EW to ENE concentric grabens are clearly observed and they interact with the NS to NNE fault system, typical of the northern sector. The analysis of the shaped intersection shows that the T-shaped and the X-shaped are the most dominant compared to the L-shaped intersection which is rarely expressed (Fig 3.30). The zone (B) covers an area of 5561 sq.km in which we have documented 156

intersections with T-shape, 95 intersections with X-shape and 2 intersections with L-shape. The X-shaped intersections in this sector are generated by the cross-cutting relationship between the faults coming from the north sector, oriented NS and the faults from the south sector, oriented EW. However, the T-shaped is generated by the intersection of some faults from the third system oriented NNW to WNW which terminate on the EW to ENE and NS to NNE faults.



**Figure 3.30.** Shapes of faults intersection in the south sample site. The prevalence of T-shaped and X-shaped intersections indicate a bi-directional extension in the south sector, the first phase of extension is EW and ESE-WNW, generate the formation of the NS and NNE-SSW faults, followed by a second extension on the NS and SSE-NNW that generate the formation of EW and ENE-WSW faults. The type of the intersections is indicated by **T**= T-shaped, **X** for X-shaped and **L** for L-shaped.

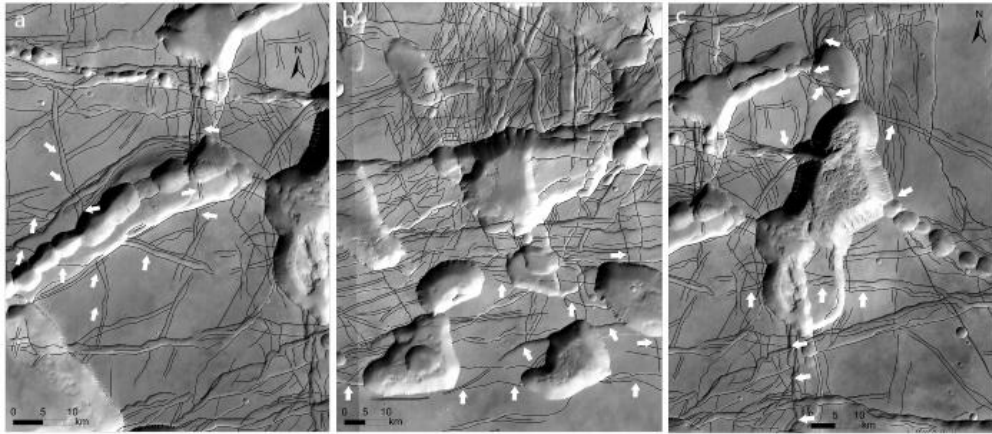
There are no major differences between the histogram of the north (A) and south zones (B) represented by the figure 3.27 and figure 3.31 respectively. Although the presence of the large extended series of concentric graben within the south sector and faults of different orientation, the L-shaped intersections are still not frequently observed. This might be explained by the fact that the faults with the same maturity level, didn't join at angles creating the L-shapes. The dominance of the T-shaped and X-shaped intersection within the zone (B) could be also confirmed by the rose diagram at the top of figure 3.31, derived from fault length. It's clear that the faults from the first system-oriented NNE-SSW and NS display a large length compared to the faults oriented EW and ENE-WSW. Hence the latter should be second-phase faults because they are less developed than the NS faults (first-phase) in terms of the total length. Hence in agreement with Collanega et al., 2020 model, we should consider two phases of bidirectional extension within this sector also: the first phase with a NS and NNE-SSW faults, followed afterward by a second phase of faulting-oriented EW and ENE-WSW. The T-shaped intersections are mainly the EW faults terminating on NS faults. We considered that the strain in this sector for the both extensional phases is equal, and it's higher compared to the north.



**Figure 3.31.** T-shaped, X-shaped and L-shaped intersection in the sample area (B) of the southern sector. The histogram represents the number of the intersections that have been distinguished on the zone (B). The rose diagram in the top right displays the orientation peaks by length of all faults within zone (B).

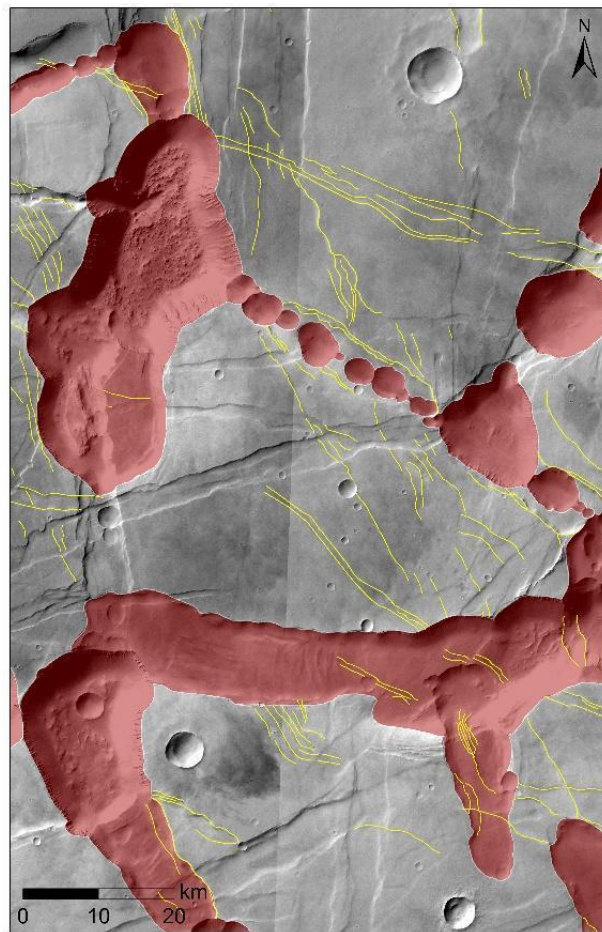
### 3.3.4. Pit chains and faulting

The network of rounded pit chains is expressed only in the highly Tectonized south regions and in connection to a group of grabens of different dimensions and orientations. The mapping of the faults and pit chains in Noctis Labyrinthus and their relationship with the grabens, shows that the pit chains followed the grabens formation and are the last event that occurred in the district (Fig 3.32). The intersection between the diverse faults system and graben in figure 3.32 and figure 3.33 displays the presence of Y-shaped intersection, generated by a high intersection angle that varies between  $90^{\circ}$ - $120^{\circ}$ . Some of the NS normal faults are observed within figure 3.32, terminate against the maximum curvature of high-sinuosity faults, displaying triple junctions of grabens, which also support the presence of the Y-shaped intersection, and this would suggest a coeval activity among the grabens and pit chains joining in Y-shapes. However, the Y-shaped intersection and display is still in discussion within this work, since we are still not sure about their shape and interconnection with the pits and pit chains.



**Figure 3.32.** HRSC basemap with fault systems, transected by pit chains (indicated by white narrow), suggesting that the pit chains formed just after the faulting phases (a) View of a pit chain area (b) Image of the southmost sector at the pit chains ends (c) Image from the northmost of the pit chains area, in limit with the smooth terrains of the north.

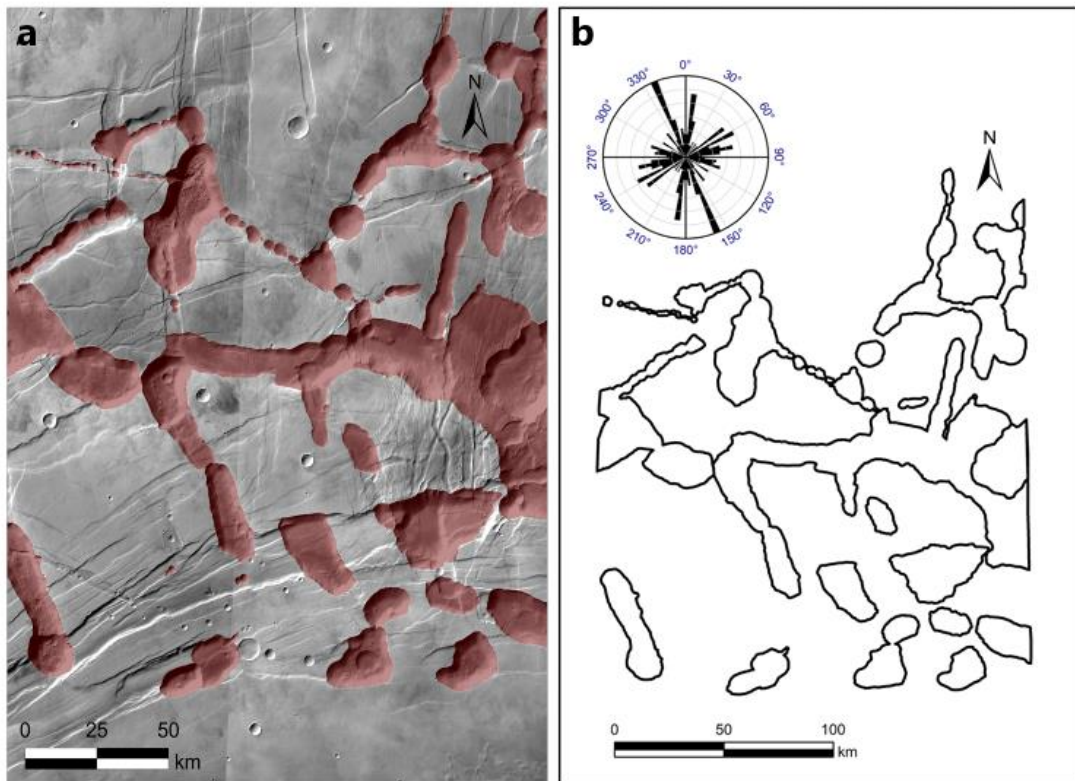
The few small size faults oriented in the NW a WNW are often following and closely connected to the pit chains edges, and they do not cut their floors, suggesting that the formation of this system is coeval or very close in time (Fig 3.33) to the pit chains formation.



**Figure 3.33.** An overview of a pit chains connected to some NW and EW faults.



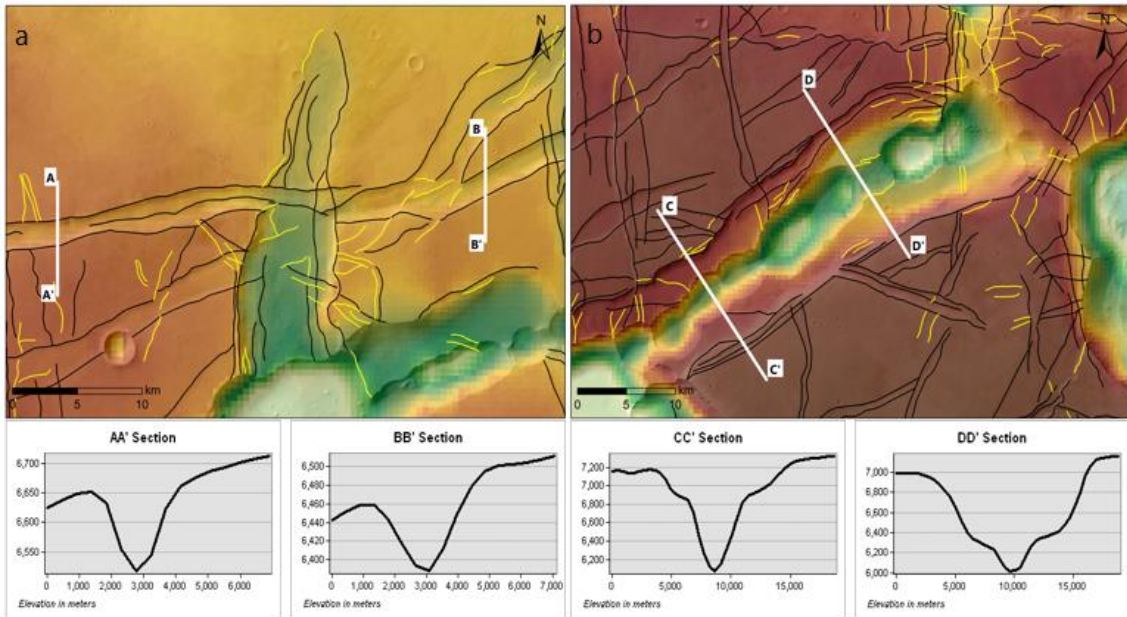
To understand the evolution of pit chains, we mapped them (Fig 3.34) with a polygon shapefile (N=24), while their edges with a continuous polyline (N=157). The highest pit chains length is of 66,547 km, while the short pit chains border is of 2km. We also measured the pit chains azimuth and plotted them in rose diagrams proportional to length (See Methodology for more details). The rose diagram in figure 3.34 shows a large scattering of azimuth distribution, with dominant peaks coincident to the direction of the main fault systems.



**Figure 3.34.** Pit chains display (a) and distribution of their directions shown in rose diagram (b). The edge of each pit was mapped by a continuous polyline and the direction of the pit chains was derived from the direction of the border's lines.

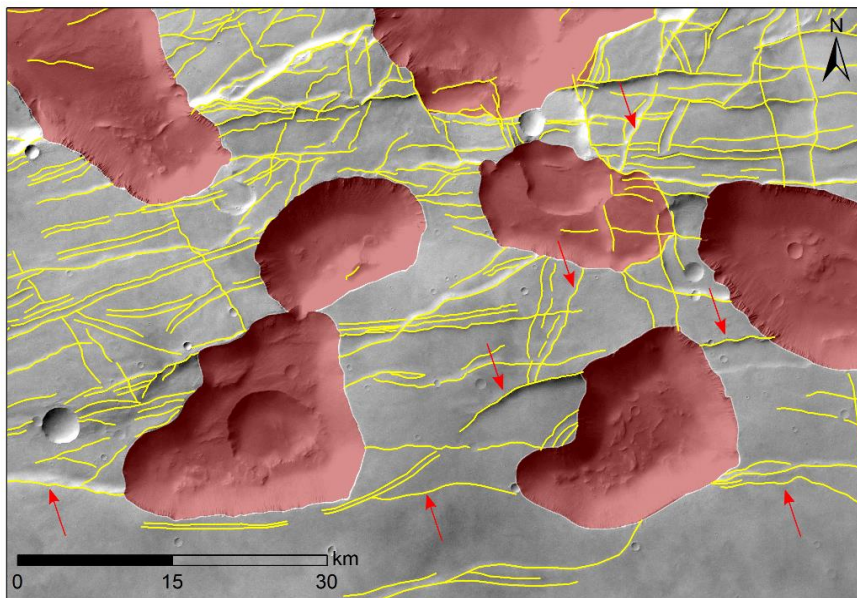
These unambiguous similarities between faults and pit chains directions, and the presence of pit chains in specific places of high strain within grabens, suggest a common process involved in their formation. In addition, it's evident that grabens associated with pit chains are characterised by a higher vertical displacement (Fig 3.35.a), up to 3600 m, with respect to the ones of the northern sector that are not related to pit chains (Fig 3.35.b). Indeed, in the southern region the pit chains appear to control the maximum vertical throw of the grabens.





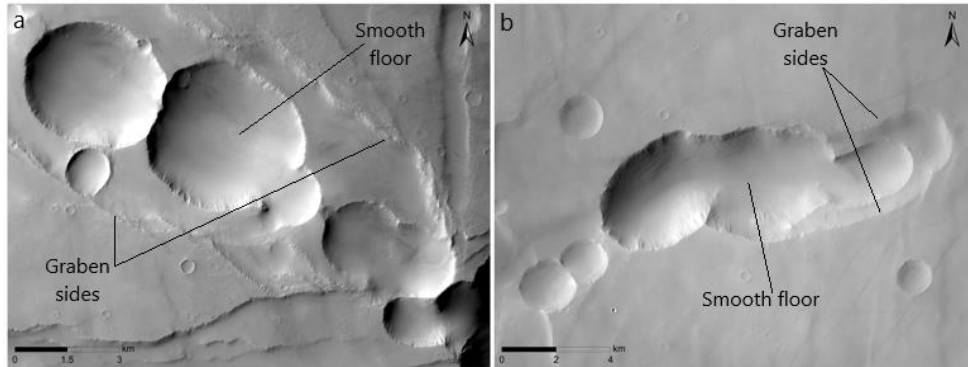
**Figure 3.35.** The maximum vertical displacement difference between faults and faults associated with pit chains (a) The topographic sections AA' and BB' show the vertical throw for some grabens not connected to pit chains (b) The maximum displacement is recorded across joint pit chains and faults.

Pit chains are bordered always by two parallel faults, clearly observed in the early stage of their formation, where they display a small and rounded shape. These borders are erased continuously and proportional to the pit chains' size. By increasing the pit chains size, the grabens edge is progressively eroded by the pit chains increasing its size, However, the tail of the grabens could be observed in the begin and the end of certain pits (Fig 3.36).



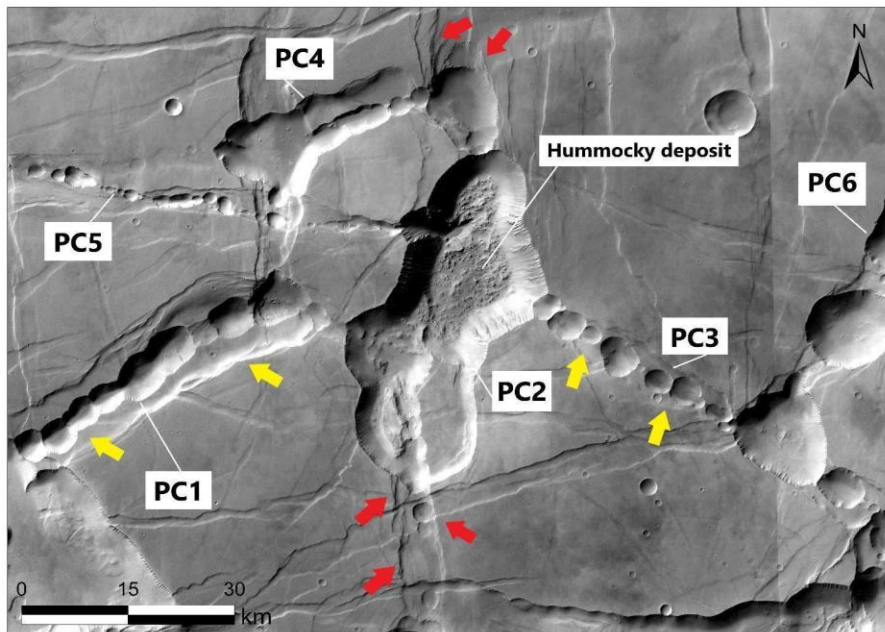
**Figure 3.36.** Series of pits and pit chains of different sizes connected with faults and grabens in the southern sector. The red arrow indicates some faults obliterated by the pit chains. Indeed, the pit chains are formed after the setup of the different fault systems.

Another evidence supporting that the pit chains are subsequent to the faults and grabens, is that the pits and pit chains floor often present a very smooth terrain without any hummocky, collapsed deposits or faults within it (Fig 3.37).



**Figure 3.37.** Composite CTX imagery example of a smooth pond-like deposit on the floor of bowl-shaped pit chains (a) Pit chains bordered by two visible parallel faults, in contrast, the image (b) displays pit chains features that obliterated the grabens ridges.

The elongated shapes of the pit chains indeed enlarge in a rhombohedral form at grabens intersection (Fig 3.38). Some pit chains overlap the graben boundaries, because of the pit chain enlargement and growth. Some others are smaller in width compared to the graben width, so they appear as coupled features with a pits series in the centre bounded by two or more parallel faults. Other pits are characterised by hummocky materials most probably indicating waste deposits derived by the collapse of their bounding walls on which ample arched-shaped niches are visible (Fig 3.38).

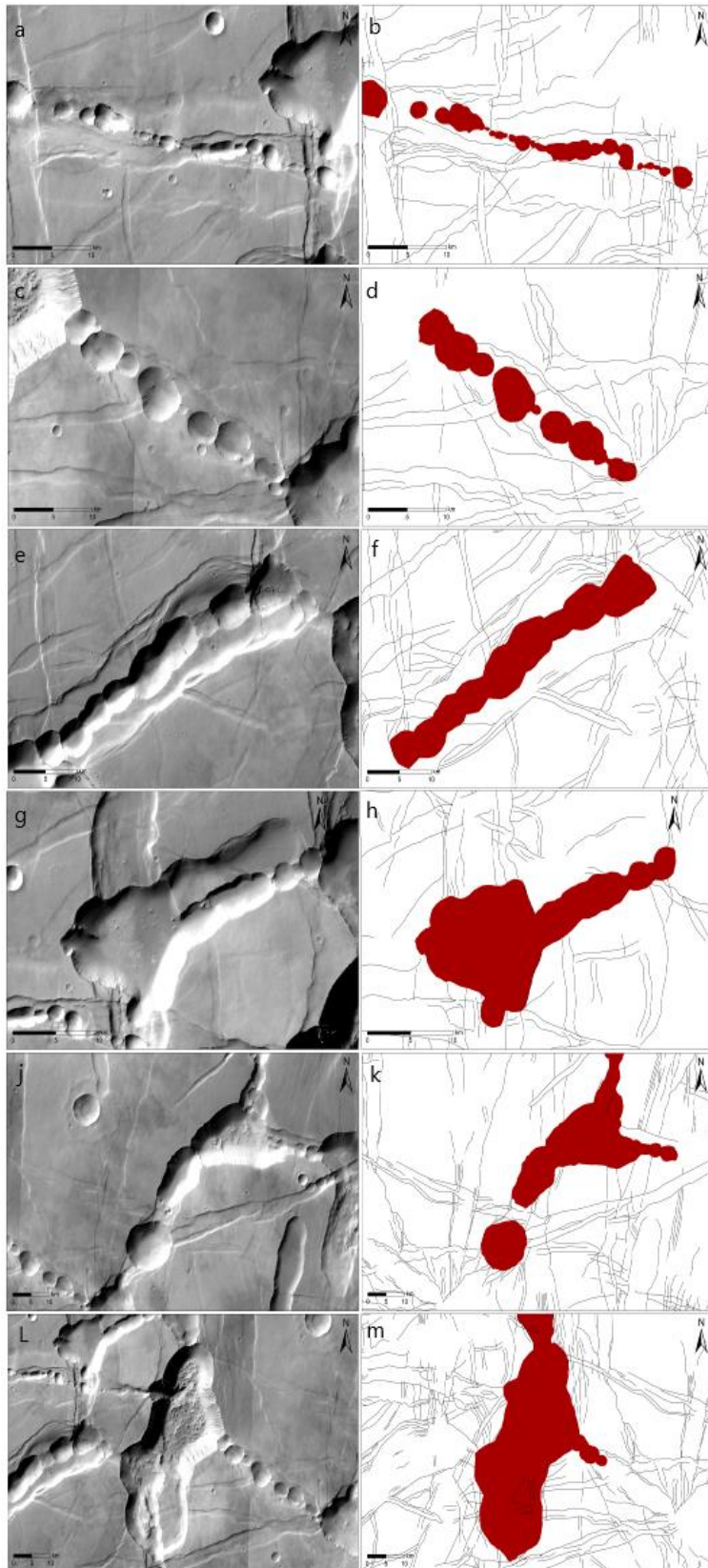


**Figure 3.38.** Overview of pit chains (PC) intersection and extension, showing a series of pit chains contained by two parallel faults. The pit chain number 2 (PC2) which is the largest one within the area, is located in the centre of the image and is connected to all the adjacent pit chains of different dimensions. The pit chains number 1, 3 and 5 (PC1, PC3 and PC5) seem to be at an early stage of the pit chain formation, where grabens borders are clearly visible and expressed all over the pit chains length and pit chains often formed by alignment of well defined single pits. The pit chains number 2, 4 and 6 (PC2, PC4 and PC6) appear to be the latest stage of the pit chains formation, displaying a large and rounded shape and

obliterating the grabens borders. The yellow arrow indicates a graben with a width greater than the pit chains and following the same trend of the pit chains. The arrow in red colour, graben with a width lower than the pit chains range, where faults disappear within the pit chain and continue outside them.

The figure 3.39, presents pit chains of diverse size and shapes, distinguished by their form and dimension. By analysing these features, we were able to identify six stages of pit chains evolution, controlled by their maturity level and relationships with the surrounding faults and grabens. The first stage of the pits and pit chains' formation is characterised by an alignment of relatively small circular depressions with smooth floors and disconnected one to each other. The second stage of the pit chain evolution is characterised by a larger dimension compared to the previous one, in this stage the pits initiate losing their circular form, and become mainly elongated rather than circular. Pit chains and faults in this level grow and follow the same trend, and pits start interacting between each other. During the third stage, the pits boundaries are hardly connected, sometimes they share the same borders, or alternatively the borders of the pits are completely merged, thus only a limited part of the pits can be identified because they appear as perfectly connected chains. The dimension of the pits in this stage is more important compared to the previous two stages. On the fourth stage, pits display as a combination of an extended chain of pit chains connected to a large rounded and scalloped pit, on the top of the ending of the chains which characterise this level of the pit's evolution. As usual, faults and graben are parallel or connected to pits on this stage, and mainly major part of these faults is superimposed by the large pits. The fifth stage shows that the pit chains assume a more lobate and distorted shape, due to mass wasting and landslides at their borders. The dimension of the pits is larger compared to the previous evolutionary stages, at this level pits become more deformed and they do not display a rounded shape anymore. The ultimate stage of the pit chains' evolution is characterised by a distinctive difference in the pit chains form; they become rhombohedral, very large and extended, in width and length. At this stage the pit chains' size is greater than the graben width, overlapping the graben boundaries, where both features grow as a parallel system.





**Figure 3.** Sketch of the evolutionary stages of the pit chains in the southern sector, indicating the growth of the pits size during each stage. The views here are from different regions of the working area. (a) and (b) are the first stage. (c) –(d) the second stage, (e) – (f) the third stage, (g) – (h) the fourth stage, (j) – (k) the fifth stage and (l) – (m) the last stage of the pit chains' evolution.

### 3.4. Discussion

The map that we produced in figure 3.9, was very helpful to identify three systems of fault, trending in different directions and identify the phases that could be recorded within Noctis Labyrinthus, based on the shaped intersection between these fault systems, following the concept of Collanega et al., 2020.

The first system of faults is a set of NS to NNE-SSW lineaments (Fig 3.13), consistent with right-lateral transtensional kinematics (Fig 3.23, Fig 3.24, Fig 3.25 and Fig 3.26). The dextral transtension on the northern sector of the studied area is expressed also by stepovers and en-echelon arrays, and many NNE SSW Riedel-like orientation on NS faults. Bistacchi et al., 2004, attributed these faults to the Noachian, potentially relating them to the evolution of the Tharsis Rise. The radially prominent grabens system around the Tharsis bulge could be explained together with the Noctis Labyrinthus NS fault system (Fig 3.40.a). However, Masson., 1977 suggested that NS and NNE-SSW faults are related to the Valles Marineris opening, and they were produced within two tectonic periods: during the first period the NNE-SSW was formed probably with other faults oriented on the ENE-WSW and NNW-SSE, producing a grid pattern that was used during the second deformational phase.

The second fault system identified is characterised by ENE-WSW and EW (Fig 3.13) trending faults. This group seems to be not coeval with the faults from the first system, however both systems crosscut and overlap each other (Fig 3.21). It's clear that these faults were active together with the NS to NNE-SSW fault system. The particularity of the EW to ENE-WSW system is that faults appear concentric to Syria Planum, with ENE-WSW direction to the west up to EW trends to the east. This concentric series of grabens seems to be generated by a radial oblate stress tensor, most probably related to the Syria Planum volcanic province. The Syria Planum underwent an extensional tectonic that probably initiated in the Late Noachian (Tanaka & Davis, 1988) together with a flexural uplift accompanied by the formation of some volcanoes (Fig 3.40.b). Masson,1977 explained the EW faults development to be related to the Valles Marineris and the sigmoidal deformation of the Noctis Labyrinthus area.

The third system of faults is oriented in NNW-SSE, NW-SE and WNW-ESE (Fig 3.15). They are not frequently distributed in the working area and concentrated mainly in the southern sector in which they are often connected to pits and pit chains. The phase responsible for this system is displayed in Fig 3.40.c.

We used faults geometries intersection and shape for determining the number of deformational phases based on the model of Collanega et al., 2020, because faults cross-cutting relationship was not helpful in our case for identifying the fault chronological orders, due to the reactivation of faults of the first and the second systems. In both sectors, the second system of EW to ENE-WSW faults seems to be the youngest one compared to the first system oriented NS to NNE-SSW. Indeed, the different shapes of the intersection between faults document a large distribution of T-shaped and X-shaped intersections, with a minor appearance of L-shaped ones (Fig 3.26 and Fig 3.30). These intersection types and the number of their distribution (Fig 3.27 and Fig 3.31) lead us to conclude that we are in a case of two-phase bidirectional extension: the first deformational phase is identified by the NS and NNE-SSW transtensional grabens that were developed



mainly on the north sector of the selected area, while during the second phase a group of EW and ENE-WSW faults were formed and displayed as a concentric graben in the south sector. Some of the ENE-WSW faults have been observed also within the northern sector, crosscutting with faults from the first phase and producing rectangular blocks. According to Collanega et al., 2020, within the model of two phases of bidirectional extension, the faults from the second phase terminate against the first phase system resulting in a shorter length compared to the faults from the first phase. In our results, the rose diagrams for the first and second system (Fig 3.12) are derived from the fault polyline, by polyline length, displaying a higher peak in the NS and NNE, delivered from the faults length, thus the faults oriented in this directions are characterised by an important length.

Furthermore, the spatial association between the faults from the third system and the pit chains (Fig 3.33, Fig 3.34 and Fig 3.37) suggest that these two features are probably formed under the same driving stress, a radial isotropic extension, responsible of the NNW-SSE, NW-SE and NW-SE, the reactivation of the first and second system and of the pit chains development (Fig 3.40.c.d).

Moreover, the development of the pit chains in the floor of the graben, in alignment with pre-existing parallel faults, and the frequent surface coalescence between these two features suggest a common process responsible for their formation and evolution (Fig 3.33, Fig 3.34 and Fig 3.35). Indeed, the pit chains coalesce always in areas where faults are densely present, as shown by the intensity maps of figure 3.18.

The first system of faults contains the NS and NNE-SSW trends, predominantly accommodating crustal extension, associated with local transtensional movement, moving southward, the ENE-WSW and EW graben develop associated to the formation of pit chains and pits, testifying a possible interaction between crustal faulting and crustal fluid circulation and accumulation. Due to the occurrence of the important volcanic area located at the southward border of Noctis Labyrinthus, which is the Syria Planum volcanic district, fluid likely may be magmatic in origin and the graben might be the expression of associated to concentric structures concerning the Syria Planum volcanic centre.

Thus, the model we propose is based on early extensional tectonics coupled with magmatic plumbing, as a reasonable assumption to explain the articulated rift network and scalloped troughs in Noctis Labyrinthus.

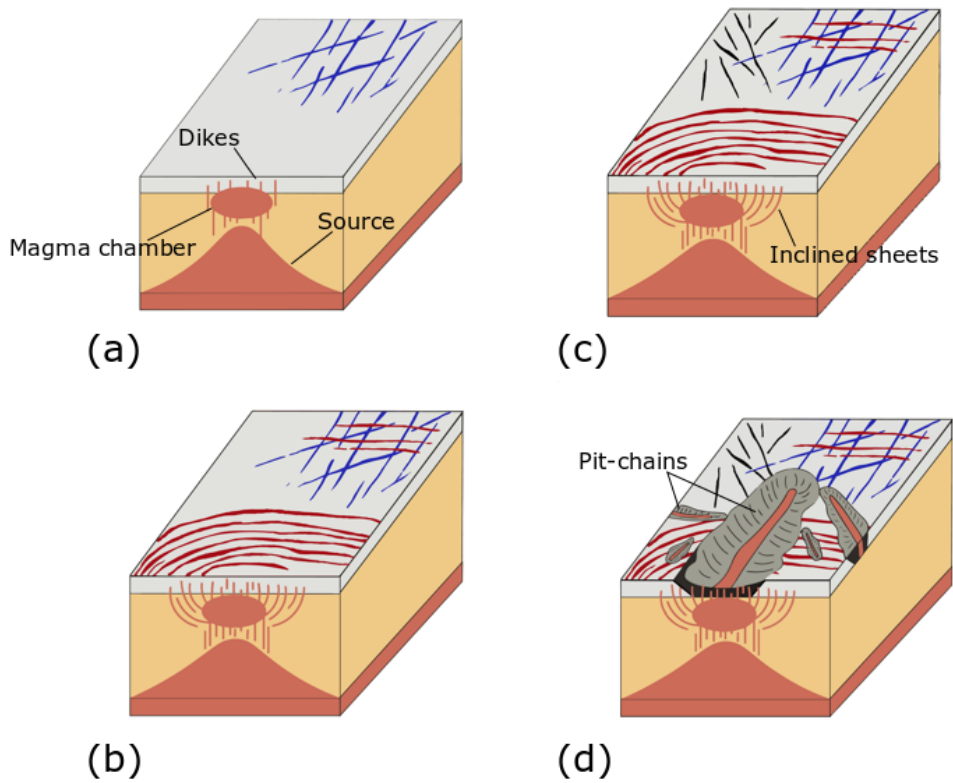
Syria Planum has a major role in the model that we propose for the deformational history of Noctis Labyrinthus. The volcanic behaviour of Syria Planum and its adjacent to Noctis Labyrinthus suggest that extended network of depressional features on this district most probably related to the surface collapse associated with the magmatic plumbing on Syria Planum. The small shield volcanoes of Syria Planum are controlling the magma channelling underneath the pre-existing grabens on Noctis Labyrinthus. In particular we assume that a group of sheet dikes departing from a deep magmatic source and the hydrothermal fluid circulation on Syria Planum were responsible for the (early) concentric grabens oriented on the EW and ENE, and later the pit chains development (Fig 3.37). After the magma emission on Syria Planum, the magmatic chamber started its

deflation, which afterward generated a crust uplift and consequently a surface collapse accompanied by the formation of the pit chains along the graben floor (Fig 3.40.d).

In summary, we believe that Noctis Labyrinthus deformational model consists of three major events, based on two major processes:

- First phase with NS and NNE-SSW transtentional graben whose origin is still undetermined but probably related to Tharsis rise evolution.
- The second phase most likely related to the Syria Planum volcanic province with the formation of concentric grabens EW to ENE oriented and reactivation of the system of the first phase radially oriented to Syria Planum. At this phase smaller pits aligned to the main grabens' trends could have also formed.
- The last phase still related to Syria Planum volcanic centre was probably responsible for an isotropic radial extension which generated the coalescence of pit chains and the development of WNW to NW system (the third faults system).

In this work we tie together a volcano-tectonic activity behind all events mentioned above, and thus Noctis Labyrinthus is the subject of an early extensional tectonic that produced a widely extended fault and volcanic processes potentially associated to a local shallow magmatic chamber, controlling dyke injection, hydrothermal activity, surface collapse and, consequently the pit chains formation and development.

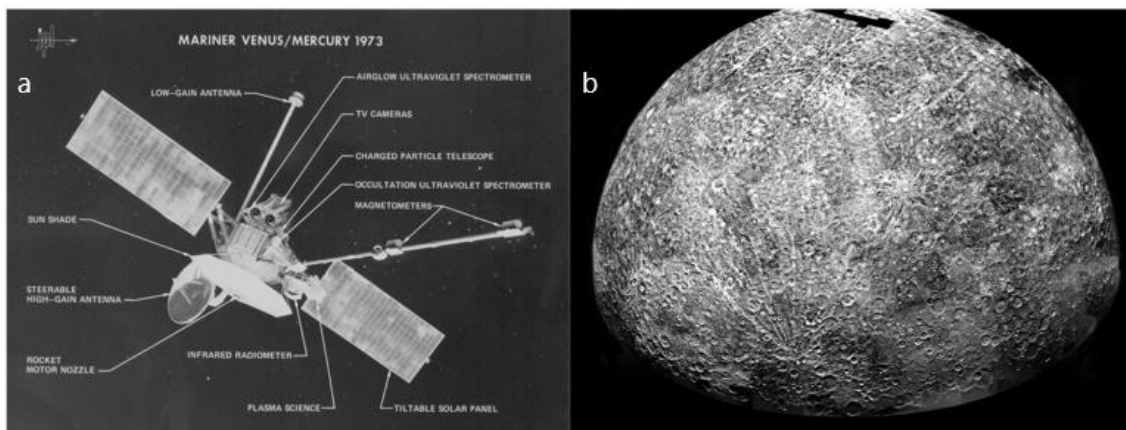


**Figure 3.40.** Sketch showing the possible deformational events within Noctis Labyrinthus (a) First phase of the bi-directional extension, generating by the formation of NS and NNE-SSW faults, mainly distributed in the north sector (b) Second phase of the bi-directional extension generates the formation of ENE-WSW and EW faults, expressed in major part on the south as concentric grabens. These concentric grabens might be related to the cone sheets directly connected to a magmatic chamber underneath Syria Planum (c) NNW and WNW faults formation (d) Pit chains formation. The figures (c) and (d) are two stages of the same phase.

## Chapter IV – Mercury: Overview

### *Missions and Exploration*

Two space missions were sent to Mars: Mariner 10 (1973-1975) and MErcury Surface, Space ENvironment, GEOchemistry, and Ranging known by MESSENGER (2004-2015). Mariner 10 (Fig 4.1) was launched on 3 November 1973, and provided a first step on the knowledge of the chemical and physical attributes of the planet, as well as a good coverage of its surface geomorphology.



**Figure 4.1.** Mariner 10 probe and mercury coverage (a) NASA Mariner 10 science instruments that were used for studying the atmosphere, surface, and physical characteristics of Venus and Mercury (b) Outbound View of Mercury as seen by Mariner 10. The image is a photomosaic, presenting the surface with heavily cratered terrains and different impact crater sizes ranging from tens to a few hundreds of kilometres (Images recognition: NASA/JLP).

In particular during the first flyby of Mariner 10, over 2000 useful pictures were produced and 45% of Mercury's surface was photographed by the M10 Television Experiment (Murray et al., 1975), and thanks to the Mariner 10 instruments (Tab 4.1). In addition, the third flyby provided a higher resolution data reaching about 100m/px (Davies et al., 1978).

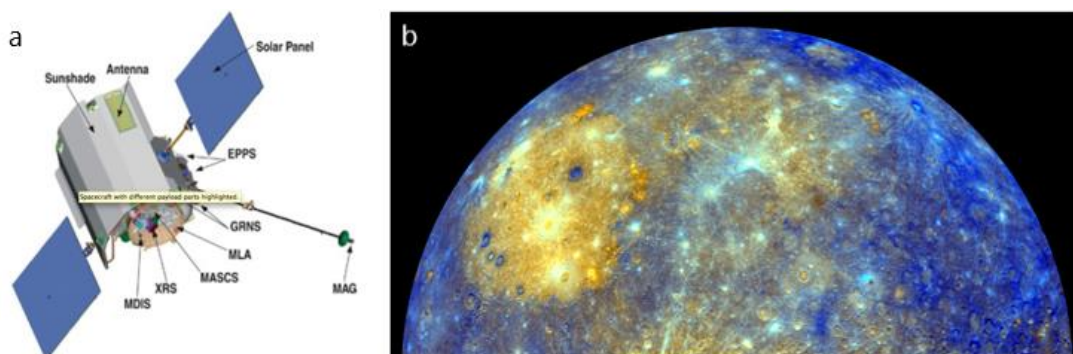
**Table 4.1.** Mariner 10's scientific experiments and the relevant instruments  
(After Rothery, 2015-Modified)

Experiment	Instrument
Television science length	Vidicon cameras fitted to twin 1.5 m focal telescopes
Infrared radiometry	Infrared radiometer
Celestial mechanics and radio science	X-and S-band radio transmitters
Magnetic field	Two triaxial fluxgate magnetometers
Plasma science	Scanning electrostatic analyser and electron spectrometer
Ultraviolet spectroscopy	Airglow spectrometer and occultation spectrometer
Charged particles	Charged particle telescopes

Thirty years after Mariner 10, the MESSENGER mission was the first spacecraft to enter the orbit of Mercury on March 18th, 2011, and the seventh NASA discovery-class mission. This probe was launched on April 4th, 2004 and orbited around Mercury for over four years. It has gained a new level of knowledge about Mercury's interior, surface

composition and features, revealing its geological history, learning more about its internal magnetic field, and discovering its water-ice polar deposits. The MESSENGER probe was composed by nine Scientific Instruments aboard (Fig 4.2):

- Mercury Dual Imaging System (MDIS)
- Gamma-ray Spectrometer (GRS)
- Neutron Spectrometer (NS)
- X-ray Spectrometer (XRS)
- Magnetometer (MAG)
- Mercury Laser Altimeter (MLA)
- Mercury Atmospheric and Surface Composition Spectrometer (MASCS)
- Energetic Particle and Plasma Spectrometer (EPPS)
- Radio Science Experiment (RS)



**Figure 4.2.** MESSENGER's science payload and Mercury surface coverage (a) MESSENGER scientific instruments. The Payload is composed of seven instruments, including three Spectrometers, an Imaging System, a Magnetometer, an Altimeter, and one Radio Science (b) Mercury MESSENGER MDIS basemap Enhanced Colour Global Mosaic, the different types of terrains result in subtle colour variations across all of the 11 WAC narrow-band colour filters. The Caloris basin, which is the largest impact basin on Mercury is visible on the west side of the image, displayed as a large bright yellow circular area, due to its infill of volcanic plains (Image recognition: Johns Hopkins University/Applied Physics Laboratory).

The Mercury Dual Imaging System (MDIS), contains the Wide-Angle Camera (WAC) that observed Mercury through 11 different filters and monochrome across the wavelength range between 395 and 1,040 nm, and the Narrow Angle Camera (NAC) which took a monochrome image at high resolution (1.5° wide view). Using MESSENGER MDIS data, 62.5% of the surface was covered with DTMs with 50 to 120 m/pixel. In addition, 12% of the surface was covered by MDIS 3-colour data at a resolution better than 120 m/pixel, and 2% of the surface by NAC high resolution images.

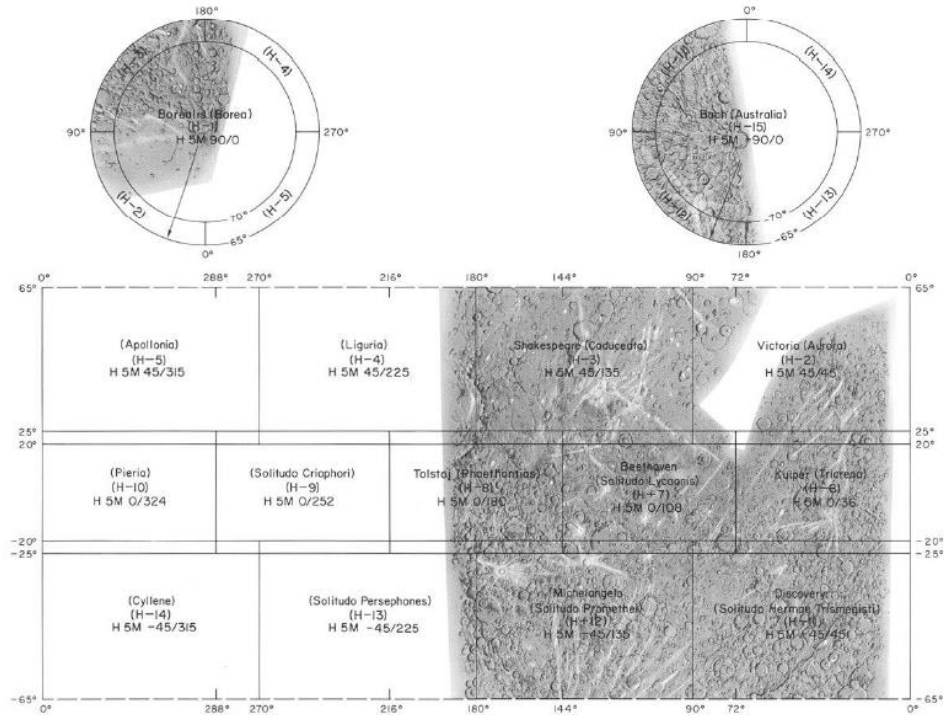
### ***Quadrangles***

After the coverage by Mariner 10 it was possible to subdivide Mercury's surface into different well-limited areas, and thus the surface of the planet has been divided into fifteen quadrangles (Davies et al., 1978), numbered according to their coordinates, starting with H-1 at the north geographic and ending with H-15 at the south pole. The naming of the Mercury quadrangles changed in the two eras of Mercury space probes Mariner 10 and MESSENGER exploration:

Mariner 10 era: During the epoch of Mariner 10, about 1000 photographs were taken revealing a surface riddled with craters and other interesting geological features. The

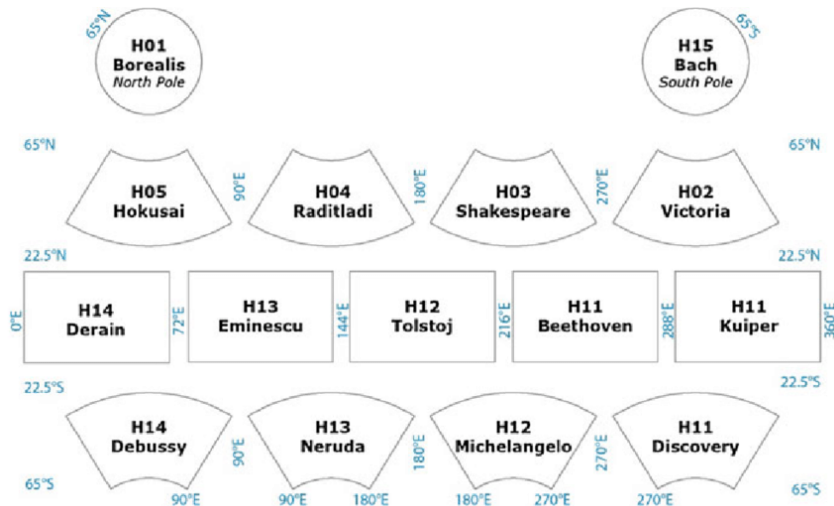


photo mosaic was composed of images from the three flybys, which allowed the distinction of some surface features as well as the variation of the albedo between terrain units (Galluzzi, 2015). This basic information helped to classify the terrains and split the surface into different quadrangles. The figure 4.3 shows Mercury's quadrangles boundaries based on the Mariner 10 background data.



**Figure 4.3.** Mercury quadrangles limits based on Mariner 10 datum. Subdivision in equirectangular projection from Davies et al., 1978. The quadrangles with a shaded relief background were named after distinctive features, whereas the names of quadrangles with a white background are derived from albedo features (after Galluzzi, 2015- Original image from Davies et al., 1978).

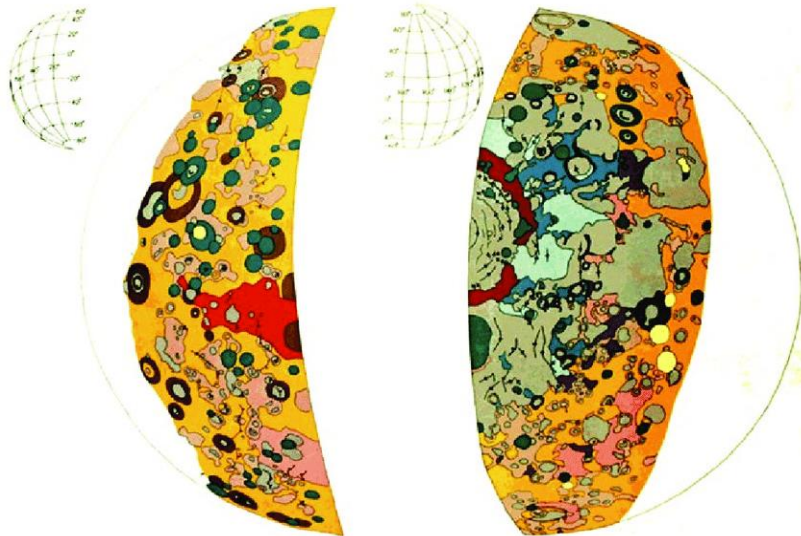
MESSENGER era: This mission acquired 88746 images but the number of quadrangles was not changed, although some names have been modified. In particular nine quadrangle names were maintained from Mariner 10 and the others have been changed. The figure 4.4 shows Mercury's quadrangle boundaries and names during and after the MESSENGER mission.



**Figure 4.4.** Mercury quadrangles limits based on MESSENGER datum. Equatorial: cylindrical projection; Mid-Latitude: Lambert conformal conic projection; Polar: stereographic projection, Coordinates are labelled on the graph (after Galluzzi, 2019).

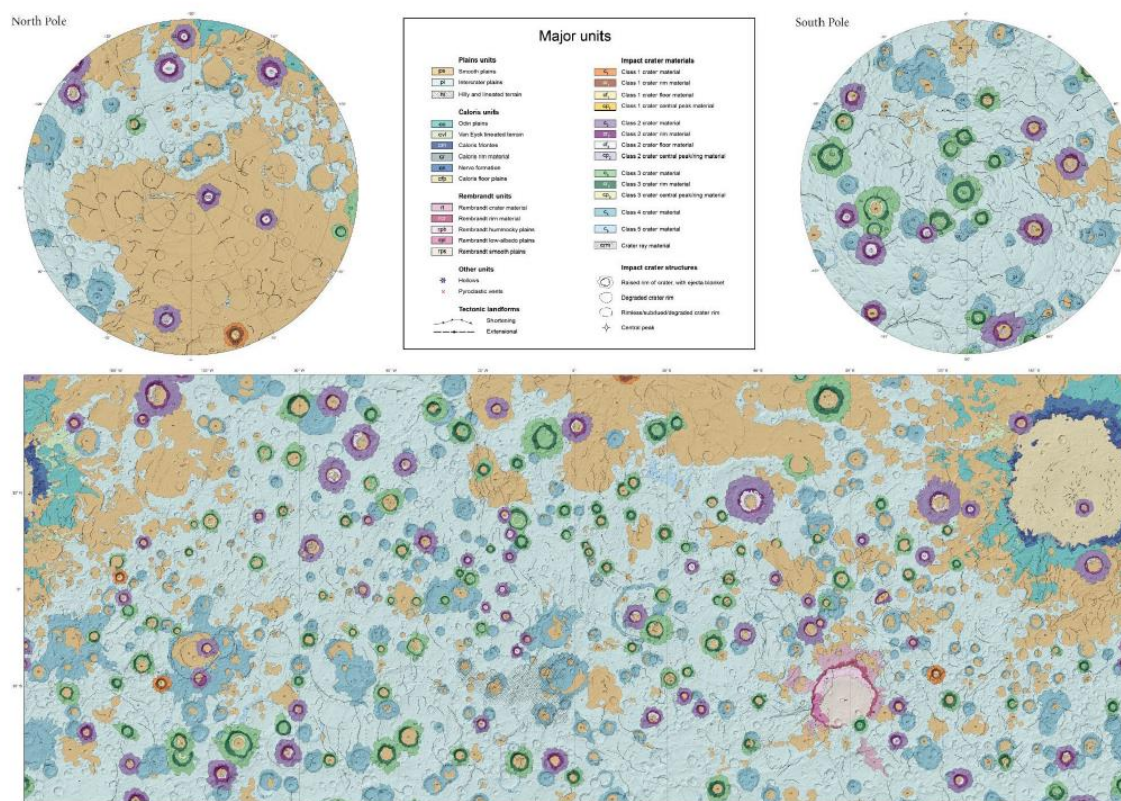
### *Geological maps*

The Mariner 10 images for Mercury lead to the release of a preliminary geological map of the surface (Fig 4.5) but also quadrangle maps that displays a basic distribution of the terrain's units, craters, and some visible lobate scarps and basins (Trask & Guest, 1975).



**Figure 4.5.** Preliminary geologic map for Mercury's surface, based on the images obtained by Mariner 10 data (original image from Trask & Guest, 1975)

At the end the mission, MESSENGER provided over 255,000 images of the planet, and this helped to deliver a new version of the geological maps of Mercury's surface (Fig 4.6) with a better detail compared to Mariner 10 maps.



**Figure 4.6** Global geological map of Mercury with 1:15M output scale. The map is a draft version, displaying the major plains units and classified craters  $\geq 90$  km in diameter (After Kinczyk et al., 2018)

In particular MDIS MESSENGER was used to deliver a series of 1:3M geological maps of the surface of Mercury in the frame of a global mapping project. The next chapter of this thesis will describe in detail this global mapping project and the mapping of the Eminescu quadrangle (H-9).

### ***Physical parameters***

The vicinity to the Sun of the innermost planet has affected many of its parameters, including its orbit, rotational and revolutionary period and its temperature. This planet has a highly elliptical and eccentric orbit (0.206), but its velocity allows it to complete an orbital period of 0.2408467 Earth years. In particular Mercury is characterised by 3:2 spin-orbit resonance. The mercurian spin period is  $\approx 58$  days and the orientation of Mercury's spin axis is characterised by an obliquity of  $2.4 \pm 0.08^\circ$  (Colombo, 1965, Margot et al., 2012, Noyelles et al., 2014).

The surface environment on Mercury is varying between very high ( $427^\circ\text{C}$ ) to very low ( $-173^\circ\text{C}$ ) temperatures, which depends on the Mercurian seasons (Tab 4.2), and consequently both latitudes and longitudes (Rognini et al., 2022). Mercury has almost no atmosphere (a weak exosphere layer), and this is the reason why its primitive surface has been greatly conserved through time due to the absence of erosion and transport of surface deposits.

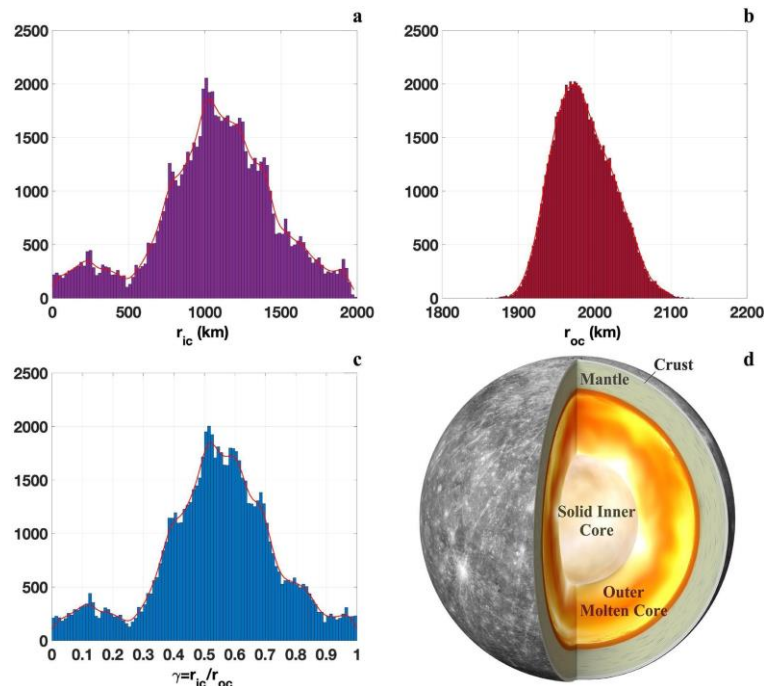
**Table 4.2** Comparative physical properties between Mercury and the Earth.

	Volume ( $10^{10}$ km <sup>3</sup> )	Equatorial radius (km)	Mean density (kg/m <sup>3</sup> )	Geometric albedo	Topographic range (km)	Surface acceleration (m/s <sup>2</sup> )	Orbit inclination (deg)
<b>Mercury</b>	6.083	2440.5	5429	0.142	7	3.70	7.004
<b>Earth</b>	108.321	6378.1	5513	0.434	20	9.78	1.848

### *Inner structure*

Although its small dimension compared to Mars, Mercury is characterised by a high bulk density (Goettel, 1988) due to the presence of a large iron core in its interior (Siegfried & Solomon, 1974). This higher density and the low global magnetic field (Ness et al., 1974) was early evidence for a large central metallic core, with a fluid outer core. This observation has been constrained by the large longitude libration of Mercury (Margot et al., 2007) and by geodetic analysis (Fig 4.7) based on radio tracking measurements from MESSENGER data, that documented a solid innermost core with nearly the same size as the Earth (Genova et al., 2019).

The study of Mercury's deep interior is fundamental to provide crucial information on the planet's bulk composition and the core cooling history. The sulfur (S) and silicon (Si) serve as principal elements alloyed with iron (Fe) in the core and are responsible for the physical fluid state of the outer molten core (Hauck et al., 2013, Genova et al., 2019).



**Figure 4.7.** The new constraints on the size of the solid inner core of Mercury by Genova et al., 2019 (a) Histogram of the inner core radius (b) Histogram of the outer core radius (c) The samples of four-shell Markov chain Monte Carlo solutions, which account for the effects of compression in the inner and outer core (d) Schematic cutaway view of Mercury's interior structure (After Genova et al., 2019).

In addition, the intrinsic magnetic field of Mercury (roughly 1% than that of the Earth) and its magnetosphere has been documented by direct observations of Mariner 10 and MESSENGER magnetometers (Ness, 1979, Benkhoff et al., 2010, Toepfer et al., 2021). This magnetic field in the vicinity of Mercury is composed of an internal and an external

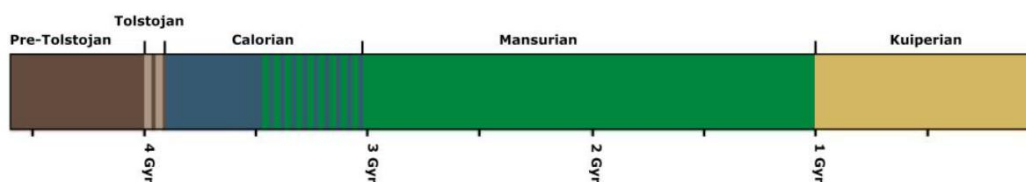


domain. The internal domain originates in the dynamo-generated field (Crustal remanent field and induction field), while the external domain originates from currents flowing in the magnetosphere (Benkhoff et al., 2010, Toepfer et al., 2021).

### ***Stratigraphic record***

The Mariner 10 and MESSENGER missions, allowed the production of geological maps and the determination of relative and absolute ages of the diverse terrains' units. Mercury's surface units were subdivided into five time-stratigraphic systems (McCauley et al., 1981, Spudis, 1985, Spudis & Guest, 1988, Galluzzi, 2016) as displayed on the Fig 4.8:

- Pre-Tolstojan system (>~4.0 Ga): identified by ancient multiring basins and extensive intercrater plains materials.
- Tolstojan system (~4.0 to ~3.9 Ga): defined by the Tolstoj basin (~356 km diameter) and ejecta, includes Mercury's oldest smooth plains materials (Spudis and Guest, 1988).
- Calorian system (~3.9 to ~ 3.5 - 3.0 Ga): defined on the base of the Caloris basin ejecta (~1525 km in diameter), identifies Mercury's youngest widespread smooth volcanic plains.
- Mansurian system (~3.5–3.0 to ~1.0 Ga): defined by Mansur crater ejecta (~75 km in diameter).
- Kuiperian system (<~1.0 Ga): defined by the young Kuiper crater materials (~62 km in diameter).



**Figure 4.8.** The geological time scale for Mercury (After Galluzzi, 2016 –Original image from van Gasselt & Neukum, 2011).

### ***Terrains***

Based on photogeological mapping using Mariner 10 datasets, Trask & Guest, 1975, classified 3 principles units:

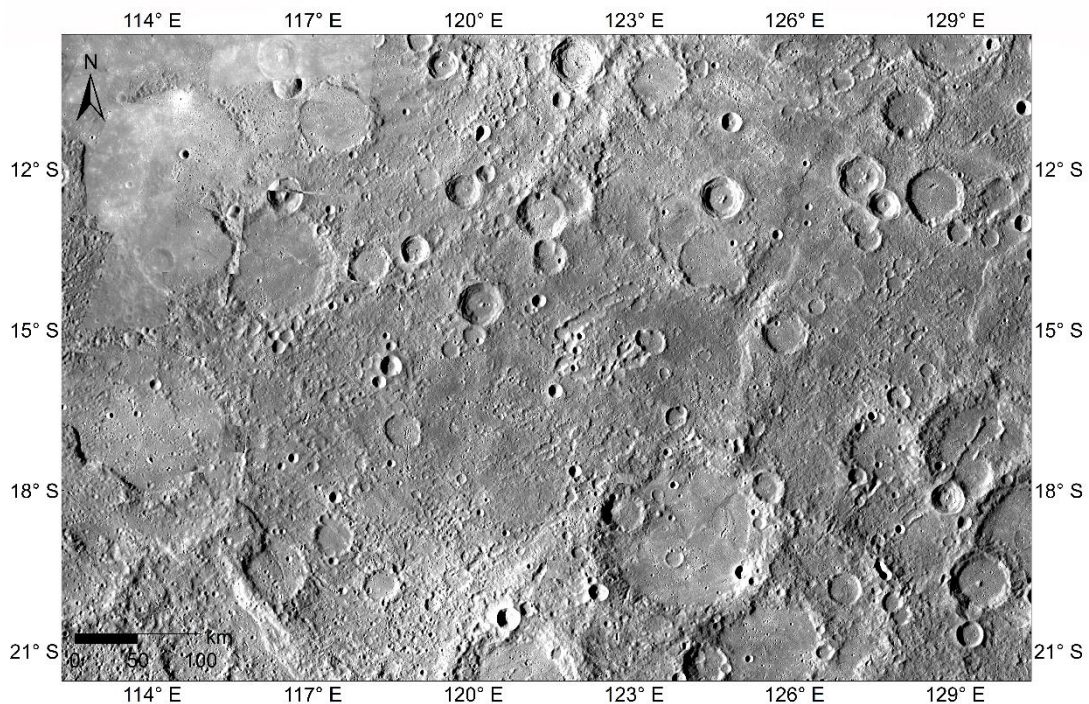
- Inter Crater Plains (ICP): highly cratered terrains, characterised by a widespread distribution of crater with dimension <10 km. These terrains are the more widespread on the surface of Mercury (Whitten *et al.*, 2014, Galluzzi, 2015) and are interpreted to be remnants of old volcanic plains (Spudis & Guest, 1988, Whitten *et al.*, 2014, Galluzzi, 2015), or the result of impact melts produced by large impact basins (Oberbeck *et al.*, 1977, Galluzzi, 2015). The topographic elevation of the intercrater plains is on average 5km.

The low reflectance materials (LRM) have been defined based on the albedo and spectral shape. These materials appear on the surface of Mercury very dark, with an albedo of 4-5% at 560 nm, and it displays a spectral slope that is substantially less red than the rest of Mercury. The LRM are not associated with flow features or other



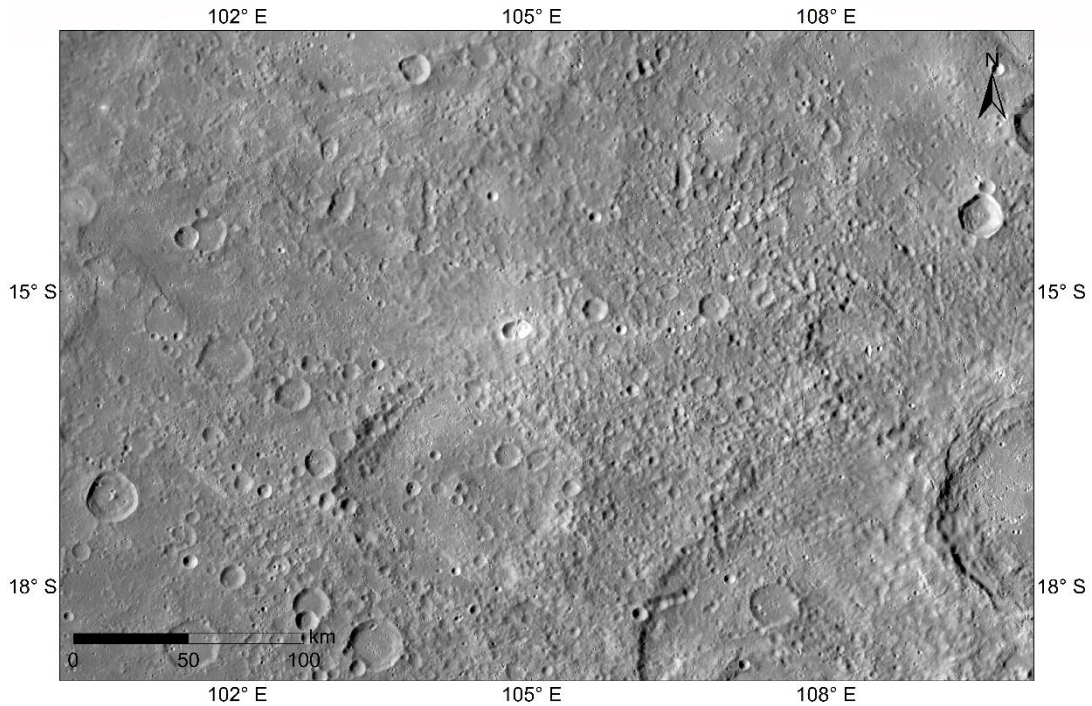
evidence of a volcanic origin, they are distributed across Mercury and typically having been excavated from depth by craters and basins (Head et al., 2011, Denevi et al., 2013 Whitten et al., 2014). In contrast to the LRM, the high-reflectance red plains (HRP) exhibit morphological evidence of volcanism (Prockter et al., 2010). The HRP appears bright relative to the surrounding materials on Mercury.

The ICP are composed mostly of LRM and do not change their texture when they merge with HRP (Whitten *et al.*, 2014, Galluzzi, 2015). The ICP seem to be related to the period of the Late Heavy Bombardment (LHB) and thus to be formed during Tolstojan to pre-Tolstojan (Whitten *et al.*, 2014, Galluzzi, 2015) periods representing the oldest surface units of Mercury (Fig 4.9).



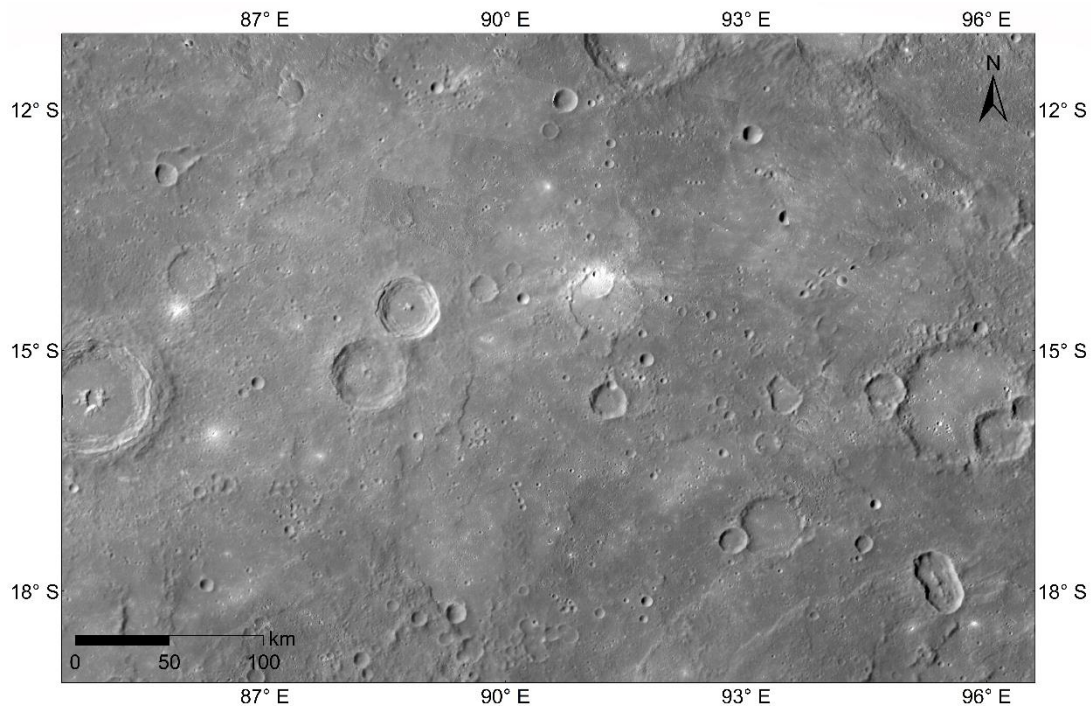
**Figure 4.9.** Intercrater plains in Eminescu (H09) quadrangle on Mercury. MDIS\_HIW2 (256m/px) with Equirectangular\_Mercury projection.

- Intermediate plains (IP): These terrains display higher crater density than smooth plains material (Galluzzi, 2015), however, they are less heavily cratered compared to the intercrater plains material (Fig 4.10). These terrains are characterised by a “patchy” distribution (Denevi et al., 2013, Whitten et al., 2014, Galluzzi, 2015), and according to the different authors they have been classified either as intermediate or intercrater plains (Whitten et al., 2014) or smooth plains materials (Denevi et al., 2013, Galluzzi, 2015). These terrains frequently appear confined between smooth and intercrater plains.



**Figure 4.10.** Intermediate plains in Eminescu (H09) quadrangle on Mercury. MDIS\_HIW2 (256m/px) with Equirectangular\_Mercury projection.

- Smooth plains (SP): As it's indicated from their denomination, this terrain unit is characterised by a relatively flat (Fig 4.11) sparsely cratered material (Trask & Guest, 1975, Galluzzi, 2015). They cover almost 27% of the Mercury's surface and they are interpreted to have originated from volcanic emissions (Trask & Guest, 1975, Trask & Strom, 1976) due to the presence of flows and neat colour contrast with the nearby materials. The terrains display a sharp boundary with the adjacent regions, and they seem to be formed probably after the LHB, around the Calorian period (of 3.7-3.9 Gyr) since they are characterised by a crater density lower than ICP. One of the smooth plain examples is the Caloris basin infilling. No major extensive volcanism has been subsequent to the Calorian system, and thus the smooth plains have been classified as the youngest geologic province on Mercury (Fig 4.11).



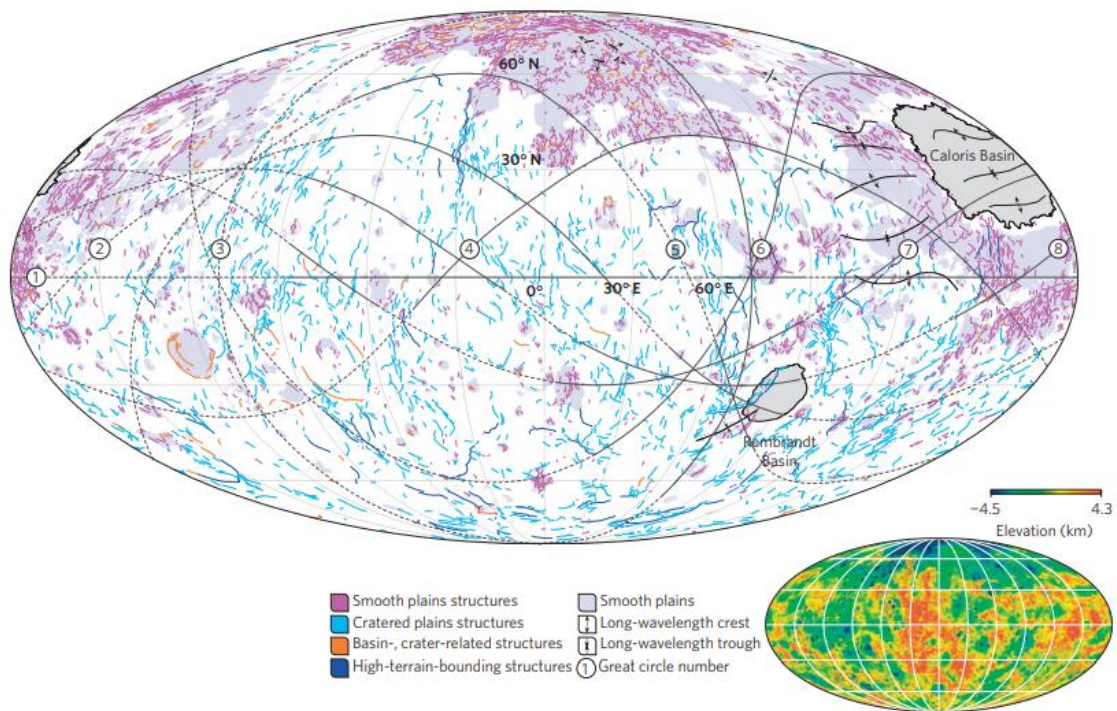
**Figure 4.11.** Smooth plains in Eminescu (H09) quadrangle on Mercury. MDIS\_BDR2 (256m/px) with Equirectangular\_Mercury projection. The exposed craters present a flat floor occupied by smooth plains (with smaller, superimposed younger craters).

- *Crater materials:* craters are classified according to their degradation level that reflects their relative age (Wood & Anderson, 1978, Spudis & Guest, 1988, Galluzzi, 2015). Considering previous studies that have been dedicated for the mapping of Mercury' surface and the analysis of the surface features, two major classification systems were identified in order to classify the craters: 1) The Lunar and Planetary Laboratory (LPL) system, which consist of five crater classes, starting with the C1 as the freshest crater to the C5 the most degraded one, based on the crater rim sharpness. This classification was developed first on Lunar craters. 2) The United States Geological Survey (USGS) system consists also of five classes but with different bases for the craters classification. The C1 crater for the USGS system is the oldest and most degraded crater, while the C5 is the fresh crater, with the lowest level of degradation. The differences between the both systems are that the LPL entrenched mostly on the rim sharpness, while the USGS system focused mainly on the craters features and internal structures (Galluzzi, 2015).

### ***Tectonics***

Unlike Mars, the surface of Mercury records tectonic features, which are dominantly contractional as shown on the figure 4.12 (Strom et al., 1975, Watters et al., 2002, Byrne et al., 2014, Fegan et al., 2017). Mercury has been considered as a one-shell planet, that has experienced a significant radial contraction primarily driven by the loss of its interior heat.

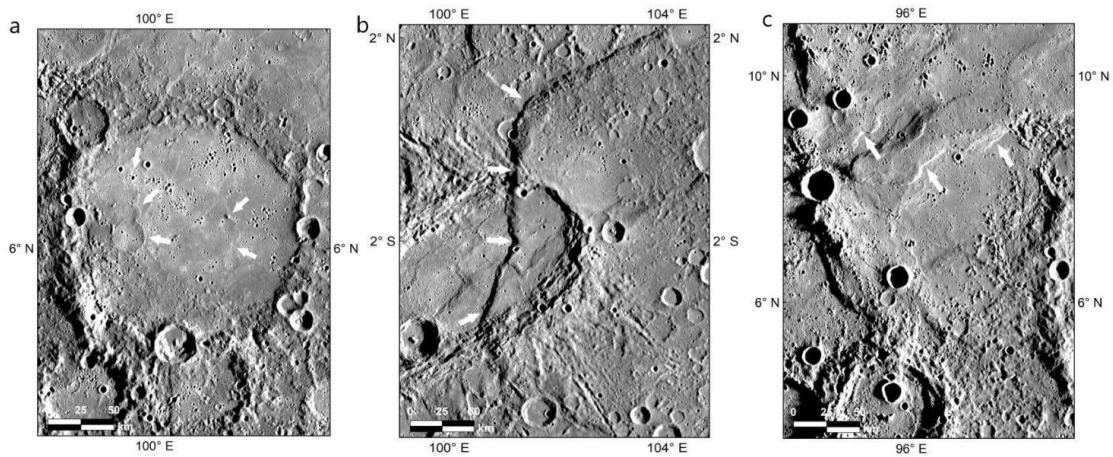




**Figure 4.12.** Global map of the 5,934 shortening structures on Mercury. The Black lines with opposing arrows mark the folds (after Byrne et al., 2014).

The contractional tectonic regime of Mercury has been confirmed by a global structural mapping of the surface by Bryne et al., 2014 (Fig 4.13), who identified 5,934 contractional structures all over the planet surface. The contractional tectonic structures on Mercury have been classified into three distinct categories (Fig 4.13):

- Wrinkle ridges: Anticlines formed by thrust faults and folding, resulting from crustal shortening (Schleicher et al., 2019).
- Lobate scarps: Curvilinear surface deformations linked to thrust faults, with a steep front scarp and a gently dipping back scarp (Massironi, 2014).
- High-relief ridges: Closely related to lobate scarps, characterised by more symmetric form and generally no clear expression of surface-breaking faults (Watters, 2021).



**Figure 4.13.** Examples of the three distinct categories of contractional structures on Mercury. Images from the Eminescu (H-09) quadrangle (a) Wrinkle ridges within the floor of the Lange crater, 6.278°N, 100.467°E (b) The renowned Beagle Rupes lobate scarp cross-cutting Sveinsdóttir crater (c) High relief ridge exhibited on the top NW of the Lange Craters. The North direction is oriented on the top, all images are taken from MDIS\_HIE (166 m/px).

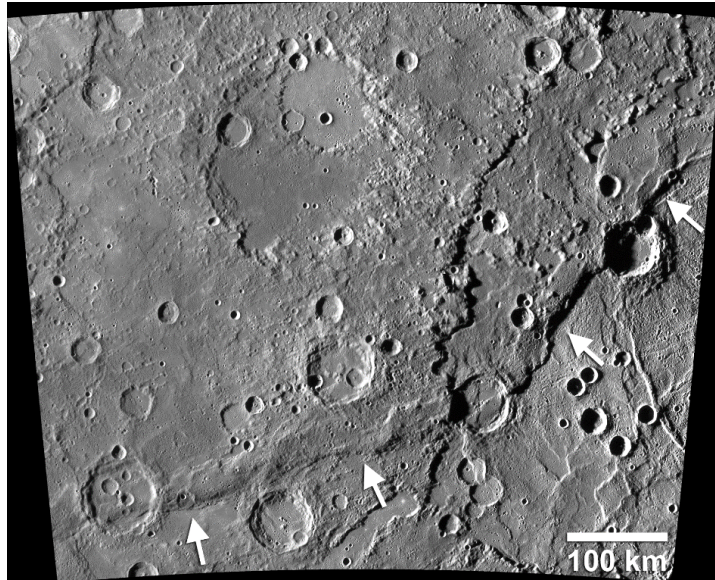
According to Watters, 2012 the tectonic landforms on Mercury can be divided into two spatially distinct classes:

- Broadly-distributed: Including all the contractional tectonic landforms mentioned above (e.g., lobate scarps, high-relief ridges, and wrinkle ridges).
- Basin-localised: Impact basins related structures (e.g., Rembrandt basin, Caloris basin).

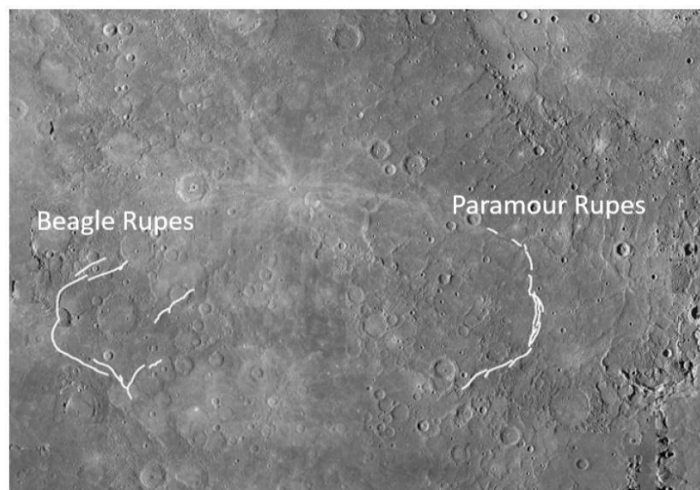
Indeed, the Mercury surface is dominated by the occurrence of contractional structures, whereas the extensional structures are restricted to the interior volcanic plains of impact basins like the Caloris Basin floor, where narrow grabens striking radially or concentrically to the basin centre cut across compressional wrinkle ridges (Strom et al., 1975, Dzurisin, 1978, Murchie et al., 2008, Watters et al., 2009, Galluzzi, 2015).

The lobate thrust faults appear to occur predominantly in intercrater plains, after the end of LHB and potentially still forming nowadays (Watters, 2021). However, a recent study by Giacomini et al., 2019, suggests that most of the major tectonic structures on Mercury's surface most likely ended at about 3.6-3.8 Gyr. One prominent lobate thrust on Mercury's surface is Enterprise Rupes, which is about ~1000 km long (Fig 4.14) and crosscut the Rembrandt's northwest rim. Other significant scarps on Mercury's surface are the Beagle and Paramour Rupes, both within the Eminescu quadrangle (H09) (Fig 4.15). These scarps and the Enterprise Rupes have been dated to about 3.7 Gyr (Giacomini et al., 2019).





**Figure 4.14.** Enterprise Rupes lobate thrust faults cross-cutting the Rembrandt basin. View centred at -31.56°N, 74.97° E (NASA/Johns Hopkins University Applied Physics Laboratory).



**Figure 4.15.** Beagle and Paramour rupes over MDIS mosaic basemaps, the two lobate scarps are with an opposite-facing vergence, bordering relatively old cratered terrains. The width of the image is 2500 km and centred at 13°E, 5°N (after Rothery, 2015 - Original source: NASA/Johns Hopkins University Applied Physics Laboratory).

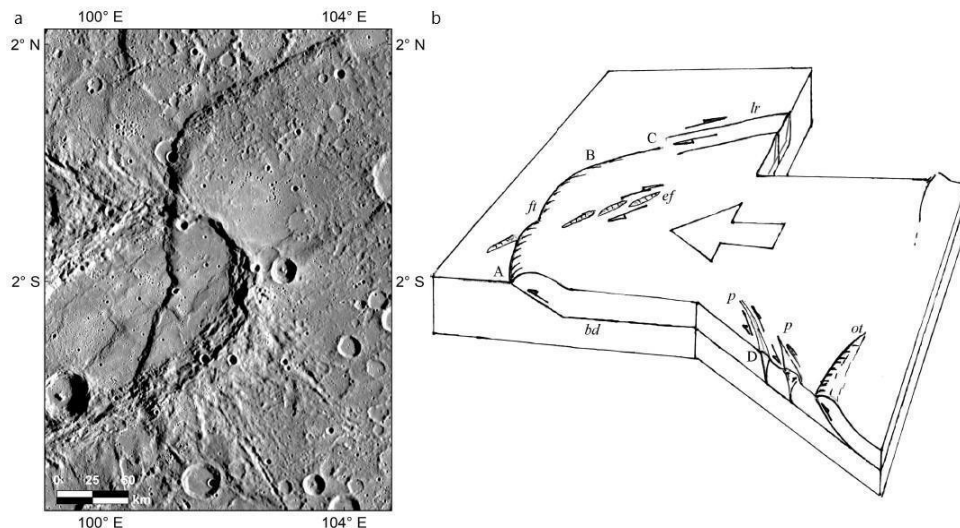
A spatial association has been frequently documented between the lobate scarps and the vents on the surface of Mercury (Pegg et al., 2021), suggesting that these faults are probably pathways for the magma and/or volatile ascent.

Wrinkle ridges on Mercury have typically hundreds of metres of relief and are generally greater than their counterparts on Mars (Watters, 1988). These lineaments are probably formed by stresses resulting from the load-induced subsidence and lithospheric flexure in response to the emplacement of thick volcanic sequences within basins with additional contribution from the global contraction.

Up to date, lobate scarps are considered one of the prominent features on Mercury's surface. These linear surface features are cross-cutting the elliptically shaped Sveinsdóttir impact crater of ~30-km-diameter (Solomon et al., 2008, Rothery & Massironi, 2010) and

jointly create a distinguishable feature within the Eminescu (H-09) Mercury quadrangle. The floor of Sveinsdóttir was flooded by smooth plains and subsequently deformed by wrinkle ridges before the Beagle rupes development. The Beagle Rupes is one of the most arcuate lobate scarps found on Mercury's surface, this scarp is formed by two convex arc segments covering 260 km in length (Rothery & Massironi, 2010). The north-south arcuate segment (Fig 4.16) turns at its northern end into a straight scarp trending approximately ENE and at its southern end into a straight scarp trending approximately ESE. Rothery & Massironi, 2010, interpreted these coupled features as a component of a linked fault system, originated by a frontal scarp bounded by transpressive lateral ramps. Hence the whole scarp limits a trapezoid area extending for at least 200 km behind the frontal scarp. This hanging-wall block of the thrust fault must be underlain by the horizon detachment constituting the fault zone at depth.

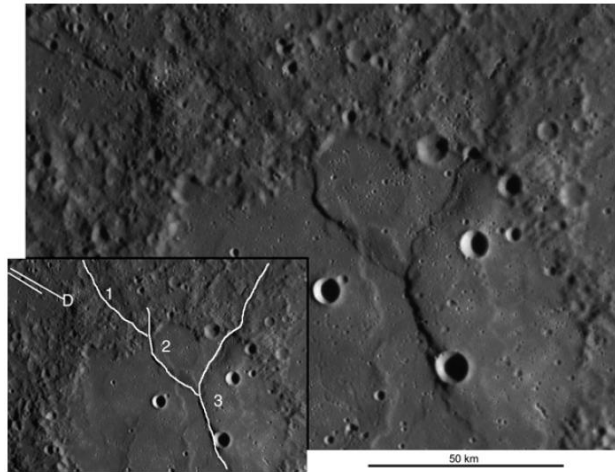
Due to the NS arcuate frontal scarp of the Beagle rupes, the main shortening direction was EW, however, in the case of a global contraction, each relay ramp could host also a shortening component together with strike-slip activity, which is right-lateral along the north ramp and left-lateral along the south ramp (Rothery & Massironi, 2010).



**Figure 4.16.** Beagle Rupes lobate scarp cross-cutting the Sveinsdóttir crater (a) MDIS\_BDR2 (256m/px) with Equirectangular\_Mercury projection (b) Schematic sketch showing the relationship between the Beagle Rupes frontal scarp and associated tectonic features (Rothery & Massironi, 2010).

The termination of the south lateral ramps is interesting by another scarp (Rothery & Massironi, 2010), forming three successively overlying scarps. As it appears from figure 4.17, the third scarp cross-cut the second one, which cross-cut the first scarp, suggesting an out-of-sequence propagation with respect to the Beagle rupes thrust fault.

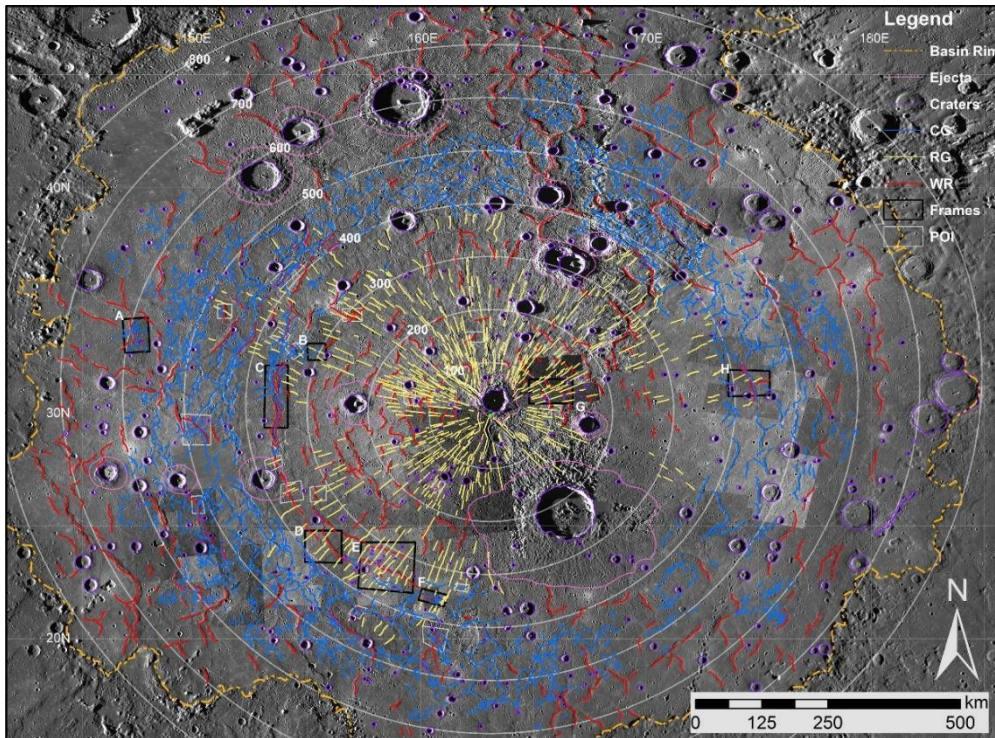
The amount of displacement on the Beagle Rupes scarp is still in discussion. Solomon et al., 2008 suggest a shortening of least one to several kilometres, based on unnamed crater of approximately 17 km in diameter, cut by the frontal scarp, distant about 30 km from the northern rim of the Sveinsdóttir crater, however, Watters et al., 2009 suggest 1 km as a lower limit, while Rothery & Massironi, 2010 suggest that the shortening varies between at least one to 3 km.



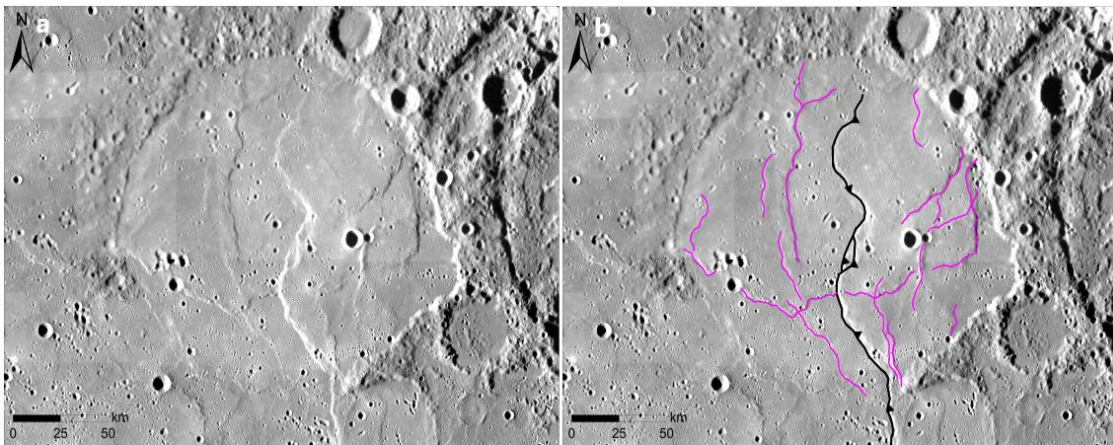
**Figure 4.17.** The Southeast of Beagle Rupes major scarp. The image shows three successively younger overlying scarps, whose relative age sequence is constrained by their cross-cutting relationships. The letter D indicates the termination of the south lateral ramp. The main back frame indicates a few wrinkle ridges associated with the Beagle Rupes system (MESSENGER NAC datum. (After Rothery & Massironi, 2010).

Not only compressional tectonics have been identified in Mercury's surface, but also extensional tectonics. The Caloris basin (Fig 4.18), the planet's largest and the youngest impact basin, (1640 km in diameter) shows radial and concentric graben, and wrinkle ridges structures, that occasionally interact (Murchie et al., 2008, Byrne et al., 2014, Cunje & Ghent, 2016). The first structures that formed in the Caloris basin are the wrinkle ridges. These wrinkle ridges were followed by radial and concentric grabens after contraction ceased (Cunje & Ghent, 2016). The process for the formation of these structures is still debated. Watters et al., 2005 suggested a major radial contraction followed by basin uplift, originated from the crust flux converging towards the centre of the basin, after its dynamical excavation. Hence a sequence of tectonic events of the basin with contraction predating the extension (Watters et al., 2009b). Alternatively, Basilevsky et al., 2011 looking at the interactions between the observed wrinkle ridges and the grabens, proposed an extension and contraction occurring in sequence. The wrinkle ridges are indeed found within smooth plains and associated with extensive lava (Fig 4.18 and Fig 4.19), they most probably are the surface expression of fault-propagation folding or fault bend folding (Strom et al., 1975, Head et al., 2008). The high-relief ridges intermingle with lobate scarps and probably share a similar origin and age according to Watters & Nimmo, 2010, Galluzzi, 2015.





**Figure 4.18.** Caloris basin and the three classes of tectonic landforms with both radial and concentric graben orientations. The dominantly concentric wrinkle ridges (WR), appearing as raised linear and/or sinuous crests. The radial graben (RG) is represented by yellow lines, while the concentric graben (CG) is shown in blue lines. The image centre: 30°N, 163°E, at simple cylindrical map projection (After Cunje & Ghent, 2016).

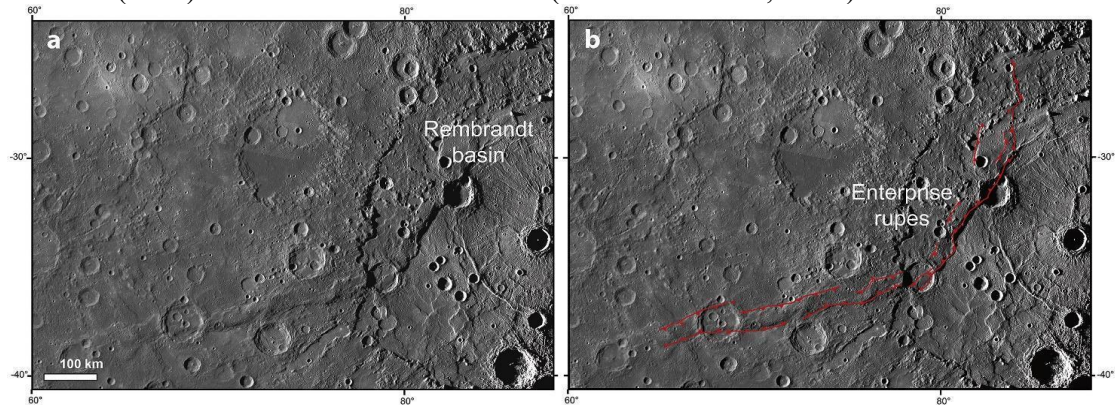


**Figure 4.19.** Wrinkle ridge in unnamed craters floor in Eminescu (H09) quadrangle. (a) Tectonized crater floor with smooth plain. (b) Lineament interpretation. The pink lines represent the wrinkle ridges, the major lobate scarp is outlined in black with a tiny triangle indicating the dip direction of the thrust. Both views are on MDIS\_HIW2 (256m/px) with Equirectangular Mercury projection.

Several thrust systems have been studied on Mercury (Giacomini et al., 2020) and one prominent example is the Enterprise Rupes (Fig 4.20) which crosscut the Rembrandt basin and is considered the longest thrust known on Mercury (Watters et al., 2009, Ferrari et al., 2015, Massironi et al., 2015, Giacomini et al., 2020). This scarp extends for 820 km, and it includes two-segment, one segment is inside the Rembrandt basin and trending SW-NE (Ferrari et al., 2015, Galluzzi et al., 2015, Giacomini et al., 2020), while the other one is expressed mainly outside the basin and is oriented WSW-ENE (Giacomini et al.,



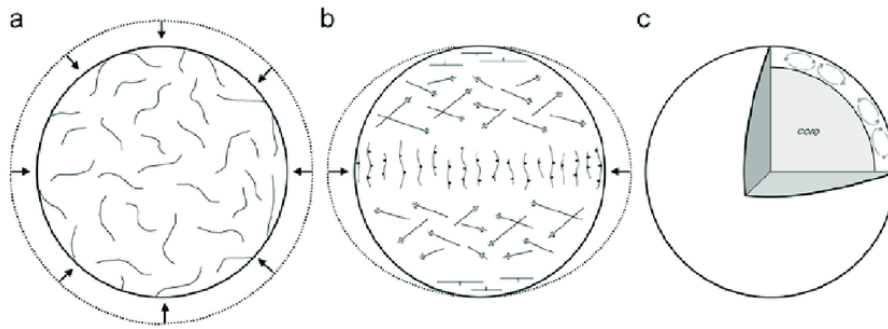
2020). The latter displays a dextral transpression in the western sector whereas sinistral transpression is visible on the NS, eastern termination of the entire Rupes. Hence the vergence of the Enterprise system is towards SE (Galluzzi et al., 2015, Massironi et al., 2015, Giacomini et al., 2020). The crater density age of the last faulting activity along the thrust system is 3.7 (+0.03/−0.04) Gyr, if Le Feuvre and Wiczorek crater Production function (LWPF) is applied and 3.8 (+0.05/−0.08) Gyr if the Neukum Production Function (NPF) is taken into consideration (Giacomini et al., 2020).



**Figure 4.20.** Enterprise thrust system located between 25.47°S and 38.68°S and 64.89°E and 84.23°E (a) Enterprise system without photo interpretation, cross-cutting the western side of the Rembrandt basin. (b) Enterprise thrust system outlined in red colour. The triangles indicate the dip direction of the thrust. MDIS BDR mosaic (166 m/pixel) in equirectangular projection (after Giacomini et al., 2020).

The contractional features could have taken place before or after the LHB. In particular three main (not mutually exclusive) tectonic models have been reported in order to explain the tectonic evolution of Mercury (Fig 4.21):

- Global contraction: this model has been suggested by Strom et al., 1975, and it is due to the secular cooling of Mercury interior (Solomon, 1976). The radial shortening has been estimated by different authors by applying the Cowie & Scholz, 1992 Displacement-Length scaling relationship on thrust faults and finally has been constrained to ~7 km (Watters & Nimmo, 2010, Di Achille, G et al., 2012, Byrne et al., 2014).
- Tidal despinning: this model has been supported by Melosh & Dzurisin, 1978 and foresees, NS trending thrust faults at a low latitude, NW-SE and NE-SW strike-slip faults at mid-latitudes and EW normal faults at high latitudes. On Mercury these attitudes have not been observed, but the model was improved by Pechmann & Melosh, 1979, Matsuyama & Nimmo, 2009, and Klimczak et al., 2015, proposed that the tidal despinning could have act together with global contraction and was able to explain the observed fault framework dominated by contraction features with a prevalent NS strike in the equatorial region.
- Mantle convection: this model was proposed by King, 2008 and predicts a pattern of sheet-like upwelling regions consistent with the distribution of lobate scarps. King, 2008 states that the mantle convection could be still active until nowadays on Mercury, however, there are no evidence of an active present mantle convection, but could have been potentially active in the early stage of the planet evolution (Michel et al., 2013, Massironi et al., 2015).



**Figure 4.21.** The three proposed tectonic models for Mercury (a) global contraction (b) Tidal despinning (c) Mantle convection (After Galluzzi, 2015- Original image from Massironi et al., 2015).

### ***Volcanism***

Extensive smooth plains and fresh floor basins have been photographed by Mariner 10, however, no volcanic edifices or vents, neither characteristic albedo contrast with the surrounding cratered terrains was identified on the surface with this probe. These observations have been improved years later by the MESSENGER flyby data, where they provided evidence of volcanic activity features on the Surface, expressed by extrusive volcanic vents, lava flow margins, pyroclastic deposits, plains of volcanic origin, and a diverse old crater with volcanic infilling. Several ghost craters have been documented to be submerged by volcanic plains often in excess of ~1.5 km in thickness. Additional evidence of volcanic emplacements has been provided by the properties and the distribution of terrain surrounding and infilling the basins as well as the color and the stratigraphic relationship between their rims and younger plains.

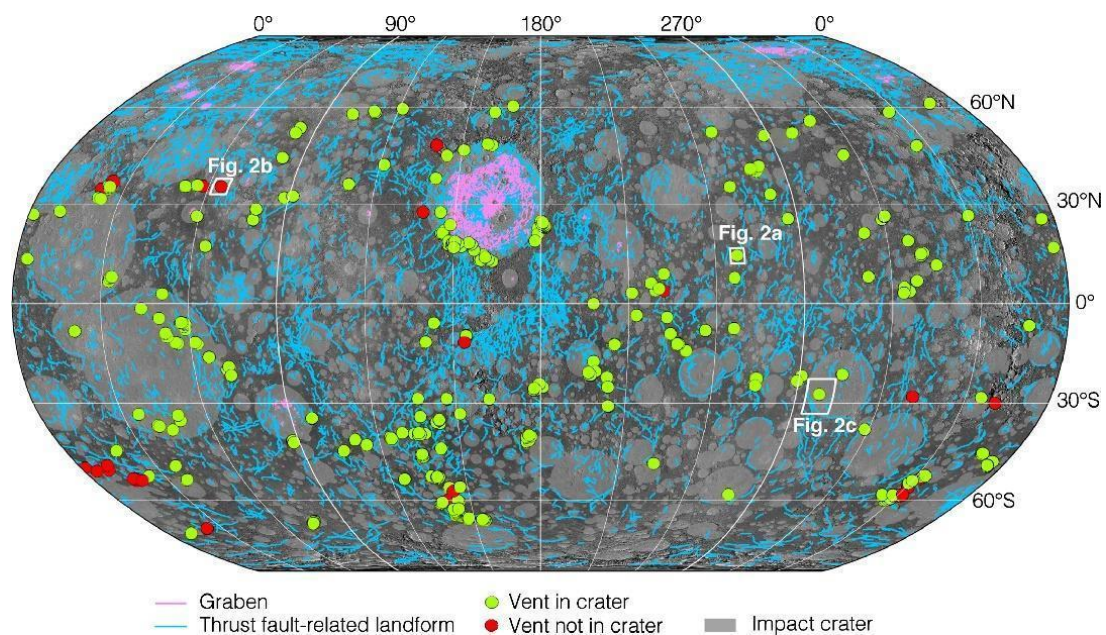
It has been finally estimated that ~27% of Mercury's surface is covered by smooth plains unquestionably attributed to volcanism (Head et al., 2008, Robinson et al., 2008, Murchie et al., 2008) that occurred probably at the LHB (Strom et al., 1975), however, the oldest plains may have resulted in part from an early planet differentiation epoch (Strom et al., 1975). The MESSENGER data was able to set up the global extent of the volcanic units on Mercury, the surface consists of multiple generations of lavas, with prominent smooth plain in the north polar region, covering more than 6% of Mercury's surface and extended plains infilling and surrounding the Caloris basin. The lava channels and extended flow lobes indicate a rapid emplacement of high-temperature and low-viscosity flood lavas (Head & Wilson, 2015).

The smooth terrains that have faced the bombardment of the LHB have been classified as intercrater plains, due to the extensive number of impact craters, while the intermediate plain between smooth and intercrater plains have been identified as intermediate plains class (Rothery, 2018).

In addition, explosive volatile-driven volcanism was widely documented on Mercury (Thomas et al., 2014). Over one hundred pit craters appear as a rimless, noncircular depression on the surface, with dimensions varying between 10 to ~80 km and up to about 4 km deep, often observed on impact crater floors, and have been interpreted to be generated by collapse calderas or explosive volcanic vents (Head & Wilson, 2015, Rothery, 2015). Many of these pits are surrounded by red materials, and outer pale

deposits are displayed around the pit for tens of kilometres, these deposits have been documented as pyroclastic ejecta, (Rothery, 2015), These features are probably related to magmatic volatile expansion close to the top of the magma conduit, or, alternatively the result from the heating of near-surface volatiles by rising magma. Several of these pits present complex floors, which can be explained by vent's migration. Frequently, pits are expressed within the impact craters, this joint relationship between these two features might suggest that impact fractures played an important role in the magma uplift regardless of the general compressive tectonic regime on Mercury (Rothery, 2018). Relative timing of the volcanic emplacements expresses a change in the volcanic eruptive style over the time with small volumes of volcanic materials released by the explosions supplanting the much larger volumes provided by the effusive events.

Furthermore, the wide distribution of the pyroclastic vents and related deposits on Mercury (Fig 4.22) has a direct implication for the planet's bulk volatile content and also the thermal evolution (Thomas et al., 2014). The pyroclastic deposits appear to be globally distributed over the surface of Mercury. The last observations by Thomas et al., 2014, mention 174 sites classified as endogenic pits, among which 150 are surrounded by deposits most likely pyroclastic in nature.

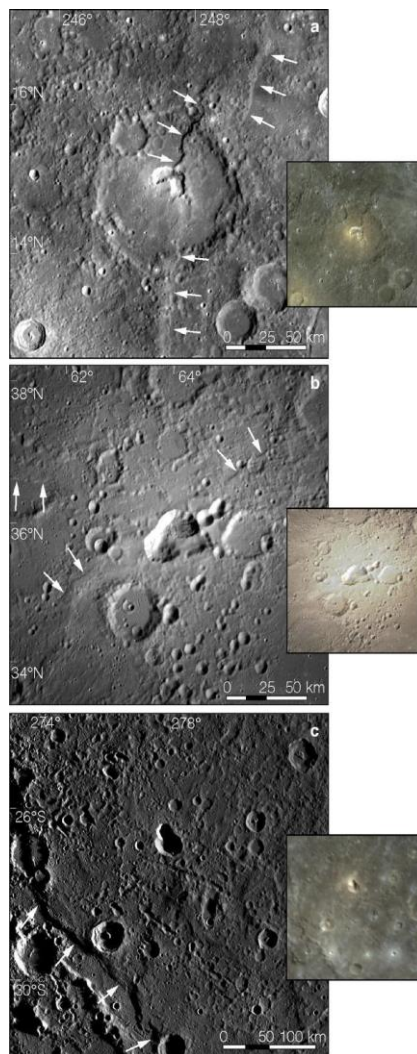


**Figure 4.22.** A global MESSANGER monochrome image mosaic in Robinson projection centred at 180°, shows the wide distribution of vents associated with pyroclastic volcanism and structural lineaments represented by normal and thrust faults. The volcanic vent data have been acquired by Thomas et al., 2015, faults data are from Byrne et al., 2013, Byrne et al., 2014, and Impact craters distribution are from Fassett et al., 2011 and Kinczyk et al., 2016 (after Klimczak et al., 2018).

The surface analysis of the volcanic plains and their associated features (e.g., flow fronts) on Mercury suggest deep magma sources, a minimal crustal storage of magma, wide and vertical dikes piercing the lithosphere and the crust, and important volumes of lava eruption which correspondingly produce long lava flows covering wide areas. It is still difficult to date the end of the flood volcanism on Mercury, either when the explosive volcanism started on Mercury. Some volcanic pits and related pyroclastic deposits date to less than 1 Gyr, and suggest multiple phases of activity (Thomas et al., 2014).



Tectonism and volcanism on Mercury are frequently intertwined, and these have been expressed through many surface features (Klimczak et al., 2018). In particular 92% of vents associated with pyroclastic deposits are in vicinity to lobate scarp, and faulted deformed zones of impact craters, which suggests that such structures might favour the occurrence of explosive volcanism on Mercury. Indeed, explosive vents are within crater's floors, rims, central peaks, or peak rings of impact basin, but a major part of them is located close to thrust faults: being distributed within a radius of about 20 km from the faults (Fig 4.23), and progressively decreasing with their distance from the tectonic structures (Klimczak et al., 2018).



**Figure 4.23.** Vents and Pyroclastic deposits displayed in monochrome (main figure) and in colour (inset) images in equirectangular projection (a) Glinka crater with pyroclastic deposit appear as a high-reflectance halo around the vent. The nearby fault is outlined with white narrows (b) The biggest pyroclastic deposit and vent on Mercury. The picture displays a thrust fault (outlined by white arrows), close to a vent 40 km in diameter associated to bright pyroclastic halo that extends for 150 km around and has a clear multispectral difference with the surrounding plains, as seen in the colour mosaic (c) Some pyroclastic deposits are located on the floor of an inferred ancient impact basin; the location of these deposits is far away from the thrust fault (about 150 km) outlined by the white arrows. No bright halos are present within the main figure, however, a spectrally distinct region around the vent is found in the color mosaic (after Klimczak et al., 2018).



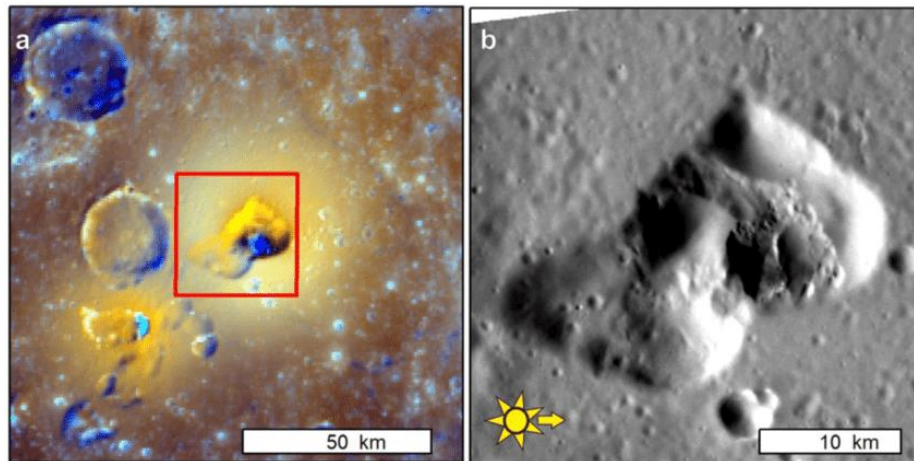
The volcanism on a one-plate planet like Mercury (Solomon, 1978), generally involves mantle partial melting and the buoyant rise of mantle diapirs. The facility for the magma to reach the surface is controlled by the density and the state of the global stress within the crust: low crust density implies magmatic density traps which inhibit the ascent and eruption of the magma, while an extensional regime enhances the ability of dikes to propagate to the surface, whereas contractional environments inhibits magma ascent and eruption (Solomon, 1978, Head & Wilson, 2008). In the context of global contraction of Mercury, the compressive regime might have inhibited magma ascent, however, some tectonic structures act as “conduits” for the magmatic ascent. The planet cooling decreases the ability of magma to reach the surface, leading to the decline and termination of the volcanic activity (Wilson & Head, 2008).

Mercury's surface displays a highly cratered terrain, with craters ranging between 100-500 km of diameter. Most of the craters are less than 100 km in diameter, and were buried by volcanic lavas, while a large basin (>500 km) is rarely displayed within the surface. From this observation comes the hypothesis of a global resurfacing initiated just after the onset of the LHB (4.0-4.1 Gyr) and continued for 300-400 Myr (Marchi et al., 2013).

This resurfacing has been supported by MESSENGER XRS measurements, which suggest the presence of rocks similar to terrestrial Mg-rich basalt, poorer in Iron than on Earth (Rothery, 2015), and probably made up of Mg-rich orthopyroxene and calcium-rich plagioclase. When erupted as lavas they would have a lower viscosity and higher temperature than most of the Earth basalts.

The volcanic activity on Mercury almost ceased at 3 Ga (Byrne et al., 2018) although some local activity has been documented at ~1 Ga, within the Raditladi basin interior, (Prockter et al., 2008, Solomon et al., 2008). The oldest terrains in Mercury record an age not older than 4.0-4.1 Gyr (Marchi et al., 2013), whereas the major basins on its surface were formed during the late phase of the Late Heavy Bombardment (Massironi et al., 2009).

Although the common presence of the volcanic vents in this planet (over three hundred were documented) only a few of them have been closely studied. These vents appear as depressions, often within crater floors and associated with pyroclastic activity (Fig 4.24). From the dispersion of the explosive deposits, it is possible to estimate the content of volatiles of the magma which generated the deposits themselves. The calculation suggests about 20,000 ppm if the volatile is H<sub>2</sub>O, about 30,000 ppm if it is S or CO, and nearly 70,000 ppm if it is SO<sub>2</sub> (Kerber et al., 2011). These deposits are particularly young having ages as young as 1.7 Ga (Thomas et al., 2014)



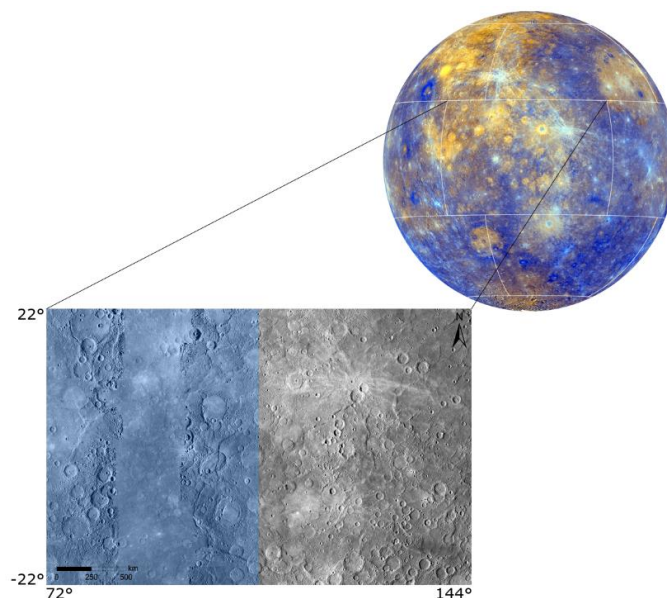
**Figure 4.24** A view of an explosive vent called Red Spot 3 (RS3) that lies 100 km inwards of the SW rim of the Caloris basin. This vent is surrounded by spectrally red deposits with at least 50 km of diameter, and including several “volcanic pits” (a) The RS3 area within the southwest of the Caloris basin. Image from the global enhanced colour mosaic by MESSENGER (after Denevi et al., 2016) (b)The internal structure of Agwo features on the MESSENGER MDIS image (55 m / pixel). The image shows multiple overlapping volcanic vents (after Pegg et al., 2021).

## Chapter V – Eminescu (H-09): Mapping and structural study

Among the fifteen quadrangles of Mercury, we selected  $\frac{1}{2}$  of the Eminescu quadrangle, in order to deliver a geological map as part of the coordinated Mercury's global mapping project (Galluzzi et al., 2019) that aims to deliver geological maps of the entire surface of Mercury.

The quadrangle covers an area between the low equatorial latitudes  $22.5^{\circ}\text{N}$ ,  $-22.5^{\circ}\text{S}$  and the longitudes  $72^{\circ}\text{E}$  to  $144^{\circ}\text{E}$ , and it is identified as H-09 (i.e., H represents Hermes, the Greek mythology equivalent of Roman Mercurius, and nine is the numbering of the quadrangle). Our work is centred within the western bisection of this quadrangle, in an area that runs from 72 to 108 longitudes and  $-22.5$  to  $22.5$  latitudes (Fig 5.1). The name of the quadrangle was proposed after the prominent Eminescu impact crater, which is located at  $10.79^{\circ}\text{N}$  and  $245.87^{\circ}\text{W}$ . This crater extends for over 125 km in diameter and is characterised by ejecta that extend up to one radius from the crater's rim and by a hollowed central peak (Schon et al., 2011). The hollows are identified as a bright deposit within the impact craters, irregular, shallow, flat-floored, and steep-sided rimless depressions. They exhibit morphologically fresh-appearing, implying a young age. It's suggested that hollows form by a loss of a volatile component from the surface without melting, however, the nature of this material is not known (Blewett et al., 2011, Thomas et al., 2014).

The crater in Mercury looks very fresh, and impacts very smooth terrains, showing only a few superposed craters. This indicates that Eminescu crater was recently formed, perhaps around one billion years ago (Schon et al., 2011). The walls for the Eminescu crater are degraded by slumping, forming distinct blocks of deposits, while the floor displays a terrain probably interested by local effusive emplacements.



**Figure 5.1.** Eminescu quadrangle on Mercury and the selected area of our work shadowed in blue. The global color mosaic has been realised over MESSENGER MDIS Basemap Enhanced Colour 665m/px with the Orthographic projection, at a center meridian  $95.264^{\circ}\text{E}$ , Latitude of origin is  $-1.657^{\circ}\text{S}$ . The false easting and northing are  $0^{\circ}$ . The basemap has been realised in the Equirectangular\_Mercury coordinate system over MDIS\_BDR2\_166m/px.

Our selection of this quadrangle was based on the following reasons: i) the presence of many interesting tectonic features (e.g., Beagle rupes, some unnamed lobate scarps, wrinkle ridges, Tectonized basins), ii) the color variation between the different terrains (bright materials on the NW side and extended dark materials in the NE and SE sides) and iii) the presence of possible hollows and pyroclastic deposits.

The map that will be delivered in the near future have been produced using the available basemaps from the NASA MESSENGER Mercury Dual Imaging Systems (MDIS) images. We have identified two main objectives within the selected area in Eminescu: i) to study the tectonics on Mercury at local scale through studding the compressive deformation in an old basin identified by "b12" and analyse the fault system kinematics and the wrinkle ridges network, ii) to deliver a Morpho-stratigraphic map for ½ of the Eminescu quadrangle in the frame to support targeting of interesting features to support the BepiColombo mission. The Eminescu quadrangle is one of the six quadrangles that were not acquired by the Mariner 10 probe, and thus not available geological maps and data have been realised to date. Hence, what make this work original is that the Morpho-stratigraphic map that we are going to deliver will be the first map that cover the surface geology of ½ of the Eminescu quadrangle with a 1:3M output scale using MDIS MESSENGER datum.

## 5.1. Basemaps and topographic datasets

The geological mapping for planetary bodies other than the planet Earth are produced by studying orbital data through "photogeologic interpretation". In particular, we used remote sensed imagery and the topography to map and interpret the surface features and put in context the different geologic units.

In our case, we used seven basemaps with different incidence angles processed by the MESSENGER team, in order to produce a Morpho-Stratigraphic map. These data were acquired by the MDIS instrument on-board MESSENGER spacecraft and available in the Planetary Data System (PDS) Imaging Node (NASA/USGS/JPL) for public use. In particular the NAC and WAC had a major role for the basemap release, the WAC images were essentially taken at 200 km altitude, while the spacecraft reached its minimum orbital distance, however, the NAC images use for the base map mosaics were taken at 13100 km of altitude (Galluzzi, 2015).

The basemaps we used are perfectly georeferenced to each other and are the following ones:

- **Mercury MESSENGER MDIS Basemap Enhanced Color Global Mosaic (665m/px):** This basemap was realised by a mosaic of images based on a global mosaic with 430, 750, and 1000 nm (Refer to the appendix, Figure A.1) bands and places the second principal component, the first principal component, and the 430/1000 ratio in the red, green, and blue channels respectively (Hawkins et al., 2007). This color composite combination is very useful for identifying, the terrain units: smooth plains usually appear in yellow colours, the pyroclastic deposits



(faculae) display orange color, the intercrater old plains are blue, and the crater rays are light cyan (Murchie et al., 2015).

- **Mercury MESSENGER MDIS Basemap MD3 Color Global Mosaic (665m/px):** A mosaicked 3-color Map Projected Multispectral (MD3) which consists of a global color map realised with the 1000, 750, and 430 nm RGB composition narrow-band filters in respectively red, green, and blue spectral channel (Refer to the appendix, Figure A.2). This basemap is important to emphasise the variations in color of the plains.
- **Mercury MESSENGER MDIS Basemap LOI Global Mosaic (166m/px):** This map is a monochrome mosaic of NAC and WAC images at 750-nm acquired at Low-Incidence Angle (Hawkins et al., 2007). This basemap is important for analysing reflectance variation (Refer to appendix, Figure A.3).
- **Mercury MESSENGER MDIS Global Basemap BDR (166m/px):** The BDR basemap consist of a monochrome map of reflectance, realised by using MDIS NAC and WAC images that best fit low emission and incidence angle (Hawkins et al., 2007). We had chosen the BDR basemap frequently as a reference layer (Refer to the appendix, Figure A.4).
- **High-incidence WEST -illumination Basemap - HIW (166m/px):** This map is a mosaic of NAC and WAC images acquired at 750 nm with a High incidence angles and a west-illumination (Hawkins et al., 2007), during the MESSENGER Extended Mission. The low illumination was chosen in purpose to accentuate low relief morphology, favouring in particular the visibility of asymmetric topography with steeper sloped to the west than to the east (Refer to the appendix, Figure A.5).
- **High-incidence East-illumination Basemap - HIE (166m/px):** The HIE basemap follows the same concept of the HIW, but with high solar incidence illumination angle from the East. As for HIW the basemap consists in a NAC and WAC mosaic with images acquired at 750 nm (Hawkins et al., 2007) during the MESSENGER Extended Mission. As the HIW basemap, the purpose was to accentuate low relief morphology (Refer to the appendix, Figure A.6). Both HIE and HOW were useful for identifying surface structures.

The High-incidence EST-illumination basemap were facing some issues related to the images illumination that was sometimes too intense from one side and completely dark from the other and thus it was impossible to identify some features or draw their continuity. Similar problems were faced with the High-incidence WEST-illumination mosaic which was even incomplete, presenting some small gaps in the NE side. The Low-Incidence Angle Basemap and Enhanced Color Global Mosaic suffered the problem of very bright reflectance on which was not possible to distinguish the surface materials, the crater rim and ejecta limits. Although the BDR was often used as reference they suffer from uneven illumination. Besides these technical issues, the result of working with all

of these basemaps together ends up by having a complete view about the surface features and the different terrains units.

It was also very important to consider the topography, which is a very essential element to interpret the morphologic features and the terrains elevation, and thus we used the data set derived from Mercury MESSENGER global DEM (Refer to the appendix, Figure A.7), holding a resolution of 665 m/px and derived from stereoisimages. The basemap covers the complete concerned region and it was accomplished by the MESSENGER team using the Integrated Software for Imagers and Spectrometers (ISIS3) and observations from MDIS (over 176,000 NAC and WAC observations). The topographic composed image was particularly useful for identifying tectonic features.

The projection plays a fundamental role in the mapping final result and the map delivering, and thus it is important to identify properly the Geographic Coordinate Systems required for any specific quadrangle or region. In our work, we adopted the Equirectangular\_Mercury projection system (Tab 5.1) since the Eminescu quadrangle is located at low latitudes (22.5°N, -22.5°S). This projection is essentially cylindrical equidistant, in which the horizontal coordinate is the longitude and the vertical coordinate is the latitude, so the standard parallel is taken as a null angle.

**Table 5.1.** The adopted geographic projection used for the raster layers.

Coordinate System	Equirectangular_Mercury
Central_meridian	180.0°
False_easting	0.0°
False_northing	0.0°
Inverse Flattening	0.0°
Datum:	D_Mercury
Semimajor Axis: 2439400.0	
Semiminor Axis: 2439400.0	

## 5.2. Mapping strategy

We present in this section the mapping tools, output scale, symbology, features classes, and the geodatabase used to produce the morpho-stratigraphic map for the ½ Eminescu quadrangle that is still under process, but will be completed shortly in the future.

We carried out the geology using ArcMap 10.5.1, although additional software has been used when needed for maps and image adjustment (e.g., QGIS 3.22.3).

### *Mapping Scale*

The selection of the mapping scale is very important for the final delivery of the map, and this is directly controlled by the basemap resolution. The standard mapping rules for Mercury global mapping project (Galluzzi et al., 2016, Mancinelli et al., 2016, Galluzzi, 2019), which have been derived from the mapping scale defined by Tobler, 1987, propose a mapping scale 2000 times the basemap resolution. Based on this mapping concept, and according for the image resolution that we are using, 1:400K mapping scale is perfect to map all the surface features (linear surface features and morphologies, geological contact,

surface features and geological units), without being in a pixelated view or occurring in potential misinterpretations of some surface features.

### *Mapping units and features classifications*

The techniques, methods and rules follow the ones adopted by Galluzzi et al., 2016, Galluzzi, 2019, Wright et al., 2019 (Please refer to these references for more details about the mapping tools). These standard rules are applied to the entire global 1:3M mapping project for Mercury and are based on the mapping standards of the US Geological Survey, PlanMAP and the federal Geographic Data Committee (FGDC) with appropriate revisions.

As a first step, we classified features according to their category into six feature units as defined in Table 5.2. Each unit includes more than one feature, and they were identified by diverse colour and/or symbology according to their type. The linear structural features like faults, have been classified into thrust, graben axis, faults, and wrinkle ridge, with certain and uncertain classes.


























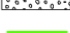










The geological contacts were identified by a polyline shapefile, in certain and approximative classes. The geological units and the surface features like bright and dark materials, rough ejecta, cluster of hollows, secondary crater chain or cluster, are mapped by a polygon shapefile, with a dedicated symbol for each feature.

These craters were subdivided into three classes according to their rim degradation degree: i) C1-heavily degraded crater: old degraded craters with sometime part of their rim is missing or overlapped by younger materials like ejecta of younger crater or smooth plains, ii) C2-degraded crater: craters with intermediate degradation, and iii) C3-well preserved crater: young and fresh impact craters characterised by clear and well visible rims and fresh impact ejecta.

The craters under 5km of diameter were not considered in our mapping, even if with clear rims, because of the small size. The terrains have been grouped according to the crater frequency distribution into three classes: i) Intermediate plains, ii) Intercrater plains and, iii) Smooth plains. The limit between the different terrain units is identified by a geological contact line, however, small single deposits like isolated bright spot, dark spot, or isolated hollow have been identified by a point feature, since they display a very limited dimension.

The craters ejecta contacts were particularly difficult to map, since the ejecta of nearby craters were often merged and overlapped. For this reason also for the crater ejecta we used approximative and certain, contacts. In addition, some crater presents a smooth floor, while others expose a hummocky floor material, and for this reason two symbology were identified according to the crater floor materials.

**Table 5.2.** Symbology used for the ½ Eminescu quadrangle mapping. Each feature unit is defined by a specific denomination and it was packed within a specific shapefile.

Feature	Symbole	Shapefile
<b>Point features</b>		
Undefined point feature		Point
isolated bright spots		
isolated dark spots		
isolated hollows		
<b>Geological contact</b>		
undefined morphology		Polyline
crest of crater rim D > 20 km		
crest of crater rimp 5 < D < 20 km		
crest of degraded or buried crater		
volcanic vent		
<b>Linear features structures</b>		
Undefined Structures		Polyline
certain fault		
certain graben axis		
certain thrust		
uncertain fault		
uncertain graben axis		
uncertain thrust		
wrinkle ridge		
<b>Geological contact</b>		
Undefined contact		Polyline
contact, approximate		
contact, certain		
<b>Surface features</b>		
uncertain surface features		Polygon
bright material		
cluster of hollows		
dark material		
rough ejecta		
secondary crater chain or cluster		
<b>Geological units</b>		
No Unit		Polygon
c1, heavily degraded crater		
c2, degraded crater		
c3, well preserved crater		
dark material		
hummocky crater floor		
intercrater plains		
intermediate plains		
smooth crater floor		
smooth plains		

### 5.3. Preliminary mapping results

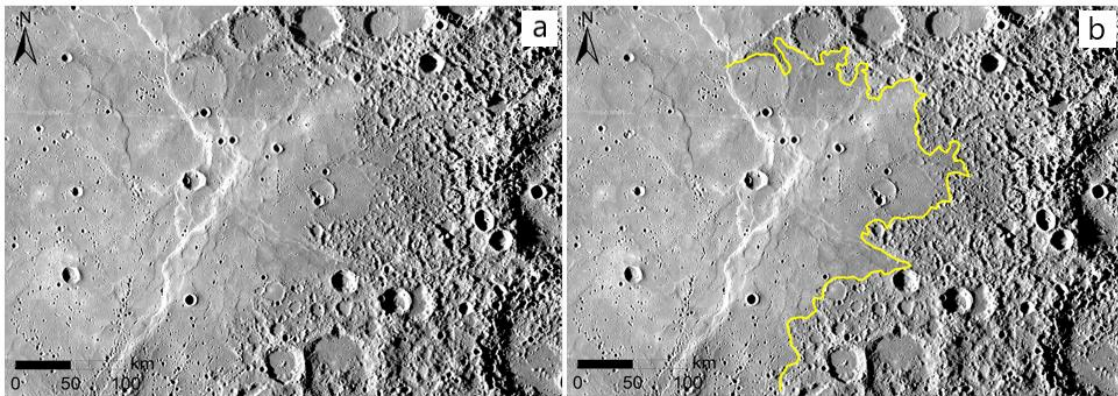
The selected area within the Eminescu quadrangle shows an interesting surface geomorphology that varies between smooth plains to very cratered and Tectonized plains (Fig 5.2). The surface records a story of intensive cratering, expressed by the large distribution of craters with diverse dimensions, some impact basins, and heavily intercrater plains. Three surface features dominate the west sector of the Eminescu quadrangle: i) Craters, ii) Lobate scarps and iii) wrinkle ridge (Fig 5.3).

According to our statistics, the craters distribution seems to be dominated by a crater with a rim that varies between 5 to 20 km (Fig 5.4 and Fig 5.5), they occupy about 72% of the total crater distribution. The large crater that are characterised by rim over 20 km and old crater with degraded or buried crater are less frequent and slightly present.



Among these ones it is worth to mention large flat-floored craters with a diameter varying between 170 to 200 kilometres displayed occasionally close to the smooth plains or surrounded by intercrater and intermediate plain: few of them present smooth infilling and a degraded and only partially conserved rim, suggesting a resurfacing by the effusive volcanism on Mercury which has been proposed to have occurred early in the planet's geological history.

Besides craters which are actually common all over the Mercury surface, We also recognized a large distribution of compressive tectonic features that evidently had a major role in the deformational story of this zone of Eminescu quadrangle (Fig 5.3). Indeed, many of the old large craters are cross-cut by lobate scarps with diverse length, and are associated with swarms of wrinkle ridges within their floor. The wrinkle ridges in particular are oriented in many different directions and seem to be formed during different stages .

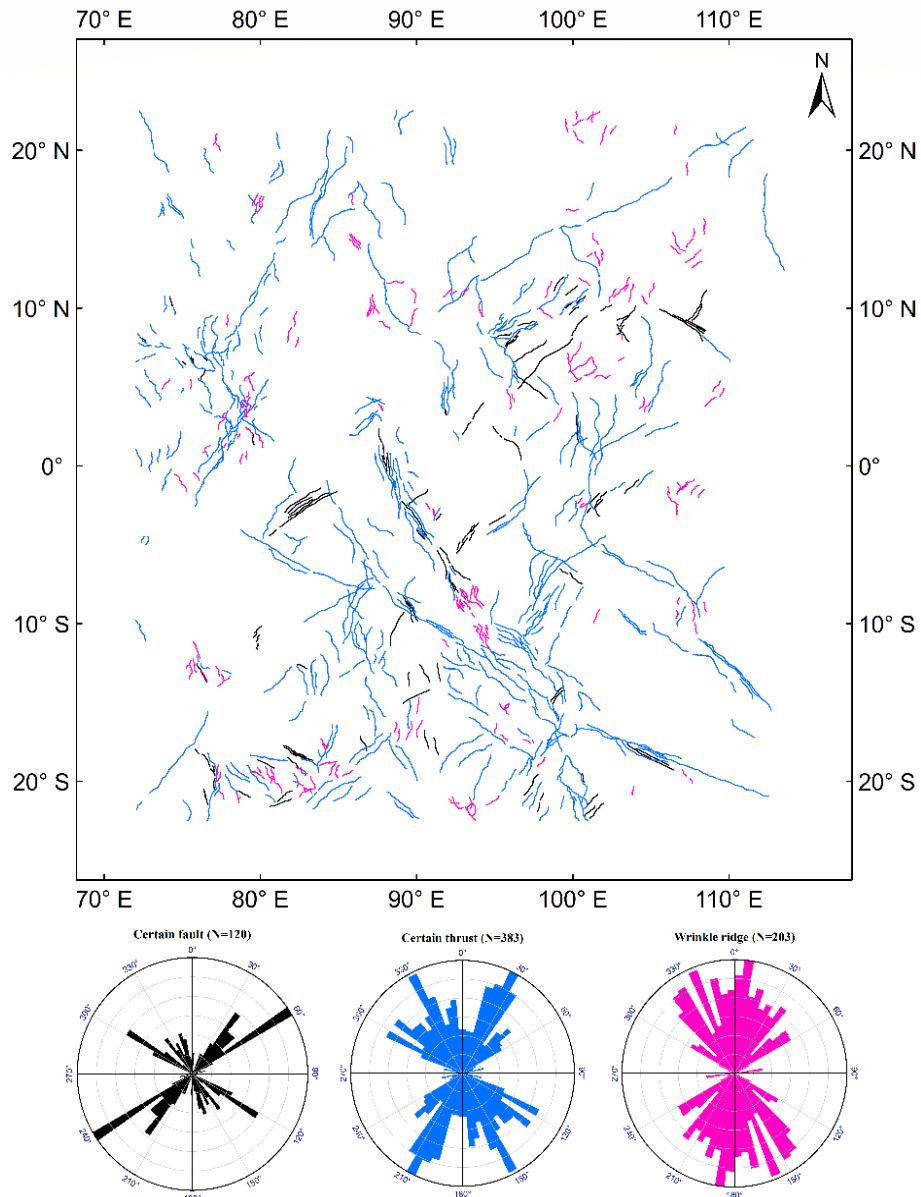


**Figure 5.2.** Topographic transition between smooth and cratered terrains (a) Intercrater and smooth plain difference within a deformed area by a large extended lobate scarp and a group of wrinkle ridge. Image over MDIS\_HIW2, with a 166m/px of resolution. View centred at 3.37°N, 78.52°E (b) Previous view in (a) with the shallow limit interpretation, outlined in yellow and defining the intercrater plain in the right side and smooth plain within the left. The same line also defines a topographic difference between higher (intercrater plain) and low (smooth plain) elevation.

We identified 203 wrinkle ridges (representing 28.75% of the total number of the linear features), 383 lobate scarps or thrust faults (representing 54.25% of the total) and 120 faults (representing 17% of the total). We checked the orientation of these linear structural features through rose diagrams. After plotting their length, derived from the polyline length, we recognized that the rose diagrams of the lobate scarps and the wrinkle ridges present some similarities in their orientations, which are instead different from the fault group. The main strikes of the different structures are the following:

- Wrinkle ridge: NE-SW, NNE-SSW (10°) and NW-SE (320°).
- Lobate Scarps: NE-SW (30°) and NW-SE (330°).
- Normal faults: NE-SW (30°-60°) and NW-SE (300°)

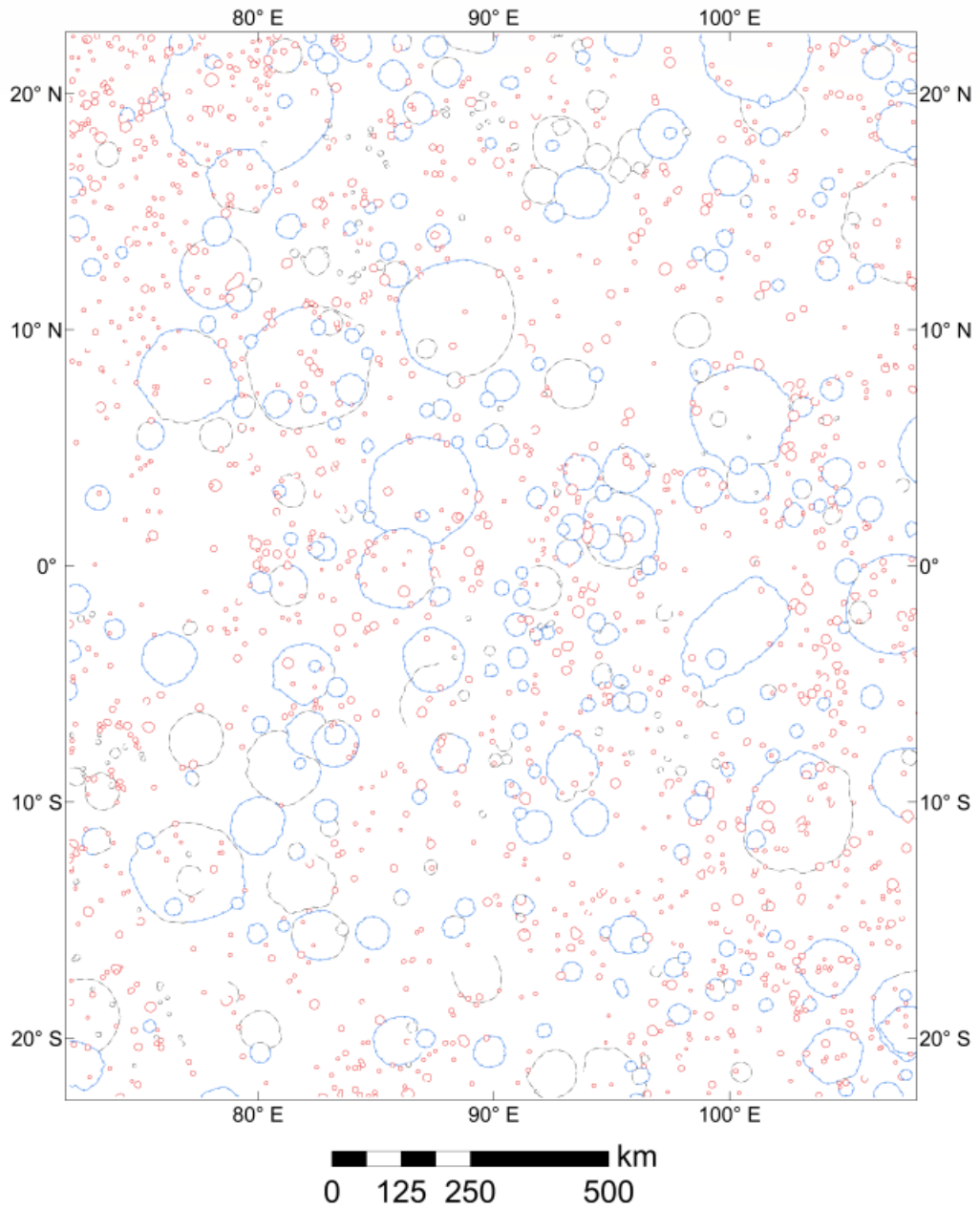
The wrinkle ridge seems to follow the same direction of the lobate scarp, which however displays a more widespread distribution. The length of lobate scarps varies between 8 to 453 km, whereas, the wrinkle ridge are much shorter reaching a maximum length of 80.345 km.



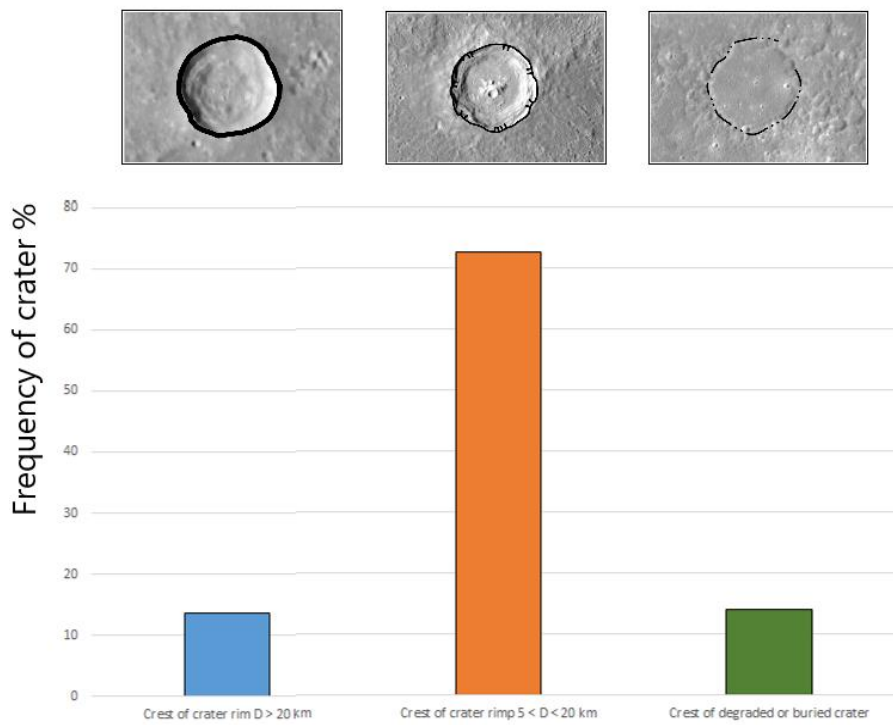
**Figure 5.3.** Map distribution and polar plots for the mapped wrinkle ridge (pink), lobate scarp (blue) and faults (black) over the selected area. These linear features are displayed in different plains units, from intercrater terrain to the smooth one, most of them are present in the south, closer to impact craters and/or within their floors. The polar plot is divided into 10° trend bins.

Some of the craters are cut by lobate scarps, and thus they can be a good target for understanding the local deformation and the relationship between different structural features generated by diverse processes. One prominent example is the Sveinsdóttir crater which is characterised by an elongated form, and crosscut by the Beagle rupes lobate scarp. The elongated form of the Sveinsdóttir crater suggests impact angles below 10-15°.

- crest of crater rim  $D > 20$  km
- crest of crater rim  $5 < D < 20$  km
- crest of degraded or buried crater

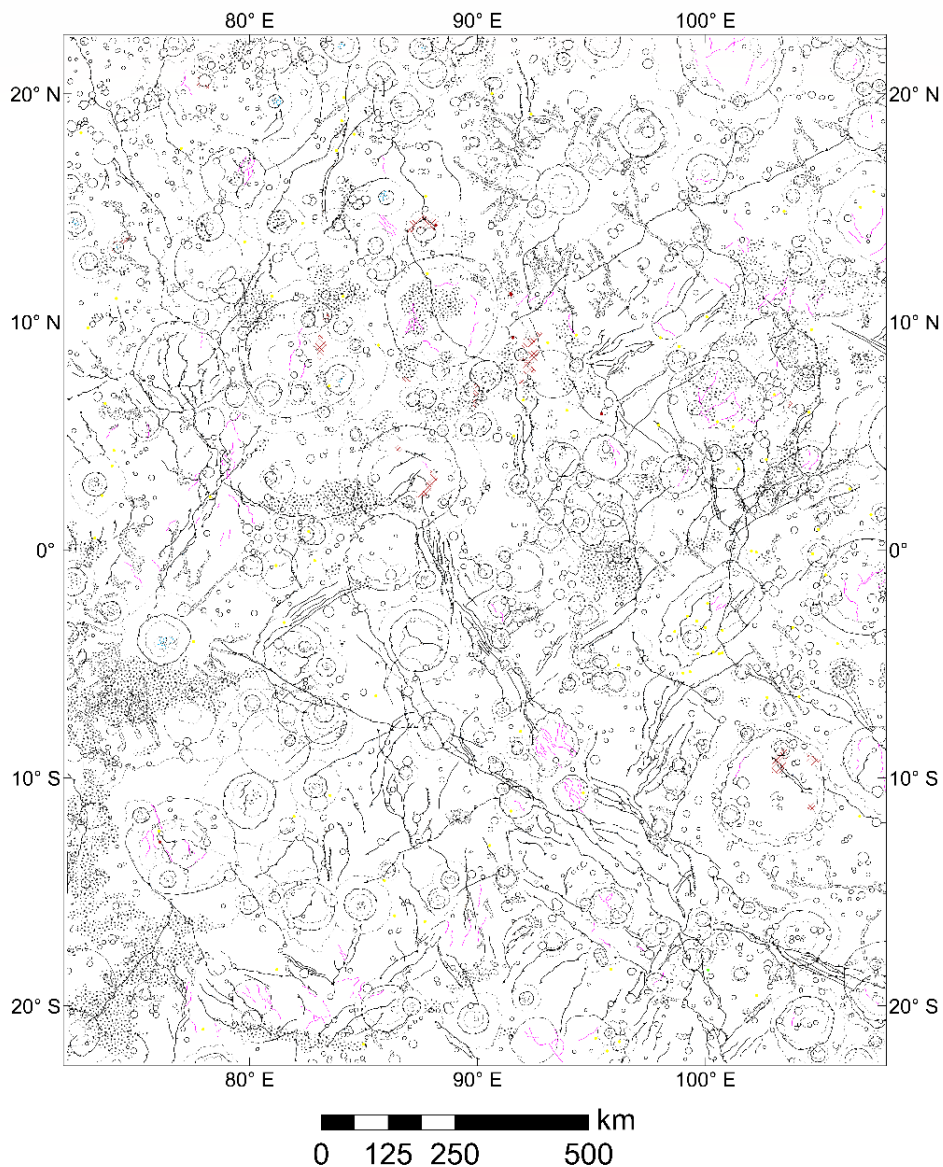


**Figure 5.4.** View over a map layer for the crater's distribution within the mapped area. The crater dimension has been identified by different symbols. A crater with  $> 20$  km of diameter is outlined in the blue rim, while the crater with a dimension between 5 km and 20 km is mapped with a red line. The degraded rim is drawn in black lines. Some craters have a mixed rim, part of it buried, while the other is clearly distinguished.



**Figure 5.5.** Histogram for the crater distribution over the complete mapped area in Eminescu quadrangle. The values show that the craters with large size and the buried craters are slightly present compared to the craters with a dimension between 5 to 20 km.





**Figure 5.6.** Map of the surface features lineaments. The linework displays the surface features, geological contacts, linear features structures, linear features morphology, and point features (Refer to Table 5.2 for the legend). All these layers will help to produce the 1/2 Eminescu quadrangle geological map (Morpho and Chrono-stratigraphic maps) in the near future.

#### **5.4. Bepicolombo-SIMBIOSYS priority target definition**

The map we produced (Fig 5.6) helped us to make a list of possible targets to be acquired by SIMBIOSYS during ESA/JAXA BepiColombo space mission. Each proposed feature is identified by an ID number (Target ID). The science work packages of SIMBIO-SYS cover the science objectives that can be carried out by the instruments, hence each target can satisfy one or more of these work packages (from WP5 to WP9, refer to table 5.3 for more details).

In addition, the SIMBIO-SYS working teams (Cremonese et al., 2020), have classified the targets into "Rank" and "Type", as described as follows :

### ***Category***

- Terrains: sample area of a morphological terrain, sample area of a geochemical terrain, faculae, bright rays far from the main crater;
- Craters: any peculiar crater, or any crater encompassing peculiar features that need geological context;
- Structures: scarps, faults, ridges, etc.;
- Volcanic: vents, putative vents, pitted grounds, pyroclastic deposits;
- Hollows: hollow fields, putative hollows;
- Other features: dark spots, bright spots, putative layering, landslides;

### ***Rank***

- Rank 1: lowest rank (e.g., MESSENGER already covered the area at lower resolution, global mapping could be enough)
- Rank 2: low rank (e.g., as above but higher resolution could help)
- Rank 3: medium rank (e.g., known large features that would benefit of better observation conditions)
- Rank 4: high rank (e.g., known or unknown features that need higher resolution or better compositional information)
- Rank 5: highest rank (e.g., main science goals or very small unknown features)

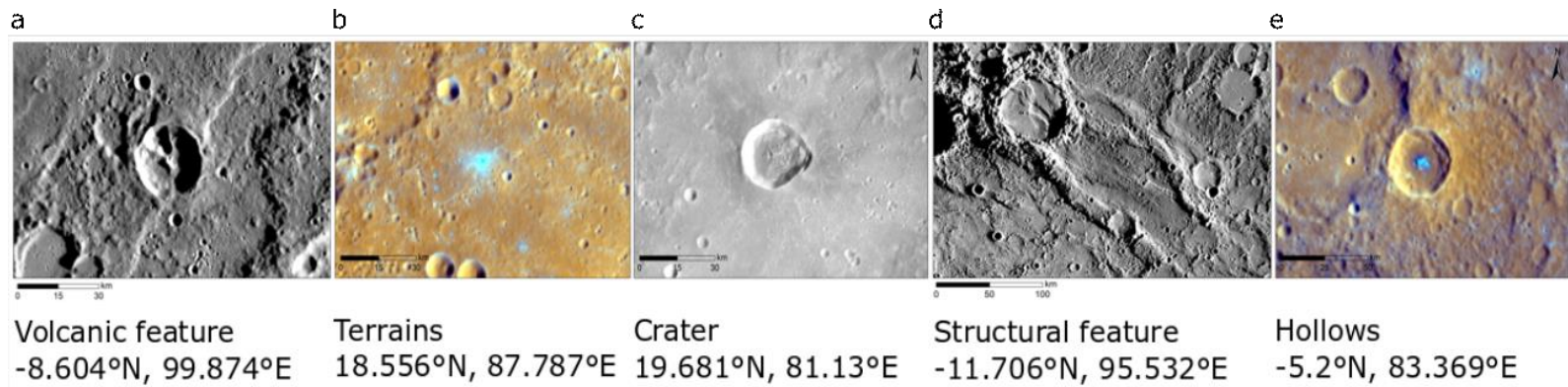
Finally in order to avoid the double selections the proposed features are identified by their geographic coordinates (Central Lat and Lon, Max Lat and Lon, and Min Lat and Lon) and are revised by the SIMBIO-SYS coordination team.

The list of all targets that we had proposed contains 38 (Tab 5.3) proposed sites to be photographed, and they are varying between Hollows (18.42% of total targets), Craters (42.10%), Structures (23.68%), Terrains (7.90%), Volcanic (2.63%) and other features (5.26%). The target distribution and samples selected features are labelled in the figure 5.7. Our selection was in accordance also with the SYMBIO-SYS team objectives and the global missions' goals, which is focused mainly in the study of the surface composition, morphology, hollows, and Mercury geology. All our features are worth to be acquired by the SIMBIOSYS instruments coverage (i.e., HRIC, STC, and VIHI), but unfortunately some features have been proposed to be partially covered due to the instruments' efficiencies. Moreover, some features should be acquired also with other instruments (i.e., MIXS, MERTIS, MGNS, BELA and SERENA), in order to obtain diverse informative layers (e.g., Spectral information, different altitudes, resolution).

**Table 5.3.** List of the proposed targets for ESA/JAXA BepiColombo space mission to Mercury, within the studied area in Eminescu H-09 quadrangle.

TARGET_ID	WG5	WG6	WG7	WG8	CEN_LAT	CEN_LON	CATEGORY	TYPE	RANK	OTH_INST
600111		Yes		Yes	18.59	88.00	terrains	bright deposits	2	MERTIS
600112		Yes		Yes	16.05	75.00	terrains	bright deposits	2	MERTIS
600113		Yes		Yes	19.62	81.00	craters	Landslide in Crater	4	MERTIS
600114		Yes		Yes	0.74	78.00	craters	Young Crater	2	MERTIS
600115		Yes		Yes	8.62	92.00	craters	Young Crater	4	MIXS + MERTIS + MGNS
600116		Yes		Yes	14.24	88.00	other features	Dark spot	3	MIXS + MERTIS + MGNS
600117		Yes		Yes	-3.93	76.00	craters	Bagryana crater	2	MERTIS
600118		Yes		Yes	15.81	94.00	craters	Complex crater	4	MERTIS
600119		Yes		Yes	-9.99	122.00	craters	Complex crater	3	MERTIS
600120		Yes	Yes	Yes	0.05	73.00	craters	Small crater	2	MERTIS
600121		Yes		Yes	2.84	73.00	craters	Small crater	2	MIXS + MERTIS + MGNS
600122		Yes		Yes	-12.47	117.00	craters	crater floor	4	MIXS + MERTIS + MGNS
600123		Yes		Yes	1.27	76.00	craters	Crater with landslide	4	MERTIS
600124		Yes		Yes	-5.17	83.00	Hollows	hollows field	4	MIXS + MERTIS
600125		Yes		Yes	6.45	96.00	craters	Crater with landslide	3	MERTIS
600126		Yes	Yes	Yes	18.17	102.00	craters	central peak	5	MERTIS
600127		Yes		Yes	-11.03	125.00	other features	Unclassified features	3	MERTIS
600128		Yes		Yes	-8.86	103.00	craters	Crater with Landslide	3	MERTIS
600129		Yes		Yes	2.53	84.00	craters	Elliptical irregular	3	MERTIS
600130		Yes		Yes	-12.34	76.00	hollows	hollows field	4	MIXS + MERTIS
600131		Yes		Yes	6.82	103.00	hollows	hollows field	4	MIXS + MERTIS
600132		Yes		Yes	1.22	113.00	hollows	hollows field	4	MIXS + MERTIS
600133		Yes		Yes	1.02	114.00	hollows	hollows field	4	MIXS + MERTIS
600134		Yes		Yes	-11.67	107.00	hollows	hollows field	4	MIXS + MERTIS
600135		Yes		Yes	-19.72	108.00	hollows	hollows field	4	MIXS + MERTIS
800118	Yes		Yes	Yes	7.91	77.00	Structures	Faulted Floor of Crater	4	MERTIS
800119	Yes			Yes	-18.89	115.00	Structures	Tectonic features	3	MERTIS
800120	Yes			Yes	-2.84	100.00	Structures	Beagle rupes and Sveinsdottir crater	4	MERTIS
800121	Yes			Yes	-12.15	96.00	Structures	Broad valley in tectonic terrains	2	MERTIS
800122	Yes			Yes	-16.07	94.00	Structures	Tectonic depression	2	MERTIS
800123	Yes			Yes	0.72	115.00	Structures	Tectonic Morphology	3	MERTIS
800124	Yes			Yes	0.24	113.00	Craters	Deformed crater floor	3	MERTIS
800125	Yes			Yes	-17.07	110.00	Structures	Faulted Floor of Crater	3	MERTIS
800126	Yes			Yes	-6.01	97.00	Terrains	Tectonized Terrains	3	MERTIS
800127			Yes	Yes	-8.61	100.00	Volcanic	Putative volcanic vents	3	MERTIS + SERENA
800128	Yes			Yes	-17.48	99.00	Structures	Tectonic intersection	3	MERTIS
800129	Yes			Yes	8.04	94.00	Craters	Deformed crater	2	MERTIS
800117	Yes			Yes	3.20	78.00	Structures	Tectonic zone	4	MERTIS + BELA

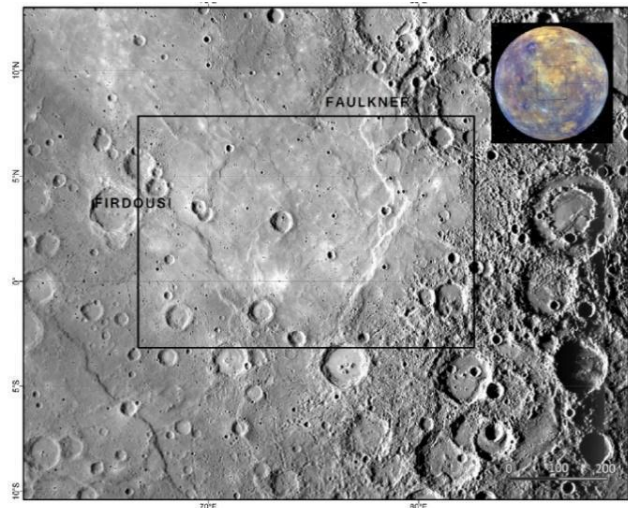
**WG5:** Interior and Tectonics. **WG6:** Surface and Composition and Laboratory Activities on Surface Analogues. **WG7:** Volcanism and Mantle Evolution. **WG8:** Stratigraphy and Geological Mapping. **WG9:** Surface-Exosphere Interactions.



**Figure 5.7.** Example of some targets that have been selected in our mapped area. Views are over diverse basemaps with different resolutions (a) Impact crater with possible hollow site in the central peak. Targets have been proposed as a hollow mark, the image is enhanced color Global Mosaic (665m/px) (b) Crater deformed by lobate scarps, this view is located in a heavily intercrater plain within the southern sector of our mapped area. The lobate scarp extended for tens of kilometres and deform the crater rim. It has been categorised as a structural feature (c) Fresh impact crater, with smooth floor and clear central pick and well-preserved rim. This feature has been selected as a sample of fresh young crater within Mercury surface (d) Terrains sample, it has been selected in order to analyse the surface color variation and composition (e) Crater that might host a volcanic vent on the north of its rim. Volcanic vents have been largely distributed within crater floors on Mercury. This crater has been classified as a possible target for a volcanic vent expression.

## 5.5. Compressive deformation within the b12 basin on Eminescu

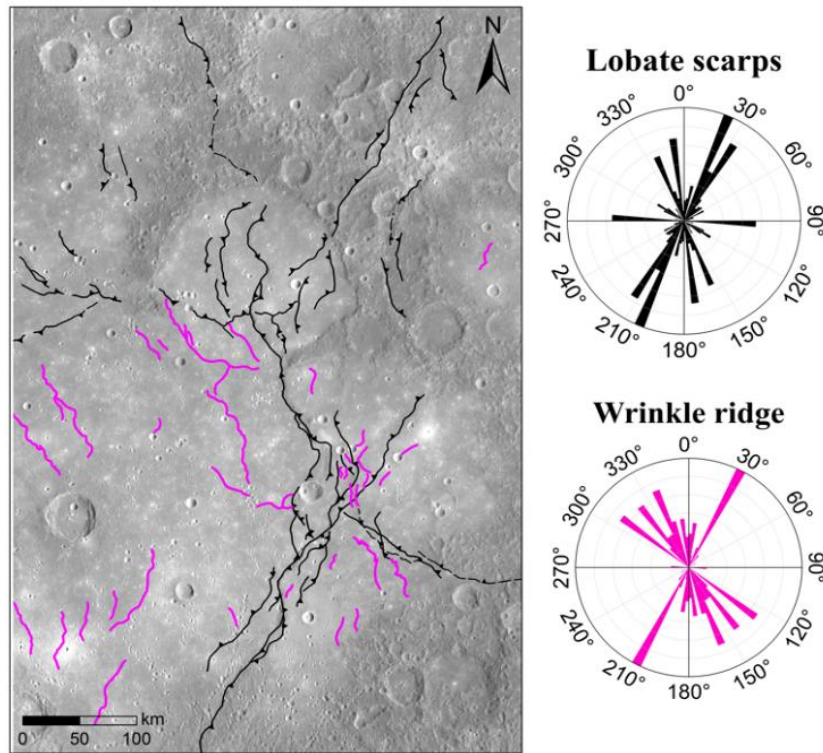
We have studied at regional scale the compressive tectonic regime in and around a basin of 550 km of diameter located at 3.7°N, 74.5°E (Fig 5.8). However, the basin is only partly included in the working area, and thus we have studied lobate scarps and wrinkle ridges only in its eastern sector. This basin was identified as “b12” by Fasset et al., 2012, and is characterised by a widely buried rim, with only 10% of completeness.



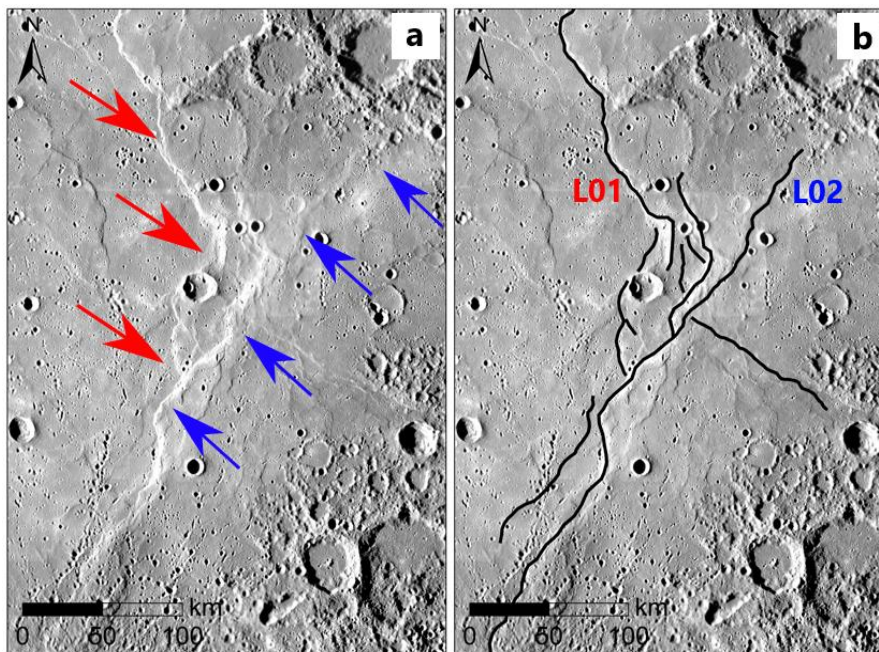
**Figure 5.8.** The b12 basin, surrounded by a smooth plain from the north, intermediate plain from the south, and a heavy intercrater plain from the SE side. On the west side of the basin is located the Firdousi crater, and on the NE is present the Faulkner crater. The basin is deformed by a group of lobate scarps that extend slightly to the north for a few kilometres (After López et al., 2015).

Both lobate scarps and wrinkle ridges are expressed within the basin floor and the surrounding plains. The lobate scarps are oriented along three prominent directions: NW-SE, NNW-SSE and NE-SW, whereas the wrinkle ridges are represented by three trends: NW-SE, NS and WNW-ESE (Fig 5.9). Most of the wrinkle ridges have the same orientation of the lobate scarps. The cross-cutting relationship between the lobate scarps of different orientations might suggest that they are formed through two deformational phases: the first phase generates NNW-SSE and NW-SE lobate scarps and it was superimposed by a second faulting phase, produced NE-SW faults (Fig 5.10).





**Figure 5.9.** The deformed zone within the right sector of b12 basin. The image is a MDIS\_HIE, centred at 2.185°N, 79.214°E. The polar plots represent the trends of lobate scarps (N= 68) and the wrinkle ridge (N= 45).

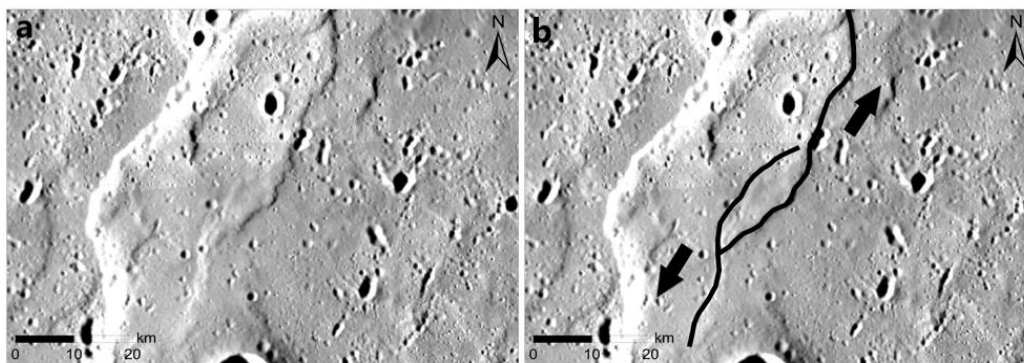


**Figure 5.10.** Cross-cutting lobate scarps within the basin eastern side. The image is a MDIS\_HIW, centred at 3.18°N, 78.388°E (a) a NW-SE lobate scarp is indicated by the red narrow and it is transected by a NE-SW lobate scarp indicated by the blue arrow (b) lobate scarps lineaments interpretation.

We classified the wrinkle ridges into two deformational phases based on the cross-cutting relationship between the different lineaments driven by a different stress orientation. The first group includes the wrinkle ridges that are spatially isolated from the lobate scarps

and oriented NW-SE and WNW-ESE. This group of wrinkle ridges appears to be formed before the lobate scarps (López et al., 2015). The second group are the wrinkle ridges oriented on NW-SE, NNW-SSE and NE-SW, and present within the lobate scarps seem to be formed at the same time of the NE-SW thrust faults.

Although the strike-slip fault is not often observed in our area, additional observation indicates a left lateral fault transurrence, in restraining bend (Fig 5.11). This left lateral kinematics is associated with the NE-SW lobate scarp, and generate the formation of a pop-up feature.



**Figure 5.11.** Strike-slip fault and restraining step-over along the eastern side of the B12 basin (a) transpressional fault NE-SW oriented with a gentle restraining bend (b) Photo interpretation of the left lateral transpressional fault in the previous image, MDIS\_BDR, V2 layer centred at 1.52°N, 78.145°E.

## 5.6. Discussion on Eminescu geological features mapping

The mapping of all apparent surface features within the ½ of the Eminescu quadrangle, helped to analyse the distribution of faults, craters and types of terrains. The preliminary mapping results have shown a large number of impact craters with 5 to 20 km of diameter, compared to the larger size impacts (>20km) and the craters with degraded and buried rim. The area that we selected in the Eminescu quadrangle seems to be resurfaced within a volcanic flow, since terrains present smooth plains and filled-flooded crater floors, suggesting that volcanism has a probable impact on this district. Thus, cratering and volcanism are the major driving processes responsible for the surface geomorphology of the mapped zone in the Eminescu (H-09) quadrangle.

The similar trend of the lobate scarps and wrinkle ridges might eventually suggest a common origin, whereas the different orientation of the rectilinear faults (Black polar plot), might suggest that they might have been generated in different phases compared to the lobate scarps and wrinkle ridge.

The structural analysis has shown that even compressional features are important in the mapped area. Lobate scarps oriented NW-SE, NNW-SSE and NE-SW, and wrinkle ridges following NW-SE, NS and WNW-ESE trends are distributed all over the area, in particular within the southern sector as shown in figure 5.6.

The geometry, orientation, kinematics and cross cutting relationships of lobate scarps and wrinkle ridges have been interpreted on a selected basin (b12).

Our analysis suggests two tectonic phases. The first phase generated NNW-SSE to NW-SE lobate scarps (L01 in Fig. 5.10), and it was superimposed afterward by a NE-SW lobate scarps which seems to be the last event that happened within this basin. We grouped the wrinkle ridges into two classes based on their trends and their spatial distribution according to the lobate scarps. The NW-SE and the WNW-ESE are interpreted to be formed even before the lobate scarp's expression. A group of NS wrinkle ridges close to the NE-SW lobate scarps seems instead to be formed at the same time to this lobate scarp. Here we propose three deformational stages/phases that led to the Tectonized old impact basin floor and the expression of a series of wrinkle ridge and lobate scarps. The first deformation led to the NW-SE and WNW-ESE wrinkle ridges, that was followed by the NE-SW and NNW-SSE lobate scarps, finally the NE-SW large extended scarps and the NS wrinkle ridges in a general left lateral transpressional kinematics.

## Chapter VI – Discussions and conclusions

Noctis Labyrinthus articulated structures and features have been objects of different interpretation through time. The processes proposed for their evolution include faulting (Masson, 1977, Bistacchi et al., 2004), magmatic activity and lava tubes formation (Leone, 2014), water-processes (Weitz et al., 2011, 2013, 2014, Rodriguez et al., 2016), karst reshaping (Baioni et al., 2017). The starting point to understand the context where Noctis Labyrinthus has been formed and developed is however the analysis of fault systems and their relationship with pit chains, both widely expressed on Noctis Labyrinthus surface.

Our analysis of the fault's geometrical attributes, distribution, orientations, kinematics and growth, represents an initial step for understanding the tectonic regime of Noctis Labyrinthus which is dominated by extensional tectonics, with some evidences of transtensional kinematics. The structural map that we produced was a direct insight also for understanding the pit chains' uneven distribution in relation to the faults system, being absent in the northern sector and well developed in the southern one.

In particular our structural analysis led us to propose a model based on two major processes:

- Early extensional tectonics: the fault systems have a major role in the creation of the connected series of troughs, and the formation of pit chains. The first tectonic phase, dominantly expressed on the northern sector, consists in a system of dextral transtensional faults NS to NNE-SSW trending. The second phase of faulting is represented by ENE-WSW to EW faults, concentric to Syria Planum uplift. The third and last deformational phase is characterised by isotropic radial extension based on the faults' intersections, where major curvilinear faults intersect minor straight faults in their points of maximum curvature. This isotropic extension was responsible for the pit chains' final development and the NNW-SSE, NW-SE and WNW-ESE faults formation.

What support our interpretation are the shapes of the intersections between faults and the analysis of the faults pit chains interaction. The intersections between NS to NNE and EW to ENE-WSW systems are indeed characterised by a major distribution of T-shaped and X-shaped intersections which according to Collanega et al., 2014 experiment can be interpreted as the expression of an asynchronous bi-directional extension where the formation of the NS to NNE system, predated the ENE-WSW and EW trends. However, the NNW-SSE, NW-SE, and WNW-ESE faults often connect the pit chains with N-S and EW grabens through Y-shaped junctions, indicating a third deformational phase dominated by radial extension.

The important role of the first two tectonic phases is the preparation of a weak, fractured zone, able to collapse under any additional stress due to volcanic plumping.

- Volcanic plumping: our view consists of a local shallow magma chamber, feeding vertical radial and cone sheeted dikes transporting the magmatic flow from deep level to the surface. The pits chain formation was likely favoured in a weak, deformed zones, able

to collapse under the plumping stress. The cone sheeted dikes in the subsurface are expressed by the series of ENE-WSW to EW grabens concentric to Syria Planum, where the volcanic centre was located. Indeed, Syrian planum is associated with numerous low relief small volcanoes corresponding to the magma source at depth that fed the dikes presumably responsible for the largest grabens and pit chains in Noctis Labyrinthus.

In summary an early extensional tectonic was responsible for the Noctis Labyrinthus deformation, weakness, so that the district was favourable for surface collapse and pit chains formation. We believe that a magma chamber located in Syria planum fed Noctis Labyrinthus district, and caused an additional stress in an already Tectonized and weak crust favouring the pit chains formation. However, many other factors could have contributed to the Noctis Labyrinthus formational story, like for example its relation with Valles Marineris extensional system, the Tharsis rise, and even the Alba patera volcano, but such a debated discussion will require further work about the role of these specific features in creating Noctis Labyrinthus.

As a supplementary work we used the MDIS MESSENGER datum to study some the lobate scarps in the Eminescu quadrangle on Mercury. Lobate scarps are the expression of surface-breaking thrust faults and, being widely distributed on Mercury surface, are thought to be the result of compressional stresses due to interior cooling and global radial contraction of the planet. Through six monochrome, two colours and one topographic basemaps we were able to carry out our mapping of the surface features that have been classified in Point features (i.g. isolated hollows, isolated bright spots, isolated dark spots), geological contacts (i.g. crest of crater, volcanic vents), linear features structures (i.g. faults, grabens axis, wrinkle ridges), surface features (i.g. bright materials, clusters of hollows, dark materials, rough ejecta, secondary crater chain), and geological units (i.g. heavily degraded crater, degraded crater, well preserved crater, smooth crater floor, hummocky crater floor). The map that we are producing will help identify all compressional features in  $\frac{1}{2}$  of the Eminescu quadrangle, by delimiting the lobate scarps and wrinkle ridges extension all over the selected area. Our interpretation suggests that the selected district on Eminescu quadrangle is largely dominated by compressional features, represented by lobate scarps and wrinkle ridges. Moreover, the analysis of the crater's distribution shows a large distribution of crater with a rim diameter between 5 to 20 km, compared to craters with rims  $< 5$  km or buried craters with diverse dimensions between 5 km to over 20 km. Furthermore, we found that some old crater with degraded rim, are partially or totally covered by younger smooth plains suggesting that volcanism have played an important role in resurfacing some crater and terrains units. Through our geological mapping, we were also able to propose 38 possible targets of interest varying between craters, hollows, terrains, vents and tectonic structures to be covered in the next future by the SIMBIOSYS instrument onboard the BepiColombo space mission. At the moment our map includes all the surface features, except the geological units that need to be completed. In the future we are indeed planning to improve the current map layer delivering a complete Morpho-Stratigraphic map.

In this thesis, we focused our attention on an old basin, partially located in the left bisector of the Eminescu quadrangle, as a sample site for investigating the compressional tectonics in the region. This old deformed basin was named "b12" by Fasset et al., 2012 and its centre is located at 3.287°N, 78.06°E. We analysed the lobate scarps and wrinkle ridges



within the basin floor in order to put in chronological order the different tectonic phases which involved the basin. Our analysis suggests two phases of deformation: i) the first one is responsible for NNW-SSE and NW-SE lobate scarps, ii) the second one of NE-SW transpressional lobate scarps. We grouped the wrinkle ridges into two classes: the first group include NW-SE and WNW-ESE wrinkle ridges, generated before the lobate scarp formation; the second group of wrinkle ridges is NE-SW trending and seems to be synchronised to the neighbour lobate scarps with the same trend.

Hence, we propose three deformational phases that lead to the tectonized old impact basin floor and are expressed by a group of wrinkle ridge and lobate scarps, formed under a stress field acting in different directions.

## Appendix A

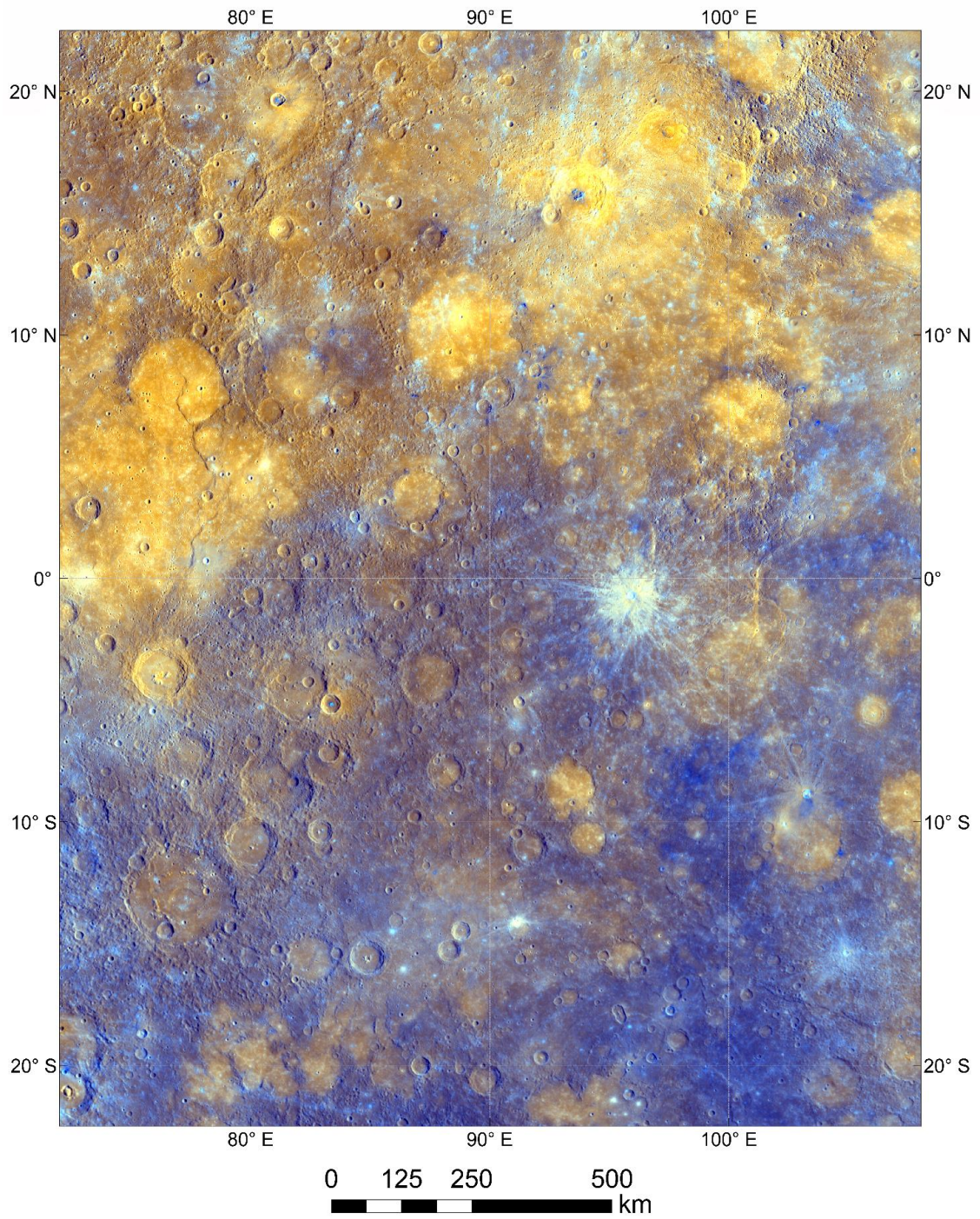
### A.1. Mercury MESSENGER MDIS Basemaps

For delivering the Morpho-Stratigraphic map for 1/2 of the Eminescu (H-09) quadrangle, we used the processed data acquired by the MDIS instrument on board the MESSENGER spacecraft, available in the Planetary Data System (PDS) Imaging Node (NASA/USGS/JPL). The figures below display the different basemaps used for the mapping with different illumination and resolution, as the following:

- Mercury MESSENGER MDIS Basemap Enhanced Color Global Mosaic with 665m/px of resolution (Figure A.1).
- Mercury MESSENGER MDIS Basemap MD3 Color Global Mosaic, bearing a resolution of 665m/px (Figure A.2).
- Mercury MESSENGER MDIS Basemap LOI Global Mosaic, characterized by 166m/px of resolution (Figure A.3).
- Mercury MESSENGER MDIS Global Basemap BDR bearing 166m/px of resolution (Figure A.4).
- High-incidence WEST -illumination Basemap - HIW, with a 166m/px of resolution (Figure A.5).
- High-incidence EAST-illumination Basemap - HIE with 166m/px of resolution (Figure A.6).

For the topography, the MLA datasets were not helpful in our case, since it does not cover more than 20% of the selected area in the Eminescu quadrangle, and thus we decided to use the Mercury MESSENGER Global DEM which covers the complete area.

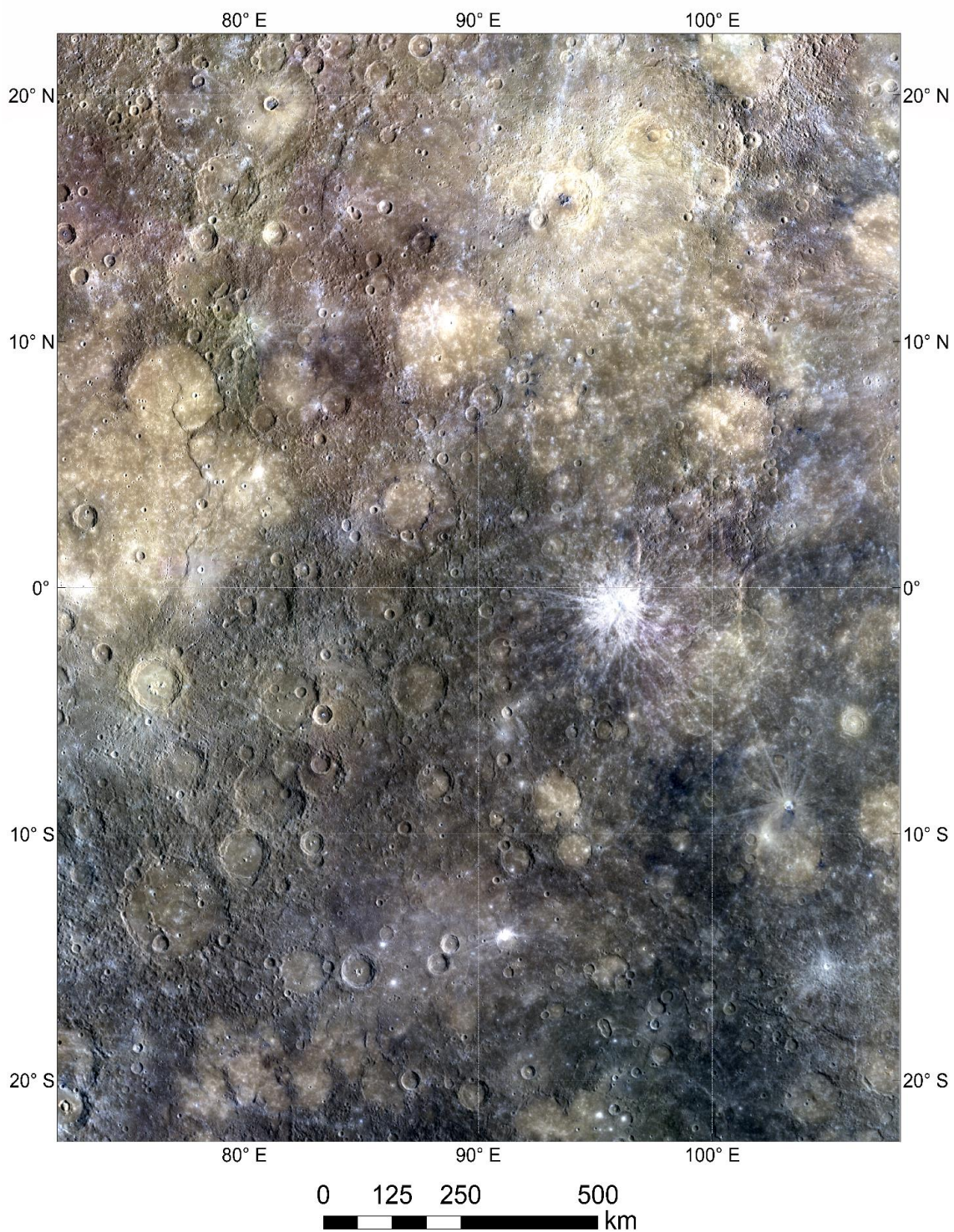
**Enhanced Color Global Mosaic (665m/px)**



**Figure A.1.** Enhanced Color Global Mosaic with 665m/px of the resolution, in Equirectangular\_Mercury projection obtained from MDIS datum mosaic based on the 430, 750, and 1000 nm spectral bands. This RGB color combination has been realised in Principal Component Analysis (PC1 and PC2) 430 over 1000 nm.



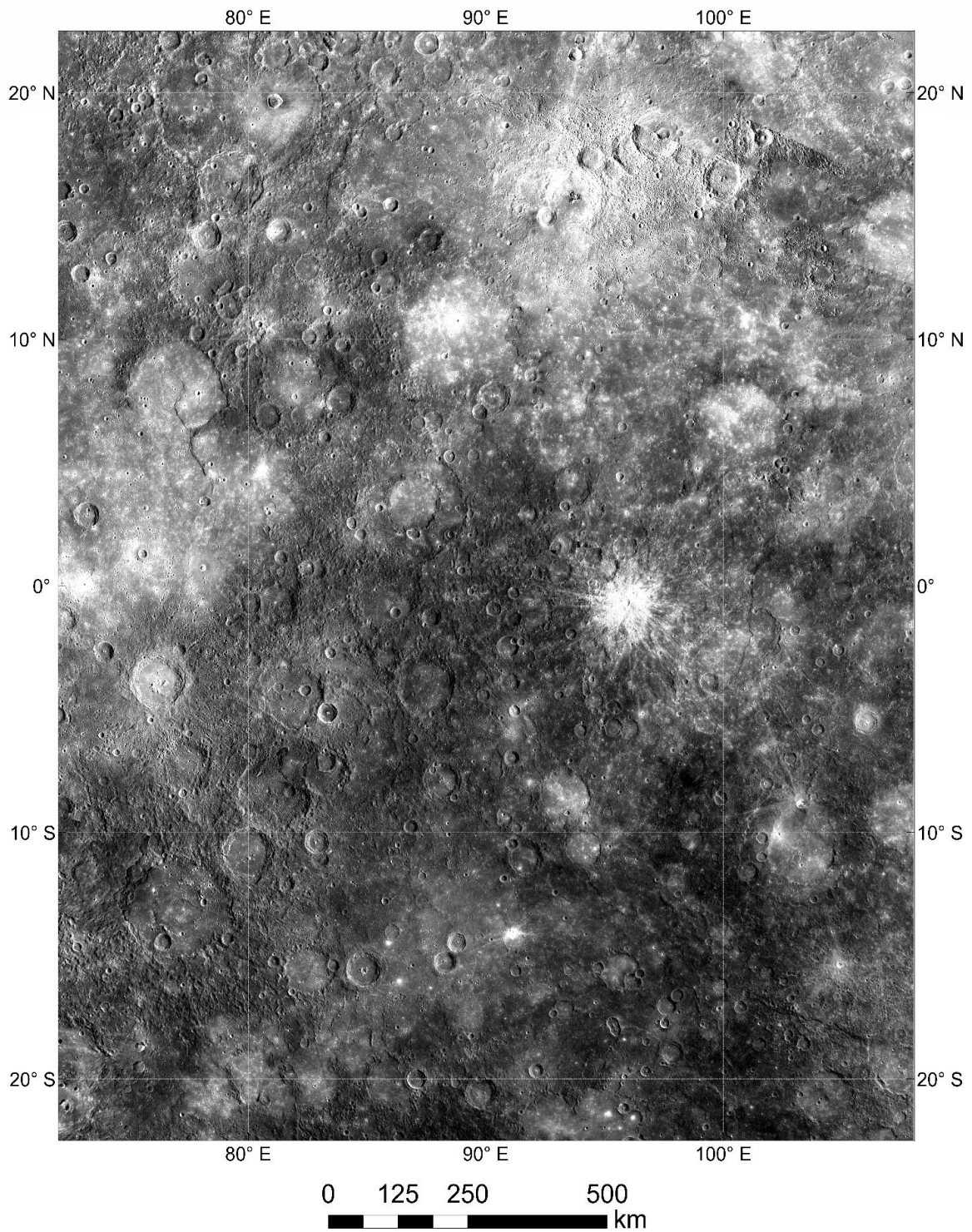
**MD3 Color Global Mosaic (665m/px)**



**Figure A.2.** MD3 Color Global Mosaic with 665m/px of resolution in Equirectangular\_Mercury projection. This RGB false-color mosaic is released in multispectral reduced data records in 1000 (red), 750 (green), and 430 nm (blue).



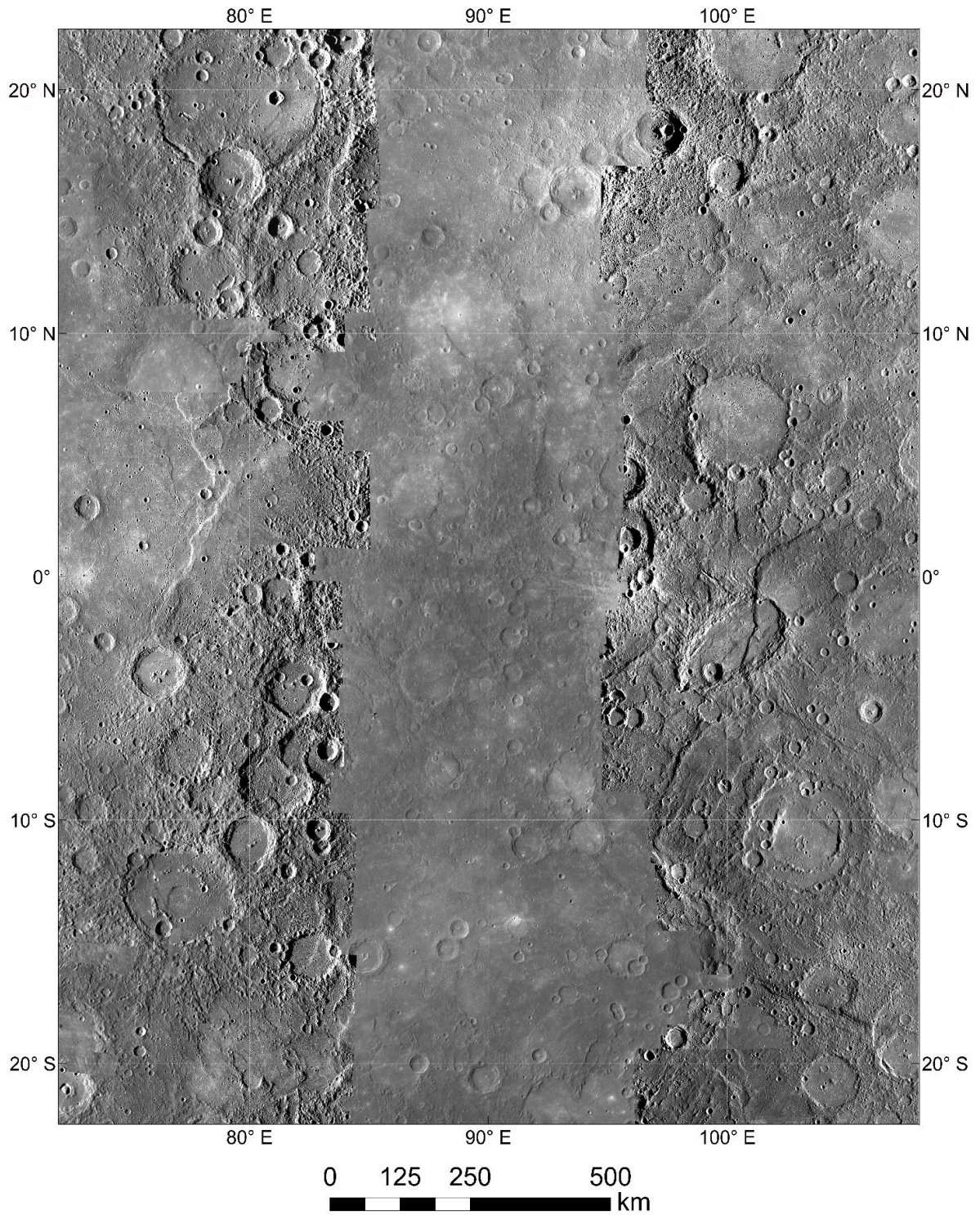
MDIS\_LOI\_V2 (166m/px)



**Figure A.3.** Low-incidence Angle Basemap with 166m/px of resolution data products comprises NAC and WAC 750-nm datum, photometrically normalised to a solar incidence angle ( $i$ ) = 30°, emission angle ( $e$ ) = 0°, and phase angle ( $g$ ) = 30°, at a spatial sampling of 256 px/degree. This basemap was useful for identifying the albedo features and ejecta.



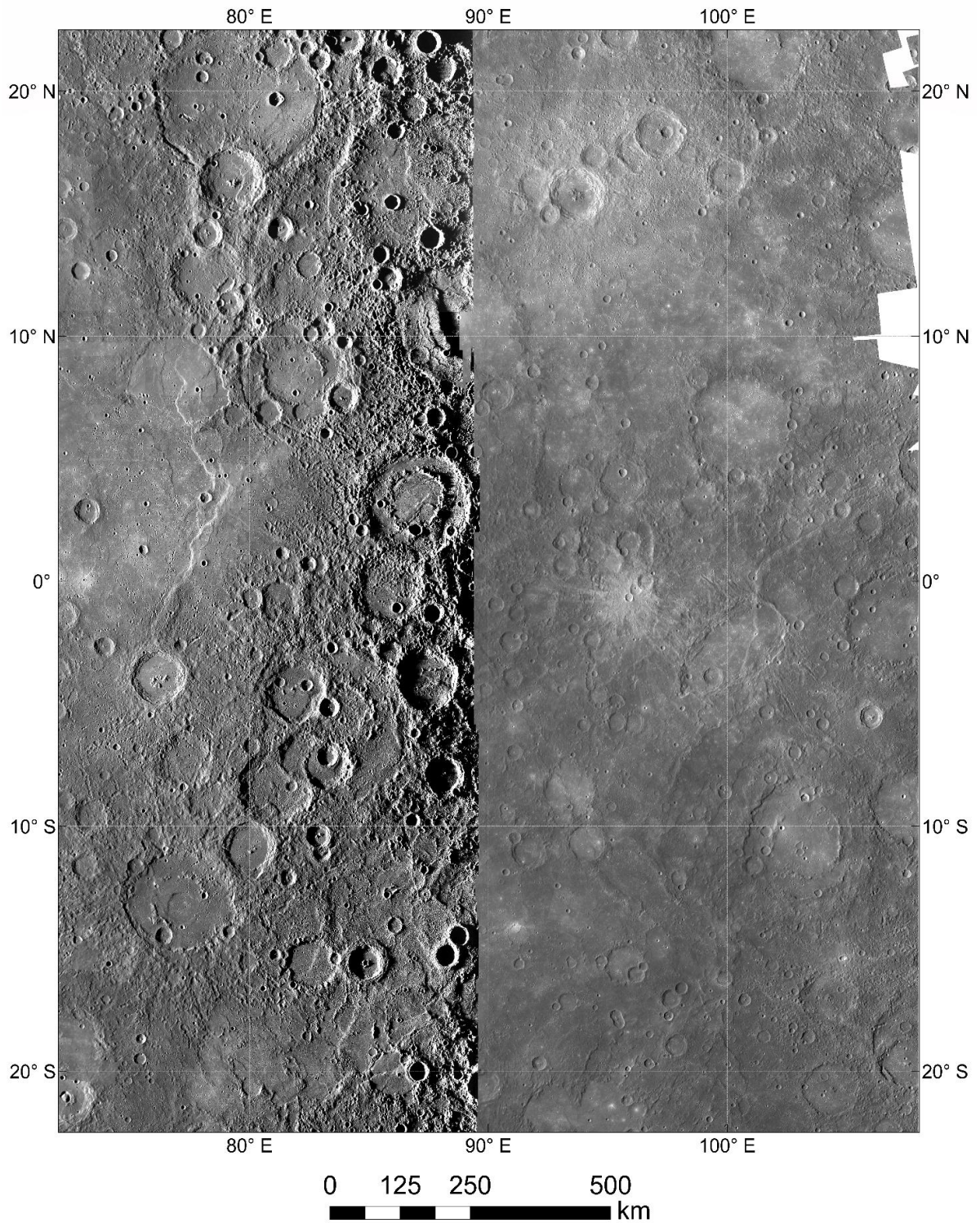
MDIS\_BDR\_V2 (166m/px)



**Figure A.4.** Basemap Reduced Data Record (BDR) over 166 m/px image resolution. This basemap has been released through mosaic monochrome images of NAC and WAC. This monochrome map of reflectance was chosen as the reference basemap for the geologic mapping since even it displays different reflectance.

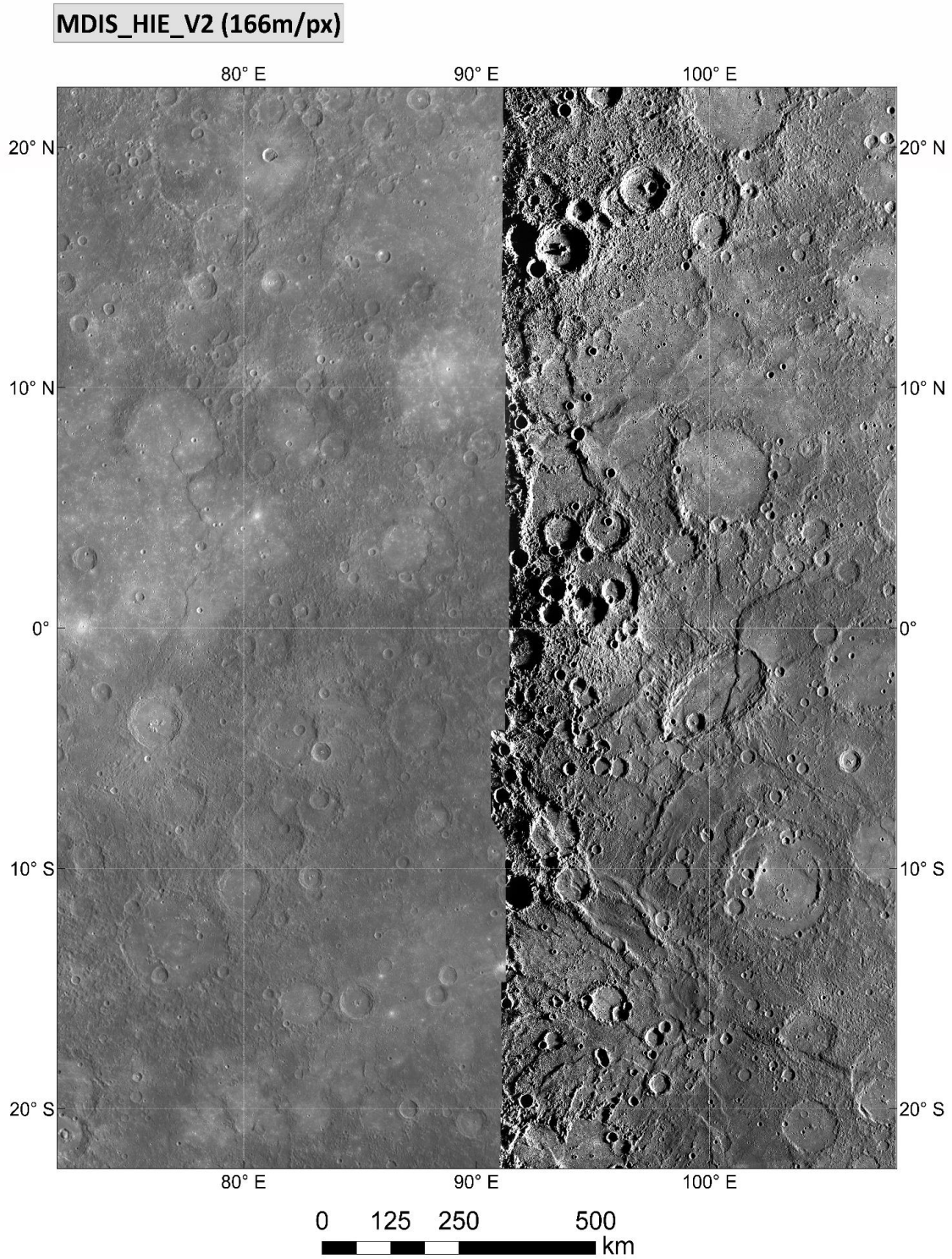


MDIS\_HIW\_V2 (166m/px)



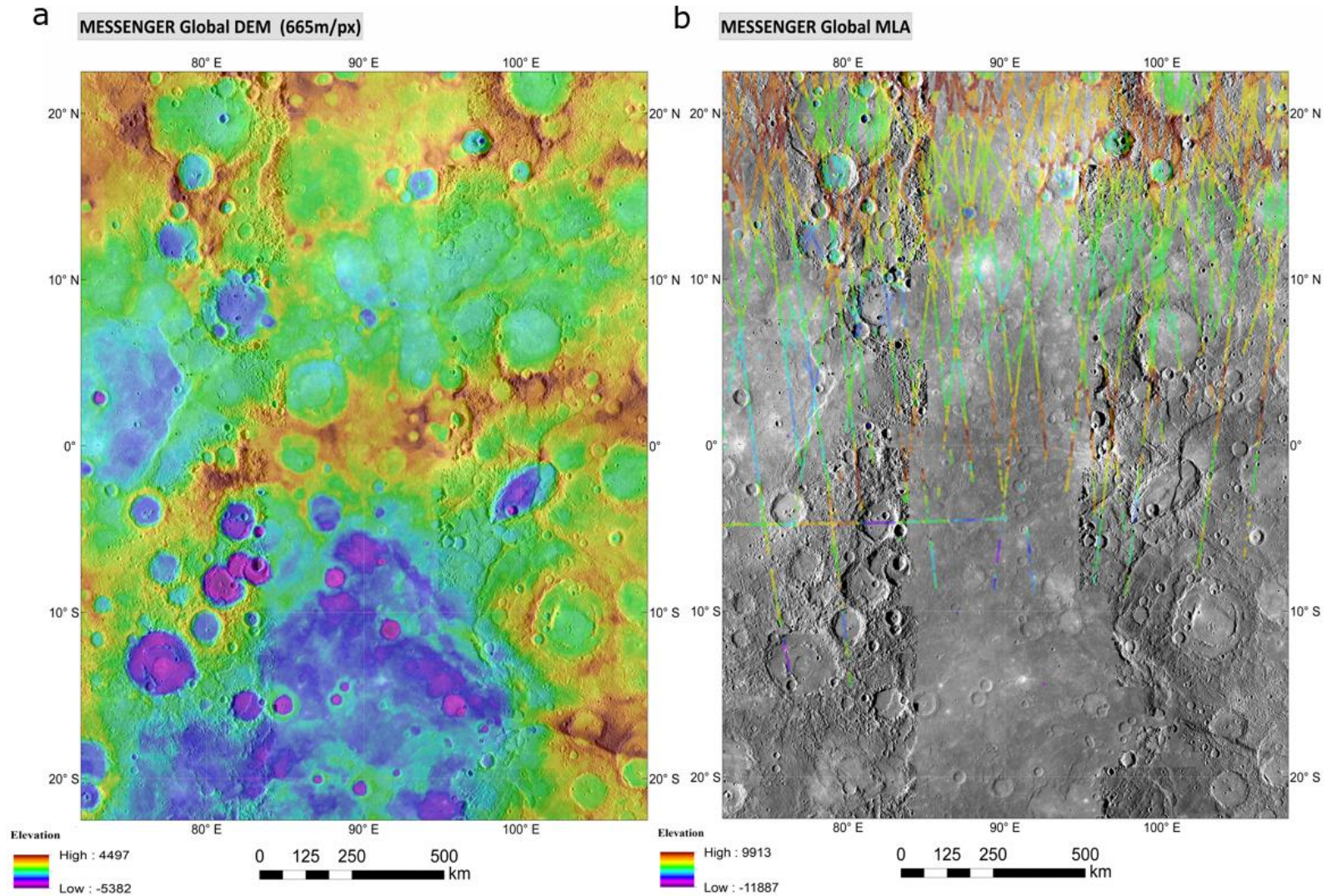
**Figure A.5.** High-incidence angle Basemap, illuminated from the west, with a 166m/px of resolution. This map is realised by mosaicked images from NAC and WAC 750 nm. This basemap presents some gaps in the NE, at  $\sim 10^\circ\text{N}$  and  $\sim 20^\circ\text{N}$  longitude. HIW data set favours asymmetric topography more steeply sloped to that west than to the east, and it is companioned by the HIE basemap.





**Figure A.6.** High solar incidence angle composed basemap illuminated from the east reduced data records for the MDIS camera system on MESSENGER. The image presented 166m/px of resolution and it was released after a NAC or WAC mosaicked images at 750 nm. This basemap is a complementary in highlights low-relief topography that is less evident.





**Figure A.7.** Topographic data used for the mapping. (a) Mercury MESSENGER Global DEM, second version produced through 1-sigma filter applied to the point cloud when processing each output pixel, with a resolution of 665m/px, displayed as colour-keyed elevation overlain by hill shaded relief. Image was released by a mosaic from the NAC and multispectral WAC camera. (b) Topographic footprints on the left bisector of Eminescu (H-09) quadrangle by MLA. The data sets are produced by the MLA Science Team at NASA in Reduced Data Records and Gridded Data Records. The MLA coverage was not covering a lot from the area, only a very limited area of  $\sim 10^\circ$  to  $20^\circ$ .



# References

- Adams, J.B., Gillespie, A.R., Jackson, M.P.A., Montgomery, D.R., Dooley, T.P., Combe, J.-P., Schreiber, B.C., 2009. Salt tectonics and collapse of Hebes Chasma, Valles Marineris, Mars. *Geology*. 37(8), 691-694. doi: <https://doi.org/10.1130/G30024A.1>
- An, L.-J., Sammis, C.G., 1996. Development of strike-slip faults: shear experiments in granular materials and clay using a new technique. *J. Struct. Geol.* 18 (8), 1061-1077. doi: [https://doi.org/10.1016/0191-8141\(96\)00012-0](https://doi.org/10.1016/0191-8141(96)00012-0)
- Anderson, E. M., 1951. The dynamics of faulting and dyke formation with application to Britain. In O. Boyd (Ed.), *The journal of geology*. Edinburgh: The University of Chicago Press. <https://doi.org/10.1086/625135>
- Anderson, R.C., Dohm, J.M., Golombek, M.P., Albert, F.C., Franklin, B.J., Tanaka, K.L., Lias, J., Peer, B., 2001. Primary centers and secondary concentrations of tectonic activity through time in the western hemisphere of Mars. *J. Geophys. Res.*, 106 (E9), 20563-20585. <https://doi.org/10.1029/2000JE001278>
- Anderson, R.C., Dohm, J.M., Haldemann, A.F.C., Hare, T.M & Baker, V.R., 2004. Tectonic histories between Alba Patera and Syria Planum, Mars. *Icarus*. 171 (1), 31-38. doi: <http://dx.doi.org/10.1016/j.icarus.2004.04.018>
- Andrews-Hanna, J.C., 2012. The formation of Valles Marineris:1. Tectonic architecture and the relative roles of extension and subsidence. *J. Geophys. Res. Planets*. 117 (E3). doi: <https://doi.org/10.1029/2011JE003953>
- Andrews-Hanna, J.C., 2012. The formation of Valles Marineris:3. Trough formation through super-isostasy, stress, sedimentation, and subsidence. *J. Geophys. Res. Planets*. 117 (E6). doi: <https://doi.org/10.1029/2012JE004059>
- Andrews-Hanna, J.C., Zuber, M.T & Hauck, S.A., 2008. Strike-slip faults on Mars: Observations and implications for global tectonics and geodynamics. *J. Geophys. Res. Planets*. 113 (E8). doi: <https://doi.org/doi:10.1029/2007JE002980>
- Andrews-Hanna, J.C & Phillips, R.J., 2005. Hydrological modeling of the Martian crust with application to the pressurization of aquifers. *J. Geophys. Res. Planets*. 110 (E1). doi: <https://doi.org/10.1029/2004JE002330>
- Angelier, J., 1979. Determination of the mean principal directions of stresses for a given fault population. *Tectonophysics*. 56 (3-4), T17-T26. doi: [https://doi.org/10.1016/0040-1951\(79\)90081-7](https://doi.org/10.1016/0040-1951(79)90081-7)
- Angelier, J., Bergerat, F., Dauteuil, O & Villedon, T., 1997. Effective tension-shear relationships in extensional fissure swarms, axial rift zone of northeastern Iceland. *J. Geophys. Res.* 19 (5), 673-685. doi: [https://doi.org/10.1016/S0191-8141\(96\)00106-X](https://doi.org/10.1016/S0191-8141(96)00106-X)
- Atmaoui, N., Kukowski, N., Stöckhert, B., König, D., 2006. Initiation and development of pull-apart basins with Riedel shear mechanism: insights from scaled clay experiments. *Int. J. Earth. Sci. (Geol. Rundsch)*, 95 (2), 225-238. doi: <https://doi.org/10.1007/s00531-005-0030-1>
- Aydin, A & Schultz, R.A., 1990. Effect of mechanical interaction on the development of strike-slip faults with echelon patterns. *J. Struct. Geol.* 12 (1), 123-129. doi: [https://doi.org/10.1016/0191-8141\(90\)90053-2](https://doi.org/10.1016/0191-8141(90)90053-2)
- Baioni, D., 2018. Karst Landforms as markers of recent climate change on Mars: An example from a late amazonian epoch evaporate-karst within a trough in western Noctis Labyrinthus. *Recent and Current Landscape Evolution of the Red Planet*. In: *Dynamic Mars*. Elsevier, 411-429. doi: <https://doi.org/10.1016/B978-0-12-813018-6.00014-5>
- Baioni, D., Tramontana, M & Hajna, N. Z., 2017. Karst landforms Within Noctis Labyrinthus, Mars. *Acta Carsologica*. 46 (1), 73-82. doi: <https://doi.org/10.3986/ac.v46i1.4704>
- Baker, D.M.H., Head, J.W., Schon, S.C., Ernst, C.M., Prockter, L.M., Murchie, S.L., Denevi, B.W., Solomon, S.C., Strom, R.G., 2011. The transition from complex crater to peak-ring basin on Mercury: New observations from MESSENGER flyby data and constraints on basin formation models. *Planet. Space Sci.* 59 (15), 1932-1948. doi: <https://doi.org/10.1016/j.pss.2011.05.010>
- Baker, V., Maruyama, S., Dohm, J., 2007. Tharsis Superplume and the Geological Evolution of Early Mars. In: Yuen, D.A., Maruyama, S., Karato, S.I., Windley, B.F. (eds) *Superplumes: Beyond Plate Tectonics*. Springer, Dordrecht. doi: [https://doi.org/10.1007/978-1-4020-5750-2\\_16](https://doi.org/10.1007/978-1-4020-5750-2_16)
- Banks, M. E., Xiao, Z., Braden, S. E., Barlow, N. G., Chapman, C. R., Fassett, C. I., & Marchi, S. S., 2017. Revised constraints on absolute age limits for Mercury's Kuiperian and Mansurian stratigraphic systems. *J. Geophys. Res. Planets*. 122 (5), 1010-1020. doi: <https://doi.org/10.1002/2016JE005254>
- Baptista, A. R., Mangold, N., Ansan, V., Baratoux, D., Lognonné, P., Alves, E. I., Williams, D. A., Bleacher, J. E., Masson, P., & Neukum, G., 2008. A swarm of small shield volcanoes on Syria Planum, Mars. *J. Geophys. Res.* 113 (E9). doi: <https://doi.org/10.1029/2007JE002945>
- Basilevsky, A.T., Neukum, G., Ivanov, B.A. et al., 2005. Morphology and geological structure of the western part of the Olympus Mons volcano on Mars from the analysis of the Mars Express HRSC imagery. *Sol Syst Res.* 39, 85-101. doi: <https://doi.org/10.1007/s11208-005-0025-2>
- Bechis, F., Giambiagi, L., García, V., Lanés, S., Cristallini, E., Tunik, M., 2010. Kinematic analysis of a transtensional fault system: The Atuel depocenter of the Neuquén basin, southern Central Andes, Argentina. *J. Struct. Geol.* 32 (7), 886-899. doi: <https://doi.org/doi:10.1016/j.jsg.2010.03.009>
- Bernhardt, H., Williams, D.A., 2021. Geology and history of the Malea Planum region: A new view of Mars' oldest large volcanic province. *Icarus*. 366, 114-518. doi: <https://doi.org/10.1016/j.icarus.2021.114518>
- Beuthe, M., Le Maistre, S., Rosenblatt, P., Pätzold, M., Dehant, V., 2012. Density and lithospheric thickness of the Tharsis Province from MEX MaRS and MRO gravity data. *J. Geophys. Res. Planets*, 117 (E4). doi: <https://doi.org/10.1029/2011JE003976>

- Bibring, J.-P., Langevin, Y., Mustard, F.J., Poulet, F., Arvidson, R., Gendrin, A., Gondet, B., Mangold, N., Pinet, P., Forget, F. et al., 2006. Global Mineralogical and Aqueous Mars History Derived from OMEGA/Mars Express Data. *Science*. 312 (5772), 400-404. doi: <https://doi.org/10.1126/science.1122659>
- Birnie, C., Fueten, F., Stesky, R., Hauber, E., 2012. Underlying structural control of small-scale faults and fractures in West Candor Chasma, Mars. *J. Geophys. Res. Planets*. 117 (E11). doi: <https://doi.org/10.1029/2012JE004144>
- Bistacchi, N., Massironi, M., Baggio, P., 2004. Large-scale fault kinematic analysis in Noctis Labyrinthus (Mars). *Planet. Space Sci.* 52 (1-3), 215-222. doi: <https://doi.org/10.1016/j.pss.2003.08.015>
- Bleacher, J.E., Greeley, R., Williams, D.A., Werner, S.C., Hauber, E., Neukum, G., 2007. Olympus Mons, Mars: Inferred changes in late Amazonian aged effusive activity from lava flow mapping of Mars Express High Resolution Stereo Camera data. *J. Geophys. Res.* 112 (E4). doi: <https://doi.org/10.1029/2006JE002826>
- Blewett, D.T., Chabot, N.L., Denevi, B.W., Ernst, C.M., Head, J.W., Izenberg, N.R., Murchie, S.L., Solomon, S.C., Nittler, L.R., McCoy, T.J., Xiao, Z., Baker, D.M., Fassett, C.I., Braden, S.E., Oberst, J., Scholten, F., Preusker, F., Hurwitz, D.M., 2011. Hollows on Mercury: MESSENGER evidence for geologically recent volatile-related activity. *Science*. 333 (6051), 1856-1859. doi: <https://doi.org/10.1126/science.1211681>
- Bramble, M.S., Mustard, J.F., Salvatore, M.R., 2017. The geological history of Northeast Syrtis Major, Mars. *Icarus*. 293, 66-93. doi: <http://dx.doi.org/10.1016/j.icarus.2017.03.030>
- Brent, M.R. & Cartwright, T.A., 1996. Distributional regularity and phonotactic constraints are useful for segmentation. *Cognition*. 61 (1-2), 93-125. doi: [https://doi.org/10.1016/S0010-0277\(96\)00719-6](https://doi.org/10.1016/S0010-0277(96)00719-6)
- Brož, B.P., 2010. Plains volcanism in Tharsis region on Mars: Ages and Rheology of Eruption. Master thesis. Charles University in Prague, Faculty of Science, Institute of Petrology and Structural Geology. Repository. [https://www.ig.cas.cz/wp-content/uploads/2018/01/Broz\\_Petr\\_master\\_thesis.pdf](https://www.ig.cas.cz/wp-content/uploads/2018/01/Broz_Petr_master_thesis.pdf)
- Brustel, C., Flahaut, J., Hauber, E., Fueten, F., Quantin, C., Stesky, R., Davies, G.R., 2017. Valles Marineris tectonic and volcanic history inferred from dikes in eastern Coprates Chasma. *J. Geophys. Res. Planets*, 122 (6), 1353-1371. doi: <https://doi.org/10.1002/2016JE005231>
- Bürgmann, R., Pollard, D.D., Martel, S.J., 1994. Slip distributions on faults: effects of stress gradients, inelastic deformation, heterogeneous host-rock stiffness, and fault interaction. *J. Struct. Geol.* 16 (12), 1675-1690. doi: [https://doi.org/10.1016/0191-8141\(94\)90134-1](https://doi.org/10.1016/0191-8141(94)90134-1)
- Byrne, P., Klimczak, C., & Şengör, A., 2018. The Tectonic Character of Mercury. In S. Solomon, L. Nittler, & B. Anderson (Eds.). *Mercury: The View after MESSENGER*. Cambridge Planetary Science, 249-286. Cambridge: Cambridge University Press. doi: <https://doi.org/10.1017/9781316650684.011>
- Byrne, P.K., Klimczak, C., Celâl Şengör, A.M., Solomon, S.C., Watters, T.R. & Hauck, S.A., 2014. Mercury's global contraction much greater than earlier estimates. *Nat. Geosci.* 7 (4), 301-307. doi: <https://doi.org/10.1038/ngeo2097>
- Carr, M.H., 1973. Volcanism on Mars. *J. Geophys. Res.* 78 (20), 4049-4062. doi: <https://doi.org/10.1029/JB078i020p04049>
- Carr, M.H., 1974. Tectonism and volcanism of the Tharsis region of Mars. *J. Geophys. Res.* 79 (26), 3943-3949. doi: <https://doi.org/10.1029/JB079i026p03943>
- Carr, M.H., Head, J.W., 2010. Geologic history of Mars. *Earth & Planet. Sci. Lett.* 294 (3-4), 185-203. doi: <https://doi.org/10.1016/j.epsl.2009.06.042>
- Carr, M.H., Saunders, R.S., Strom, R.G., Wilhelms, D.E., 1984. *The Geology of the Terrestrial Planets*. NASA Special Publications, NASA SP-469. Bibcode: 1984NASSP.469.....C
- Cartwright, J. A., Trudgill, B. D., Mansfield, C. S., 1995. Fault growth by segment linkage: An explanation for scatter in maximum displacement and trace length data from the Canyonlands Grabens of SE Utah. *J. Struct. Geol.* 17 (9), 1319-1326. doi: [https://doi.org/10.1016/0191-8141\(95\)00033-A](https://doi.org/10.1016/0191-8141(95)00033-A)
- Chen, Z. & Jin, Z.-H., 2006. Magma-driven subcritical crack growth and implications for dike initiation from a magma chamber. *Geophys. Res. Lett.* 33 (19), L19307. doi: <https://doi.org/10.1029/2006GL026979>
- Childs, C., Manzocchi, T., Walsh, J.J., Bonson, C.G., Nicol, A., Schöpfer, M.P.J., 2009. A geometric model of fault zone and fault rock thickness variations. *J. Struct. Geol.* 31 (2), 117-127. doi: <https://doi.org/10.1016/j.jsg.2008.08.009>
- Childs, C., Watterson, J., Walsh, J.J., 1995. Fault overlap zones within developing normal fault systems. *Geol. Soc. Spec. Publ.* 152 (3), 535-549. doi: <https://doi.org/10.1144/gsjgs.152.3.0535>
- Chuang, F.C., Crown, D.A., Berman, D.C., 2019. Geology of the northeastern flank of Apollinaris Mons, Mars: Constraints on the erosional history from morphology, topography, and crater populations. *Icarus*. 333, 385-403. doi: <https://doi.org/10.1016/j.icarus.2019.06.008>
- Citrona, R.L., Manga, M., Tan, E., 2018. A hybrid origin of the Martian crustal dichotomy: Degree-1 convection antipodal to a giant impact. *Earth & Planet. Sci. Lett.* 491, 58-66. doi: <https://doi.org/10.1016/j.epsl.2018.03.031>
- Clark, R.M. & Cox, S.J.D., 1996. A modern regression approach to determining fault displacement-length scaling relationships. *J. Struct. Geol.* 18 (2-3), 147-152. doi: [http://dx.doi.org/10.1016/S0191-8141\(96\)80040-X](http://dx.doi.org/10.1016/S0191-8141(96)80040-X)
- Collanega, L., Corti, G., Breda, A., Massironi, M. & Keir, D., 2020. 3D Extension at Plate Boundaries Accommodated by Interacting Fault Systems. *Sci. Rep.* 10 (1), 8669. doi: <https://doi.org/10.1038/s41598-020-65599-5>
- Cooke, M.L., 1997. Fracture localization along faults with spatially varying friction. *J. Geophys. Res.* 102 (B10), 22425-22434. doi: <https://doi.org/10.1029/97JB01829>

- Cowie, P.A & Scholz, C.H., 1992. Displacement-length scaling relationship for faults: data synthesis and discussion. *J. Struct. Geol.*14 (10), 1149-1156. doi: [https://doi.org/10.1016/0191-8141\(92\)90066-6](https://doi.org/10.1016/0191-8141(92)90066-6)
- Cowie, P.A., Malinverno, A., Ryan, W.B.F., Edwards, M.H., 1994. Quantitative fault studies on the East Pacific Rise: A comparison of sonar imaging techniques. *J. Geophys. Res.: Solid Earth.* 99 (B8), 15205-15218. doi: <https://doi.org/10.1029/94JB00041>
- Cowie, P.A., Scholz, C.H., 1992. Physical explanation for the displacement-length relationship of faults using a post-yield fracture mechanics model. *J. Struct. Geol.*14 (10), 1149-1156. doi: [https://doi.org/10.1016/0191-8141\(92\)90065-5](https://doi.org/10.1016/0191-8141(92)90065-5)
- Cowie, P.A., Shipton, Z.K., 1998. Fault tip displacement gradients and process zone dimension. *J. Struct. Geol.* 20 (8), 983-997. doi: [https://doi.org/10.1016/S0191-8141\(98\)00029-7](https://doi.org/10.1016/S0191-8141(98)00029-7)
- Cowie, P.A., Sornette, D., Vanneste, C., 1995. Multifractal scaling properties of a growing fault population. *Geophys. J. Int.* 122 (2), 457-469. doi: <https://doi.org/10.1111/j.1365-246X.1995.tb07007.x>
- Cowie, P.A., Vanneste, C., Sornette, D., 1993. Statistical physics model for the spatiotemporal evolution of faults. *J. Geophys. Res.: Solid Earth.*98 (B12), 21809-21821. doi: <https://doi.org/10.1029/93JB02223>
- Cowie, P.A., Scholz, C.H., 1992. Growth of Faults by Accumulation of Seismic Slip. *J. Geophys. Res.: Solid Earth.*97 (B7), 11085-11095. doi: <https://doi.org/10.1029/92JB00586>
- Cox, S.J.D & Scholz, C.H., 1988. On the formation and growth of faults: an experimental study, *J. Struct. Geol.*10 (4), 413-430. doi: [https://doi.org/10.1016/0191-8141\(88\)90019-3](https://doi.org/10.1016/0191-8141(88)90019-3)
- Cox, S.J.D., & Scholz, C.H., 1988. Rupture initiation in shear fracture of rocks: an experimental study. *J. Geophys. Res.: Solid Earth.* 93(B4), 3307-3320. doi: <https://doi.org/10.1029/JB093iB04p03307>
- Crane, K. T., & Klimczak, C., 2017. Timing and rate of global contraction on Mercury. *Geophys. Res. Lett.*44 (7), 3082-3089, doi: <https://doi.org/10.1002/2017GL072711>
- Cremonese, G., Capaccioni, F., Capria, M.T. et al., 2020. SIMBIO-SYS: Scientific Cameras and Spectrometer for the BepiColombo Mission. *Space.Sci.Rev.*216 (5). 75. doi: <https://doi.org/10.1007/s11214-020-00704-8>
- Cremonese, G., Capria, M.T., Achilli, V., Angrilli, F et al., 2004. MEMORIS: a wide angle camera for the BepiColombo mission. *Adv. Space Res.*33 (12), 2182-2188. doi: [https://doi.org/10.1016/S0273-1177\(03\)00448-4](https://doi.org/10.1016/S0273-1177(03)00448-4)
- Crosta, G. B., Frattini, P., Valbuzzi, E., & De Blasio, F. V., 2018. Introducing a new inventory of large Martian landslides. *Earth & Space Sci.*5 (4), 89-119. doi: <https://doi.org/10.1002/2017EA000324>
- Davis, K., Burbank, D.W., Fisher, D., Wallace, S., Nobes, D., 2005. Thrust-fault growth and segment linkage in the active Ostler fault zone, New Zealand. *J. Geophys. Res.*27 (8), 1528-1546. doi: <https://doi.org/10.1016/j.jsg.2005.04.011>
- Davis, P. A., Tanaka, K. L., Golombek, M. P., 1995. Topography of closed depressions, scarps, and graben in the North Tharsis region of Mars: Implications for shallow crustal discontinuities and graben formation. *Icarus.*114 (2), 403-422. doi: <https://doi.org/10.1006/icar.1995.1071>
- Davis, P.A & Golombek, M.P., 1990. Discontinuities in the shallow Martian crust at Lunae, Syria, and Sinai Plana. *J. Geophys. Res.: Solid Earth.* 95 (B9), 14231-14248. doi: <https://doi.org/10.1029/JB095iB09p14231>
- Dawers, N.H., Anders, M.H., Scholz, C.H., 1993. Growth of normal faults: displacement-length scaling. *Geology.*21 (12), 1107-1110. doi: [https://doi.org/10.1130/0091-7613\(1993\)021<1107:GONFDL>2.3.CO;2](https://doi.org/10.1130/0091-7613(1993)021<1107:GONFDL>2.3.CO;2)
- De Blasio, F.V., 2011. Landslides in Valles Marineris (Mars): A possible role of basal lubrication by sub-surface ice. *Planet. Space Sci.*59 (13), 1384-1392. doi: <https://doi.org/10.1016/j.pss.2011.04.015>
- De Joussineau, G., Mutlu, O., Aydin, A., Pollard, D.D., 2007. Characterization of strike-slip fault-splay relationships in sandstone. *J. Struct. Geol.* 29 (11), 1831-1842. doi: <https://doi.org/10.1016/j.jsg.2007.08.006>
- Denevi, B. W., Ernst, C. M., Meyer, H. M., Robinson, M. S., Murchie, S. L., Whitten, J. L., et al., 2013. The distribution and origin of smooth plains on Mercury. *J. Geophys. Res. Planets.*118, 891-907. doi: <https://doi.org/10.1002/jgre.20075>
- Dohm, J. M., and K. L. Tanaka., 1999. Geology of the Thaumasia region, Mars: plateau development, valley origins, and magmatic evolution. *Planet. Space Sci.* 47 (3-4), 411-431. doi: [https://doi.org/10.1016/S0032-0633\(98\)00141-X](https://doi.org/10.1016/S0032-0633(98)00141-X)
- Dohm, J.M., Baker, V.R., Maruyama, S., Anderson, R.C., 2007. Traits and evolution of the Tharsis superplume, Mars. In: Yuen, D.A., Maruyama, S., Karato, S.-I., Windley, B.F. (Eds.), *Superplumes: Beyond Plate Tectonics*. Springer, 523-537. doi: [http://dx.doi.org/10.1007/978-1-4020-5750-2\\_17](http://dx.doi.org/10.1007/978-1-4020-5750-2_17)
- Dohm, J.M., Williams, J.-P., Anderson, R.C., Ruiz, J., McGuire, P.C., Komatsu, G., Davila, A.F., Ferris, J.C., Schulze-Makuch, D., Baker, V.R., Boynton, W.V., Fairen, A.G., Hare, T.M., Miyamoto, H., Tanaka, K.L., Wheelock, S.J., 2009. New evidence for a magmatic influence on the origin of Valles Marineris, Mars. *J. Volcanol. Geotherm. Res.*185 (1-2), 12-27. doi: <http://dx.doi.org/10.1016/j.jvolgeores.2008.11.029>
- Du, Y & Aydin, A., 1995. Shear fracture patterns and connectivity at geometric complexities along strike-slip faults. *J. Geophys. Res.*100 (B9), 18093-18102. doi: <https://doi.org/10.1029/95JB01574>
- Dzurisin, D., 1978. The tectonic and volcanic history of Mercury as inferred from studies of scarps, ridges, troughs and other lineaments. *J. Geophys. Res.*83 (B10), 4883-4906. doi: <https://doi.org/10.1029/JB083iB10p04883>
- Elliott, D., 1976. A Discussion on natural strain and geological structure - The energy balance and deformation mechanisms of thrust sheets. *Phil. Trans. Roy. Soc. London.* 283 (1312), 289-312. doi: <https://doi.org/10.1098/rsta.1976.0086>

- Ernst, C.M., Murchie, S.L., Barnouin, O.S., Robinson, M.S., Denevi, B.W., Blewett, D.T., Head, J.W., Izenberg, N.R., Solomon, S.C., Roberts, J.H., 2010. Exposure of spectrally distinct material by impact craters on Mercury: Implications for global stratigraphy. *Icarus*. 209 (1), 210-223. doi: <https://doi.org/10.1016/j.icarus.2010.05.022>
- Ernst, R. E., Grosfils, E. B., Mège, D., 2001. Giant Dike Swarms: Earth, Venus, and Mars. *Annu. Rev. Earth Planet. Sci.* 29, 489-534. doi: <https://doi.org/10.1146/annurev.earth.29.1.489>
- Fassett, C. I., Head, J.W., Baker, D.M.H., Zuber, M.T., Smith, D.E., Neumann, G.A., Solomon, S.C., Klimczak, C., Strom, R.G., Chapman, C.R., Prockter, L.M., Phillips, R.J., Oberst, J., Preusker, F., 2012. Large impact basins on Mercury: Global distribution, characteristics, and modification history from MESSENGER orbital data. *J. Geophys. Res.* 117 (E12), E00L08. doi: <http://dx.doi.org/10.1029/2012JE004154>
- Fassett, C.I., Kadish, S.J., Head, J.W., Solomon, S.C., Strom, R.G., 2011. The global population of large craters on Mercury and comparison with the Moon. *Geophys. Res. Lett.* 38 (10), L10202. doi: <https://doi.org/10.1029/2011GL047294>
- Fegan, E.R., Rothery, D.A., Marchi, S., Massironi, M., Conway, S.J., Anand, M., 2017. Late movement of basin-edge lobate scarps on Mercury. *Icarus*. 288, 226-234. doi: <http://dx.doi.org/10.1016/j.icarus.2017.01.005>
- Ferrill, D.A., Wyrick, D.Y., Morris, A.P., Sims, D.W., Franklin, N.M., 2004. Dilational fault slip and pit chain formation on Mars. *Geol. Soc. Am. Bull.* 114 (10). doi: [http://dx.doi.org/10.1130/1052-5173\(2004\)014%3C4:DFSAPC%3E2.0.CO;2](http://dx.doi.org/10.1130/1052-5173(2004)014%3C4:DFSAPC%3E2.0.CO;2)
- Fialko, Y. A., & Rubin, A.M., 1999. Thermal and mechanical aspects of magma emplacement in giant dike swarms. *J. Geophys. Res.* 104 (B10), 23033-23049. doi: <https://doi.org/10.1029/1999JB900213>
- Flahaut, J., Mustard, J.F., Quantin, C., Clenet, H., Allemand, P., Thomas, P., 2011. Dikes of distinct composition intruded into Noachian-aged crust exposed in the walls of Valles Marineris. *Geophys. Res. Lett.* 38(15), 1-7. doi: <http://dx.doi.org/10.1029/2011GL048109>
- Flahaut, J., Quantin, C., Allemand, P., Thomas, P., & Le Deit, L., 2010. Identification, distribution and possible origins of sulfates in Capri Chasma (Mars), inferred from CRISM data. *J. Geophys. Res.* 115 (E11), E11007. doi: <https://doi.org/10.1029/2009JE003566>
- Forsythe, R.D. & Zimbelman, R., 1988. Is the Gordii Dorsum escarpment on Mars an exhumed transcurrent fault? *Nature*. 336, 143-146. doi: <https://doi.org/10.1038/336143a0>
- Fossen, H & Gabrielsen, R.H., 1996. Experimental modeling of extensional fault systems by use of plaster. *J. Struct. Geol.* 18 (5), 673-687. doi: [https://doi.org/10.1016/S0191-8141\(96\)80032-0](https://doi.org/10.1016/S0191-8141(96)80032-0)
- Fossen, H & Hesthammer, J., 1997. Geometric analysis and scaling relations of deformation bands in porous sandstone. *J. Struct. Geol.* 19 (12), 1479-1493. doi: [https://doi.org/10.1016/S0191-8141\(97\)00075-8](https://doi.org/10.1016/S0191-8141(97)00075-8)
- Frey, H., 1979. Martian canyons and African rifts: Structural comparisons and implications. *Icarus*. 37, 142-155. doi: [https://doi.org/10.1016/0019-1035\(79\)90122-2](https://doi.org/10.1016/0019-1035(79)90122-2)
- Frey, H., Sakimoto, S.E.H., Roark, J.H., 1999. Discovery of a 450 km diameter, multi-ring basin on Mars through analysis of MOLA topographic data. *Geophys. Res. Lett.* 26 (12), 1657-1660. doi: <https://doi.org/10.1029/1999GL900357>
- Fu, X.-F., Lan, X., Meng, L.-D., Wang, H.-X., Liu, Z.-B., Guo, Z.-Q., Chen, Z.-H., 2016. Characteristics of fault zones and their control on remaining oil distribution at the fault edge: a case study from the northern Xingshugang Anticline in the Daqing Oilfield, China. *Pet. Sci.* 13, 418-433. doi: <https://doi.org/10.1007/s12182-016-0116-3>
- Galluzzi, V., Guzzetta, L., Ferranti, F., Di Achille, G., Rothery, D. A., & Palumbo, P., 2016. Geology of the Victoria quadrangle (H02), Mercury. *J. Maps*. 12, 227-238. doi: <https://doi.org/10.1080/17445647.2016.1193777>
- Galluzzi, V., 2015. Structural analysis of the Victoria quadrangle (H2) of Mercury based on NASA MESSENGER data. Ph.D thesis. University of Napoli. doi: <https://doi.org/10.6092/UNINA/FEDOA/10434>
- Galluzzi, V., 2019. Multi-mapper projects: Collaborative Mercury Mapping. In H. Hargitai (Ed.), *Planetary cartography and GIS*. 207–218. doi: [https://doi.org/10.1007/978-3-319-62849-3\\_9](https://doi.org/10.1007/978-3-319-62849-3_9)
- Galluzzi, V., Di Achille, G., Ferranti, L., Popa, C., Palumbo, P., 2014. Faulted craters as indicators for thrust motions on Mercury. *Geol. Soc. Spec. Publ.* 401(1), 313-325. doi: <http://dx.doi.org/10.1144/SP401.17>
- Galluzzi, V., Ferranti, L., Massironi, M., Giacomini, L., Guzzetta, L., & Palumbo, P., 2019. Structural analysis of the Victoria quadrangle fault systems on Mercury: Timing, geometries, kinematics, and relationship with the high-Mg region. *J. Geophys. Res. Planets*. 124 (10), 2543-2562. doi: <https://doi.org/10.1029/2019JE005953>
- Giacomini, L., 2010. Geological mapping and analysis of Daedalia Planum lava field (Mars). Ph.D thesis. University of Padova. <http://hdl.handle.net/11577/3422244>
- Giacomini, L., Massironi, M., Galluzzi, V., Ferrari, S., Palumbo, P., 2020. Dating long thrust systems on Mercury: New clues on the thermal evolution of the planet. *Geosci. Front.* 11 (3), 855-870. doi: <https://doi.org/10.1016/j.gsf.2019.09.005>
- Golombek, M.P., Phillips, R.J., 2010. Mars tectonics. *Planetary Tectonics* 11, 183e232. Harder, H., Christensen, U.R., 1996. A one-plume model of Martian mantle convection. *Nature* 380 (6574), 507. doi: <https://doi.org/10.1038/380507a0>
- Grady, M.M., 2020. Exploring Mars with Returned Samples. *Space.Sci.Rev.* 216 (51). doi: <https://doi.org/10.1007/s11214-020-00676-9>
- Greeley, R & Spudis, P.D., 1981. Volcanism on mars. *Rev. Geophys.* 19 (1), 13-41. doi: <https://doi.org/10.1029/RG019i001p00013>



- Greeley, R., Schneid, B. D., 1991. Magma generation on Mars: Amounts, rates, and comparisons with Earth, moon, and Venus. *Science*, 254 (5034), 996-998. doi: <https://doi.org/10.1126/science.254.5034.996>
- Gudmundsson, A., 1990. Emplacement of dikes, sills and crustal magma chambers at divergent plate boundaries. *Tectonophysics*, 176 (3-4), 257-275. doi: [https://doi.org/10.1016/0040-1951\(90\)90073-H](https://doi.org/10.1016/0040-1951(90)90073-H)
- Gudmundsson, A., 1992. Formation and growth of normal faults at the divergent plate boundary in Iceland. *Terra Nova*, 4 (4), 464-471. doi: <https://doi.org/10.1111/j.1365-3121.1992.tb00582.x>
- Gudmundsson, A., 2000. Fracture dimensions, displacements, and fluid transport. *J. Struct. Geol.* 22 (9), 1221-1231. doi: [http://dx.doi.org/doi:10.1016/S0191-8141\(00\)00052-3](http://dx.doi.org/doi:10.1016/S0191-8141(00)00052-3)
- Gudmundsson, A., 2006. How local stresses control magma-chamber ruptures, dyke injections, and eruptions in composite volcanoes. *Earth.Sci. Rev.* 79 (1-2), 1-31. doi: <https://doi.org/10.1016/j.earscirev.2006.06.006>
- Hardy, S., 2021. Discrete Element Modelling of Pit Crater Formation on Mars. *Geosci.* 11, 268. doi: <https://doi.org/10.3390/geosciences11070268>
- Harrison, K.P. & Grimm, R.E., 2004. Tharsis recharge: a source of groundwater for Martian outflow channels. *Geophys. Res. Lett.* 31 (14), L14703. doi: <https://doi.org/10.1029/2004GL020502>
- Hartmann, W.K., Neukum, G., 2001. Cratering chronology and evolution of Mars. *Space.Sci.Rev.* 96, 165-194. doi: <https://doi.org/10.1023/A:1011945222010>
- Hartmann, W.K., 1999. Martian cratering VI: Crater count isochrons and evidence for recent volcanism from Mars Global Surveyor. *Meteorit. Planet. Sci.* 34 (2), 167-177. doi: <https://doi.org/10.1111/j.1945-5100.1999.tb01743.x>
- Hauber, E. & Kronberg, P., 2005. The large Thaumasia graben on Mars: Is it a rift? *J. Geophys. Res. Planets.* 110 (E7), E07003. doi: <http://dx.doi.org/10.1029/2005JE002407>
- Hauber, E., Brož, P., Jagert, F., Jodłowski, P., Platz, T., 2011. Very recent and wide-spread basaltic volcanism on Mars. *Geophys. Res. Lett.* 38 (10), 1-5. doi: <https://doi.org/doi:10.1029/2011GL047310>
- Hauber, E., Grott, M., Kronberg, P., 2010. Martian rifts: Structural geology and geophysics. *Earth.Planet. Sci. Lett.* 294 (3-4), 393-410. doi: <http://dx.doi.org/10.1016/j.epsl.2009.11.005>
- Hawkins, S.E., Boldt, J.D., Darlington, E.H. et al., 2007. The Mercury dual imaging system on the MESSENGER spacecraft. *Space Sci. Rev.* 131 (1-4), 247-338. doi: <https://doi.org/10.1007/s11214-007-9266-3>
- Head, J. W., Chapman, C. R., Strom, R. G., Fassett, C. I., Denevi, B. W., Blewett, D. T., et al., 2011. Flood volcanism in the northern high latitudes of Mercury revealed by MESSENGER. *Science*, 333 (6051), 1853-1856. doi: <https://doi.org/10.1126/science.1211997>
- Head, J. W., Kreslavsky, M. A., S. Pratt., 2002. Northern lowlands of Mars: Evidence for widespread volcanic flooding and tectonic deformation in the Hesperian Period. *J. Geophys. Res. Planet.* 107 (E1), 3-29. doi: <http://dx.doi.org/10.1029/2000JE001445>
- Head, J.W., Chapman, C.R., Domingue, D.L. et al. 2007., The Geology of Mercury: The View Prior to the MESSENGER Mission. *Space.Sci.Rev.* 131, 41-84. doi: <https://doi.org/10.1007/s11214-007-9263-6>
- Head, J.W., Murchie, S.L., Prockter, L.M., Robinson, M.S., Solomon, S.C., Strom, R.G., Chapman, C.R., Watters, T.R., McClintock, W.E., Blewett, D.T., Gillis-Davis, J.J., 2008. Volcanism on Mercury: evidence from the first MESSENGER flyby. *Science*. 321(5885), 69-72. doi: <https://doi.org/10.1126/science.1159256>
- Head, J.W., Murchie, S.L., Prockter, L.M., Robinson, M.S., Solomon, S.C., Strom, R.G., Chapman, C.R., Watters, T.R., McClintock, W.E., Blewett, D.T., Gillis-Davis, J.J., 2008. Volcanism on Mercury: evidence from the first MESSENGER flyby. *Science*, 321 (80), 69-72. doi: <https://doi.org/10.1126/science.1159256>
- Helgason, J., 1999. Formation of Olympus Mons and the aureole-escarpment problem on Mars. *Geology*. 27 (3), 231-234. doi: [https://doi.org/10.1130/0091-7613\(1999\)027<0231:FOOMAT>2.3.CO;2](https://doi.org/10.1130/0091-7613(1999)027<0231:FOOMAT>2.3.CO;2)
- Hodges, C. A. & H. J. Moore., 1994. Atlas of Volcanic Landforms on Mars. U.S. Gov. Print. Off., Washington D. C.
- Horvath, D.G., Moitra, P., Hamilton, C.W., Craddock, R.A., Andrews-Hanna, J.C., 2021. Evidence for geologically recent explosive volcanism in Elysium Planitia, Mars. *Icarus*. 365, 114499. doi: <https://doi.org/10.1016/j.icarus.2021.114499>
- Isherwood, R.J., Jozwiak, L.M., Jansen, J.C., Andrews-Hanna, J.C., 2013. The volcanic history of Olympus Mons from paleo-topography and flexural modelling. *Earth Planet.Sci. Lett.* 363, 88-96. doi: <http://dx.doi.org/10.1016/j.epsl.2012.12.020>
- Ivanov, M. A., Korteniemi, J., Kostama, V.-P., Aittola, M., Raitala, J., Glamoclija, M., Marinangeli, L., Neukum, G., 2005. Major episodes of the hydrologic history in the region of Hesperia Planum, Mars. *J. Geophys. Res. Planets.* 110 (E12), E12S21. doi: <https://doi.org/10.1029/2005JE002420>
- Ivanov, M.A., Head, J.W., 2006. Alba Patera, Mars: Topography, structure, and evolution of a unique late Hesperian–early Amazonian shield volcano. *J. Geophys. Res. Planets.* 111 (E9), E09003, doi: <https://doi.org/doi:10.1029/2005JE002469>
- Jackson, M.P.A., Adams, B.J., Dooley, T.P., Gillespie, A.R., Montgomery, D.R., 2011. Modeling the collapse of Hebes Chasma, Valles Marineris, Mars. *Geol. Soc. Am. Bull.* 123 (7-8), 1596-1627. doi: <https://doi.org/10.1130/B30307.1>
- Johnson, C.L., Phillips, R.J., 2005. Evolution of the Tharsis region of Mars: insights from magnetic field observations. *Earth Planet. Sci. Lett.* 230 (3-4), 241-254. doi: <https://doi.org/doi:10.1016/j.epsl.2004.10.038>

- Kerber, L., Head, J.W., Blewett, D.T., Solomon, S.C., Wilson, L., Murchie, S.L., Robinson, M.S., Denevi, B.W., Domingue, D.L., 2011. The global distribution of pyroclastic deposits on Mercury: The view from MESSENGER flybys 1–3. *Planet. Space Sci.* 59 (15), 1895-1909. doi: <https://doi.org/10.1016/j.pss.2011.03.020>
- Kim, Y.-S & Sanderson, D.J., 2005. The relationship between displacement and length of faults: A review. *Earth-Sci. Rev.* 68 (3-4), 317-334. doi: <http://dx.doi.org/10.1016/j.earscirev.2004.06.003>
- Kim, Y.S., Andrews, J.R., Sanderson, D.J., 2001. Reactivated strike-slip faults: examples from north Cornwall, UK. *Tectonophysics.* 340 (3-4), 173-194. doi: [http://dx.doi.org/10.1016/S0040-1951\(01\)00146-9](http://dx.doi.org/10.1016/S0040-1951(01)00146-9)
- Kinczyk, M. J., Prockter, L. M., Byrne, P. K., Denevi, B. W., Ostrach, L. R et al., 2018. A global geological map of Mercury. *Mercury. EPSC. Vol.13.* Geneva.
- Kinczyk, M. J., Prockter, L. M., Byrne, P. K., Susorney, H. C.M., Chapman, C. R., 2020. A morphological evaluation of crater degradation on Mercury: Revisiting crater classification with MESSENGER data. *Icarus.* 341, 113637. doi: <https://doi.org/10.1016/j.icarus.2020.113637>
- Klimczak, C., Crane, K.T., Habermann, M.A., Byrne, P.K., 2018. The spatial distribution of Mercury's pyroclastic activity and the relation to lithospheric weaknesses. *Icarus.* 315, 115-123. doi: <https://doi.org/10.1016/j.icarus.2018.06.020>
- Kling, C. L., Byrne, P. K., Atkins, R. M., Wegmann, K. W., 2021. Tectonic deformation and volatile loss in the formation of Noctis Labyrinthus, Mars. *J. Geophys. Res. Planets.* 126 (11), e2020JE006555. doi: <https://doi.org/10.1029/2020JE006555>
- Kronberg, P., Hauber, E., Grott, M., Werner, S.C., Schafer, T., Gwinner, K., Giese, B., Masson, P., Neukum, G., 2007. Acheron Fossae, Mars: tectonic rifting, volcanism, and implications for lithospheric thickness. *J. Geophys. Res.* 112 (E4), E04005. doi: <https://doi.org/10.1029/2006JE002780>
- Larson, S.K., 2007. The Origins of Four Paterae of Malea Planum, Mars. Ph.D thesis. Brigham young university - Provo, Utah. <https://scholarsarchive.byu.edu/etd/1079>
- Lenardic, A., Nimmo, F., Moresi, L., 2004. Growth of the hemispheric dichotomy and the cessation of plate tectonics on Mars. *J. Geophys. Res. Planets.* 109 (E2), E02003. doi: <https://doi.org/10.1029/2003JE002172>
- Leone, G., 2014. A network of lava tubes as the origin of Labyrinthus Noctis and Valles Marineris on Mars. *J. Volcanol. Geotherm.* 277, 1-8. doi: <http://dx.doi.org/10.1016/j.jvolgeores.2014.01.011>
- López, V., Ruiz, J., Vázquez, A., 2015. Evidence for two stages of compressive deformation in a buried basin of Mercury. *Icarus.* 254, 18-23. doi: <http://dx.doi.org/10.1016/j.icarus.2015.03.018>
- Lucchitta, B.K., 1979. Landslides in Valles Marineris, Mars. *J. Geophys. Res.* 84 (B14), 8097-8113. doi: <https://doi.org/10.1029/JB084iB14p08097>
- Lucchitta, B.K., Isbell, N.K., Howington, A., Kraus, A., 1994. Topography of Valles Marineris: implications for erosional and structural history. *J. Geophys. Res.* 99 (E2), 3783-3798. doi: <https://doi.org/10.1029/93JE03095>
- Lucchitta, B.K., McEwen, A.S., Clow, G.D., Geissler, P.E., Singer, R.B., Schultz, R.A., and Squyres, S.W., 1992. The canyon system of Mars. In Kieffer, H.H., et al (Eds). *Mars. Univ. of Ariz. Press*, 453-492.
- Massironi, M., Byrne, P.K., van der Bogert, C.H., 2014. Lobate Scarp. In: *Encyclopedia of Planetary Landforms.* Springer, New York, NY. doi: [https://doi.org/10.1007/978-1-4614-9213-9\\_491-1](https://doi.org/10.1007/978-1-4614-9213-9_491-1)
- Massironi, M., Cremonese, G., Marchi, S., Martellato, E., Mottola, S., Wagner, R.J., 2009. Mercury's geochronology revised by applying Model Production Functions to Mariner 10 data: geological implications. *Geophys. Res. Lett.* 36 (21), L21204. doi: <https://doi.org/10.1029/2009GL040353>
- Masson, P., 1997. Structure Pattern analysis of Noctis Labyrinthus-Valles Marineris regions of Mars. *Icarus.* 30 (1), 49-62. doi: [http://dx.doi.org/10.1016/0019-1035\(77\)90120-8](http://dx.doi.org/10.1016/0019-1035(77)90120-8)
- Masson, P., 1985. Origin and evolution of Valles Marineris region of Mars. *Adv.Space.Res.* 5 (8), 83-92. doi: [https://doi.org/10.1016/0273-1177\(85\)90244-3](https://doi.org/10.1016/0273-1177(85)90244-3)
- Mège, D., 2001. Uniformitarian plume tectonics: The post-Archean Earth and Mars. In R. E. Ernst and K. L. Buchan (Eds.). *Mantle Plumes: Their Identification Through Time.* *Geol. Soc. Am.* 352, 141-164. doi: <https://doi.org/10.1130/0-8137-2352-3.141>
- Mège, D., Bourgeois, O., 2011. Equatorial glaciations on Mars revealed by gravitational collapse of Valles Marineris wallslopes. *Earth Planet. Sci. Lett.* 310 (3-4), 182-191. doi: <https://doi.org/10.1016/j.epsl.2011.08.030>
- Mège, D., Cook, A. C., Garel, E., Lagabrielle, Y., Cormier, M.H., 2003. Volcanic rifting at Martian grabens. *J. Geophys. Res.* 108 (E5), E55044. doi: <https://doi.org/10.1029/2002JE001852>
- Mège, D., Ernst, R. E., 2001. Contractual effects of mantle plumes on Earth, Mars, and Venus. In R. E. Ernst and K. L. Buchan (Eds.). *Mantle Plumes: Their Identification Through Time.* *Geol. Soc. Am.* 352, 103-140. doi: <https://doi.org/10.1130/0-8137-2352-3.103>
- Mège, D., Korme, T., 2004. Fissure eruption of flood basalts from statistical analysis of dyke fracture length. *J. Volcanol. Geotherm. Res.* 132 (1-2), 77-92. doi: [http://dx.doi.org/10.1016/S0377-0273\(03\)00317-2](http://dx.doi.org/10.1016/S0377-0273(03)00317-2)
- Mège, D., Masson, P., 1996. A plume tectonics model for the Tharsis province, Mars. *Planet. Space Sci.* 44 (12), 1499-1546. doi: [https://doi.org/10.1016/S0032-0633\(96\)00113-4](https://doi.org/10.1016/S0032-0633(96)00113-4)
- Mège, D., Masson, P., 1996. Amounts of crustal stretching in Valles Marineris, Mars. *Planet. Space Sci.* 44 (8), 749-781. doi: [http://dx.doi.org/10.1016/0032-0633\(96\)00013-X](http://dx.doi.org/10.1016/0032-0633(96)00013-X)

- Melosh, H. J., Williams, C. A., Jr., 1989. Mechanics of graben formation in crustal rocks: A finite element analysis. *J. Geophys. Res.* 94 (B10), 13961-13973. doi: <https://doi.org/10.1029/JB094iB10p13961>
- Misra, S., Mandal, N., Chakraborty, C., 2009. Formation of Riedel shear fractures in granular materials: Findings from analogue shear experiments and theoretical analyses. *Tectonophysics*. 471 (3-4), 253-259. doi: <https://doi.org/10.1016/j.tecto.2009.02.017>
- Montgomery, D.R., Gillespie, A., 2005. Formation of Martian outflow channels by catastrophic dewatering of evaporite deposits. *Geology*. 33 (8), 625-628. doi: <http://dx.doi.org/10.1130/G21270.1>
- Montgomery, D.R., Som, S.M., Jackson, M.P.A., Schreiber, B.C., Gillespie, A.R., Adams, J.B., 2009. Continental-scale salt tectonics on Mars and the origin of Valles Marineris and associated outflow channels. *Geol. Soc. Am. Bull.* 121 (1-2), 117-133. doi: <https://doi.org/10.1130/B26307.1>
- Morris, E. C. & Tanaka, K.L., 1994. Geologic maps of the Olympus Mons region of Mars. Map. 1:2,000,000. Miscellaneous investigations series, map I-2327. Reston, VA: U.S. Geological Survey. doi: <https://doi.org/10.3133/i2327> Muraoka, H & Kamata, H., 1983. Displacement distribution along minor fault traces. *J. Struct. Geol.* 5 (5), 483-495. doi: [https://doi.org/10.1016/0191-8141\(83\)90054-8](https://doi.org/10.1016/0191-8141(83)90054-8)
- Mouginis-Mark, P. J., L. Wilson, and M. Zuber., 1992. The physical volcanology of Mars. Univ. of Ariz. Press, 424-452.
- Murchie, S.L., Klima, R.L., Denevi, B.W., Ernst, C.M., Keller, M.R., Domingue, D.L., Blewett, D.T., Chabot, N.L., Hash, C.D., Malaret, E., Izenberg, N.R., Vilas, F., Nittler, L.R., Gillis-Davis, J.J., Head, J.W., Solomon, S.C., 2015. Orbital multispectral mapping of Mercury with the MESSENGER Mercury Dual Imaging System: Evidence for the origins of plains units and low-reflectance material. *Icarus*. 254, 287-305. doi: <https://doi.org/10.1016/j.icarus.2015.03.027>
- Murchie, S.L., Watters, T.R., Robinson, M.S., Head, J.W., Strom, R.G., Chapman, C.R., Solomon, S.C., McClintock, W.E., Prockter, L.M., Domingue, D.L., Blewett, D.T., 2008. Geology of the Caloris basin, Mercury: a view from MESSENGER. *Science*, 321 (5885), 73-76. doi: <https://doi.org/10.1126/science.1159261>.
- Neukum, G., Jaumann, R., Hoffmann, H., Hauber, E., Head, J.W., Basilevsky, A.T., Ivanov, B.A., Werner, S, C., van Gasselt, S., Murray, J.B, McCord, T & the HRSC Co-Investigator Team., 2004. Recent and episodic volcanic and glacial activity on Mars revealed by the High Resolution Stereo Camera. *Nature*. 432, 971-979. doi: <https://doi.org/doi:10.1038/nature03231>
- Okubo, C. H & S. J. Martel., 1998. Pit crater formation on Kilauea volcano, Hawaii. *J. Volcanol. Geotherm. Res.* 86 (1-4), 1-18. doi: [https://doi.org/10.1016/S0377-0273\(98\)00070-5](https://doi.org/10.1016/S0377-0273(98)00070-5)
- Okubo, C.H & Schultz, R.A., 2006. Variability in Early Amazonian Tharsis stress state based on wrinkle ridges and strike-slip faulting. *J. Struct. Geol.* 28 (12), 2169-2181. doi: <https://doi.org/10.1016/j.jsg.2005.11.008>
- Okubo, C.H., Lewis, K.W., McEwen, A.S., Kirk, R.L., 2002. Relative age of interior layered deposits in southwest Candor Chasma based on high-resolution structural mapping. *J. Struct. Geol.* 113 (E12). doi: <https://doi.org/doi:10.1029/2008JE003181>
- Okubo, C.H., Schultz, R.A., Chan, M.A., Komatsu, G., 2009. Deformation band clusters on Mars and implications for subsurface fluid flow. *Geol. Soc. Am. Bull.* 121 (3-4), 474-482. doi: <https://doi.org/10.1130/B26421.1>
- Peacock, D. C. P., Sanderson, D. J., 1991. Displacement, segment linkage and relay ramps in normal fault zones. *J. Struct. Geol.* 13 (6), 721-733. doi: [https://doi.org/10.1016/0191-8141\(91\)90033-F](https://doi.org/10.1016/0191-8141(91)90033-F)
- Peacock, D.C.P., Anderson, M.W., 2012. The Scaling of Pull-Aparts and Implications for Fluid Flow in Areas with Strike-Slip Faults. *J. Pet. Geol.* 35 (4), 389-399. doi: <https://doi.org/10.1111/j.1747-5457.2012.00537.x>
- Pegg, D. L., Rothery, D. A., Balme, M. R., Conway, S. J., 2021. Explosive vent sites on mercury: Commonplace multiple eruptions and their implications. *Icarus*. 365, 114510. doi: <https://doi.org/10.1016/j.icarus.2021.114510>
- Pegg, D. L., Rothery, D. A., Conway, S. J., Balme, M. R., 2021. A fault surface exposed on Mercury. *Planet. Space Sci.* 201, 105223. doi: <https://doi.org/10.1016/j.pss.2021.105223>
- Pegg, D., Rothery, D.A., Balme, M., Conway, S.J., Malliband, C.C., Man, B., 2021. Geology of the Debussy quadrangle (H14), Mercury. *J. Maps*. 17 (2), 859-870. doi: <https://doi.org/10.1080/17445647.2021.1996478>
- Petropoulos, B., Macris, C., 1989. Physical parameters of the martian atmosphere. *Earth, Moon, and Planets.* 46 (1), 1-30. doi: <https://doi.org/10.1007/BF00056296>
- Peulvast, J.-P., Masson, P.L., 1993. Erosion and tectonics in Central Valles Marineris (Mars): a new morpho-structural model. *Earth, Moon, and Planets.* 61(3), 191-217. doi: <https://doi.org/10.1007/BF00572245>
- Peulvast, J.-P., Mège, D., Chiciak, J., Costard, F., Masson, P.L., 2001. Morphology, evolution and tectonics of Valles Marineris wallslopes (Mars). *Geomorphology*. 37 (3-4), 329-352. doi: [https://doi.org/10.1016/S0169-555X\(00\)00085-4](https://doi.org/10.1016/S0169-555X(00)00085-4)
- Platz, T., Byrne, P.K., Massironi, M., Hiesinger, H., 2015. Volcanism and tectonism across the inner solar system: an overview. *Geol. Soc. Spec. Publ.* 401 (1), 1-56. doi: <http://dx.doi.org/10.1144/SP401.22>
- Platz, T., Michael, G., Tanaka, K.L., Skinner Jr, J.A., Fortezzo., C.M., 2013. Crater-based dating of geological units on Mars: Methods and application for the new global geological map. *Icarus*. 225 (1), 806-827. doi: <http://dx.doi.org/10.1016/j.icarus.2013.04.021>
- Plescia, J. B., 1981. The Tempe volcanic province of Mars and comparisons with the Snake River Plains of Idaho. *Icarus*, 45, 586-601. doi: [https://doi.org/10.1016/0019-1035\(81\)90024-5](https://doi.org/10.1016/0019-1035(81)90024-5)
- Plescia, J. B., 1991. Graben and extension in northern Tharsis, Mars. *J. Geophys. Res. Planets.* 96 (E3), 18883-18895. doi: <https://doi.org/10.1029/91JE02005>

- Plescia, J.B. & Saunders, R.S., 1982. Tectonic history of the Tharsis region. *J. Geophys. Res.* 87(12), 9775-979. doi: <https://doi.org/10.1029/JB087iB12p09775>
- Polit, A.T., Schultz, R.A., Soliva, R., 2009. Geometry, displacement-length scaling, and extensional strain of normal faults on Mars with inferences on mechanical stratigraphy of the Martian crust. *J. Struct. Geol.* 31 (7), 662-673. doi: <http://dx.doi.org/10.1016/j.jsg.2009.03.016>
- Prockter, L.M., Ernst, C.M., Denevi, B.W., Chapman, C.R., Head, J.W., Fassett, C.I., Merline, W.J., Solomon, S.C., Watters, T.R., Strom, R.G., Cremonese, G., Marchi, S., Massironi, M., 2010. Evidence for young Volcanism on Mercury from the Third MESSENGER Flyby. *Science*, 329 (80). 668-671. doi: <https://doi.org/10.1126/science.1188186>
- Quantin, C., Allemand, P., Delacourt, C., 2004. Morphology and geometry of Valles Marineris landslides. *Planet. Space Sci.* 52 (11), 1011-1022. doi: <https://doi.org/10.1016/j.pss.2004.07.016>
- Quantin, C., Allemand, P., Mangold, N., Delacourt, C., 2004. Ages of Valles Marineris (Mars) landslides and implications for canyon history. *Icarus*. 172 (2), 555-572. doi: <https://doi.org/10.1016/j.icarus.2004.06.013>
- Richardson, J.A., Bleacher, J.E., Glaze, L.S., 2013. The volcanic history of Syria Planum, Mars. *J. Volcanol. Geotherm. Res.* 252, 1-13. doi: <http://dx.doi.org/10.1016/j.jvolgeores.2012.11.007>
- Roach, L.H., Mustard, J.F., Swayze, G., Milliken, R.E., Bishop, J.L., Murchie, S.L., Lichtenberg, K., 2010. Hydrated mineral stratigraphy of Ius Chasma, Valles Marineris. *Icarus*. 206 (1), 253-268. doi: <https://doi.org/10.1016/j.icarus.2009.09.003>
- Robinson, C.A., 1995. The crustal deformation of Mars. *Earth, Moon and Planets.* 69 (3), 249-269. doi: <https://doi.org/10.1007/BF00643787>
- Robinson, C.A., 1995. The crustal dichotomy of Mars. *Earth Moon Planet.* 69 (3), 249-269. doi: <https://doi.org/10.1007/BF00643787>
- Rodriguez, J.A.P., Kargel, J.S., Baker, V.R., Gulick, V.C., Berman, D.C., Fairén, A.G., Linares, R., Zarroca, M., Yan, J., Miyamoto, H., Glines, N., 2015. Martian outflow channels: how did their source aquifers form, and why did they drain so rapidly? *Sci. Rep.* 5 (1), 13404. doi: <http://dx.doi.org/10.1038/srep13404>
- Rodriguez, J.A.P., Leonard, G.J., Kargel, J.S., Domingue, D., Berman, D.C., Banks, M., Zarroca, M., Linares, R., Marchi, S., Baker, V.R., Webster, K.D., Sykes, M., 2020. The Chaotic Terrains of Mercury Reveal a History of Planetary Volatile Retention and Loss in the Innermost Solar System. *Sci. Rep.* 10 (1), 4737. doi: <https://doi.org/10.1038/s41598-020-59885-5>
- Rodriguez, J.A.P., Sasaki, S., Dohm, J.M., Tanaka, K.L., Strom, B., Kargel, J., Kuzmin, R., Miyamoto, H., Spray, J.G., Fairén, A.G., 2005. Control of impact crater fracture systems on subsurface hydrology, ground subsidence, and collapse, Mars. *J. Geophys. Res.* 110 (E6), 1-22. doi: <https://doi.org/10.1029/2004JE002365>
- Rodriguez, J.A.P., Zarroca, M., Linares, R., Gulick, V., Weitz, C.M., Yan, J., Fairén, A.G., Miyamoto, H., Platz, T., Baker, V., Kargel, J., Glines, N., Higuchi, K., 2016. Groundwater flow induced collapse and foolding in Noctis Labyrinthus, Mars. *Planet. Space Sci.* 124, 1-14. doi: <https://doi.org/10.1016/j.pss.2015.12.009>
- Rognini, E., Mura, A., Capria, M. T., Milillo, A., Zinzi, A., Galluzzi, V., 2022. Effects of Mercury surface temperature on the sodium abundance in its exosphere. *Planet. Space Sci.* 212, 105397. doi: <https://doi.org/10.1016/j.pss.2021.105397>
- Rothery, D.A., 2015. *Planet Mercury: From Pale Pink Dot to Dynamic World.* Springer-Praxis, Heidelberg. doi: <https://doi.org/10.1007/978-3-319-12117-8>
- Rothery, D.A., Barraud, O., Besse, S., Carli, C., Pegg, D.L., Wright, J., Zambon, F., 2021. On the asymmetry of Nathair Facula, Mercury. *Icarus*. 355 (107300), 114180. doi: <https://doi.org/10.1016/j.icarus.2020.114180>
- Rothery, D.A., Massironi, M., 2010. Beagle Rupes - Evidence for a basal decollement of regional extent in Mercury's lithosphere. *Icarus*. 209 (1), 256-261. doi: <https://doi.org/10.1016/j.icarus.2009.12.009>
- Rothery, D.A., Massironi, M., Alemanno, G. et al., 2020. Rationale for BepiColombo Studies of Mercury's Surface and Composition. *Space Sci. Rev.* 216 (4), 66. doi: <https://doi.org/10.1007/s11214-020-00694-7>
- Rubin, A. M., 1992. Dike-induced faulting and graben subsidence in volcanic rift zones. *J. Geophys. Res.* 97 (B2), 1839-1858. doi: <https://doi.org/10.1029/91JB02170>
- Rubin, A.M., 1995. Propagation of magma-filled cracks. *Annu. Rev. Earth. Planet. Sci.* 23, 287-336. doi: <https://doi.org/10.1146/annurev.earth.23.050195.001443>
- Ruj, T., Komatsu, G., Pasckert, J.H., and Dohm, J.M., 2019. Timings of early crustal activity in southern highlands of Mars: Periods of crustal stretching and shortening. *Geosci. Front.* 10 (3), 1029-1037. doi: <https://doi.org/10.1016/j.gsf.2018.05.016>
- Schlische, R.W., Young, S.S., Ackerman, R.V., Gupta, A., 1996. Geometry and scaling relation of a population of a very small rift related normal faults. *Geology*. 24 (8), 683-686. doi: [https://doi.org/10.1130/00917613\(1996\)024<0683:GASROA>2.3.CO;2](https://doi.org/10.1130/00917613(1996)024<0683:GASROA>2.3.CO;2)
- Scholz, C.H. & Cowie, P. A., 1990. Determination of total strain from faulting using slip measurements. *Nature*. 346 (6287), 837-839. doi: <https://doi.org/10.1038/346837a0>
- Schon, S.C., Head, J.W., Baker, D.M.H., Ernst, C.M., Prockter, L.M., Murchie, S.L., Solomon, S.C., 2011. Eminescu impact structure: Insight into the transition from complex crater to peak-ring basin on Mercury. *Planet. Space Sci.* 59 (15), 1949-1959. doi: <https://doi.org/10.1016/j.pss.2011.02.003>
- Schultz, R.A., 1988. Multiple-process origin of Valles Marineris basins and troughs, Mars. *Planet. Space Sci.* 46 (6-7), 827-834. doi: [https://doi.org/10.1016/S0032-0633\(98\)00030-0](https://doi.org/10.1016/S0032-0633(98)00030-0)



- Schultz, R.A., 1989. Strike-slip faulting of ridged plains near Valles Marineris, Mars. *Nature*. 341 (6241), 424-426. doi: <http://dx.doi.org/10.1038/341424a0>
- Schultz, R.A., 1991. Structural development of Coprates Chasma and western Ophir Planum, Valles Marineris Rift, Mars. *J. Geophys. Res.* 96 (E5), 22777-22792. doi: <https://doi.org/10.1029/91JE02556>
- Schultz, R.A., 1997. Displacement-length scaling for terrestrial and Martian faults: implication for Valles Marineris and shallow planetary grabens. *J. Geophys. Res.* 102 (B6), 12009-12015. doi: <https://doi.org/10.1029/97JB00751>
- Schultz, R.A., 2000. Fault-population statistics at the Valles Marineris extensional province, Mars: Implications for segment linkage, crustal strains, and its geodynamical development. *Tectonophysics*, 316 (1-2), 169-193. doi: [http://dx.doi.org/10.1016/S0040-1951\(99\)00228-0](http://dx.doi.org/10.1016/S0040-1951(99)00228-0)
- Schultz, R.A., Fori, A.N., 1996. Fault -length statistics and implications of graben sets at Candor Mensa, Mars. *J. Struct. Geol.* 18 (2-3), 373-383. doi : [https://doi.org/10.1016/S0191-8141\(96\)80057-5](https://doi.org/10.1016/S0191-8141(96)80057-5)
- Schultz, R.A., Fossen, H., 2002. Displacement-length scaling in three dimensions: the importance of the aspect ratio and application to deformation bands. *J. Struct. Geol.* 24 (9), 1389-1411. doi: [https://doi.org/10.1016/S0191-8141\(01\)00146-8](https://doi.org/10.1016/S0191-8141(01)00146-8)
- Schultz, R.A., Hauber, E., Kattenhorn, S.A., Okubo, C.H., Watters, T.R., 2010. Interpretation and analysis of planetary structures. *J. Struct. Geol.* 32 (6), 855-875. doi: <http://dx.doi.org/10.1016/j.jsg.2009.09.005>
- Schultz, R.A., Lin, J., 2001. Three-dimensional normal faulting models of the Valles Marineris, Mars, and geodynamic implications. *J. Geophys. Res. Solid Earth*. 106 (B8), 16549-16566. doi: <https://doi.org/10.1029/2001JB000378>
- Schultz, R.A., Okubo, C.H., Wilkins, S.J., 2006. Displacement-length scaling relations for faults on the terrestrial planets. *J. Struct. Geol.* 28 (12), 2182-2193. doi: <https://doi.org/10.1016/j.jsg.2006.03.034>
- Schultz, R.A., Soliva, R., Fossen, H., Okubo, C.H., Reeves, D.M., 2008. Dependence of displacement-length scaling for fractures and deformation bands on the volumetric changes across them. *J. Struct. Geol.* 30 (11), 1405-1411. doi: <http://dx.doi.org/10.1016/j.jsg.2008.08.001>
- Schultz, R.A., 1989. Strike-slip faulting of ridged plains near Valles Marineris, Mars. *Nature*. 341 (6241), 424-426. doi: <https://doi.org/10.1038/341424a0>
- Schultz, R.A., 1995. Gradients in extension and strain at Valles Marineris, Mars. *Planet. Space Sci.* 43 (12), 1561-1566. doi: [https://doi.org/10.1016/0032-0633\(95\)00111-5](https://doi.org/10.1016/0032-0633(95)00111-5)
- Schultz, R.A., 1998. Multiple-process origin of Valles Marineris basins and troughs, Mars. *Planet. Space Sci.* 46 (6-7), 827-834. doi: [http://dx.doi.org/10.1016/S0032-0633\(98\)00030-0](http://dx.doi.org/10.1016/S0032-0633(98)00030-0)
- Schultz, R.A., 2000. Fault-population statistics at the Valles Marineris Extensional Province, Mars: Implication for segment linkage, crustal strains, and its geodynamical development. *Tectonophysics*. 316 (1-2), 169-193. doi: [https://doi.org/10.1016/S0040-1951\(99\)00228-0](https://doi.org/10.1016/S0040-1951(99)00228-0)
- Schultz, R.A., 2003. A method to relate initial elastic stress to fault population strains. *Geophys. Res. Lett.* 30 (11), 1593. doi: <http://dx.doi.org/10.1029/2002GL016681>
- Schultz, R.A., Watters, T.R., 2001. Forward mechanical modeling of the Amenthes Rupes thrust fault on Mars. *Geophys. Res. Lett.* 28 (24), 4659-4662. doi: <https://doi.org/10.1029/2001GL013468>
- Schultz, R.A., 1999. Understanding the process of faulting: Selected challenges and opportunities at the edge of the 21st century. *J. Struct. Geol.* 21 (8-9), 985-993. doi: [https://doi.org/10.1016/S0191-8141\(99\)00025-5](https://doi.org/10.1016/S0191-8141(99)00025-5)
- Scott, D.H & Tanaka, K.L. 1986. Geologic map of the western equatorial region of Mars. *U.S. Geol. Surv. Misc. Inv. Map* 1-1802-A. doi: <https://doi.org/10.3133/i1802A>
- Scott, David H & Carr, Michael H., 1978. Geologic Map of Mars: U.S. Geological Survey Investigations. Series I-1083, scale 1:2500000. <http://pubs.er.usgs.gov/publication/i1083>
- Sleep, N. H., 1994. Martian plate tectonics. *J. Geophys. Res.* 99 (E3), 5639-5655. doi: <https://doi.org/10.1029/94JE00216>
- Sleep, N.H & Phillips, R.J., 1985. Gravity and lithospheric stress on the terrestrial planets with reference to the Tharsis region. *J. Geophys. Res. Solid Earth.* 90 (B6), 4469-4489. doi: <https://doi.org/10.1029/JB090iB06p04469>
- Soliva, R., & Schulz, R. A., 2008. Distributed and localized faulting in extensional settings: Insight from the north Ethiopian Rift-Afar transition area. *Tectonics*. 27(2). doi: <https://doi.org/10.1029/2007TC002148>
- Soliva, R., Benedicto, A., 2004. A linkage criterion for segmented normal faults. *J. Struct. Geol.* 26 (12), 2251-2267. doi: <https://doi.org/10.1016/j.jsg.2004.06.008>
- Soliva, R., Benedicto, A., 2005. Geometry, scaling relation and spacing of vertically restricted normal faults. *J. Struct. Geol.* 27 (2), 317-325. doi: <https://doi.org/10.1016/j.jsg.2004.08.010>
- Soliva, R., Benedicto, A., Maerten, L., 2006. Spacing and linkage of confined normal faults: importance of mechanical thickness. *J. Geophys. Res. Solid Earth.* 111(B1), 1-17. doi: <http://dx.doi.org/10.1029/2004JB003507>
- Soliva, R., Schultz, R.A., Benedicto, A., 2005. Three-dimensional displacement-length scaling and maximum dimension of normal faults in layered rocks. *Geophys. Res. Lett.* 32(16), 1-4. doi: <http://dx.doi.org/10.1029/2005GL023007>

- Solomon, S.C., McNutt Jr, R.L., Watters, T.R., Lawrence, D.J., Feldman, W.C., Head, J.W., Krimigis, S.M., Murchie, S.L., Phillips, R.J., Slavin, J.A., Zuber, M.T., 2008. Return to Mercury: A global perspective on MESSENGER's first Mercury flyby. *Science*.321(5885), 59-62. doi: <https://doi.org/10.1126/science.1159706>
- Solomon, S.C.,1976. Some aspects of core formation in Mercury. *Icarus*, 28 (4), 509-521. doi: [https://doi.org/10.1016/0019-1035\(76\)90124-X](https://doi.org/10.1016/0019-1035(76)90124-X)
- Strom, R.G., Chapman, C.R., Merline, W.J., Solomon, S.C., Head, J.W., 2008. Mercury cratering record viewed from MESSENGER's first flyby. *Science*. 321(5885), 79-81. doi: <https://doi.org/10.1126/science.1159317>
- Strom, R.G., Trask, N.J., Guest, J.E., 1975. Tectonism and volcanism on Mercury. *J. Geophys. Res.* 80 (17), 2478-2507. doi: <https://doi.org/10.1029/JB080i017p02478>
- Sylvester, A.G., 1988. Strike-slip faults. *Geol. Soc. Am. Bull.*100 (11), 1666-1703. doi: [http://dx.doi.org/10.1130/0016-7606\(1988\)100<1666:ssf>2.3.CO;2](http://dx.doi.org/10.1130/0016-7606(1988)100<1666:ssf>2.3.CO;2)
- Tanaka, K. L., Golombek, M. P. & Banerdt, W. B., 1991. Reconciliation of stress and structural histories of the Tharsis region of Mars. *J. Geophys. Res.* 96 (E1), 15617-15633. doi: <https://doi.org/10.1029/91JE01194>
- Tanaka, K.L., 1986. The stratigraphy of Mars. *J. Geophys. Res.*, 91 (19), 139-158. doi: <https://doi.org/10.1029/JB091iB13p0E139>
- Tanaka, K.L., Davis, P.A., 1988. Tectonic history of the Syria planum province of Mars. *J. Geophys. Res. Solid Earth.* 93 (B12), 14893-14917. doi: <https://doi.org/10.1029/JB093iB12p14893>
- Taylor, N.C., Johnson, J.H., Herd, R.A., Regan, C.E., 2020. What can Olympus Mons tell us about the Martian lithosphere? *J. Volcanol. Geotherm. Res.* 402, 106981. doi: <https://doi.org/10.1016/j.jvolgeores.2020.106981>
- Thomas, R. J., Rothery, D. A., Conway, S. J & Anand, M., 2014. Mechanisms of explosive volcanism on Mercury: Implications from its global distribution and morphology. *J. Geophys. Res.* 119 (10), 2239-2254. doi: <https://doi.org/10.1002/2014JE004692>
- Thomas, R.J., Rothery, D.A., Conway, S.J., Anand, M., 2014. Hollows on Mercury: materials and mechanisms involved in their formation. *Icarus*. 229, 221-235. doi: <https://doi.org/10.1016/j.icarus.2013.11.018>
- Thomas, R.J., Rothery, D.A., Conway, S.J., Anand, M., 2014. Hollows on Mercury: Materials and mechanisms involved in their formation. *Icarus*. 229,221-235. doi: <https://doi.org/10.1016/j.icarus.2013.11.018>
- Thomas, T.R., 1988. Wrinkle ridge assemblages on the terrestrial planets. *J. Geophys. Res. Solid Earth.* 93 (B9), 10236-10254. doi: <https://doi.org/10.1029/JB093iB09p10236>
- Thompson, R. N & Gibson, S. A., 1991. Subcontinental mantle plumes, hotspots and pre-existing thinspots. *J. Geol. Soc.*148 (6), 973-977. doi: <https://doi.org/10.1144/gsjgs.148.6.0973>
- Torabi, A., Alaei, B., Libak, A., 2019. Normal fault 3D geometry and displacement revisited: Insights from faults in the Norwegian Barents Sea. *Mar. Pet. Geol.* 99,135-155. doi: <https://doi.org/10.1016/j.marpetgeo.2018.09.032>
- Torabi, A., Berg, S.S., 2011. Scaling of faults distributes: A review. *Mar. Pet. Geol.* 28 (8), 1444-1460. doi: <http://dx.doi.org/10.1016/j.marpetgeo.2011.04.003>
- Trask, N. J & Guest, J. E., 1975. Preliminary geologic terrain map of Mercury. *J. Geophys. Res.* 80 (17), 2461-2477. doi: <https://doi.org/10.1029/JB080i017p02461>
- Uzel, U., 2016. Field evidence for normal fault linkage and relay ramp evolution: the Kırkağaç Fault Zone, western Anatolia (Turkey). *Geodin. Acta.* 28 (4), 311-327. doi: <https://doi.org/10.1080/09853111.2016.1184778>
- Walsh, J. J & Watterson, J., 1987. Distribution of cumulative displacement and of seismic slip on a single normal fault surface. *J. Struct. Geol.* 9 (8), 1039-1046. doi: [https://doi.org/10.1016/0191-8141\(87\)90012-5](https://doi.org/10.1016/0191-8141(87)90012-5)
- Walsh, J. J & Watterson, J., 1991. Geometric and kinematic coherence and scale effects in normal fault systems. *Geol. Soc. Spec. Publ.* 56 (1),193-203. doi: <http://dx.doi.org/10.1144/GSL.SP.1991.056.01.13>
- Walsh, J. J & Watterson, J., 1992. Populations of faults and fault displacements and their effects on estimates of fault-related regional extension. *J. Struct. Geol.* 14 (6),701-712. doi: [https://doi.org/10.1016/0191-8141\(92\)90127-I](https://doi.org/10.1016/0191-8141(92)90127-I)
- Walsh, J.J., Bailey, W.R., Childs, C., Nicol, A., Bonson, C.G., 2003. Formation of segmented normal faults: a 3-D perspective. *J. Struct. Geol.* 25 (8), 1251-1262. doi: [https://doi.org/10.1016/S0191-8141\(02\)00161-X](https://doi.org/10.1016/S0191-8141(02)00161-X)
- Walsh, J.J., Watterson, J., 1988. Analysis of the relationship between displacement and dimensions of faults. *J. Struct. Geol.*10 (3), 239-247. doi: [https://doi.org/10.1016/0191-8141\(88\)90057-0](https://doi.org/10.1016/0191-8141(88)90057-0)
- Walsh, J.J., Watterson, J., Bailey, W.R., Childs, C., 1999. Fault relays, bends and branch-lines. *J. Struct. Geol.* 21 (8-9), 1019-1026. doi: [https://doi.org/10.1016/S0191-8141\(99\)00026-7](https://doi.org/10.1016/S0191-8141(99)00026-7)
- Walsh, J.J., Watterson, J., Yielding, G., 1991. The importance of small-scale faulting in regional extension. *Nature*. 351 (6325),391-393. doi: <https://doi.org/10.1038/351391a0>
- Walter, T.R & Troll, V.R., 2001. Formation of caldera periphery faults: an experimental study. *Bull. Volcanol.* 63 (2), 191-203. doi: <http://dx.doi.org/10.1007/s004450100135>

- Watters, T., Robinson, M., Banks, M. et al., 2012. Recent extensional tectonics on the Moon revealed by the Lunar Reconnaissance Orbiter Camera. *Nat. Geosci.* 5, 181-185. doi: <https://doi.org/10.1038/ngco1387>
- Watters, T.R., 1988. Wrinkle ridge assemblages on the terrestrial planets. *J. Geophys. Res. Solid Earth.* 93 (B9), 10236-10254. doi: <https://doi.org/10.1029/JB093iB09p10236>
- Watters, T.R., 1993. Compressional tectonism on Mars. *J. Geophys. Res.* 98 (E9), 17049-17060. doi: <https://doi.org/10.1029/93JE01138>
- Watters, T.R., 2021. A case for limited global contraction of Mercury. *Commun. Earth Environ.* 2 (1),9. doi: <https://doi.org/10.1038/s43247-020-00076-5>
- Watters, T.R., Daud, K., Banks, M.E., Selvans, M.M., Chapman, C.R & Ernst, C.M., 2016. Recent tectonic activity on Mercury revealed by small thrust fault scarps. *Nat. Geosci.* 9 (10), 743-747. doi: <https://doi.org/10.1038/ngco2814>
- Watters, T.R., Head, J.W., Solomon, S.C., Robinson, M.S., Chapman, C.R., Denevi, B.W., Fassett, C.I., Murchie, S.L., Strom, R.G., 2009. Evolution of the Rembrandt Impact Basin on Mercury. *Science.* 324 (5927), 618-621. doi: <https://doi.org/10.1126/science.1172109>
- Watters, T.R., Maxwell, T.A., 1986. Orientation, Relative Age, and Extent of the Tharsis Plateau Ridge System. *J. Geophys. Res.* 91 (B8), 8113-8125. doi: <https://doi.org/10.1029/JB091iB08p08113>
- Watters, T.R., McGovern, P.J., Irwin, R.P., 2007. Hemispheres Apart: The Crustal Dichotomy on Mars. *Annu. Rev. Earth Planet. Sci.* 35, 621-652. doi: <https://doi.org/10.1146/annurev.earth.35.031306.140220>
- Watters, T.R., Nimmo, F., Robinson, M.S., 2005. Extensional troughs in the Caloris Basin of Mercury: Evidence of lateral crustal flow. *Geology.* 33 (8), 669-672. doi: <https://doi.org/10.1130/G21678AR.1>
- Watters, T.R., Robinson, M.S., 1999. Lobate scarps and the Martian crustal dichotomy. *J. Geophys. Res.* 104 (E8), 18981-18990. doi: <https://doi.org/10.1029/1998JE001007>
- Watters, T.R., Robinson, M.S., Bina, C.R., Spudis, P.D., 2004. Thrust faults and the global contraction of Mercury. *Geophys. Res. Lett.* 31 (4), L04701. doi: <https://doi.org/10.1029/2003GL019171>
- Watters, T.R., Schultz, R.A., Robinson, M.S., Cook, A.C., 2002. The mechanical and thermal structure of Mercury's early lithosphere. *Geophys. Res. Lett.* 29 (11), 37-1-37-4. doi: <https://doi.org/10.1029/2001GL014308>
- Watters, T.R., 2003. Thrust faults along the dichotomy in the eastern hemisphere of Mars. *J. Geophys. Res.* 108(E6), 5054. doi: <http://dx.doi.org/10.1029/2002JE001934>
- Watterson, J., 1986. Fault dimensions, displacements and growth. *Pure Appl. Geophys.* 124 (1-2), 365-373. doi: <https://doi.org/10.1007/BF00875732>
- Weitz, C.M & Bishop, J.L., 2014. Diversity of hydrated minerals and deposits at Noctis Labyrinthus: implications for the late Hesperian to Amazonian aqueous activity on Mars. *Int. Conf. Mars.* 1791, 1222. Bibcode: 2014LPICo1791.1222W
- Weitz, C.M., Bishop, J.L., Grant, J.A., 2013. Gypsum, opal, and fluvial channels within a trough of Noctis Labyrinthus, Mars: implications for aqueous activity during the late Hesperian to Amazonian. *Planet. Space Sci.* 87, 130-145. doi: <https://doi.org/10.1016/j.pss.2013.08.007>
- Weitz, C.M., Bishop, J.L., Thollot, P., Mangold, N., Roach, L.H., 2011. Diverse mineralogies in two troughs of Noctis Labyrinthus, Mars. *Geology.* 39 (10), 899-902. doi: <http://dx.doi.org/10.1130/G32045.1>
- Werner, S.C., 2009. The global martian volcanic evolutionary history. *Icarus.* 201(1), 44-68. doi: <https://doi.org/10.1016/j.icarus.2008.12.019>
- Werner, S.C., Tanaka, K.L., Skinner Jr, J.A., 2011. Mars: The evolutionary history of the northern lowlands based on crater counting and geologic mapping. *Planet. Space Sci.* 59 (11-12), 1143-1165. doi: <https://doi.org/10.1016/j.pss.2011.03.022>
- Westaway, R., 1994. Quantitative analysis of populations of small faults. *J. Struct. Geol.* 16 (9), 1259-1273. doi: [https://doi.org/10.1016/0191-8141\(94\)90068-X](https://doi.org/10.1016/0191-8141(94)90068-X)
- White, R. & McKenzie, D., 1989. Magmatism at rift zones: The generation of volcanic continental margins and flood basalts. *J. Geophys. Res. Solid Earth.* 94 (B6), 7685-7729. doi: <https://doi.org/10.1029/JB094iB06p07685>
- Whitten, J.L., Head, J.W., Denevi, B.W., Solomon, S.C., 2014. Intercrater plains on Mercury: insights into unit definition, characterization, and origin from MESSENGER datasets. *Icarus.* 241., 97-113. doi: <https://doi.org/10.1016/j.icarus.2014.06.013>
- Wilkins, S.J & Gross, M.R., 2002. Normal fault growth in layered rocks at Split Mountains, Utah: influence of mechanical stratigraphy on dip linkage, fault restriction and fault scaling. *J. Struct. Geol.* 24 (9), 1413-1429. doi: [https://doi.org/10.1016/S0191-8141\(01\)00154-7](https://doi.org/10.1016/S0191-8141(01)00154-7)
- Wilkins, S.J & Schultz, R.A., 2003. Cross faults in extensional settings: Stress triggering, displacement localization, and implications for the origin of blunt troughs at Valles Marineris, Mars. *J. Geophys. Res.* 108 (E6), 5056. doi: <http://dx.doi.org/10.1029/2002JE001968>
- Wilkins, S.J., Gross, M.R., Wacker, M., Eyal, Y., Engelder, T., 2001. Faulted joints: Kinematics, displacement-length scaling relations and criteria for their identification. *J. Struct. Geol.* 23 (2-3), 315-327. doi: [https://doi.org/10.1016/S0191-8141\(00\)00098-5](https://doi.org/10.1016/S0191-8141(00)00098-5)
- Willemsse, E.J.M., 1997. Segmented normal faults: Correspondence between three-dimensional mechanical models and field data. *J. Geophys. Res. Solid Earth.* 102 (B1), 675-692. doi: <https://doi.org/10.1029/96JB01651>
- Willemsse, E.J.M., Pollard, D.D., 1998. On the orientation and pattern of wing cracks and solution surfaces at the tips of a sliding flaw of fault. *J. Geophys. Res. Solid Earth.* 103 (B2), 2427-2438. doi: <https://doi.org/10.1029/97JB01587>

- Williams, J.-P., Paige, D.A., Manning, C.E., 2003. Layering in the wall rock of Valles Marineris: intrusive and extrusive magmatism. *Geophys. Res. Lett.* 30 (12), 1623. doi: <https://doi.org/10.1029/2003GL017662>
- Williams, J.-P., Nimmo, F., Moore, W.B., Paige, D.A., 2008. The formation of Tharsis on Mars: What the line-of-sight gravity is telling us. *J. Geophys. Res.* 113 (E10), E10011. doi: <https://doi.org/doi:10.1029/2007JE003050>
- Wilson, L & Head, J. W., 1983. A comparison of volcanic eruption processes on Earth, Moon, Mars, Io, and Venus. *Nature.* 302, 663-669. doi: <https://doi.org/10.1038/302663a0>
- Wilson, L., Head, J.W., 1994. Mars: Review and analysis of volcanic eruption theory and relationships to observed landforms. *Rev. Geophys.* 32 (3), 221-263. doi: <https://doi.org/10.1029/94RG01113>
- Wise, D.U., Golombek, M.P., McGill, G.E., 1979. Tharsis Province of Mars: geologic sequence, geometry, and a deformation mechanism. *Icarus* 38, 456-472. doi: [https://doi.org/10.1016/0019-1035\(79\)90200-8](https://doi.org/10.1016/0019-1035(79)90200-8)
- Wright, J., Rothery, D. A., Balme, M. R., & Conway, S. J., 2019. Geology of the Hokusai quadrangle (H05), Mercury. *J. Maps*, 15(2), 509-520. doi: <https://doi.org/10.1080/17445647.2019.1625821>
- Wyrick, D., Ferrill, D.A., Morris, A.P., Colton, S.L., Sims, D.W., 2004. Distribution, morphology, and origins of Martian pit crater chains. *J. Geophys. Res.* 109(E6), E06005. doi: <http://dx.doi.org/10.1029/2004JE002240>
- Xu, S.-S., Nieto-Samaniego, A.F., Alaniz-Álvarez, S.A., Velasquillo Martínez, L.G., 2005. Effect of sampling and linkage on fault length and length-displacement relationship. *Int.J.Earth.Sci.* 95 (5), 841-853. doi: <https://doi.org/10.1007/s00531-005-0065-3>
- Yin, A., 2012. An episodic slab-rollback model for the origin of the Tharsis rise on Mars: Implications for initiation of local plate subduction and final unification of a kinematically linked global plate-tectonic network on Earth. *Lithosphere.* 4 (6), 553-593. doi: <https://doi.org/10.1130/L195.1>
- Yin, A., 2012. Structural analysis of the Valles Marineris fault zone: Possible evidence for large-scale strike-slip faulting on Mars. *Lithosphere.* 4 (4), 286-330. doi: <http://dx.doi.org/10.1130/L192.1>
- Young-Seog, K., Peacock, D.C.P., Sanderson, D.J., 2003. Mesoscale strike-slip faults and damage zones at Marsalforn, Gozo Island, Malta. *J. Struct. Geol.* 25 (5), 793-812. doi: [https://doi.org/10.1016/S0191-8141\(02\)00200-6](https://doi.org/10.1016/S0191-8141(02)00200-6)
- Young-Seog, K., Peacock, D.C.P., Sanderson, D.J., 2004. Fault damage zones. *J. Struct. Geol.* 26 (3), 503-517. doi: <https://doi.org/10.1016/j.jsg.2003.08.002>
- Young-Seog, K., Sanderson, D.J., 2004. Similarities between strike-slip faults at different scales and a simple age determining method for active faults. *Isl. Arc.* 13 (1), 128-143. doi: <https://doi.org/10.1111/j.1440-1738.2003.00410.x>
- Zhang, Z., Chen, J.Y. & Lin, J., 2008. Stress interactions between normal faults and adjacent strike-slip faults of 1997 Jiashi earthquake swarm. *Sci.China.Earth.Sci.* 51 (3), 431-440. doi: <https://doi.org/10.1007/s11430-008-0023-6>
- Zulauf, G., Gutiérrez-Alonso, G., Kraus, R., Petschick, R., Potel, S., 2011. Formation of chocolate-tablet boudins in a foreland fold and thrust belt: A case study from the external Variscides (Almogrove, Portugal). *J. Struct. Geol.* 33 (11), 1639-1649. doi: <https://doi.org/10.1016/j.jsg.2011.08.009>
- Zulauf, G., Zulauf, J., Hastreiter, P., Tomandl, B., 2003. A deformation apparatus for three-dimensional coaxial deformation and its application to rheologically stratified analogue material. *J. Struct. Geol.* 25 (3), 469-480. doi: [https://doi.org/10.1016/S0191-8141\(02\)00023-8](https://doi.org/10.1016/S0191-8141(02)00023-8)
- Zulauf, J., Zulauf, G., Göttlich, G., Peinl, M., 2014. Formation of chocolate-tablet boudins: Results from scaled analogue models. *J. Struct. Geol.* 68 (1), 97-111. doi: <https://doi.org/10.1016/j.jsg.2014.09.005>